Analysis and design of metasurface antennas for simultaneous beamforming in transmission and reflection

Alessio Berto

Thèse de doctorat

Analysis and Design of Metasurface Antennas for Simultaneous Beamforming in Transmission and Reflection

Thèse de doctorat de Sorbonne Université

École doctorale n°391, Science Mécaniques, Acoustique, Electronique et Robotique de Paris (SMAER)
Spécialité de doctorat: Génie électrique, électronique, photonique et systèmes
Unité de recherche: CEA-Leti, Geeps

Thèse présentée et soutenue à Grenoble, le 7 Novembre 2024, par

Alessio BERTO

Composition du jury:

Muriel Darces Professeure des universités, Sorbonne Université	Présidente
Francesca Vipiana Professeure des universités, Politecnico di Torino	Rapportrice
María García Vigueras Maître de conférences, INSA Rennes	Rapportrice
Carlos Molero Chercheur, University of Granada	Examinateur
Guido Valerio Professeur des universités, Sorbonne Université	Directeur
Francesco Foglia Manzillo Ingénieur de recherche, CEA-Leti	Co-encadrant
Nelson Fonseca Innovation Manager, Anywaves	Invité

Well, here at last, dear friends, on the shores
of the Sea comes the end of our fellowship in Middle-earth.
Go in peace! I will not say: do not weep; for not all tears are an evil.

John Ronald Reuel Tolkien

Contents

List of Figures vii

List of Tables xi

Acronyms xiii

List of Symbols xv

Acknowledgements xvii

Abstract xix

Synthèse de la recherche xxi

1 Introduction 1
- 1.1 Background . . . 2
- 1.2 Motivation . . . 4
- 1.3 Outline . . . 5

2 State of the Art 7
- 2.1 Metamaterials: An Electromagnetic Revolution . . . 8
- 2.2 From Metamaterials to Metasurfaces . . . 10
- 2.3 Metasurface Model . . . 11
  - 2.3.1 Taxonomy . . . 13
  - 2.3.2 Scattering Response . . . 17
- 2.4 Metasurface Analysis . . . 19
  - 2.4.1 Sheet impedance cascade . . . 21
  - 2.4.2 Dispersion Study: Passband and Stopband . . . 22
  - 2.4.3 Transverse Resonance Method . . . 24
- 2.5 Intelligent surfaces for wireless enhancement . . . 25
- 2.6 Transmit-Reflect array . . . 27
  - 2.6.1 Design Approaches . . . 28
  - 2.6.2 Mode Switching . . . 28
  - 2.6.3 Frequency Selection . . . 30
  - 2.6.4 Aperture Division . . . 32
  - 2.6.5 Energy Splitting . . . 32
- 2.7 Chapter Landmarks . . . 38

3 Metasurfaces for simultaneous refraction and reflection 39
- 3.1 Huygens' Metasurfaces . . . 40
- 3.2 Analytical Model . . . 41
  - 3.2.1 Free space condition . . . 45

3.3 Arbitrary Amplitude Condition of Scattered Fields for a MS between Different Media . . . 45
3.3.1 Equal Amplitude Condition . . . 48
3.4 Arbitrary Division of Incident Power into Scattered Fields for a MS in Free Space . . . 48
3.4.1 Equal amplitude . . . 50
3.5 Design of TRA H-MS Cells as Cascades of Impedance Sheets . . . 52
3.5.1 Design with Two Impedance Sheets . . . 53
3.5.2 Design with Three Impedance Sheets . . . 56
3.6 Impedance Sheet Design using Patterned Metal Layers . . . 57
3.6.1 Patch . . . 59
3.6.2 Dog-bone . . . 60
3.6.3 Meander . . . 61
3.7 Chapter Landmarks . . . 63

4 Transmit-Reflect arrays: Design and Characterization 65
4.1 Introduction . . . 66
4.2 Geometrical optics approach . . . 67
4.2.1 Focal Source . . . 68
4.2.2 Unit cells . . . 69
4.2.3 Model for the Analysis of The Transmitted Field . . . 70
4.2.4 Model for the Analysis of The Reflected Field . . . 72
4.2.5 Transmit-Reflect-array Model . . . 73
4.3 Unit Cells Design . . . 73
4.3.1 Dielectric slabs: thickness impact . . . 74
4.3.2 Scattering response . . . 74
4.3.3 Impedance sheet physical implementation . . . 75
4.3.4 Oblique Incidence . . . 78
4.3.5 Fabrication Constraints . . . 79
4.4 Transmit-Reflect-Array Design . . . 82
4.4.1 Steering at $\theta^{ta} = 15°$ and $\varphi^{ta} = 0°$ . . . 84
4.4.2 Steering at $\theta^{ta} = 30°$ and $\varphi^{ta} = 0°$ . . . 86
4.4.3 Steering at $\theta^{ta} \geq 60°$ and $\varphi^{ta} = 0°$ . . . 86
4.5 Measurements . . . 89
4.5.1 Transmit-Reflect-array of 60×60 elements . . . 90
4.5.2 Transmit-Reflect-array of 80×80 elements . . . 92
4.5.3 Transmit-Reflect-array of 120×120 elements . . . 94
4.6 Literature Comparison . . . 98
4.7 Chapter Landmarks . . . 101

5 Towards independent beamforming 103
5.1 Bi-anisotropic Metasurfaces . . . 104
5.2 Analytical Model . . . 105
5.2.1 Analysis of a lossless O-BIMS in free space . . . 107

5.3 Conditions for an Arbitrary Division of the Scattered Power 107
5.4 Conditions for Equalizing Transmitted and Reflected Power 108
5.4.1 Solution for the electrical susceptance 109
5.4.2 Solution for the magneto-electric coupling factor 111
5.5 Design of a power-splitting O-BIMS as a cascade of sheet impedances . . 112
5.5.1 Two-sheet Design 112
5.5.2 Three-sheet design 114
5.6 Preliminary design of TRA Unit-Cells using O-BIMSs 115
5.7 Chapter Landmarks 121

6 Conclusion **123**
6.1 Research Summary 124
6.2 Perspective 125
6.2.1 TRA design with independent beams 125
6.2.2 Circular Polarization 126
6.2.3 Reconfigurability 126

A Cells robustness under oblique incidence **127**
A.1 Oblique incidence: $\phi_\tau = 15°$ 128
A.2 Oblique incidence: $\phi_\tau = 105°$ 128
A.3 Oblique incidence: $\phi_\tau = 285°$ 128

List of Publications **131**

References **133**

Curriculum Vitæ **147**

List of Figures

0.1 Modèle de Métasurface éclairé par une onde plane à incidence normale xxii
0.2 Conception préliminaire des cellules H-MS pour TRA xxiii
0.3 TRA Prototype et configuration des mesures xxiv
0.4 Conception préliminaire des cellules O-BIMS pour TRA xxv

2.1 Padilla's Metamaterial 9
2.2 Periodic structures classification 10
2.3 Metasurface categories 11
2.4 General metasurface model 12
2.5 Scattering model of a generic metasurface 12
2.6 Three-layer metasurface model 19
2.7 Four and two port models of metasurfaces 21
2.8 Attenuation and phase constant for a three-layer metasurface 23
2.9 Attenuation and phase constant for a three-layer metasurface with closed bandgaps 24
2.10 TRM applied to a three-layer metasurface 24
2.11 Computed propagation constant for TE and TM modes using TRM . . . 25
2.12 General RIS scenario 26
2.13 Space-fed array taxonomy 27
2.14 TRAs based on Mode Switching Strategy 29
2.15 TRAs based on Frequency Selection Strategy 31
2.16 TRAs based on Aperture Division Strategy 33
2.17 TRAs based on Energy Splitting Strategy: part 1 34
2.18 TRAs based on Energy Splitting Strategy: part 2 35

3.1 H-MS illuminated by a normal incident y-polarized wave propagating along positive z-axis 41
3.2 H-MS illuminated by a normal incident y-polarized wave propagating along negative z-axis 43
3.3 Scattering coefficients for a H-MS in between two dielectric regions with different electric permittivity 44
3.4 Scattering parameters of a H-MS located in free space 46
3.5 Solutions of arbitrary amplitude intensity of scattered fields for an isotropic, lossless and reciprocal H-MS between different media 47
3.6 Solutions for equal amplitude of scattered fields for a H-MS between two different media 49
3.7 Solutions of arbitrary amplitude intensity of scattered fields for an isotropic, lossless and reciprocal H-MS in free space 50

3.8 Solutions for equal amplitude of scattered fields for an isotropic, lossless and reciprocal H-MS between different media . . . 51
3.9 Two-layer MS model . . . 53
3.10 Phase range limit for a two-layer H-MS cell in function of X_{m_A} . . . 55
3.11 Phase range limit for a two-layer H-MS cell in function of X_{m_B} . . . 56
3.12 Sheet impedances variation for a three-layer H-MS in free space implementing equal amplitude scattered fields . . . 57
3.13 Impedance sheet evaluation: simulation setup . . . 58
3.14 Square patch geometry and full-wave parametric analysis . . . 59
3.15 Patch equivalent circuit and frequency behavior of the sheet impedance 59
3.16 Dog-bone geometry and full-wave parametric analysis . . . 60
3.17 Dog-bone equivalent circuit and frequency behavior of the sheet impedance . . . 61
3.18 Meander geometry and full-wave parametric analysis . . . 62
3.19 Meander equivalent circuit and frequency behavior of the sheet impedance . . . 63

4.1 Trasmitarray antenna model . . . 67
4.2 Focal source patterns comparison: ideal and commercial ATM 10-dBi horn . . . 69
4.3 Comparison of elements pattern . . . 70
4.4 Trasmitarray model with discretizazion of spillover area . . . 71
4.5 Reflectarray antenna model . . . 72
4.6 Scattering phases and optimum surface parameters of the four H-MS-based TRA cells . . . 74
4.7 Dielectric slab thickness impact on the sheet impedance for each H-MS-based TRA cell . . . 75
4.8 Designed scattering coefficient magnitudes of the four H-MS-based TRA cells . . . 75
4.9 Designed scattering coefficient phases of the four H-MS-based TRA cells 76
4.10 Metal pattern of each H-MS-based TRA cell external layer . . . 76
4.11 Metal pattern of each H-MS-based TRA cell inner layer . . . 77
4.12 Scattering parameter amplitudes of the designed H-MS-based TRA cell 79
4.13 Scattering parameter phases of the designed H-MS-based TRA cells . . 79
4.14 Oblique incidence amplitude variation for $\phi_\tau = 195°$ . . . 80
4.15 Oblique incidence phase variation for $\phi_\tau = 195°$ . . . 80
4.16 Sheet impedance variation as a function of frequency of the four H-MS-based TRA cells . . . 81
4.17 Design of the four H-MS-based TRA cells with commercial stack-up . . 82
4.18 Scattering parameter magnitudes of the four H-MS-based TRA cells with commercial stack-up . . . 83
4.19 Scattering parameter phases of the four H-MS-based TRA cells with commercial stack-up . . . 83
4.20 Magnitude and phase distribution of the focal source field impinging the 60×60 elements TRA . . . 84

4.21 Maximum directivity, gain and aperture efficiency as a function of F/D for a TRA with broadside radiation . . . 84
4.22 Phase distribution on a 60 × 60 TRA for beam steering at $\theta_{st}^{ta} = 15°$ and $\phi_{st}^{ta} = 0°$ . . . 85
4.23 Comparison cuts at $\phi = 0°$ for for the 60 × 60 elements Transmit-Reflect-array (TRA) steering at $\theta_{st}^{ta} = 15°$ . . . 85
4.24 Phase distribution on a 60 × 60 TRA for beam steering at $\theta_{st}^{ta} = 30°$ and $\phi_{st}^{ta} = 0°$ . . . 86
4.25 Comparison cuts at $\phi = 0°$ for the 60 × 60 elements TRA steering at $\theta_{st}^{ta} = 30°$ . . . 87
4.26 Phase distribution on a 60 × 60 TRA for beam steering at $\theta_{st}^{ta} = 60°$ and $\phi_{st}^{ta} = 0°$ . . . 87
4.27 Comparison radiation patterns at $\varphi = 0°$ for 60 × 60 TRA steering at $\theta_{st}^{ta} = 60°$ and $\phi_{st}^{ta} = 0°$ . . . 88
4.28 Comparison radiation patterns of a 60 × 60 TRA for steering angles $\theta_{st}^{ta} > 60°$ and $\phi_{st}^{ta} = 0°$ . . . 89
4.29 Prototype and measurement setup . . . 90
4.30 Comparison radiation patterns at $\varphi = 0°$ for 60 × 60 TRA steering at $\theta_{st}^{ta} = 30°$ and $\phi_{st}^{ta} = 0°$ . . . 91
4.31 Comparison maximum gain and aperture efficiency of the 60 × 60 elements TRA pointing at $\theta_{st}^{ta} = 30°$ and $\phi_{st}^{ta} = 0°$ as a function of frequency . . . 91
4.32 Copolar and crosspolar variation of the 60 × 60 elements TRA pointing at $\theta_{st}^{ta} = 30°$ and $\phi_{st}^{ta} = 0°$ as a function of frequency. . . . 92
4.33 Magnitude and phase distribution of the focal source field impinging the 80 × 80 elements TRA . . . 93
4.34 Phase distribution on a 80 × 80 TRA for beam steering at $\theta_{st}^{ta} = 30°$ and $\phi_{st}^{ta} = 0°$ . . . 93
4.35 Comparison radiation patterns at $\varphi = 0°$ for 80 × 80 TRA steering at $\theta_{st}^{ta} = 30°$ and $\phi_{st}^{ta} = 0°$ . . . 94
4.36 Comparison maximum gain and aperture efficiency of the 80 × 80 elements TRA pointing at $\theta_{st}^{ta} = 30°$ and $\phi_{st}^{ta} = 0°$ as a function of frequency . . . 95
4.37 Copolar and crosspolar variation of the 80 × 80 elements TRA pointing at $\theta_{st}^{ta} = 30°$ and $\phi_{st}^{ta} = 0°$ as a function of frequency . . . 95
4.38 Magnitude and phase distribution of the focal source field impinging the 120 × 120 elements TRA . . . 96
4.39 Phase distribution on a 120 × 120 TRA for beam steering at $\theta_{st}^{ta} = 30°$ and $\phi_{st}^{ta} = 0°$ . . . 96
4.40 Comparison radiation patterns at $\varphi = 0°$ for 120 × 120 TRA steering at $\theta_{st}^{ta} = 30°$ and $\phi_{st}^{ta} = 0°$ . . . 97
4.41 Comparison maximum gain and aperture efficiency of the 120 × 120 elements TRA pointing at $\theta_{st}^{ta} = 30°$ and $\phi_{st}^{ta} = 0°$ as a function of frequency 98
4.42 Copolar and crosspolar variation of the 120 × 120 elements TRA pointing at $\theta_{st}^{ta} = 30°$ and $\phi_{st}^{ta} = 0°$ as a function of frequency. . . . 99

5.1 Bi-Isotropic MS illuminated by a normal incident y-polarized wave propagating along positive z-axis . . . 105
5.2 Electric susceptance: solutions for a OBIMS in free space with equal amplitude scattered fields . . . 109
5.3 Transmission coefficient phase: solutions for a OBIMS in free space with equal amplitude scattered fields . . . 110
5.4 Reflection coefficient phase: solutions for a OBIMS in free space with equal amplitude scattered fields . . . 110
5.5 Scattering phases difference: solutions for a OBIMS in free space with equal amplitude scattered fields . . . 111
5.6 Magnetoelectric factor: solutions for a OBIMS in free space with equal amplitude scattered fields . . . 112
5.7 Phase coverage for a two-layer OBIMS with equal amplitude scattered fields: solution A . . . 114
5.8 Phase coverage for a two-layer OBIMS with equal amplitude scattered fields: solution B . . . 114
5.9 Reflection coefficient phase coverage of a three-layer OBIMS with fixed transmission coefficient phase . . . 116
5.10 Reflection coefficient phase coverage of a three-layer OBIMS for four fixed transmission coefficient phases . . . 116
5.11 Scattering parameters of four O-BIMS-based TRA cells having fixed transmission phase . . . 119
5.12 Scattering parameters of four O-BIMS-based TRA cells having fixed reflection phase . . . 120

A.1 Oblique incidence amplitude variation for $\phi_\tau = 15°$ . . . 129
A.2 Oblique incidence amplitude variation for $\phi_\tau = 105°$ . . . 129
A.3 Oblique incidence amplitude variation for $\phi_\tau = 285°$ . . . 129
A.4 Oblique incidence phase variation for $\phi_\tau = 15°$ . . . 130
A.5 Oblique incidence phase variation for $\phi_\tau = 105°$ . . . 130
A.6 Oblique incidence phase variation for $\phi_\tau = 285°$ . . . 130

List of Tables

2.1 Classification of reciprocal metasurfaces 16
2.2 State-of-the-art on Transmit-Reflect-Arrays 37

4.1 ATM 10-dBi pyramidal horn characteristics 69
4.2 H-MS-based TRA cells: theoric scattering phases, corresponding MS characteristic parameters and computed sheet impedances 74
4.3 Metal patterns dimensions for $\phi_\tau = 15°$ H-MS-based TRA cell 77
4.4 Metal patterns dimensions for $\phi_\tau = 105°$ H-MS-based TRA cell 77
4.5 Metal patterns dimensions for $\phi_\tau = 195°$ H-MS-based TRA cell 78
4.6 Metal patterns dimensions for $\phi_\tau = 285°$ H-MS-based TRA cell 78
4.7 Theoretical vs. Designed sheet impedances at 30 GHz for each H-MS-based TRA cell 78
4.8 Sheet impedances of the four H-MS-based TRA cells 80
4.9 Comparison of prototypes to state-of-the-art TRAs 100

5.1 Surface parameters of the sixteen O-BIMS-based TRA cells 118
5.2 Sheet impedances of the sixteen three-layer O-BIMS-based TRA cells . . 118

Acronyms

AD	Aperture Division
AUT	Antenna Under Test
BFN	Beam Forming Network
Bi-HGA	Bidirectional High Gain Antenna
BMS	Bi-anisotropic Metasurface
EM	electromagnetic
E-MS	Electric Metasurface
EBG	Electromagnetic Band-Gap
ES	Energy Splitting
FPGA	Field Programmable Gate Array
FS	Frequency Selection
FSS	Frequency Selective Surface
H-MS	Huygens' Metasurface
HPBW	Half Power Beam-Width
IoT	Internet of Things
GAD	Geometrical Aperture Division
MoSw	Mode Switching
MM	Metamaterial
M-MS	Magnetic Metasurface
MS	Metasurface
O-BIMS	Omega-Type Bi-Isotropic Metasurface
PIN	Positive Intrinsic Negative
RA	Reflectarray
RF	Radio-Frequency
RIS	Reconfigurable Intelligent Surface
SAF	Superposition of the Aperture Fields
SLL	Side Lobe Level
SNR	Signal-to-Noise Ratio
SRE	Smart Radio Environment

STAR-RIS	Simultaneous Transmitting and Reflecting Reconfigurable Intelligent Surface
TA	Transmitarray
TE	Transverse Electric
TM	Transverse Magnetic
TRA	Transmit-Reflect-array
TRM	Transverse Resonance Method
5G	fifth-generation
6G	sixth-generation

List of Symbols

Symbol	Value	Dimension	Description
c_0	3×10^8	meter/second [m/s]	Speed of light in vacuum
ε_0	8.85×10^{-12}	Farad/meter [F/m]	Vacuum permittivity
μ_0	$4\pi \times 10^{-7}$	Henry/meter [H/m]	Vacuum permeability
η_0	120π	Ohm [Ω]	Free space impedance

Acknowledgements

EMBARKING on this three-year PhD journey has been one of the most challenging, yet rewarding, experiences of my life. Moving to a foreign country, unfamiliar with the language and culture, added an extra layer of difficulty to an already demanding academic path. There were moments of struggle, but these years have also been incredibly enriching, both academically and personally. I had the privilege to work on topics that genuinely fascinated me, which made the hard work all the more worthwhile.

Throughout this journey, I grew not just as a researcher but as an individual. The people I met and shared this experience with, fellow students, professors, and collaborators, played a significant role in shaping my perspective, on both research and life itself. The opportunities I had to travel and attend international conferences broadened my horizons, offering me the chance to exchange ideas and present my work to a wider community. I still remember the thrill of submitting my first article and the blend of excitement and anxiety when I presented my research at the first conference I attended.

None of this would have been possible without the support of many incredible people. At every step, I was fortunate to be surrounded by those who encouraged me, challenged me, and made this experience truly unforgettable. For this reason, I would now like to take a moment to express my gratitude to all of them.

First and foremost, I would like to express my sincere gratitude to my supervisors. I am truly thankful to Dr. Francesco Foglia Manzillo for valuing my work and for guiding me through every stage of my research. Your encouragement and insightful feedback have been instrumental in my academic and personal growth. I deeply appreciate the collaborative relationship we built, and I sincerely hope to have the opportunity to work with you again in the future. I am also profoundly grateful to Prof. Guido Valerio. Your expertise and thoughtful feedback have been invaluable to my progress. I deeply appreciate the time and effort you invested in supporting me, and I am truly thankful for your guidance throughout this journey.

I would like now to sincerely thank the wonderful people I met here in Grenoble transforming my ordinary days into exciting and memorable ones. I thanks my Italian friends Edoardo, Simone, Tarek, Filippo, Paolo, Nicolò, Giancarlo, Thomas, Carolina and Sara for all the laughter we shared during our lunches together. Those moments made the days more enjoyable. I'm also deeply grateful to my french friends Marie and Paul for helping me learn French and for the wonderful nights out and dinners we had. Additionally, I want to thank as well Matteo, whose company I cherished for both the laughter and the deep discussions we shared.

I would also like to thank my colleagues, who made the work environment more enjoyable and stimulating. A special thanks to Antonio, Alessio, and Luca for the jokes, laughter, and invaluable support during our working hours; their company made each

day lighter. I am also sincerely grateful to our lab supervisor, Christophe, for his availability, professionalism, and genuine interest in ensuring that my PhD progressed smoothly.

I would like to express my gratitude to all my friends from Trieste and Torino. I deeply appreciate how our friendship has endured despite the distance, and I'm grateful for the remote support and the time you made to meet with me.

Finally, I want to express my deepest gratitude to my girlfriend Sanja for her unwavering love and support. Your encouragement and understanding have been a constant source of strength and inspiration throughout this journey.

Last but not least, I want to thank my parents. Your endless support, love, and encouragement along all my life have helped me even during the toughest times. I am deeply grateful for the sacrifices you've made and the unwavering faith you have shown in me. This achievement is as much yours as it is mine. Thank you for everything.

Abstract

IN the second decade of the new millennium, novel communication paradigms and technologies have emerged to meet the growing demands of a world becoming increasingly data-centric and data-dependent. Reconfigurable Intelligent Surfaces (RISs) play a crucial role in this vibrant context by enabling the realization of Smart Radio Environments (SREs) capable of sustaining a continuous connection between physical and digital worlds. Implemented as reconfigurable arrays, these low-cost electromagnetic (EM) surfaces achieve energy efficiency by recycling existing radio waves in the SRE. Among different candidates for designing Reconfigurable Intelligent Surfaces, Metasurfaces (MSs) have garnered significant attention due to their low fabrication costs and exceptional capabilities for EM wave manipulation.

In the last few years, the concept of Simultaneous Transmitting and Reflecting Reconfigurable Intelligent Surface (STAR-RIS) arose as a cutting-edge development of traditional RISs. By simultaneously enabling both refraction and reflection radiation, these devices utilize the electromagnetic spectrum more efficiently, significantly enhancing the coverage and quality of wireless networks. STAR-RISs can be implemented as Transmit-Reflect-array (TRA) antennas, structures comprising both Transmitarray (TA) and Reflectarray (RA) functionalities. However, designing the array cells is challenging due to time-consuming full wave optimizations.

In this manuscript, the criticality is approached by a rigorous analytical point of view. First, by examining the behavior of a reciprocal MS with electric and magnetic response, referred as Huygens' Metasurface (H-MS), the relation between its surface parameter that allows an arbitrary control of the transmission and reflection coefficients amplitude is derived. However, an independence of refracted and reflected beam steering angles cannot be achieved. Second, the design procedure of four meta-atoms to realize a uniform 2-bit quantization is presented. To verify the cells behavior in a non-periodic environment, a tool for the analysis of TRA radiation characteristics has been developed based on physical optics and array theory. Lastly, this design procedure has been verified through the realization and experimental characterization of several TRA prototypes.

To overcome the limit encountered by realizing H-MS elements for the design of TRAs, Metasurfaces (MSs) that posses a bi-anisotropic response have been investigated. Due to the presence of more degree of freedom in the form of surface parameters, a fully independent control of both transmission and reflection phases is achieved. A preliminary design of sixteen meta-atoms to realize a uniform 2-bit quantization in both refraction and reflection is presented.

This research defines a comprehensive set of tools for the design of TRAs, exploiting limits due to the choice of particular Metasurface (MS) elements and how to overcome them.

Synthèse de la recherche

AU cours de la deuxième décennie de l'actuel millénaire, de nouveaux paradigmes et de nouvelles technologies de communication sont apparus pour répondre aux exigences croissantes d'un monde de plus en plus centré, et dépendant, de l'échange de données. Les Surfaces Intelligentes Reconfigurables (SIRs), ou en anglais "*Reconfigurable Intelligent Surfaces*", jouent un rôle crucial dans ce contexte dynamique. En effet, elles permettent la réalisation d'environnements intelligents capables de traiter et de transférer de grandes quantités d'informations. Mises en œuvre sous forme de réseaux reconfigurables, ces surfaces sont peu coûteuses et très efficaces, puisqu'elles utilisent l'énergie des ondes radio dans l'espace environnant. Parmi les différents candidats possibles pour la réalisation des SIR, les métasurfaces, ou en anglais "*Metasurfaces*", ont suscité un grand intérêt en raison de leur faible coût de fabrication et de leur exceptionnelle capacité à manipuler les ondes électromagnétiques, aussi bien réfléchies que réfractées, et ce, quelles que soient les conditions imposées à leurs paramètres caractéristiques.

Ces dernières années ont vue l'émergence des réseaux transmetteurs ou réflecteurs pour la réalisation de RIS. Cependant, de telles technologies ne fonctionnant qu'en émission ou transmission, elles impliquent donc une faible couverture spatial du signal émis et laissent place à des zones d'ombre. Récemment, la fonctionnalité des SIR a été élargie pour combiner ces deux fonctions, sous le nom de Surfaces Intelligentes Reconfigurables avec Transmission et Réflexion Simultanées (TRS-SIR). Pour réaliser ces focntions conjointement, des antennes positionnées en réseau étant à la fois émettrices et réfléchissantes sont utilisées. On les appele (TRA) pour Transmit Reflect Antenna en anglais. Le travail présenté dans ce manuscrit s'inscrit dans ce contexte. Nous montrons comment mettre en œuvre des cellules de métasurface introduisant une division arbitraire de la puissance entre le champ transmis et le champ réfléchi.

Pour soucis de simplicité, l'analyse commence par des métasurfaces de Huygens sans perte. Les coefficients de diffusion sont dérivés en fonction des paramètres de surface, c'est-à-dire la susceptance et la réactance, en considérant la structure comme éclairée par une onde plane sous incidence normale, comme le montre la Fig. 0.1.

En imposant l'égalité suivante entre les modules des coefficients de réflexion et de transmission :

$$|\tau| = |\Gamma|, \tag{0.1}$$

une relation est dérivée qui relie la suceptance électrique et la réactance magnétique de la surface. Cependant, la différence entre les phases des coefficients de transmission et de réflexion est fixe et égale à 90∘. Les faisceaux rayonés sont donc dépendant l'un de l'autre. À partir de ces analyses, quatre cellules fonctionnant à 30 GHz ont été conçues

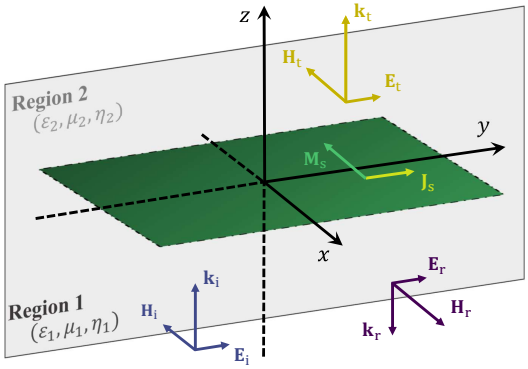

FIGURE 0.1 : Métasurface infinie entre deux régions aux propriétés matérielles différentes, éclairées par un champ incident normal, en ligne bleue, provenant de la Région 1. Les champs réfléchis et transmis sont représentés par des lignes violettes et jaunes, respectivement.

pour réaliser un TRA avec une quantification uniforme de 2-bit de la phase en transmission et en réflexion. Les cellules ont été construites comme une superposition de trois couches métallique séparées par deux substrats diélectriques. Les quatre valeurs de phase de transmission suivantes ont été choisies pour les méta-atomes : $\phi_{\tau_1} = 15°$, $\phi_{\tau_2} = 105°$, $\phi_{\tau_3} = 195°$ et $\phi_{\tau_4} = 285°$. Les paramètres de surface qui leur sont associés et les phases de réflexion sont présentés respectivement dans les Fig. 0.2a et Fig. 0.2b.

En connaissant les paramètres de surface d'un méta-atome, nous avons pu déterminer les impédances que devaient avoir chacune des couches métalliques en supposant des conditions aux limites périodiques. Les motifs métalliques de chaque couche ont été choisis sur la base de géométries simples, telles que des méandres, afin de synthétiser un comportement inductif ou capacitif.

Lors de la réalisation des méta-atomes, l'épaisseur commerciale des substrats et l'effet de la colle pour maintenir la structure complète ont également été pris en compte. La conception complète de chaque cellule est illustrée à la Fig. 0.2c, Fig. 0.2d, Fig. 0.2e et Fig. 0.2f. L'amplitude des coefficients de diffusion se situe entre −4 dB et −2 dB dans une largeur de bande relative de 5% centrée sur 30 GHz. La largeur de bande est principalement limitée par la variation en fréquence des impédances des couches conçues. Dans la même bande, les déphasages relatifs introduits par les différentes cellules, en transmission et en réflexion, sont approximativement des multiples de 90° comme évoqué plus haut.

Pour concevoir un TRA avec une quantification uniforme de la distribution de phase, en transmission et en réflexion, un modèle d'analyse basé sur l'optique physique et la théorie des réseaux est proposé. En utilisant l'outil développé, plusieurs TRAs fonctionnant à 30 GHz et ayant un profil de phase optimisé pour diriger les faisceaux réfléchis et réfractés à différents angles ont été analysés. Des comparaisons avec des simulations électromagnétiques sont présentées. Enfin, plusieurs prototypes ont été fabriqués et les résultats des mesures sont comparés à l'outil dévelopé et aux résultats des simulations électromagnétiques.

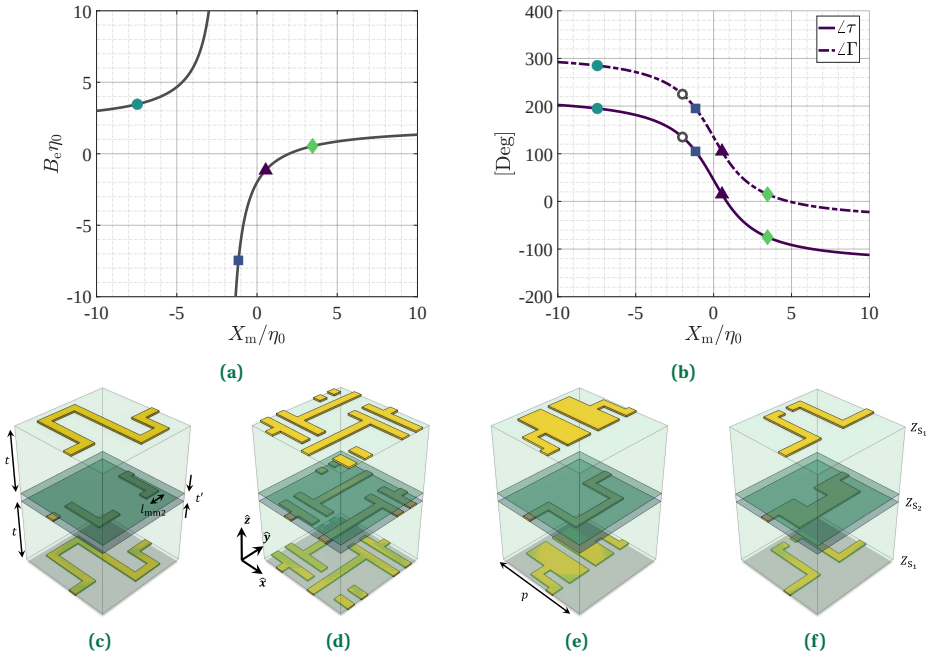

FIGURE 0.2 : (a) Lieu des paramètres de surface décrits par la solution A dérivée de (0.1) et (b) phases des coefficients de transmission et de réflexion pour cette solution. Les symboles indiquent les caractéristiques des quatre cellules conçues. Méta-atomes TRA fabriqués, avec une période $p = 1,2$ mm, mettant en oeuvre à 30 GHz, en transmission, un déphasage de : (c) $\phi_{\tau_1} = 15°$, (d) $\phi_{\tau_2} = 105°$, (e) $\phi_{\tau_3} = 195°$ et (f) $\phi_{\tau_4} = 285°$. Les épaisseurs des substrats et des couches de liaison sont respectivement de 0,787 mm et 100 μm.

Parmi les différents TRA fabriqués, il est intéressant de souligner le prototype de taille $144 \times 144\,\text{mm}^2$, illustré à la Fig. 0.3a et Fig. 0.3b. La distance focale est de 99.4 mm et la distribution de phase sur le réseau est telle que le faisceau transmis dépointe à $\theta = 30°$ et $\varphi = 0°$. En réflexion, étant donné la différence de 90° entre les phases de transmission et réflexion, le champ est rayonné à $\theta = 150°$ et $\varphi = 0°$. La comparaison entre notre modèle analytique et les résultats des mesures est présentée à la Fig. 0.3c. Nous pouvons noter qu'un très bon accord est obtenu entre les deux courbes. Le faisceau transmis mesuré présente un gain maximal égal à 26.4 dBi avec $\eta_{\text{ap}} = 36.4\%$. Cependant, un léger strabisme dans la direction de l'orientation est présent, ce qui fait que le faisceau pointe vers $\theta = 31°$. Les résultats calculés analytiquement et mesurés s'accordent tous deux sur un niveau de lobes secondaires de −18 dB. Les deux faisceaux réfractés présentent une largeur de faisceau à mi-puissance de 4°. La Fig. 0.3d présente la stabilité des faisceaux en fonction de la fréquence. Il est possible d'observer que, dans la bande de fréquence qui nous intéresse, de 29 à 31 GHz, l'erreur de pointage reste faible. De plus, le niveau de la polarisation croisée est inférieur à −30,dB en transmission et à −34,dB en réflexion.

Pour surmonter la contrainte de direction entre les faisceaux réfléchis et réfracté, une autre classe de structures a été étudiée. En effet, les cellules de métasurface bianostropes de type oméga peuvent obtenir une phase indépendante de la transmission à la réflexion

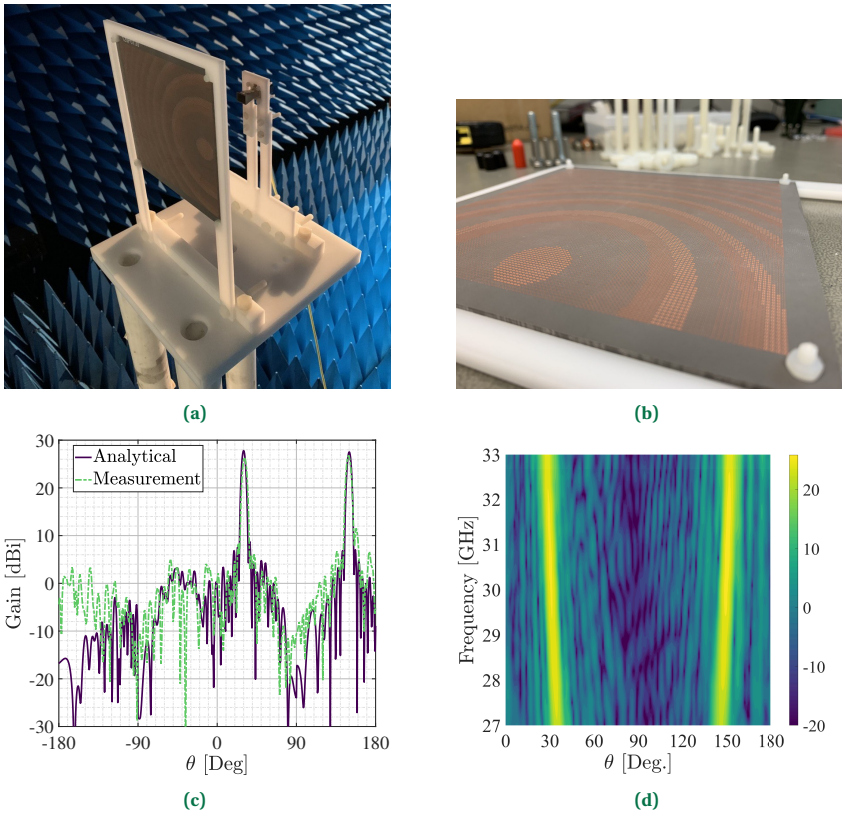

FIGURE 0.3 : (a) Configuration de mesure dans la chambre anéchoïque et (b) prototype de réseau d'antennes de taille $14.4 \times 14.4\lambda_d^2$. (c) Diagramme de rayonnement mesuré à $\varphi = 0°$. (d) Stabilité des faisceaux transmis et réfléchis en fonction de la fréquence.

en raison de la présence d'un autre degré de liberté sous la forme d'un coefficient de surface supplémentaire. Si l'isotropie est imposée à ce type de structure, la relation (0.1) est retrouvée lorsqu'une onde plane sous incidence normale éclaire la surface.

En partant des relations entre les coefficients de surface obtenus, on conçoit 16 méta-cellules qui permettent une quantification de phase uniforme de 2-bit, tant en transmission qu'en réflexion. En effet, pour chaque état de transmission, quatre état de réflexion doivent exister afin de garantir des directions de dépointage différentes de chaque côté de la structure. Les Fig. 0.4a et Fig. 0.4b montrent les réponses en phase et en amplitude des quatre cellules pour l'état de phase de transmission $\phi_\tau = 90°$. Dans la bande 28-32 GHz, les phases $\angle\Gamma$ de ces cellules sont ensuite espacées de $90° \pm 10°$. Les quatre cellules correspondant à l'état de phase $\angle\tau = 90°$ atteignent bien cette valeur à 30 GHz et gardent cette valeur sur toute la bande. L'amplitude des coefficient τ et Γ varie entre -4 dB et -2 dB sur la bande $[28, 31]$ GHz fournissant ainsi une largeur bande relative de 10%. Les Fig. 0.4c et Fig. 0.4d montrent qu'un comportement à large bande similaire est observé pour les quatre cellules caractérisées par l'état de phase de réflexion

$\phi_\Gamma = 105°$. Les valeurs de $|\tau|$ et $|\Gamma|$ sont très proches de -3 dB à 30 GHz, comme prescrit par la procédure de conception. On obtient ainsi une largeur de bande relative de 13% centrée sur 30 GHz, avec une amplitude des coefficients de diffusion comprise entre -4 dB et -2 dB.

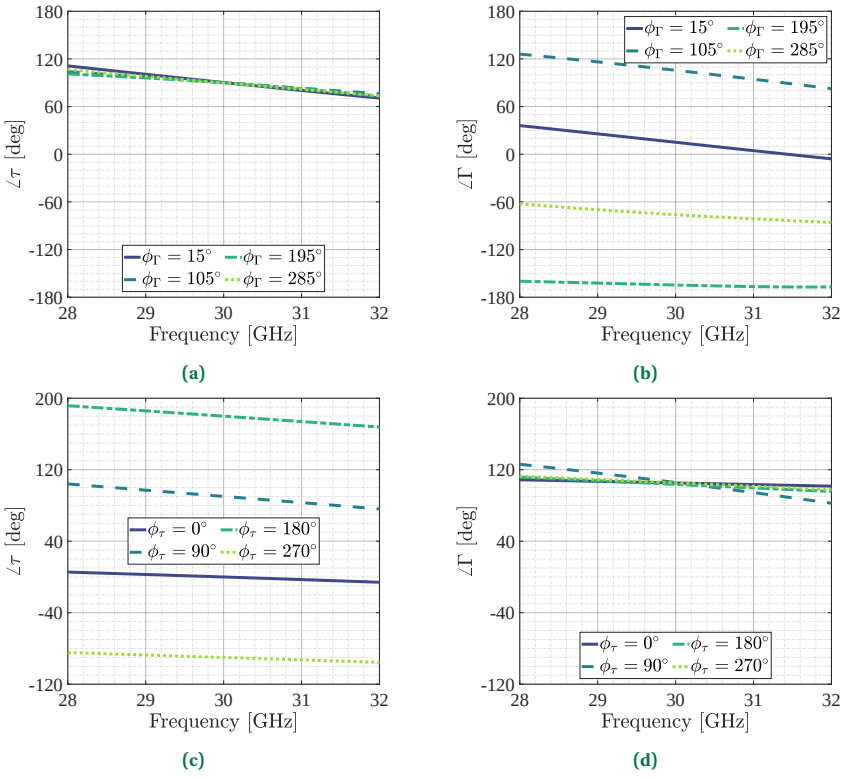

FIGURE 0.4 : Phases des coefficients de (a) réflexion et de (b) transmission en fonction de la fréquence de quatre cellules avec $\angle\tau = 90°$ à 30 GHz. Phases des coefficients de (c) réflexion et de (d) transmission en fonction de la fréquence de quatre cellules avec $\angle\Gamma = 105°$ à 30 GHz.

1

Introduction

All human knowledge begins with intuitions,
proceeds from thence to concepts,
and ends with ideas.

Immanuel Kant

This first chapter serves as a concise introduction to the topic presented throughout the manuscript. An outline is proposed to indicate each chapter subject.

1

1.1. BACKGROUND

APERE AUDE! No better words could be chosen to start an experimental dissertation since they embody the craving for scientific awareness that has driven these three years of research. Employed by Horatius[1] and looslely translated as "*Dare to know things through reason!*", it became the adage of the "Age of Enlightenment" with Kant's definition [2]. This sentence represents the striving of knowledge and criticism that characterized the XVII and the XVIII centuries but, it has always been intrinsic to the human soul, leading scientists, century after century, to learn about nature and the laws by which it is governed. As for the interest in controlling fire, mankind had, since ancient times, a strong interest in electrical phenomena that eventually lead it to exploit this kind of energy and the electromagnetic (EM) interactions of matter. However, as the saying goes "*Rome ne fu pas faite toute en un jour*" [3], which means "*Rome wasn't built in a day*", this did not happen overnight. Over the centuries, scientists gradually defined electric and magnetic phenomena through study and experimentation. Nevertheless, it was in 1865 that the ultimate expression of these studies were linked, derived and organized by Maxwell [4], then written in a reduced form, as we know them now, by Heavyside[2] [9], [10]. Thanks to these works and the ones that followed, a better comprehension of the EM phenomena allowed the emergence of numerous applications in a wide variety of fields. In particular, in a world where information rarely traveled across the globe, the turning point came with the invention of radio and wireless transmissions, driven by the experiments of Nikola Tesla and Guglielmo Marconi [11], [12]. From this time on, a succession of breakthroughs characterized the XX and XXI centuries: television, mobile phone, Internet and satellite networks, to name a few.

At this point, someone could ask: can human curiosity stop here? Of course not. New discoveries led to novel studies and experiments with interesting insights of the existing scientific knowledge. Unsurprisingly, the field of telecommunications was no exception[3]. Satellite and terrestrial networks started demanding faster, low-latency, ultra-reliable communications, requiring the use of new Radio-Frequency (RF) bands, at higher frequencies due to overcrowding of the RF bands, and bigger data rates. In this fertile environment for technological advancement, researchers have begun looking to quasi-optical systems, over the past decade, as solutions for deep space exploration and links between satellites due to extremely wide bandwidth [14]. Albeit attempts to use these systems for ground-to-space communications with error mitigation techniques have been explored, RF systems working in Ka-band and, between satellites, in V-band

[1] The Roman lyric poet of Augustus' era uses this expression as an exhortation to his friend Maximus Lollius to pursue wisdom and moral integrity [1, line 40].

[2] The English scientist spent nearly a decade comprehending and reducing Maxwell's equations from 20 to just 4 using a vectorial formulation [5]. The interested reader will find in [6] a very deep and precise analysis of all the studies, publications and works conducted by Heaviside. Some little reviews on his life and the specific procedure to derive the Maxwell equations in vectorial form can be found instead in [7] and [8], respectively.

[3] Notably, Phil Edholm of Nortel Networks has made an intriguing observation regarding the evolution of the communications industry. Edholm's law, as it is known, forecasts that bandwidth and data rates will double approximately every 18 months, mirroring the exponential growth predicted by Moore's law for the number of transistors [13].

have continued to be preferred due to an inadequate market for optical communications and problems related to atmospheric propagation [15], [16]. At the same time, this vibrant environment of scientific research also affected terrestrial networks.

With the exponential increase in electronic devices, a whole new concept of the Internet, called Internet of Things (IoT), emerged, where every system can communicate and interface with others through wireless channels. Among the myriad of applications that appeared on the horizon, the infrastructural one began to grow. The novel concept of *smart* city, that arose at the dusk of the previous millennium, with the following Robert E. Hall definition finally had a reason to emerge [17]:

> *"[…] urban center of the future, made safe, secure environmentally green, and efficient because all structures - whether for power, water, transportation, etc. are designed, constructed, and maintained making use of advanced, integrated materials, sensors, electronics, and networks which are interfaced with computerized systems comprised of databases, tracking, and decision-making algorithms. […]"*

Another push in this direction came in recent years with the phone companies' deployment of the fifth-generation (5G) technology standard for cellular networks [18]. With a massive data rate increase, better area coverage, low latency and higher energy efficiency, fast connections between devices was no more a dream.

However, in an ever-changing world, where everyday life is becoming progressively more data-centric and data-dependent, this is no longer enough. For this reason, the scientific research has already begun to explore solutions for turning future wireless networks into "*smart*" platforms, capable of adapting to the environment and supporting even higher data rates. Thus, the upcoming sixth-generation (6G) technology systems will be responsible for creating a seamless connection between the physical and digital domains, advancing the vision of a fully interconnected world [19]. To satisfy this demanding specification, two challenges need to be addressed: avoiding lack of service under harsh propagation environments and limiting the high-power consumption of wireless interfaces, e.g. transceivers [20]. To overcome the first limitation, the concept of Smart Radio Environment (SRE) emerged: an intelligent, adaptable space capable of actively processing and transferring information [21], [22]. To realize such vision, a structure, that can shape incoming EM waves and capable of updating itself when the environment changes, is required. Nevertheless, the second challenge, mentioned before, still needs to be addressed and it should not be ignored: this device must be energy-constrained and re-use radio-wave energy in the SRE. Based on these requirements, a brand new technology emerged in the wireless community: the Reconfigurable Intelligent Surfaces (RISs), low cost EM surfaces implemented as reconfigurable arrays or programmable liquid crystals [23].

In this exciting period of scientific research on RISs, Metasurfaces (MSs) are proving to be an outstanding candidate due to their inexpensive fabrication and ability of extreme EM wave manipulation for transmitted and reflected fields [24]. This dissertation wedges itself into this fervent context, showing how simultaneous refraction and reflection can be achieved from MSs through an elegant mathematical definition, particularly suitable for a straightforward design not requiring time-consuming optimization procedures. Experimental results support these claims.

1

1.2. MOTIVATION

Starting with a comprehensive study of the literature on MSs, it quickly became clear why they captured the researchers' attention. Their easy realization and planar profile make them a perfect fit for telecommunications. Their ability to shape EM fields led to a myriad of applications: absorbers, cloaking, polarizers, leaky waves, lenses, imaging and as antennas for tailoring aperture fields, to name a few [25]–[31].

The latter case has garnered the most interest from the wireless community as a perfect candidate for RISs design. Specifically, research has focused on utilizing these structures to tailor transmitted or reflected fields in IoT applications, enabling control and enhancement of wireless signals. Pre-existing solutions that align with the concept of MS, and consequently RIS, include space-fed devices denominated Transmitarrays (TAs) and Reflectarrays (RAs) [32], [33]. Due to their capability of adjusting the phase of transmitted and reflected signals, respectively, RISs can steer beams towards specific receivers, optimize signal paths based on real-time channel conditions, and achieve high gain and directive patterns, thereby enhancing the overall coverage and improving the Signal-to-Noise Ratio (SNR) [23], [34], [35].

Furthermore, a cutting-edge development has recently emerged as an extension of traditional RISs: Simultaneous Transmitting and Reflecting Reconfigurable Intelligent Surfaces (STAR-RISs), devices capable of simultaneously radiating in refraction and reflection [36]–[40]. Their dual functionality allows a more efficient use of the electromagnetic spectrum and enhances the coverage and quality of wireless networks. By electronically control the surface characteristic parameters, STAR-RIS properties can be adjusted in real-time allowing adaptive beamforming and improved signal manipulation. While TAs and RAs are good solutions for RISs, on the other hand emerging structures under the name of Transmit-Reflect-arrays (TRAs), that combine these two features, are a perfect match for STAR-RISs. However, given the novelty of this topic, the literature is still in its earliest days: as an example, some works consider simultaneous transmission and reflection through Geometrical Aperture Division (GAD) or Superposition of the Aperture Fields (SAF) strategies [41], [42]. By alternating TA and RA elements, it has also been shown the capability of generating multiple beams in transmission and reflection [43]. Nevertheless, these solutions have low aperture efficiency values due to the inability to use all of the array available area. Other recent works have achieved this feature of implementing simultaneous transmission and reflection employing the entire antenna area [44], [45]. They also added some other functionalities as reconfigurability [46], polarization conversion [47]–[50], and generation of vortex beams [51]. However, all of this works are based on an extensive numerical analysis of the array elements to obtain the desired transmission and reflection properties for the antenna array design.

This dissertation stands as a milestone in this topic, establishing the fundamentals to study MSs for simultaneous manipulation of refracted and reflected fields. In fact, along the text, a mathematical method is proposed to derive in closed form the optimal constitutive MS parameters in such a way that TRA cells can be rapidly designed. In this way, aperture efficiency problems related to the use of techniques such as GAD or SAF can be avoided, given the dual functionality of the array elements. Moreover, the proposed analysis can be used to in case of reconfigurable TRAs. Knowing the optimum surface characteristic parameters, these values can be encoded in the cells to synthesize

the desired binary states, similarly to what Kim *et al.* with H-MSs [52].

1.3. OUTLINE

The main topic of the manuscript is the description of a new mathematical derivation for the optimal parameters of the MS for simultaneous manipulation of refracted and reflected fields, and the subsequent design of devices exploiting this formulation. However, before dealing with this specific topic, Chapter 2 presents how the concept of Metamaterial (MM) was born and the need of a low-profile structure that led to the emergence of MSs. Then, an overview on the MS model, taxonomy and methods of analysis are provided. In this context, possible applications are listed with a strong emphasis on spatially fed arrays and STAR-RIS.

The upcoming chapters are arranged in two main parts, following a thread of exposure from a particular case to its generalization. On one hand, Chapter 3 and Chapter 4 provide the study and implementation of the surface parameters for an isotropic H-MS to achieve simultaneous transmission and reflection. On the other, Chapter 5 extends the analysis considering an Omega-Type Bi-Isotropic Metasurface (O-BIMS) showing how it is possible to overcome certain limitations imposed by the use of H-MSs.

Going into more detail, Chapter 3 presents at first the optimum surface parameters for an isotropic H-MS when arbitrary power division between refracted and reflected fields is imposed. Then, by focusing on the particular case of an evenly split of the incident power between refraction and reflection, it is found that there is a limitation on the generation of independent transmitted and reflected beams. Additional studies are then conducted to determine the minimum number of layers required for designing H-MSs capable of simultaneous transmission and reflection. Insights on the metallic patterns that realize these impedance sheets concludes the chapter.

Building on this foundation, Chapter 4 focuses on the practical design and implementation of H-MSs. To verify the optimal surface parameters derived in Chapter 3, H-MS cells are realized as cascaded structures composed of three sheet impedances spaced by two dielectric slabs. Subsequently, multiple TRAs are designed using these elements, and their full-wave behavior is analyzed. Several of these structures were fabricated, and measurement results are compared against simulation data.

As previously mentioned, Chapter 5 extends the analysis presented in Chapter 3. It demonstrates the generation of independent transmitted and reflected beams by incorporating additional surface parameters, enabled by the bi-isotropic properties of the analyzed structure. This chapter further explores the minimum number of layers needed to design O-BIMSs capable of simultaneous transmission and reflection. Additionally, a preliminary design for O-BIMS elements realized as a cascade of three sheet impedances spaced by two dielectric slabs is proposed.

Finally, Chapter 6 summarizes the findings from this research, offering a comprehensive review of the studies conducted over the past years. It also provides insights into potential future developments in this field.

2

State of the Art

An idea must not be judged by its immediate result.

Nikola Tesla

This chapter starts exploring the historical emergence of MM concept and subsequent advent of its low-profile equivalent under the name of MS. After this brief review of past research accomplishments, the general MS model described as a set of homogenized parameters is presented and, depending on the behavior of these values, a classification is proposed. Different techniques to analyze MS are discussed and applications in which they can be employed are treated. To conclude, a review on the novel concepts of STAR-RIS and TRA are presented, emphasizing how MSs fits as perfect candidate for these usages.

2.1. Metamaterials: An Electromagnetic Revolution

In the realm of scientific progress, multiple discoveries have risen from the depths of human curiosity with profound impact. Among these, Metamaterials (MMs) deserve honorable mention. The advent of these structures represents a crucial transformation in our understanding of the material world as extraordinary phenomena emerge from mundane reality in mythical or fantastic literature. Fëanor, in J.R.R. Tolkien's legendarium, creates three Silmarils, magnificent jewels crafted from the essence of the two trees of Valinor and holding within them a brilliance and power unmatched by any other creation. Hence, his peerless skill and profound comprehension of the world's hidden properties permitted him to forge such artifacts. Similarly, visionary scientists who dared to question the limitations of natural substances, sought to create materials that could transcend the conventional bounds of physics. Their efforts paved the way for a new era of innovation, enabling the design of materials with enhanced capabilities.

But was this revolutionary journey swift? Were there few or many contributors? And how did it begin? As for every scientific discovery, it undoubtedly took a considerable amount of time and involved numerous pioneers before the term "*Metamaterial*" came into use. Generally, the academic community agrees that Veselago's work laid the theoretical groundwork for subsequent insights[1]. Back in 1968[2], when these structures were called artificial dielectrics, he pondered the behavior of propagating electromagnetic waves in materials with negative electric permittivity, ε, and magnetic permeability, μ [54]. His conceptual research revealed that the incident wavefront bends in a manner that yields a negative refractive index and a backward wave[3].

However, these insights remained largely dormant due to the inability to engineer such materials at the time. Three decades later, three seminal works emerged, experimentally demonstrating and elucidating potential applications aligned with the studies pioneered by the Russian researcher. The first, in 2000, showcased an engineered structure capable of simultaneously exhibiting negative electric permittivity and magnetic permeability within the same frequency band [57]. Moreover, it experimentally confirmed that electromagnetic waves do not propagate in a medium where only one of these material constants is negative, but propagation is restored when both are negative. The second, in the same year, showed possible applications for these new kinds of materials by employing an unconventional lens made of a silver slab with negative refractive index [58]. This work demonstrated extremely interesting capabilities, such as focusing light and restoring the phase of propagating waves and amplitude of evanescent states. The last one, in 2001, already uses the term "*Metamaterial*" instead of "*artificial dielectric*". It experimentally demonstrated the unusual direction of scattered electromagnetic waves by a prism with negative refraction index, validating Veselago's theory [59]. These

[1] A decade before Veselago's work, an earlier publication broadly addressed the topic of wave propagation in a medium with a negative refractive index [53]

[2] To be precise, Veselago's article was published in English this year, but its Russian publication was in 1967.

[3] Backward waves have been studied since at least 1904, when Lamb suggested their existence, although his examples pertained more to mechanical systems [55]. Later, in the same year, Schuster extended this concept to electromagnetism [56].

four works together sparked a surge of research publications in the field of artificial dielectrics.

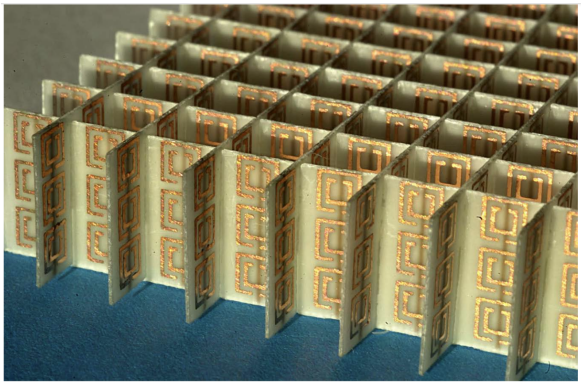

Figure 2.1: Negative refractive index material prototype developed by Padilla *et al.* [60].

After this historical excursus, a question arises: when was the term "*Metamaterial*" coined? The first accredited use and definition of this word is attributed to Rodger Walser at the start of the XXI century[4,5]:

> *"Metamaterials are defined as macroscopic composites having a man-made, three dimensional, periodic cellular architecture designed to produce an optimized combination, not available in nature, of two or more responses to a specific excitation. Each cell contains metaparticles, macroscopic constituents designed with low dimensionality that allow each component of the excitation to be isolated and separately maximized. The metamaterial architecture is selected to strategically recombine local quasi-static responses, or to combine or isolate specific non-local responses."*

The choice of this name underscores his intention to highlight that these structures can achieve performance *beyond* the limits of conventional composites. Indeed, the term "Metamaterial" is a compound word where the prefix *meta-* comes from Greek ($\mu\varepsilon\tau\acute{\alpha}$) meaning "*beyond*"[6,7]. The composite exhibits distinct properties that are not present in the individual components. These unique characteristics arise from the specific three-dimensional arrangement and interaction of its constituent elements while still maintaining large-scale homogeneity. This last consideration underscores the importance of selecting sub-wavelength molecules so that spatial inhomogeneities

[4] R. Walser employed this term for the first time in 2000 [61], followed by another publication in 2001 [62]. Nevertheless, he already used it in September 1999 in the general invitation for a DARPA workshop [63], [64]. It is clear now why Shelby employed in 2001 the term "Metamaterial" in his work.

[5] For more historical information on RF Metamaterial, the interested reader can refer to [64], [65]. A very deep analysis of the early years of concept development in the USA are detailed in [63]. Additionally, [66] provides a comprehensive overview of the congresses and meetings that paved the way for this flourishing research field with scientific works of both Former Soviet Union and the West.

[6] A similar definition can be found on the site of *Virtual Institute for Artificial Electromagnetic Materials and Metamaterials*: `https://www.metamorphose-vi.org/index.php/metamaterials`

[7] It is important to note that defining "Metamaterial" was not a trivial matter. Common definition, such as properties "not found in nature" or "not observed in constituent materials" are not entirely accurate. Therefore, a more fitting term has been employed to describe MM properties: "*emergence*" [67]–[69]

are negligible and unique effective material parameters can be employed to describe the medium's characteristics.

2.2. FROM METAMATERIALS TO METASURFACES

Following our exploration of the historical context and the challenges the scientific community faced in defining the term *Metamaterial* in Section 2.1, we can now delve into the spectrum of possibilities this technology offers at the application level. As three-dimensional arranged particles, these structures are widely employed for multiple electromagnetic purposes: from cloaking to imaging, antennas to sensing and communications systems to absorbers [70]–[76]. Nevertheless, these applications face three common problems: significant space occupied, substantial energy losses within the bulk material, challenges in fabrication, especially at the nanoscale, and difficulty in integrating 3D structures with existing photonic and electronic systems [77]–[80]. Therefore, why not engineer a 2D structure instead of a bulky 3D one? A decade after the definition of *Metamaterial*, its bi-dimensional equivalent arose under the name of *Metasurface*, further energizing the already dynamic scientific research. Due to their low profile nature, structures exhibiting reduced losses can be engineered with applications spanning from microwave to optical frequencies. These include those previously identified for MMs, as well as emerging uses such as RISs, innovative wave-guiding structures, and flat lenses, among others [24]–[26], [29], [30], [81].

In the first decade of the XXI century, before the advent of MSs, another kind of periodic structure draw the scientific community attention: Electromagnetic Band-Gap (EBG) and one of their categories called Frequency Selective Surface (FSS). Nevertheless, they differ from MSs based on their electromagnetic behaviour. This distinction can be done by defining three regions (see Fig. 2.2), where a composite material can be assigned depending of its electromagnetic behaviour at different frequencies [82].

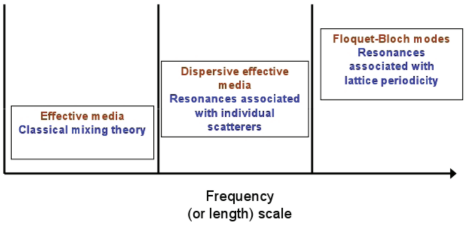

Figure 2.2: Metasurface distinction with respect to electromagnetic bandgap structures [82].

The first region considers frequencies at which the wavelength is much larger than the periodicity of the composite scatterers. To extract the equivalent-effective properties of the material, classical electromagnetic formulas are employed. Typical examples that falls in this category are thin-film materials. The second region is similar to the previous one in terms of periodicity with respect to the wavelength. However, the elements are engineered with patterns that induce resonances at the desired frequency, causing the composite to behave as an effective medium with inherent frequency-dependent material properties. MSs falls under this definition. The last region, the one where

EBGs are associated to, considers the case where the periodicity is comparable or bigger then the wavelength. In this case the structure cannot be seen anymore as an effective medium and Floquet Bloch mode expansion approaches need to be employed for their analysis.

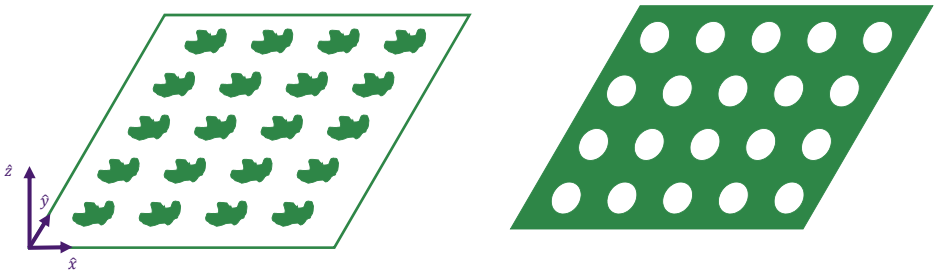

Figure 2.3: Metasurface categories: (a) metafilm and (b) metascreen

After defining the differences between MSs versus other periodic structures, different subclasses of MSs can be identified. By classifying on the basis of the composition of the scatterers, three categories can be established: metafilm, metascreen and an hybrid solution between these two extremes [82]. The first refers to an array of distinct metallized scatterers while the second one to a surface with periodically spaced apertures as reported in Fig. 2.3. MSs considered in the following chapters falls in the third hybrid class.

2.3. METASURFACE MODEL

With the definition of the term *Metasurface* now clear, how they can be effectively modeled to obtain the desired manipulation of electromagnetic fields is discussed in this section. Previous works showed analysis of MSs providing purely electric response to control EM waves [83]–[85]. The addition of a magnetic behavior was shown to dramatically decrease reflection losses and increase their efficiency [86]–[88]. For a more complete control of an electromagnetic wave front's polarization and phase, anisotropy and magnetoelectric coupling have been incorporated in the metasurface design. This level of generality is suitable to define a model and describe the structure operation.

Macroscopically, these surfaces can be considered as infinitesimally thin sheets separating two regions with different electric and magnetic properties as shown in Fig. 2.4. The structure acts as a discontinuity that performs desired field manipulations through the Schelkunoff's equivalence principle[8]: the total fields above, $(\mathbf{E}_2, \mathbf{H}_2)$, and below the MS, $(\mathbf{E}_1, \mathbf{H}_1)$, are obtained by properly design surface electric and magnetic

[8] Known as Schelkunoff's surface principle,it is an extension of Love's formulation. Notably, Love developed rigorously Huygens' theorem specifying secondary sources in terms of fictious electric and magnetic currents [89] [90] [91]

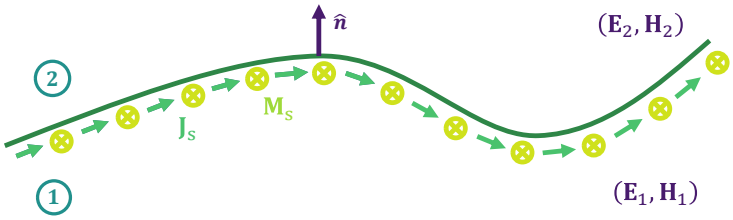

Figure 2.4: General metasurface model.

currents, $\mathbf{J}_s$ and $\mathbf{M}_s$ respectively [92].

$$\mathbf{J}_s = \hat{\mathbf{n}} \times (\mathbf{H}_2 - \mathbf{H}_1) \,, \tag{2.1a}$$

$$\mathbf{M}_s = -\hat{\mathbf{n}} \times (\mathbf{E}_2 - \mathbf{E}_1) \,, \tag{2.1b}$$

where $\hat{\mathbf{n}}$ is the unit vector normal to the surface. Let us consider now that an incoming electromagnetic wave in Region 1, described by an electric field $\mathbf{E}_i$ and magnetic one $\mathbf{H}_i$, illuminates the structure as in Fig. 2.5.

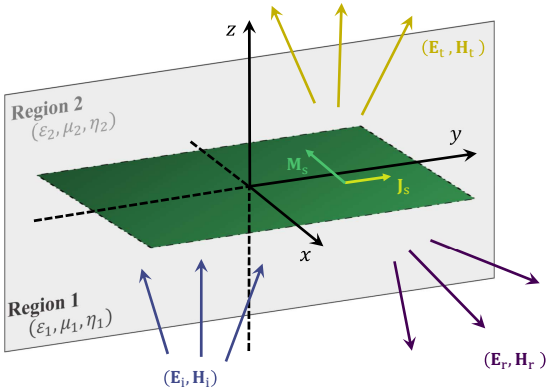

Figure 2.5: Scattering from an infinite lossless MS illuminated by a plane wave.

A reflected, $\mathbf{E}_r$ and $\mathbf{H}_r$, and refracted, $\mathbf{E}_t$ and $\mathbf{H}_t$, fields will appear: the total electric and magnetic contributions in the first region are $\mathbf{E}_1 = \mathbf{E}_i + \mathbf{E}_r$ and $\mathbf{H}_1 = \mathbf{H}_i + \mathbf{H}_r$. On the other hand, $\mathbf{H}_2 = \mathbf{H}_t$ and $\mathbf{E}_2 = \mathbf{E}_t$ are the ones in the refractive region. To ensure that these current densities are passively induced on the surface, a set of homogenized parameters must be introduced. There are three possible equivalent form: surface polarizabilities, susceptibilities or impedances/admittances. Due to the absence of volume, constitutive parameters such as permeability or permittivity cannot be properly defined [93].

In this manuscript, the latter one will be considered, since this formulation can lead to simple closed-forms for the reflection and transmission coefficients under plane wave incidence. After introducing the impedance boundary condition that relates its

average tangential fields to the fields discontinuities, (2.1) becomes:

$$\underline{\mathbf{Y}}_{\mathrm{e}}\,\mathbf{E}_{\mathrm{m}}^{\mathrm{tn}}+\underline{\boldsymbol{\chi}}\,\mathbf{H}_{\mathrm{m}}^{\mathrm{tn}}=\hat{\mathbf{n}}\times(\mathbf{H}_2-\mathbf{H}_1)=\underline{\mathbf{n}}\,(\mathbf{H}_2-\mathbf{H}_1)\,, \tag{2.2a}$$

$$\underline{\boldsymbol{\Upsilon}}\,\mathbf{E}_{\mathrm{m}}^{\mathrm{tn}}+\underline{\mathbf{Z}}_{\mathrm{m}}\,\mathbf{H}_{\mathrm{m}}^{\mathrm{tn}}=-\hat{\mathbf{n}}\times(\mathbf{E}_2-\mathbf{E}_1)=-\underline{\mathbf{n}}\,(\mathbf{E}_2-\mathbf{E}_1)\,. \tag{2.2b}$$

The unit vector $\hat{\mathbf{n}}$ can be substituted with no loss of meaning by the rotation matrix $\underline{\mathbf{n}}$, defined in contrast with the identity matrix $\underline{\mathbf{I}}$ as:

$$\underline{\mathbf{n}}=\begin{bmatrix}0&-1\\1&0\end{bmatrix}\qquad\underline{\mathbf{I}}=\begin{bmatrix}1&0\\0&1\end{bmatrix}. \tag{2.3}$$

The matrix $\underline{\mathbf{Y}}_{\mathrm{e}}$ represents the electric admittance on the MS due to $\mathbf{J}_{\mathrm{s}}$ while $\underline{\mathbf{Z}}_{\mathrm{m}}$ is the magnetic impedance due to $\mathbf{M}_{\mathrm{s}}$. The electromagnetic and magnetoelectric coupling are expressed by $\underline{\boldsymbol{\chi}}$ and $\underline{\boldsymbol{\Upsilon}}$, respectively. All these parameters are tensor quantities to take into account anisotropy (*e.g.* useful for polarization transformation), and are defined generically:

$$\underline{\mathbf{a}}=\begin{bmatrix}a^{\mathrm{ii}}&a^{\mathrm{ij}}\\a^{\mathrm{ji}}&a^{\mathrm{jj}}\end{bmatrix}. \tag{2.4}$$

The average electric tangential field is defined as $\mathbf{E}_{\mathrm{m}}^{\mathrm{tn}}=(\mathbf{E}_1+\mathbf{E}_2)/2$, while the magnetic one as $\mathbf{H}_{\mathrm{m}}^{\mathrm{tn}}=(\mathbf{H}_1+\mathbf{H}_2)/2$. Then, (2.2) can be written in matrix form:

$$\begin{pmatrix}\mathbf{J}_{\mathrm{s}}\\\mathbf{M}_{\mathrm{s}}\end{pmatrix}=\begin{pmatrix}\underline{\mathbf{Y}}_{\mathrm{e}}&\underline{\boldsymbol{\chi}}\\\underline{\boldsymbol{\Upsilon}}&\underline{\mathbf{Z}}_{\mathrm{m}}\end{pmatrix}\begin{pmatrix}\mathbf{E}_{\mathrm{m}}^{\mathrm{tn}}\\\mathbf{H}_{\mathrm{m}}^{\mathrm{tn}}\end{pmatrix}. \tag{2.5}$$

2.3.1. TAXONOMY

Bi-anisotropic MSs can be classified based on their operational characteristics, electromagnetic response and structural properties.

Firstly, depending on their attributes, MSs can be categorized in reciprocal and non-reciprocal, with both lossy and lossless cases considered. The property of reciprocity introduces the following relations[9] on the characteristic parameter tensors: $\underline{\mathbf{Y}}_{\mathrm{e}}=\underline{\mathbf{Y}}_{\mathrm{e}}^{\mathrm{T}}$, $\underline{\mathbf{Z}}_{\mathrm{m}}=\underline{\mathbf{Z}}_{\mathrm{m}}^{\mathrm{T}}$ and $\underline{\boldsymbol{\chi}}=-\underline{\boldsymbol{\Upsilon}}^{\mathrm{T}}$. By adding the lossless attribute, both magnetic impedance and electric admittance tensors become purely imaginary $\left(\Re\mathfrak{e}\left\{\underline{\mathbf{Y}}_{\mathrm{e}}\right\}=\Re\mathfrak{e}\left\{\underline{\mathbf{Z}}_{\mathrm{m}}\right\}=0\right)$, while both magnetoelectric and electromagnetic coupling tensors become purely real $\left(\Im\mathfrak{m}\left\{\underline{\boldsymbol{\chi}}\right\}=\Im\mathfrak{m}\left\{\underline{\boldsymbol{\Upsilon}}\right\}=0\right)$. When a MS is non-reciprocal, the following relations hold: $\underline{\mathbf{Y}}_{\mathrm{e}}\neq\underline{\mathbf{Y}}_{\mathrm{e}}^{\mathrm{T}}$, $\underline{\mathbf{Z}}_{\mathrm{m}}\neq\underline{\mathbf{Z}}_{\mathrm{m}}^{\mathrm{T}}$ and $\left(\Re\mathfrak{e}\left\{\underline{\boldsymbol{\chi}}\right\},\Re\mathfrak{e}\left\{\underline{\boldsymbol{\Upsilon}}\right\}\right)\neq 0$. Under this assumption, by adding the lossless condition, constrains[10] on the MS characteristic parameters are introduced: $\underline{\mathbf{Y}}_{\mathrm{e}}=\underline{\mathbf{Y}}_{\mathrm{e}}^{\dagger}$, $\underline{\mathbf{Z}}_{\mathrm{m}}=\underline{\mathbf{Z}}_{\mathrm{m}}^{\dagger}$ and $\underline{\boldsymbol{\chi}}=\underline{\boldsymbol{\Upsilon}}^{\dagger}$.

Another possible categorization of MSs is based on their EM response. A bi-anisotropic behavior, as reported in (2.5), considers $\left(\underline{\mathbf{Y}}_{\mathrm{e}},\underline{\boldsymbol{\chi}},\underline{\boldsymbol{\Upsilon}},\underline{\mathbf{Z}}_{\mathrm{m}}\right)\neq\underline{\mathbf{0}}$. When a combination of electric and magnetic response is present with no electromagnetic and

[9] The superscript "T" reported in these relations represents the transpose operation.
[10] The superscript "†" reported in these relations represents the transpose conjugate operation.

magnetoelectric coupling, the structure is called H-MS and $\underline{\boldsymbol{\chi}} = \underline{\boldsymbol{\Upsilon}} = \underline{\mathbf{0}}$ holds. The last two cases consider a purely electric or magnetic behavior. The first, referred to as Electric Metasurface (E-MS), presents only $\underline{\mathbf{Y}}_{\mathrm{e}} \neq \underline{\mathbf{0}}$ while the other one, called Magnetic Metasurface (M-MS), shows just $\underline{\mathbf{Z}}_{\mathrm{m}} \neq \underline{\mathbf{0}}$.

2

Reciprocal MSs can be classified based on their structural properties. The main distinction defines the concepts of isotropy, bi-isotropy, anisotropy and bi-anisotropy related to the surface parameters and how each of them affect the boundary conditions.

ISOTROPY

An isotropic medium is characterized by a high degree of spatial symmetry leading to an EM response that is unaffected by the media position with respect to the incident field. In terms of surface parameters, the electric admittance and magnetic impedance of an isotropic MS reduce to scalar quantities, $\underline{\mathbf{Y}}_{\mathrm{e}} = Y_{\mathrm{e}}\underline{\mathbf{I}}$ and $\underline{\mathbf{Z}}_{\mathrm{m}} = Z_{\mathrm{m}}\underline{\mathbf{I}}$, and if no electromagnetic and magnetoelectric coupling $\left(\underline{\boldsymbol{\chi}} = \underline{\boldsymbol{\Upsilon}} = \underline{\mathbf{0}}\right)$. The boundary conditions in (2.5) reduce to:

$$\begin{pmatrix} \mathbf{J}_{\mathrm{s}} \\ \mathbf{M}_{\mathrm{s}} \end{pmatrix} = \begin{pmatrix} Y_{\mathrm{e}}\underline{\mathbf{I}} & \underline{\mathbf{0}} \\ \underline{\mathbf{0}} & Z_{\mathrm{m}}\underline{\mathbf{I}} \end{pmatrix} \begin{pmatrix} \mathbf{E}_{\mathrm{m}}^{\mathrm{tn}} \\ \mathbf{H}_{\mathrm{m}}^{\mathrm{tn}} \end{pmatrix}. \tag{2.6}$$

It is clear that both surface parameter tensors are diagonal and, due to isotropy, the following relationships holds: $Y_{\mathrm{e}}^{\mathrm{ii}} = Y_{\mathrm{e}}^{\mathrm{jj}}$, $Y_{\mathrm{e}}^{\mathrm{ij}} = Y_{\mathrm{e}}^{\mathrm{ji}} = 0$, $Z_{\mathrm{m}}^{\mathrm{ii}} = Z_{\mathrm{m}}^{\mathrm{jj}}$ and $Z_{\mathrm{m}}^{\mathrm{ij}} = Z_{\mathrm{m}}^{\mathrm{ji}} = 0$.

ANISOTROPY

When a medium or material is not presenting a spatial symmetry and its behavior or physical properties vary on the direction, it is called anisotropic. A MS that presents this behavior requires a tensor description. However, $\underline{\chi} = \underline{\Upsilon} = \underline{\mathbf{0}}$ still holds. The boundary conditions in (2.5) becomes:

$$\begin{pmatrix} \mathbf{J}_{\mathrm{s}} \\ \mathbf{M}_{\mathrm{s}} \end{pmatrix} = \begin{pmatrix} \underline{\mathbf{Y}}_{\mathrm{e}} & \underline{\mathbf{0}} \\ \underline{\mathbf{0}} & \underline{\mathbf{Z}}_{\mathbf{m}} \end{pmatrix} \begin{pmatrix} \mathbf{E}_{\mathrm{m}}^{\mathrm{tn}} \\ \mathbf{H}_{\mathrm{m}}^{\mathrm{tn}} \end{pmatrix}, \tag{2.7}$$

where, in this case, $Y_{\mathrm{e}}^{\mathrm{ii}} \neq Y_{\mathrm{e}}^{\mathrm{jj}}$, $Y_{\mathrm{e}}^{\mathrm{ij}} = Y_{\mathrm{e}}^{\mathrm{ji}} \neq 0$, $Z_{\mathrm{m}}^{\mathrm{ii}} \neq Z_{\mathrm{m}}^{\mathrm{jj}}$ and $Z_{\mathrm{m}}^{\mathrm{ij}} = Z_{\mathrm{m}}^{\mathrm{ji}} \neq 0$.

BI-ISOTROPY

Bi-isotropy is a property of materials in electromagnetics that are both isotropic and exhibit coupling between the electric and magnetic fields. In a MS that presents this behavior, applied electric fields induce electric and also (equivalent) magnetic currents. Analogously, applied magnetic fields induce (equivalent) magnetic and also electric currents. These materials are generally described using constitutive relations that include coupling terms: $\left(\underline{\boldsymbol{\chi}}, \underline{\boldsymbol{\Upsilon}}\right) \neq \underline{\mathbf{0}}$. However, due to isotropy, all surface parameters are scalar quantities and their descriptions vary depending if the structure has a chiral or omega behavior. If the MS shows chirality, besides the expression of $\underline{\mathbf{Y}}_{\mathrm{e}}$ and $\underline{\mathbf{Z}}_{\mathrm{m}}$ that apply as in the isotropic case, $\underline{\boldsymbol{\chi}} = -\chi\underline{\mathbf{I}}$ and $\underline{\boldsymbol{\Upsilon}} = \Upsilon\underline{\mathbf{I}}$ hold. Moreover, due to chirality, $\chi^{\mathrm{ii}} = -\Upsilon^{\mathrm{jj}}$. The boundary conditions in (2.5) becomes:

$$\begin{pmatrix} \mathbf{J}_{\mathrm{s}} \\ \mathbf{M}_{\mathrm{s}} \end{pmatrix} = \begin{pmatrix} Y_{\mathrm{e}}\underline{\mathbf{I}} & -\chi\underline{\mathbf{I}} \\ \Upsilon\underline{\mathbf{I}} & Z_{\mathrm{m}}\underline{\mathbf{I}} \end{pmatrix} \begin{pmatrix} \mathbf{E}_{\mathrm{m}}^{\mathrm{tn}} \\ \mathbf{H}_{\mathrm{m}}^{\mathrm{tn}} \end{pmatrix}. \tag{2.8}$$

Metasurfaces presenting a bi-isotropic omega response are characterized by the following relations: $\underline{\underline{\boldsymbol{\chi}}} = -\chi\underline{\underline{\mathbf{n}}}$ and $\underline{\underline{\boldsymbol{\Upsilon}}} = -\Upsilon\underline{\underline{\mathbf{n}}}$. Then $\chi^{ij} = -\Upsilon^{ji}$. This kind of structures, are denominated as O-BIMS. The boundary conditions in (2.5) becomes:

$$\begin{pmatrix} \mathbf{J}_s \\ \mathbf{M}_s \end{pmatrix} = \begin{pmatrix} Y_e\underline{\underline{\mathbf{I}}} & -\chi\underline{\underline{\mathbf{n}}} \\ -\Upsilon\underline{\underline{\mathbf{n}}} & Z_m\underline{\underline{\mathbf{I}}} \end{pmatrix} \begin{pmatrix} \mathbf{E}_m^{tn} \\ \mathbf{H}_m^{tn} \end{pmatrix}. \tag{2.9}$$

BI-ANISOTROPY

Bi-anisotropy generalizes the concept of anisotropy and bi-isotropy. Bi-anisotropic materials have direction-dependent properties (anisotropy) and exhibit coupling between electric and magnetic fields. Their properties are described by tensors rather than scalar values, making their response dependent on the direction and type of applied electromagnetic fields. The general case of a bi-anisotropic MS presents in the boundary condition the presence of all four surface parameters tensors as in (2.5).

As for O-BIMSs, a distinction between chiral and omega behavior can be made [94]. A bi-anisotropic MS is defined chiral when the relation $\chi^{ii} \neq \Upsilon^{jj}$ is satisfied. On the other hand, it is omega when $\chi^{ij} \neq 0$ and $\Upsilon^{ji} \neq 0$.

Table 2.1: Reciprocal and lossless metasurface taxonomy based on their structural properties in terms of admittances and impedances.

			Bi–Isotropic		Bi–Anisotropic	
class	**Isotropic**	**Anisotropic**	**Chiral**	**Omega**	**Chiral**	**Omega**
Reciprocal	$Y_{\mathrm{e}}^{\mathrm{ii}} = Y_{\mathrm{e}}^{\mathrm{jj}}$ $Y_{\mathrm{e}}^{\mathrm{ij}} = Y_{\mathrm{e}}^{\mathrm{ji}} = 0$ $Z_{\mathrm{m}}^{\mathrm{ii}} = Z_{\mathrm{m}}^{\mathrm{jj}}$ $Z_{\mathrm{m}}^{\mathrm{ij}} = Z_{\mathrm{m}}^{\mathrm{ji}} = 0$ $\underline{\boldsymbol{\chi}} = 0$	$Y_{\mathrm{e}}^{\mathrm{ii}} \neq Y_{\mathrm{e}}^{\mathrm{jj}}$ $Y_{\mathrm{e}}^{\mathrm{ij}} = Y_{\mathrm{e}}^{\mathrm{ji}} \neq 0$ $Z_{\mathrm{m}}^{\mathrm{ii}} \neq Z_{\mathrm{m}}^{\mathrm{jj}}$ $Z_{\mathrm{m}}^{\mathrm{ij}} = Z_{\mathrm{m}}^{\mathrm{ji}} \neq 0$ $\underline{\boldsymbol{\chi}} = 0$	$Y_{\mathrm{e}}^{\mathrm{ii}} = Y_{\mathrm{e}}^{\mathrm{jj}}$ $Z_{\mathrm{m}}^{\mathrm{ii}} = Z_{\mathrm{m}}^{\mathrm{jj}}$ $\chi^{\mathrm{ii}} = \chi^{\mathrm{jj}} \neq 0$ $\chi^{\mathrm{ij}} = \chi^{\mathrm{ji}} = 0$	$Y_{\mathrm{e}}^{\mathrm{ij}} = Y_{\mathrm{e}}^{\mathrm{ji}} = 0$ $Z_{\mathrm{m}}^{\mathrm{ij}} = Z_{\mathrm{m}}^{\mathrm{ji}} = 0$ $\chi^{\mathrm{ii}} = \chi^{\mathrm{jj}} = 0$ $\chi^{\mathrm{ij}} = -\chi^{\mathrm{ji}} \neq 0$	$\chi^{\mathrm{ii}} \neq \chi^{\mathrm{jj}}$	$\chi^{\mathrm{ij}} \neq 0$ $\chi^{\mathrm{ij}} \neq 0$
Lossless	$\mathfrak{Re}\{\underline{\mathbf{Y}}_{\mathrm{e}}\} = \mathfrak{Re}\{\underline{\mathbf{Z}}_{\mathrm{m}}\} = 0$	$\mathfrak{Re}\{\underline{\mathbf{Y}}_{\mathrm{e}}\} = \mathfrak{Re}\{\underline{\mathbf{Z}}_{\mathrm{m}}\} = 0$	$\mathfrak{Re}\{\underline{\mathbf{Y}}_{\mathrm{e}}\} = \mathfrak{Re}\{\underline{\mathbf{Z}}_{\mathrm{m}}\} = 0$ $\mathfrak{Im}\{\underline{\boldsymbol{\chi}}\} = 0$		$\mathfrak{Re}\{\underline{\mathbf{Y}}_{\mathrm{e}}\} = \mathfrak{Re}\{\underline{\mathbf{Z}}_{\mathrm{m}}\} = 0$ $\mathfrak{Im}\{\underline{\boldsymbol{\chi}}\} = 0$	

2.3.2. SCATTERING RESPONSE

The boundary conditions reported in (2.2) allow to directly relate the MS scattering properties to its constitutive parameters [95]. When an x-polarized wave is normally incident to the Bi-anisotropic Metasurface (BMS) from Region 1 as in Fig. 2.5, electric and magnetic fields of this hemispace are defined as $\mathbf{E}_1 = \mathbf{I}_x + \mathbf{S}^x_{11}$ and $\mathbf{H}_1 = \eta_1^{-1}\underline{\mathbf{n}}\left(\mathbf{I}_x + \mathbf{S}^x_{11}\right)$. Then, the fields in Region 2 are written as $\mathbf{E}_2 = \mathbf{S}^x_{21}$ and $\mathbf{H}_2 = \eta_2^{-1}\underline{\mathbf{n}}\,\mathbf{S}^x_{21}$. Then, $\mathbf{I}_x = (1 \quad 0)^T$, $\mathbf{S}^x_{11} = \left(\mathbf{S}^{xx}_{11} \quad \mathbf{S}^{yx}_{11}\right)^T$ and $\mathbf{S}^x_{21} = \left(\mathbf{S}^{xx}_{21} \quad \mathbf{S}^{yx}_{21}\right)^T$. By inserting the values of the fields in the two regions in (2.2), the following expressions are derived:

$$\frac{\underline{\underline{\mathbf{Y}}}_e}{2}\left(\mathbf{I}_x + \mathbf{S}^x_{11} + \mathbf{S}^x_{21}\right) + \frac{\underline{\underline{\boldsymbol{\chi}}}\,\underline{\mathbf{n}}}{2}\left(\frac{\mathbf{I}_x}{\eta_1} - \frac{\mathbf{S}^x_{11}}{\eta_1} + \frac{\mathbf{S}^x_{21}}{\eta_2}\right) = -\left(\frac{-\mathbf{I}_x}{\eta_1} + \frac{\mathbf{S}^x_{11}}{\eta_1} + \frac{\mathbf{S}^x_{21}}{\eta_2}\right), \tag{2.10a}$$

$$\frac{\underline{\underline{\boldsymbol{\Upsilon}}}}{2}\left(\mathbf{I}_x + \mathbf{S}^x_{11} + \mathbf{S}^x_{21}\right) + \frac{\underline{\underline{\mathbf{Z}}}_m\,\underline{\mathbf{n}}}{2}\left(\frac{\mathbf{I}_x}{\eta_1} - \frac{\mathbf{S}^x_{11}}{\eta_1} + \frac{\mathbf{S}^x_{21}}{\eta_2}\right) = -\underline{\mathbf{n}}\left(-\mathbf{I}_x - \mathbf{S}^x_{11} + \mathbf{S}^x_{21}\right), \tag{2.10b}$$

leading to the closed-form expression of the following linear system:

$$\begin{pmatrix} \mathbf{S}^x_{12} \\ \\ \mathbf{S}^x_{22} \end{pmatrix} = \begin{pmatrix} \frac{\underline{\underline{\mathbf{Y}}}_e}{2} - \frac{\underline{\underline{\boldsymbol{\chi}}}\,\underline{\mathbf{n}}}{2\eta_1} + \frac{\underline{\underline{\mathbf{I}}}}{\eta_1} & \frac{\underline{\underline{\mathbf{Y}}}_e}{2} + \frac{\underline{\underline{\boldsymbol{\chi}}}\,\underline{\mathbf{n}}}{2\eta_2} + \frac{\underline{\underline{\mathbf{I}}}}{\eta_2} \\ \\ \frac{\underline{\underline{\boldsymbol{\Upsilon}}}}{2} - \frac{\underline{\underline{\mathbf{Z}}}_m\,\underline{\mathbf{n}}}{2\eta_1} - \underline{\mathbf{n}} & \frac{\underline{\underline{\boldsymbol{\Upsilon}}}}{2} + \frac{\underline{\underline{\mathbf{Z}}}_m\,\underline{\mathbf{n}}}{2\eta_2} + \underline{\mathbf{n}} \end{pmatrix}^{-1} \begin{pmatrix} -\frac{\underline{\underline{\mathbf{Y}}}_e\mathbf{I}_x}{2} - \frac{\underline{\underline{\boldsymbol{\chi}}}\,\underline{\mathbf{n}}\,\mathbf{I}_x}{2\eta_1} + \frac{\mathbf{I}_x}{\eta_1} \\ \\ -\frac{\underline{\underline{\mathbf{Z}}}_m\,\underline{\mathbf{n}}\,\mathbf{I}_x}{2\eta_1} - \frac{\underline{\underline{\boldsymbol{\Upsilon}}}\mathbf{I}_x}{2} + \underline{\mathbf{n}}\,\mathbf{I}_x \end{pmatrix}. \tag{2.11}$$

To find $\mathbf{S}^x_{22} = \left(\mathbf{S}^{xx}_{22} \quad \mathbf{S}^{yx}_{22}\right)^T$ and $\mathbf{S}^x_{12} = \left(\mathbf{S}^{xx}_{12} \quad \mathbf{S}^{yx}_{12}\right)^T$, the expressions for $\mathbf{E}_1$, $\mathbf{E}_2$, $\mathbf{H}_1$ and $\mathbf{H}_2$ needs to be considered due to the fact this time the incoming wavefront is illuminating the structure from Region 2. The fields are then expressed as $\mathbf{E}_2 = \mathbf{I}_x + \mathbf{S}^x_{22}$, $\mathbf{H}_2 = \eta_2^{-1}\underline{\mathbf{n}}\left(-\mathbf{I}_x + \mathbf{S}^x_{22}\right)$, $\mathbf{E}_1 = \mathbf{S}^x_{12}$ and $\mathbf{H}_1 = -\eta_1^{-1}\underline{\mathbf{n}}\,\mathbf{S}^x_{12}$. As before, by inserting the values of the fields in the two regions in (2.2), the following expressions are derived:

$$\frac{\underline{\underline{\mathbf{Y}}}_e}{2}\left(\mathbf{I}_x + \mathbf{S}^x_{12} + \mathbf{S}^x_{22}\right) + \frac{\underline{\underline{\boldsymbol{\chi}}}\,\underline{\mathbf{n}}}{2}\left(-\frac{\mathbf{I}_x}{\eta_2} - \frac{\mathbf{S}^x_{12}}{\eta_1} + \frac{\mathbf{S}^x_{22}}{\eta_2}\right) = -\left(-\frac{\mathbf{I}_x}{\eta_2} + \frac{\mathbf{S}^x_{12}}{\eta_1} + \frac{\mathbf{S}^x_{22}}{\eta_2}\right), \tag{2.12a}$$

$$\frac{\underline{\underline{\boldsymbol{\Upsilon}}}}{2}\left(\mathbf{I}_x + \mathbf{S}^x_{12} + \mathbf{S}^x_{22}\right) + \frac{\underline{\underline{\mathbf{Z}}}_m\,\underline{\mathbf{n}}}{2}\left(-\frac{\mathbf{I}_x}{\eta_2} - \frac{\mathbf{S}^x_{12}}{\eta_1} + \frac{\mathbf{S}^x_{22}}{\eta_2}\right) = -\underline{\mathbf{n}}\left(\mathbf{I}_x - \mathbf{S}^x_{12} + \mathbf{S}^x_{22}\right), \tag{2.12b}$$

leading, as shown previously, to the closed-form expression of the following linear system:

$$\begin{pmatrix} \mathbf{S}^x_{12} \\ \\ \mathbf{S}^x_{22} \end{pmatrix} = \begin{pmatrix} \frac{\underline{\underline{\mathbf{Y}}}_e}{2} - \frac{\underline{\underline{\boldsymbol{\chi}}}\,\underline{\mathbf{n}}}{2\eta_1} + \frac{\underline{\underline{\mathbf{I}}}}{\eta_1} & \frac{\underline{\underline{\mathbf{Y}}}_e}{2} + \frac{\underline{\underline{\boldsymbol{\chi}}}\,\underline{\mathbf{n}}}{2\eta_2} + \frac{\underline{\underline{\mathbf{I}}}}{\eta_2} \\ \\ \frac{\underline{\underline{\boldsymbol{\Upsilon}}}}{2} - \frac{\underline{\underline{\mathbf{Z}}}_m\,\underline{\mathbf{n}}}{2\eta_1} - \underline{\mathbf{n}} & \frac{\underline{\underline{\boldsymbol{\Upsilon}}}}{2} + \frac{\underline{\underline{\mathbf{Z}}}_m\,\underline{\mathbf{n}}}{2\eta_2} + \underline{\mathbf{n}} \end{pmatrix}^{-1} \begin{pmatrix} -\frac{\underline{\underline{\mathbf{Y}}}_e\,\mathbf{I}_x}{2} + \frac{\underline{\underline{\boldsymbol{\chi}}}\,\underline{\mathbf{n}}\,\mathbf{I}_x}{2\eta_2} + \frac{\mathbf{I}_x}{\eta_2} \\ \\ \frac{\underline{\underline{\mathbf{Z}}}_m\,\underline{\mathbf{n}}\,\mathbf{I}_x}{2\eta_2} - \frac{\underline{\underline{\boldsymbol{\Upsilon}}}\mathbf{I}_x}{2} - \underline{\mathbf{n}}\,\mathbf{I}_x \end{pmatrix}. \tag{2.13}$$

The expressions of the couple $\left(\mathbf{S}^y_{11}, \mathbf{S}^y_{21}\right)$ and $\left(\mathbf{S}^y_{22}, \mathbf{S}^y_{12}\right)$ are derived by changing $\mathbf{I}_x$ in

$\mathbf{I}_y = (0 \quad 1)^T$. The complete scattering matrix can then be written as [95]:

$$\underline{\mathbf{S}} = \begin{pmatrix} \underline{\mathbf{S}}_{11} & \underline{\mathbf{S}}_{12} \\ \underline{\mathbf{S}}_{21} & \underline{\mathbf{S}}_{22} \end{pmatrix} = \begin{pmatrix} \frac{\underline{\mathbf{Y}}_e}{2} - \frac{\underline{\boldsymbol{\chi}}\,\underline{\mathbf{n}}}{2\eta_1} + \frac{\underline{\mathbf{I}}}{\eta_1} & \frac{\underline{\mathbf{Y}}_e}{2} + \frac{\underline{\boldsymbol{\chi}}\,\underline{\mathbf{n}}}{2\eta_2} + \frac{\underline{\mathbf{I}}}{\eta_2} \\ \frac{\underline{\boldsymbol{\Upsilon}}}{2} - \frac{\underline{\mathbf{Z}}_m\,\underline{\mathbf{n}}}{2\eta_1} - \underline{\mathbf{n}} & \frac{\underline{\boldsymbol{\Upsilon}}}{2} + \frac{\underline{\mathbf{Z}}_m\,\underline{\mathbf{n}}}{2\eta_2} + \underline{\mathbf{n}} \end{pmatrix}^{-1} \times$$

$$\times \begin{pmatrix} -\frac{\underline{\mathbf{Y}}_e}{2} - \frac{\underline{\boldsymbol{\chi}}\,\underline{\mathbf{n}}}{2\eta_1} + \frac{\underline{\mathbf{I}}}{\eta_1} & -\frac{\underline{\mathbf{Y}}_e}{2} + \frac{\underline{\boldsymbol{\chi}}\,\underline{\mathbf{n}}}{2\eta_2} + \frac{\underline{\mathbf{I}}}{\eta_2} \\ -\frac{\underline{\boldsymbol{\Upsilon}}}{2} - \frac{\underline{\mathbf{Z}}_m\,\underline{\mathbf{n}}}{2\eta_1} + \underline{\mathbf{n}} & -\frac{\underline{\boldsymbol{\Upsilon}}}{2} + \frac{\underline{\mathbf{Z}}_m\,\underline{\mathbf{n}}}{2\eta_2} - \underline{\mathbf{n}} \end{pmatrix}. \tag{2.14}$$

Due to the bi-anisotropy behavior, the scattering matrix results in a full 4×4 matrix. Starting from this expression, the MS characteristic parameters are defined as [95]:

$$\underline{\boldsymbol{\Lambda}} = \begin{pmatrix} \underline{\mathbf{Y}}_e & \underline{\boldsymbol{\chi}} \\ \underline{\boldsymbol{\Upsilon}} & \underline{\mathbf{Z}}_m \end{pmatrix} = 2 \begin{pmatrix} \frac{\underline{\mathbf{I}}}{\eta_1} - \frac{\underline{\mathbf{S}}_{11}}{\eta_1} - \frac{\underline{\mathbf{S}}_{21}}{\eta_2} & \frac{\underline{\mathbf{I}}}{\eta_2} - \frac{\underline{\mathbf{S}}_{12}}{\eta_1} - \frac{\underline{\mathbf{S}}_{22}}{\eta_2} \\ \underline{\mathbf{n}} + \underline{\mathbf{n}}\,\underline{\mathbf{S}}_{11} - \underline{\mathbf{n}}\,\underline{\mathbf{S}}_{21} & -\underline{\mathbf{n}} + \underline{\mathbf{n}}\,\underline{\mathbf{S}}_{12} - \underline{\mathbf{n}}\,\underline{\mathbf{S}}_{22} \end{pmatrix} \times$$

$$\times \begin{pmatrix} \underline{\mathbf{I}} + \underline{\mathbf{S}}_{11} + \underline{\mathbf{S}}_{21} & \underline{\mathbf{I}} + \underline{\mathbf{S}}_{12} + \underline{\mathbf{S}}_{22} \\ \frac{\underline{\mathbf{n}}}{\eta_1} - \frac{\underline{\mathbf{n}}\,\underline{\mathbf{S}}_{11}}{\eta_1} + \frac{\underline{\mathbf{n}}\,\underline{\mathbf{S}}_{21}}{\eta_2} & -\frac{\underline{\mathbf{n}}}{\eta_2} - \frac{\underline{\mathbf{n}}\,\underline{\mathbf{S}}_{12}}{\eta_1} + \frac{\underline{\mathbf{n}}\,\underline{\mathbf{S}}_{22}}{\eta_2} \end{pmatrix}^{-1}. \tag{2.15}$$

From (2.14), the total surface characteristic parameters required to realize a specific S-matrix can be evaluated. These are degree of freedom of the structure. Generally speaking, a BMS has 16 complex values as entries for $\underline{\boldsymbol{\Lambda}}$. When the surface is reciprocal and port impedances identical, the S-matrix is symmetric and $\underline{\mathbf{S}} = \underline{\mathbf{S}}^T$. In this case, the total number of independent variables reduces from 16 to 10. Nevertheless, each of this entry is a complex number with a real and imaginary part. The amount of free variables is 20. If the MS is lossless, then $\underline{\mathbf{S}}^T\underline{\mathbf{S}}^\dagger = \underline{\mathbf{I}}$. In this way, the total amount of free variables reduces to 10. Intuitively, this value can be extracted from the reciprocity attribute of a lossless MS: $\underline{\mathbf{Y}}_e = \underline{\mathbf{Y}}_e^T$, $\underline{\mathbf{Z}}_m = \underline{\mathbf{Z}}_m^T$ means there are a total of 3, 4 and again 3 free variables for each characteristic parameter, respectively.

By restricting to the case of single polarization, $\underline{\mathbf{S}}_{mn} = S_{mn}\underline{\mathbf{I}}$, the scattering matrix reduces to the one of a two port network [96]:

$$\underline{\mathbf{S}} = \begin{pmatrix} S_{11} & S_{12} \\ S_{21} & S_{22} \end{pmatrix}. \tag{2.16}$$

Each entry of the matrix is a complex value with a total of 8 degree of freedom. If the MS is reciprocal with identical port impedances, $S_{21} = S_{12}$, then the unknowns reduce to 6. When the MS is also lossless, three independent equations can be extracted:

$$|S_{11}|^2 + |S_{12}|^2 = 1, \tag{2.17a}$$

$$|S_{22}|^2 + |S_{21}|^2 = 1\,. \tag{2.17b}$$

$$S_{11}S_{12}^{\dagger} + S_{22}S_{21}^{\dagger} = |S_{11}||S_{12}|e^{j(\angle S_{11} - \angle S_{12})} + |S_{22}||S_{21}|e^{j(\angle S_{22} - \angle S_{21})} = 0\,. \tag{2.17c}$$

2.4. METASURFACE ANALYSIS

So far, how to model a MS and its taxonomy depending on the values its charactherics parameters assume have been explored. But how can it be designed to achieve the desired EM field manipulations? There are multiple techniques applicable depending on the application. One way, that is considered along this work, is to consider the MS elements as a cascade of sheet impedances alternated with dielectric slabs, forming a layered structure which can guide and manipulate electromagnetic waves. Starting from this model, different methods can be employed to evaluate the scattering parameters of MS cells, when illuminated by a normally incident plane wave, as well as to analyze and engineer the dispersion properties of the modes propagating across and along a MS.

A very powerful tool for these kind of layered structures is the transmission, or $ABCD$, matrix. By considering each layer as a two or more two-port networks, the complete behavior in terms of impedance, admittance and scattering representations can be computed by multiplying the transfer matrices of each layer. By way of example, consider a lossless MS unit cell composed by three impedance surfaces interleaved by two identical dielecric slabs, as shown in Fig. 2.6. Assume that the MS is periodic along the $\hat{\mathbf{x}}$ and $\hat{\mathbf{y}}$ direction, and that is illuminated by a plane wave propagating along $\hat{\mathbf{z}}$.

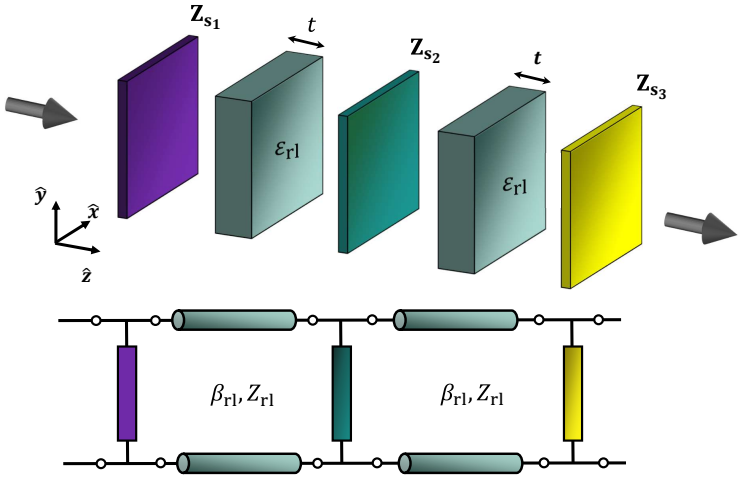

Figure 2.6: Geometry and equivalent circuit model of a Metasurface unit cell comprising three sheet admittances.

For analytic purpose, the sheets are purely imaginary admittances, $\underline{\mathbf{Y}}_{\mathrm{s_i}} = j\underline{\mathbf{B}}_{\mathrm{s_i}}$, with $\underline{\mathbf{B}}_{\mathrm{s_i}}$ being the tensor susceptance of each metal layer. The dielectrics have thickness t and characteristic impedance Z_{rl}. The currents and voltages on either side of each unit cell can be related using a transfer matrix approach [95]. The 4×4 $ABCD$ matrix of the

unit cell in Fig. 2.6 will be:

$$\underline{\mathbf{T}}_{\mathrm{TOT}} = \underline{\mathbf{T}}_{\mathrm{s}_1}\,\underline{\mathbf{T}}_{\mathrm{RL}}\,\underline{\mathbf{T}}_{\mathrm{s}_2}\,\underline{\mathbf{T}}_{\mathrm{RL}}\,\underline{\mathbf{T}}_{\mathrm{s}_3} = \begin{bmatrix} \underline{\mathbf{A}} & \underline{\mathbf{B}} \\ \underline{\mathbf{C}} & \underline{\mathbf{D}} \end{bmatrix}. \tag{2.18}$$

Each transfer matrix related to the sheet admittances and dielectric slabs in the cascade are defined as follow:

$$\underline{\mathbf{T}}_{\mathrm{Y_{s_i}}} = \begin{bmatrix} \underline{\mathbf{I}} & \underline{\mathbf{0}} \\ \underline{\mathbf{n}}\,\underline{\mathbf{Y}}_{\mathrm{s_i}} & \underline{\mathbf{I}} \end{bmatrix} \quad \underline{\mathbf{T}}_{\mathrm{RL}} = \begin{bmatrix} \cos(\beta_{\mathrm{rl}}\,t)\underline{\mathbf{I}} & -jZ_{\mathrm{rl}}\sin(\beta_{\mathrm{rl}}\,t)\underline{\mathbf{n}} \\ jY_{\mathrm{rl}}\sin(\beta_{\mathrm{rl}}\,t)\underline{\mathbf{n}} & \cos(\beta_{\mathrm{rl}}\,t)\underline{\mathbf{I}} \end{bmatrix}, \tag{2.19}$$

where $\beta_{\mathrm{rl}} = 2\pi\sqrt{\varepsilon_{\mathrm{rl}}}/\lambda_{\mathrm{op}}$ is the propagation constant in the dielectric, which has a relative permittivity $\varepsilon_{\mathrm{rl}}$, and λ_{op} is the free-space operating wavelength at frequency f_{op}. The scattering coefficients of the structure are related to the $ABCD$ matrix of the cascaded sheet admittances or the single layers by the following expression [95], [97]:

$$\begin{pmatrix} \underline{\mathbf{S}}_{11} & \underline{\mathbf{S}}_{12} \\ \underline{\mathbf{S}}_{21} & \underline{\mathbf{S}}_{22} \end{pmatrix} = \begin{pmatrix} -\underline{\mathbf{I}} & \dfrac{\underline{\mathbf{B}}\,\underline{\mathbf{n}}}{\eta_2} + \underline{\mathbf{A}} \\ \dfrac{\underline{\mathbf{n}}}{\eta_1} & \dfrac{\underline{\mathbf{D}}\,\underline{\mathbf{n}}}{\eta_2} + \underline{\mathbf{C}} \end{pmatrix}^{-1} \begin{pmatrix} \underline{\mathbf{I}} & \dfrac{\underline{\mathbf{B}}\,\underline{\mathbf{n}}}{\eta_2} - \underline{\mathbf{A}} \\ \dfrac{\underline{\mathbf{n}}}{\eta_1} & \dfrac{\underline{\mathbf{D}}\,\underline{\mathbf{n}}}{\eta_2} - \underline{\mathbf{C}} \end{pmatrix}, \tag{2.20}$$

where η_1 and η_2 are the characteristic impedances of the region below and above the MS, respectively. An arbitrary structure transfer matrix entries can be extracted from (2.20) in function of the scattering parameters:

$$\begin{bmatrix} \underline{\mathbf{A}} & \underline{\mathbf{B}} \\ \underline{\mathbf{C}} & \underline{\mathbf{D}} \end{bmatrix} = \begin{pmatrix} \underline{\mathbf{I}} + \underline{\mathbf{S}}_{11} & \underline{\mathbf{S}}_{12} \\ \dfrac{\underline{\mathbf{n}}}{\eta_1}\left(\underline{\mathbf{I}} - \underline{\mathbf{S}}_{11}\right) & -\dfrac{\underline{\mathbf{n}}}{\eta_1}\underline{\mathbf{S}}_{12} \end{pmatrix} \begin{pmatrix} \underline{\mathbf{S}}_{21} & \underline{\mathbf{I}} + \underline{\mathbf{S}}_{22} \\ \dfrac{\underline{\mathbf{n}}}{\eta_2}\underline{\mathbf{S}}_{\mathbf{21}} & \dfrac{\underline{\mathbf{n}}}{\eta_2}\left(-\underline{\mathbf{I}} + \underline{\mathbf{S}}_{22}\right) \end{pmatrix}^{-1}. \tag{2.21}$$

A generic structure transfer matrix is related to its impedance matrix trough the following expression [98]:

$$\begin{bmatrix} \underline{\mathbf{A}} & \underline{\mathbf{B}} \\ \underline{\mathbf{C}} & \underline{\mathbf{D}} \end{bmatrix} = \begin{pmatrix} \underline{\mathbf{Z}}_{11}\,\underline{\mathbf{Z}}_{21}^{-1} & \underline{\mathbf{Z}}_{11}\,\underline{\mathbf{Z}}_{21}^{-1}\,\underline{\mathbf{Z}}_{22} - \underline{\mathbf{Z}}_{12} \\ \underline{\mathbf{Z}}_{21}^{-1} & \underline{\mathbf{Z}}_{21}^{-1}\,\underline{\mathbf{Z}}_{22} \end{pmatrix}. \tag{2.22}$$

When a linear polarized and normal incident wave impinges the MS, both transfer and impedance matrices entries reported in (2.22) reduces to a two-port network problem [96]:

$$\begin{bmatrix} A & B \\ C & D \end{bmatrix} = \begin{bmatrix} \dfrac{Z_{11}}{Z_{21}} & \dfrac{|Z|}{Z_{21}} \\ \dfrac{1}{Z_{21}} & \dfrac{Z_{22}}{Z_{21}} \end{bmatrix}, \tag{2.23}$$

where $|Z| = Z_{11}Z_{22} - Z_{21}Z_{12}$.

2.4.1. SHEET IMPEDANCE CASCADE

This method can be used in the synthesis of MS cells with certain characteristics on scattering parameters by knowing the $\underline{\mathbf{\Lambda}}$ matrix. Firstly, spatially fed MS under plane wave incidence can be modeled, in general, as a four-port microwave device, characterized in terms of an impedance matrix, see Fig. 2.7a.

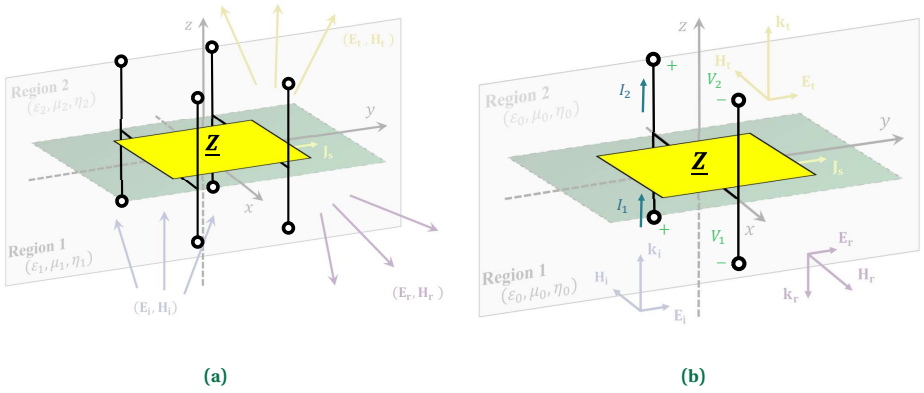

(a) (b)

Figure 2.7: (a) Four and (b) two port models of matesurfaces under bianisotropy and isotropy condition, respectively.

Specifically, the impedance matrix relates the currents and voltages applied to the ports of the device. In the case of translating field boundary conditions to an equivalent Z-matrix, the ports of the MS can be thought of as the two half-spaces containing the desired fields for Transverse Electric (TE) and Transverse Magnetic (TM) polarized incident waves. Isotropic MSs can instead be modeled as two-port networks, see Fig. 2.7b. One port of the equivalent network will represent the domain of the normally incident plane wave while the second port will resemble the domain of the refracted plane wave. As the electric field is analogous to a voltage and the magnetic field is analogous to a current, the boundary conditions can be rearranged into a matrix format to resemble that of a microwave two-port network [99]:

$$\begin{pmatrix} V_1 \\ V_2 \end{pmatrix} = \begin{pmatrix} Z_{11} & Z_{12} \\ Z_{21} & Z_{22} \end{pmatrix} \begin{pmatrix} I_1 \\ -I_2 \end{pmatrix} \quad \Longleftrightarrow \quad \begin{pmatrix} \mathbf{E}_1 \\ \mathbf{E}_2 \end{pmatrix} = \begin{pmatrix} Z_{11} & Z_{12} \\ Z_{21} & Z_{22} \end{pmatrix} \begin{pmatrix} \mathbf{H}_1 \\ -\mathbf{H}_2 \end{pmatrix}. \tag{2.24}$$

Reciprocal O-BIMS are modeled as a two-port networks in case of a normally incident plane wave polarized along $\hat{\mathbf{y}}$. By combining (2.5) with (2.24), after some manipulations, the entries of the symmetric impedance matrix can be linked to the surface parameters Y_e, Z_m and χ as follows [100]:

$$\begin{pmatrix} Z_{11} & Z_{12} \\ Z_{21} & Z_{22} \end{pmatrix} = \begin{pmatrix} \dfrac{(\chi-2)^2}{4Y_\mathrm{e}} + \dfrac{Z_\mathrm{m}}{4} & \dfrac{4-\chi^2}{4Y_\mathrm{e}} - \dfrac{Z_\mathrm{m}}{4} \\ \dfrac{4-\chi^2}{4Y_\mathrm{e}} - \dfrac{Z_\mathrm{m}}{4} & \dfrac{(\chi+2)^2}{4Y_\mathrm{e}} + \dfrac{Z_\mathrm{m}}{4} \end{pmatrix}. \tag{2.25}$$

By realizing the MS as a cascade of three sheet impedances or admittances, three degrees of freedom are provided to emulate the three surface properties Z_m, Y_e and χ shown in Fig. 2.6. The impedance sheets Z_{s_1}, Z_{s_2} and Z_{s_3} are derived by equating 2.23 with the $ABCD$ matrix obtained by the layers cascade [100]:

$$Z_{s_1} = \frac{Z_{rl}\tan(\beta_{rl}t)}{j + Z_{rl}\tan(\beta_{rl}t)\dfrac{Z_{22}+Z_{21}}{Z_{11}Z_{22}-Z_{21}^2}}, \tag{2.26a}$$

$$Z_{s_2} = -\frac{\left[Z_{rl}\tan(\beta_{rl}t)\right]^2 \dfrac{Z_{21}}{Z_{11}Z_{22}-Z_{21}^2}}{\sec^2(\beta_{rl}t) - 2jZ_{rl}\tan(\beta_{rl}t)\dfrac{Z_{21}}{Z_{11}Z_{22}-Z_{21}^2}}, \tag{2.26b}$$

$$Z_{s_3} = \frac{Z_{rl}\tan(\beta_{rl}t)}{j + Z_{rl}\tan(\beta_{rl}t)\dfrac{Z_{11}+Z_{21}}{Z_{11}Z_{22}-Z_{21}^2}}. \tag{2.26c}$$

These expressions allows to rapidly compute the sheet impedances Z_{s_1}, Z_{s_2} and Z_{s_3} by knowing the target $\underline{\mathbf{\Lambda}}$ matrix through (2.25).

2.4.2. DISPERSION STUDY: PASSBAND AND STOPBAND

The previous methods can be used to evaluate the transmitted and reflected fields of a MS under plane-wave incidence. This is a scattering problem, where an EM source is defined and the field excited by the source in the presence of the MS is computed.

For the sake of completeness, it is important to remember that the same analytic tools can be used also to determine the modes propagating across a periodic series of layers and MSs, or propagating along a surface in a layered environment. In this case no source is present and the features of the mode (propagation and attenuation constants, etc) need to be computed [96], [101].

For example, the frequency dispersion of the modes propagating in an isotropic, reciprocal and lossless three-layer MS shown in Fig. 2.6 can be analyzed assuming that it is periodic along z-axis. Then, a wave with propagation constant $k_z = \alpha_z + j\beta_z$, where α_z and β_z are respectively the attenuation and phase constants, is supposed moving along $+z$. The transfer matrix approach is used to relate the voltages and currents on either side of each n-th unit cell [96]:

$$\begin{bmatrix} V_n \\ I_n \end{bmatrix} = \underline{\mathbf{T}}_{TOT} \begin{bmatrix} V_{n+1} \\ I_{n+1} \end{bmatrix} = \begin{bmatrix} V_{n+1}e^{k_z p} \\ I_{n+1}e^{k_z p} \end{bmatrix}. \tag{2.27}$$

The $ABCD$ matrix obtained by the cascade of all the elements with periodicity $p = 2t$ is defined as:

$$\underline{\mathbf{T}}_{TOT} = \underline{\mathbf{T}}_{s_1}\underline{\mathbf{T}}_{RL}\underline{\mathbf{T}}_{s_2}\underline{\mathbf{T}}_{RL}\underline{\mathbf{T}}_{s_3} = \begin{bmatrix} A & B \\ C & D \end{bmatrix}. \tag{2.28}$$

For isotropic MS, the transfer matrices related to the sheet admittances and dielectric slabs reported in (2.19) reduces to:

$$\underline{\mathbf{T}}_{Y_{s_i}} = \begin{bmatrix} 1 & 0 \\ Y_{s_i} & 1 \end{bmatrix} \quad \underline{\mathbf{T}}_{RL} = \begin{bmatrix} \cos(\beta_{rl} t) & -jZ_{rl}\sin(\beta_{rl} t) \\ jY_{rl}\sin(\beta_{rl} t) & \cos(\beta_{rl} t) \end{bmatrix}. \tag{2.29}$$

By inserting (2.28) in (2.27), the following simplified expression can be found:

$$\begin{bmatrix} A - e^{k_z p} & B \\ C & D - e^{k_z p} \end{bmatrix} \begin{bmatrix} V_{n+1} \\ I_{n+1} \end{bmatrix} = 0. \tag{2.30}$$

Due to reciprocity, the determinant of (2.28) is $AD - BC = 1$. Moreover, to find a non trivial solution, it is necessary that the determinant of (2.30) vanishes. Based on these conditions, the following expression is obtained:

$$1 + e^{2k_z p} - (A + D)e^{k_z p} = 0. \tag{2.31}$$

The MS is assumed symmetric, $Y_{s_1} = Y_{s_3}$, and with inductive sheet admittances, $Y_{s_1} = j/(\omega L_1)$ and $Y_{s_2} = j/(\omega L_2)$. Then, the expression of A and D in (2.31) are calculated by inserting (2.19) in (2.28). Therefore, equation (2.31) reads as:

$$\begin{aligned} \cosh\Phi = \cos^2(\beta_{rl} t) - \frac{2Z_{rl}}{\omega L_1}\sin(\beta_{rl} t)\cos(\beta_{rl} t) - \sin^2(\beta_{rl} t) \\ + \frac{Z_{rl}^2}{\omega^2 L_1 L_2}\sin^2(\beta_{rl} t) - \frac{Z_{rl}}{\omega L_2}\sin(\beta_{rl} t)\cos(\beta_{rl} t), \end{aligned} \tag{2.32}$$

where $\Phi = k_z p$. In Fig. 2.8 are reported the values of α_z and β_z for $L_1 = 2\,\text{nH}$, $L_2 = 3\,\text{nH}$, $t = 1.4\,\text{mm}$ and $\varepsilon_{rl} = 3$.

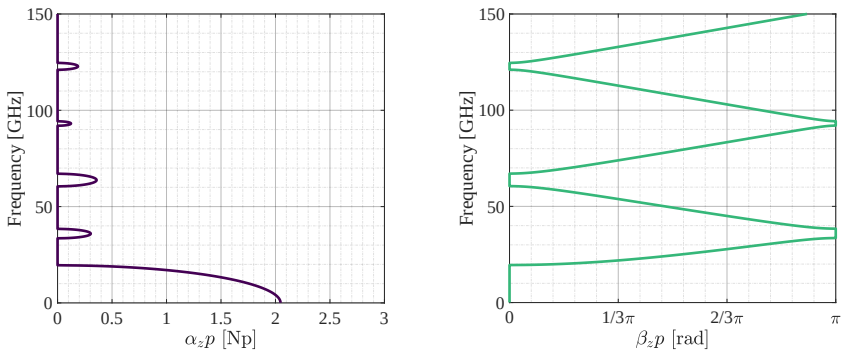

Figure 2.8: (a) Attenuation constant and, (b), propagation constant for $L_1 = 2\text{nH}$ and $L_2 = 3\text{nH}$.

It is observed that bengaps are present in the stopbands at different frequencies. In order to close these bandgaps and achieve a wideband behavior, $\Phi = \pi$ is enforced in (2.31):

$$\left[\cos(\beta_{rl} t) - \frac{Z_{rl}}{\omega L_1}\sin(\beta_{rl} t)\right]\left[2\cos(\beta_z t) - \frac{Z_{rl}}{\omega L_2}\sin(\beta_{rl} t)\right] = 0. \tag{2.33}$$

It is clear that the relation $L_1 = 2L_2$ ensures that the first bandgap is closed, as shown in Fig. 2.9 where the behavior of α_z and β_z are reported for $L_1 = 4\,\text{nH}$ and $L_2 = 2\,\text{nH}$ [102].

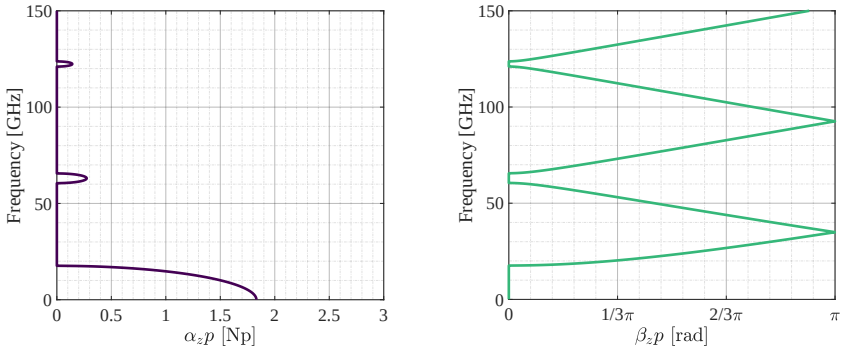

Figure 2.9: (a) Attenuation constant and, (b), propagation constant for $L_1 = 4\text{nH}$ and $L_2 = 2\text{nH}$.

2.4.3. TRANSVERSE RESONANCE METHOD

The modes propagating along a MS and their resonance frequencies can be computed using the Transverse Resonance Method (TRM). This technique is a powerful tool for the analysis of structures fed for instance with a coaxial pin and based on the propagation of surface waves or radiating due to leaky modes.

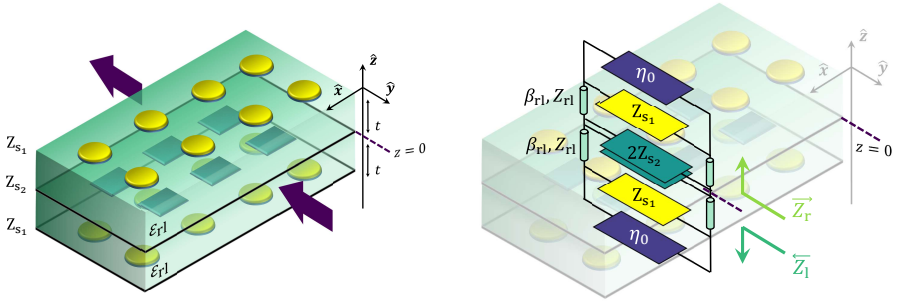

Figure 2.10: (a) Three-layer symmetric, reciprocal and isotropic MS and (b) TRM circuit model.

To understand the capabilities of this method, an isotropic, reciprocal and symmetric MS working at $f_{op} = 30\,\text{GHz}$, comprising three sheet impedances and spaced by two dielectric slabs is considered (see Fig. 2.10a). The spacers have thickness $t = 1.4\,\text{mm}$ and electric permittivity $\varepsilon_{rl} = 3$. Due to symmetry, the external layers are equal, $Z_{s_1} = Z_{s_3}$. The inner layer is located at $z = 0$ and the MS circuit model is reported in Fig. 2.10b.

To apply the TRM, a reference plane that splits the MS equivalent network in two circuits is established: in this case the xy-plane at $z = 0$. Then, by enforcing the Kirchoff

laws of currents and voltages at this section, the following conditions are enforced:

$$\overleftarrow{Z_{\mathrm{l}}} = -\overrightarrow{Z_{\mathrm{r}}}, \tag{2.34a}$$

$$\overleftarrow{Y_{\mathrm{l}}} = -\overrightarrow{Y_{\mathrm{r}}}. \tag{2.34b}$$

Due to circuit symmetry (see Fig. 2.10), $\overleftarrow{Z_{\mathrm{l}}} = \overrightarrow{Z_{\mathrm{r}}}$ and also $\overleftarrow{Y_{\mathrm{l}}} = \overrightarrow{Y_{\mathrm{r}}}$. Then, from Fig. 2.10, $\overrightarrow{Z_{\mathrm{r}}}$ and $\overrightarrow{Y_{\mathrm{r}}}$ are evaluated:

$$\overleftarrow{Z_{\mathrm{l}}} = \frac{2Z_{\mathrm{rl}}Z_{\mathrm{s_2}}\left[Z_{\mathrm{L}} + jZ_{\mathrm{rl}}\tan\left(k_{\mathrm{rl}}t\right)\right]}{2Z_{\mathrm{s_2}}\left[Z_{\mathrm{rl}} + jZ_{\mathrm{L}}\tan\left(k_{\mathrm{rl}}t\right)\right] + Z_{\mathrm{rl}}\left[Z_{\mathrm{L}} + jZ_{\mathrm{rl}}\tan\left(k_{\mathrm{rl}}t\right)\right]}, \tag{2.35a}$$

$$\overleftarrow{Y_{\mathrm{l}}} = \frac{Y_{\mathrm{s_2}}}{2} + Y_{\mathrm{rl}}\frac{Y_{\mathrm{L}} + jY_{\mathrm{rl}}\tan\left(k_{\mathrm{rl}}t\right)}{Y_{\mathrm{rl}} + jY_{\mathrm{L}}\tan\left(k_{\mathrm{rl}}t\right)}, \tag{2.35b}$$

where $Z_{\mathrm{L}} = \eta_0 Z_{\mathrm{s_1}} / \left(\eta_0 + Z_{\mathrm{s_1}}\right)$. To find the propagation constant k_{t} of the modes propagating on the xy-plane, the expressions in (2.35) are inserted in (2.34). For TE modes, the free space impedance η_0 is equal to $\eta_0^{\mathrm{TE}} = 2\pi f_{\mathrm{op}}\mu_0 / k_{\mathrm{zfs}}$ while in the slab is $Z_{\mathrm{rl}}^{\mathrm{TE}} = 2\pi f_{\mathrm{op}}\mu_0 / k_{\mathrm{ztl}}$. The propagation constant along $\hat{\mathbf{z}}$ is $k_{\mathrm{zfs}} = \sqrt{k_{\mathrm{op}}^2 - k_{\mathrm{t}}^2}$ and $k_{\mathrm{ztl}} = \sqrt{k_{\mathrm{op}}^2\varepsilon_{\mathrm{rl}} - k_{\mathrm{t}}^2}$ for free space and slabs, respectively. Similarly, TM modes have the following impedance expressions $\eta_0^{\mathrm{TM}} = k_{\mathrm{zfs}} / \left(2\pi f_{\mathrm{op}}\varepsilon_0\varepsilon_{\mathrm{r}}\right)$ and $Z_{\mathrm{rl}}^{\mathrm{TM}} = k_{\mathrm{ztl}} / \left(2\pi f_{\mathrm{op}}\varepsilon_0\varepsilon_{\mathrm{rl}}\right)$. The propagation constant at the working frequency f_{op} is $k_{\mathrm{op}} = 2\pi f_{\mathrm{op}}\sqrt{\varepsilon_0\mu_0}$.

The TE and TM modes propagating in the structure are evaluated numerically from (2.34) and reported in Fig. 2.11.

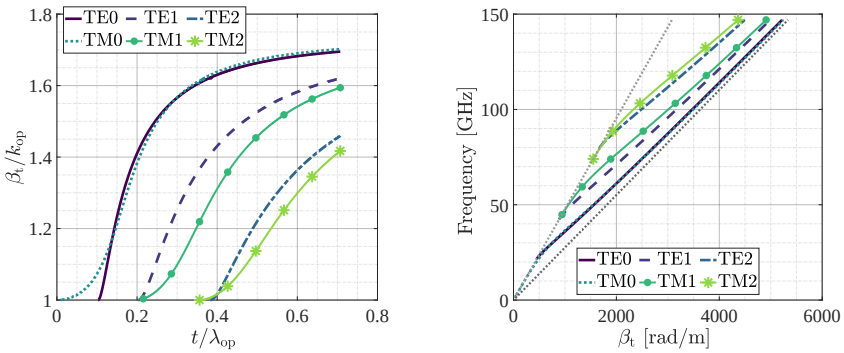

Figure 2.11: Propagation constant of TE and TM modes as a function of (a) normalized dielectric thickness and (b) frequency.

2.5. INTELLIGENT SURFACES FOR WIRELESS ENHANCEMENT

As already introduced in Chapter 1, MSs have found in this ever-changing world a perfect spot in the design of surfaces that can tailor EM waves and adapt to environment

changes. Denominated as RISs, these structures are a pretty recent discovery employed to implement so called *smart* environments. The first pioneering works are younger then a decade. After the general concept of *intelligent surface* to implement SRE [21], [22], the publications that paved the way to the employment of MSs for Reconfigurable Intelligent Surface (RIS) networks came in 2019 [23], [24].

Recently, an upgraded version of the classical RIS concept emerged. Defined as STAR-RIS, it allows simultaneous refraction and reflection to increase indoor and outdoor signal coverage, as reported in Fig. 2.12 [38]. The picture considers general scenarios where this technology offers an incredible flexibility. For example, a signal coming from a satellite or base station that illuminates a STAR-RIS placed on the Stadium wall is sent both to users on streets and inside on grandstands.

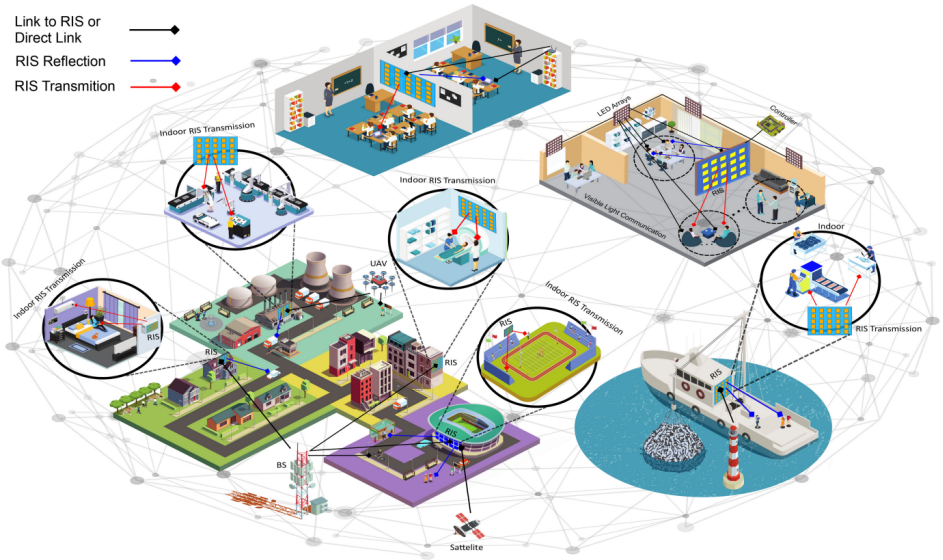

Figure 2.12: General application scenarios of STAR-RIS networks [38, Fig. 1].

There are three ways of implementing STAR-RISs: by mean of energy splitting, mode-commutation and time switching [37]. The first one divides arbitrarily the incident power on the surface between the transmitted and reflected signals. The energy allocation in the scattered waves and the phase distribution on the surface are configured to satisfy the wireless links requirements. In the mode-commutation operation, STAR-RIS elements are divided into two groups. One of them operates in transmission mode, the other one in reflection. The STAR-RIS can be considered as formed by a *reflecting*- and *transmitting*-only RIS. This solution is not employing the full available area and has worse performances in terms of efficiency with respect to the energy-splitting case. Time switching strategy is based on a periodically switch of all STAR-RIS cells between transmission and reflection mode, creating a blind time frame.

To enhance signal strength and minimize interference, TRAs can be employed in STAR-RIS scenarios due to their high-gain directional simultaneous transmission and

reflection.

2.6. TRANSMIT-REFLECT ARRAY

Space-fed array antennas, as TAs or RAs, are excellent solutions for RIS networks due to their capability of tailoring refracted or reflected waves. The absence of a Beam Forming Network (BFN) greatly reduces the losses due to RF phase shifters, power dividers and cables. Moreover, these array structures are energy-constrained capable of focusing incoming EM waves to obtain narrow beams. For a more precise control of phase, amplitude, and polarization of refracted or reflected wavefronts, these antennas require sub-wavelength cells, making them well-suited for MS applications.

Since both TAs and RAs are suitable for RIS networks, a device that can combine these two functionalities, referred as TRA, would be required for STAR-RIS scenarios (see Fig. 2.13).

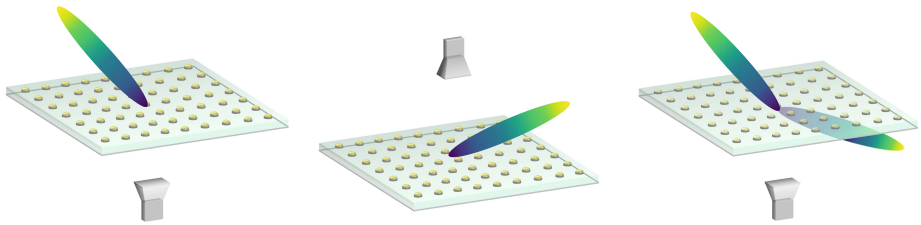

(a) (b) (c)

Figure 2.13: Three possible designs for space-fed antenna arrays: (a) TA, (b) RA and (c) TRA

This leads to an important question: Is it possible to integrate TA and RA functionalities into a single structure, and if so, what are the key challenges and considerations involved in achieving this integration? The pioneering work of Lau *et al.* in 2010 started addressing these problems considering reconfigurable array elements [103]. By precisely biasing varactor diodes, their design allowed the antenna to switch between TA and RA operation modes, setting the stage for future research in this direction.

Building on this preliminary work, three more seminal studies moved the first steps in designing space-fed bi-directional antenna arrays. In 2015, Malhat *et al.* advanced in the research by successfully integrating transmission and reflection capabilities at different frequencies through the use of plasma cells [104]. Their design demonstrated an innovative approach to frequency-selective dual functionality, operating at 19.75 GHz for refraction and 19.75 GHz for reflection. In 2016, Xu *et al.* introduced a MS design comprising linear polarization conversion and radiation pattern diversity [105]. Notably, simultaneous TA and RA functionality was obtained near the central frequency, while single-mode operation was observed at lower and higher frequencies for refracted and reflected beam, respectively. However, achieving simultaneous transmission and reflection across the entire band remained a challenge. Cai *et al.* made significant strides in 2017 by implementing a MS with EM wave focusing, in TA mode, or bending, in RA mode, or both simultaneously based on the incident field's linear polarization [106].

Around the same time (2018), Cai *et al.*, Yi *et al.* and Yang *et al.* took a significant leap forward by demonstrating the implementation of a simultaneous transmission and reflection within a single structure [44], [48], [107]. While the first achieved both operation modes with a 45° polarized feed, the others demonstrated to achieve a refracted and reflected field 90° rotated with respect to the incident linear polarized wave. Notably, Yi *et al.* addressed the criticality of dependent transmitted and reflected beams, solved by adding extra layers to their design structure. On the other hand, Yang *et al.* extended the analysis from linear to circular polarization of the incident and scattered fields.

With Yang's work, the concept of "*Transmit-Reflect-array*" (TRA) was finally formalized and employed in the following publications to indicate these novel Bidirectional High Gain Antenna (Bi-HGA).

2.6.1. Design Approaches

Although the topic is relatively recent, a significant amount of publications has already emerged in the literature regarding TRA antennas. These contributions can be categorized based on several key factors: materials used, cells realization, and bi-directional functionality implementation. Each of these aspects plays a crucial role in defining the performance, efficiency, and applicability of these antennas in different scenarios.

The material choice affects TRA electromagnetic properties, cost, and ease of fabrication. Indeed, metal-only or dielectric cells have established manufacturing techniques and predictable performances. The firsts ensure minimal losses and thickness very small maintaining an high efficiency [48], [108]–[110]. The seconds can control phase and amplitudes of waves with a wideband behavior [111]. However, MMs, MSs or FSS have been recently employed due to their ability of combining more functionalities together by engineering theirs constitutive parameters [47], [51], [112].

Based on the desired behavior of the array, various techniques can be applied in the elements design. For instance, anisotropic resonators can be employed to achieve polarization conversion [48], [49], [113], [114]. On the other hand, reconfigurability can be introduced by integrating active devices, such as varactors and Positive Intrinsic Negative (PIN) diodes [42], [46], [115]–[122]

The last category is defined upon the implementation of transmit-reflect functionality. There are four possible techniques to achieve this behaviour: Mode Switching (MoSw), Frequency Selection (FS), Aperture Division (AD), Energy Splitting (ES).

2.6.2. Mode Switching

The MoSw approach consists of changing from TA to RA functionality through the use of active components, as shown in Fig. 2.14. Lau *et al.*, in 2010, presented a 6×6 elements reconfigurable array working at $f_d = 5.7$ GHz [103]. To switch between the two operation modes, each varactor on the cells is biased between $0 - 20$ V, as shown in Fig. 2.14a. An element spacing of $0.57\lambda_d$ was considered and the experimental results showed a maximum gain at broadside of 12.3 dBi in transmission and 10 dBi in reflection. These low values of gain for both beams were maily caused by a low efficiency feeding system and element losses.

Zhang *et al.* proposed another electrically reconfigurable TRA capable of switching TA to RA functionality using a single PIN diode, as reported in Fig. 2.14b [123].The

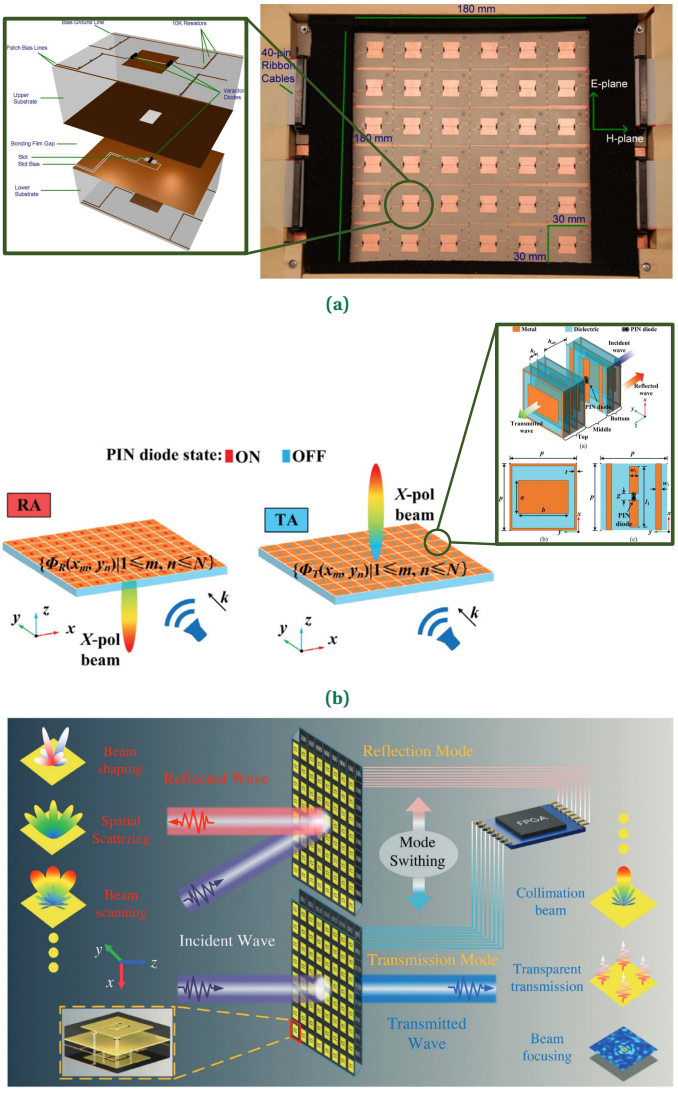

Figure 2.14: Examples of TRA based on MoSw strategy. (a) Approach based on cells with integrated varactors to commute between transmission and reflection [103]. (b) Startegy involving elements with integrated PIN diodes [123]. (c) Reconfigurable TRA with PIN diodes controlled by an Field Programmable Gate Array (FPGA) [119].

structure comprises 9×9 elements with periodicity $0.4\lambda_d$ working at $f_d = 10\,\text{GHz}$. The designed prototype has a gain in transmission and reflection of 17.3 dBi and 17.2 dBi, respectively. They corresponds to an aperture efficiency of 32.2% and 33.7%. Moreover, differently from Lau *et al.*, a precise phase distribution in both refraction and reflection

is obtained by fitting the phase response function for TA or RA operations. In this way, an higher gain and aperture efficiency are obtained.

A greater variety of functionalities were introduced by Yin *et al.* (see Fig. 2.14c) [119]. By employing meta-atoms with PIN diodes, the transmission and reflection modes are obtained by controlling the voltage across these active elements through a FPGA. To verify the designed cells capability, thy fabricated a prototype of 12×12 meta-particles of periodicity $0.4\lambda_d$ and working at $f_d = 3.5$ GHz. Notably, through the FPGA coding, beam shaping,spatial scattering and beam scanning can be achieved.

Nevertheless, in all these works, a simultaneous transmission and reflection cannot be achieved and the cells losses are mainly due to the active devices.

2.6.3. Frequency Selection

The FS strategy, differently from the MoSw, involves the design of TRAs that implements both TA and RA functionalities at only one frequency and singularly at different frequencies. As introduced before, in 2015, Malhat *et al.* obtained a frequency-selective dual functionality, operating at 19.75 GHz for refraction and 19.39 GHz for reflection [104]. The novelty of this work resides in the elements consisting of an ionizing gas as conductive material (see Fig. 2.15a). The array comprises 13×13 elements with periodicity $0.7\lambda_d$ working at $f_d = 19.5$ GHz. However, the authors work is purely analytical, no experimental results are presented.

In 2016, Xu *et al.* designed and fabricated a 15×15 elements array having periodicity $0.3\lambda_d$ and working at $f_d = 9$ GHz [105]. In their work, the antenna shows a TA, RA or TRA functionality depending on the frequency. Indeed, from $f = 8$ GHz to $f = 9$ GHz the array works in transmission, at $f = 10$ GHz in reflection and at $f = 9.3$ GHz both behaviors are present. The antenna element acts as a polarization converter, trasmitting in co-polarization and reflecting in same cross-polarized wave as the incident one. The fabricated prototype, shown in Fig. 2.15b, shows a measured peak gain in transmission of 18.5 dBi, corresponding to an aperture efficiency of 28%. In reflection, 13.1 dBi and 31% have been obtained. At $f = 9.3$ GHz, the TRA behavior determines an energy splitting betweem the scattered fields showing for both beams a gain of 15.8 dBi.

The work of Zhong *et al.* improves the previous design obtaining higher gain and lower losses in their 9×9 elements array [124]. The cells are designed as a cascade of four layers plus a fifth that implements the RA mode, (see Fig. 2.15c). They have periodicity equal to $0.6\lambda_d$ at the working frequency $f_d = 11$ GHz. From $f = 8.4$ GHz to $f = 10.8$ GHz the array works in transmission mode while from $f = 10.8$ GHz to $f = 13$ GHz in reflection. At $f = 10.8$ GHz the array achieve simultaneous transmission and reflection. The forward and backward peak gain is 18.2 dBi and 18.2 dBi respectively

It is worth to mention also the multi-functional antenna of Yang *et al.* [125]. This array of FSS elements depending on the frequency band of the incident field, implement TA or RA operation mode. The schematic view is reported in Fig. 2.15d. Through the cross dipoles inserted in the cross slots placed in the middle layer, the tranmission at Ku-band can be controlled. On the other hand, reflection characteristics at Ka- and K-band are managed by the double square rings at top and bottom layer. The fabricated prototype shows at Ku-band a peak gain of 23.8 dBi with an aperture efficiency of 40% at 14.25 GHz and 1 dB gain bandwidth of 6.5%. At Ka-band, the measurements present

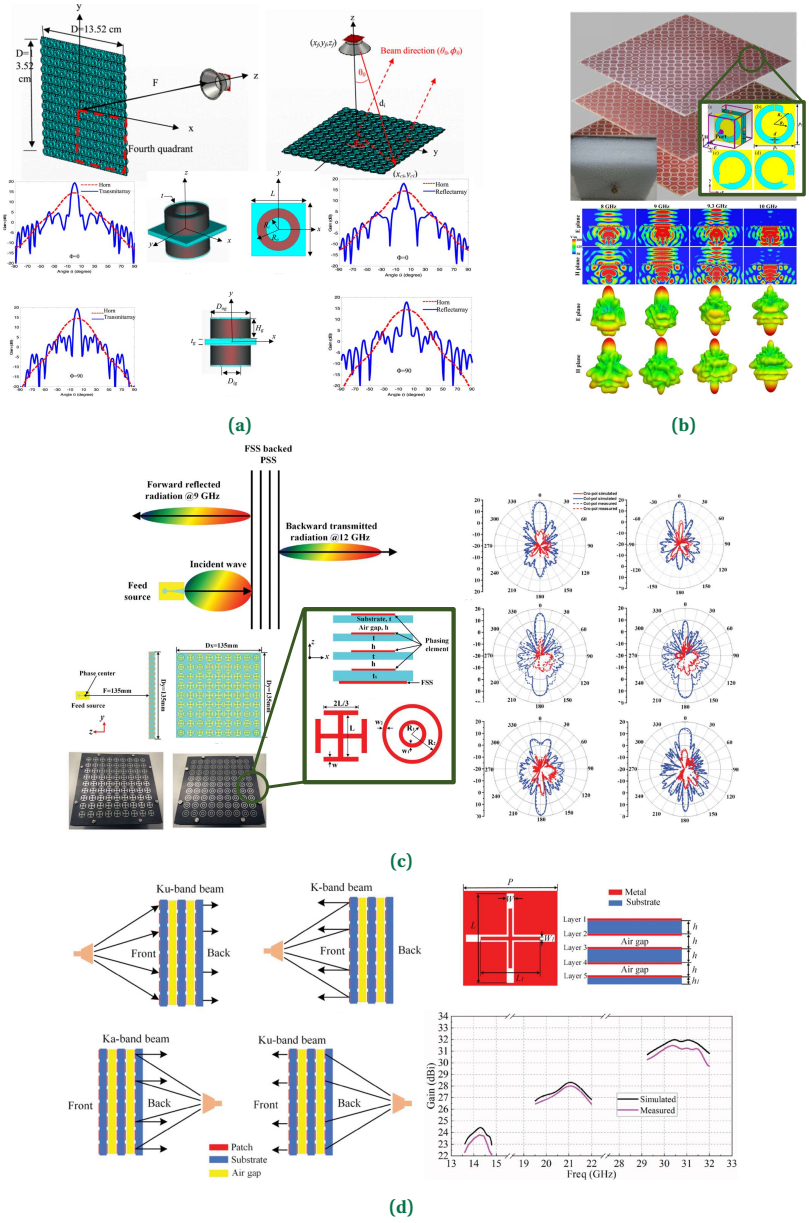

Figure 2.15: Examples of TRA based on FS strategy. (a) Approach based on elements consisting of an ionizing gas as conductive material [104]. (b) Strategy involving elements that tailor fields in both reflection and transmission at a specific frequency [105]. (c) This solution involves a five layer cascade to obtain higher gain and broadband behavior [124]. (d) FSS with elements optimized to work in transmission or reflection in different frequency band allowing multiple operation for satellite communications [125].

a peak gain of 31.5 dBi at 30.5 GHz with an aperture efficiency of 47%. The 1 dB gain bandwidth is 7.1%. At *K*-band, a peak gain of 28 dBi with an aperture efficiency of 44% at 21 GHz and 1 dB gain bandwidth of 7.3% is measured.

Nevertheless, all these designs required a change in the feed frequency to switch the operation mode. Moreover, when it is supported, TRA functionality is available just at one frequency limiting the possible applications for STAR-RIS.

2.6.4. Aperture Division

The AD approach involves the use an array section in TA mode and the other one in RA mode, as showed in the collection of works reported in Fig. 2.16.

In this context, several techniques can be employed to implement this aperture area division. Liu *et al.* presented an array cells disposition that is called SAF, reported in Fig. 2.16a, where 45.3% of the radiation units operate in transmission mode while others in reflection mode [41]. With this technique, simultaneous TA and RA functionalities can be achieved at the expense of the aperture efficiency. From the measured results of a fabricated prototype, the authors obtained maximum gain of 21.4 dBi with a 1 dB gain bandwidth of 6.7% for the transmitted beam. In reflection, a maximum gain of 24.4 dBi with a 1 dB gain bandwidth of 9.3% was achieved. A similar technique was employed also by Yang *et al.* and Mu *et al.* [114], [121]. The first proposed meta-atoms with circular polarization conversion placed in the array aperture through a genetic algorithm-based method. Notably, this displacements allow the generation of four beams two in transmission and reflection as shown in Fig. 2.16d. The measured prototype shows a wide bandwidth: 30.7% for TA mode and 47.5% for RA mode. Mu *et al.*, on the other hand, introduced reconfigurability by placing PIN diodes in the elements (see Fig. 2.16e). The scanning capability is obtained by controlling each array element with a FPGA to change the phase distribution on the aperture. Moreover by digitally modify the response of the meta-atoms, TA, RA or TRA operations can be obtained.

Another techniques to implement this aperture area division is called GAD. Yu *et al.* compared on a reconfigurable array the results obtained by implementing GAD and SAF, as reported in Fig. 2.16b [42]. They showed that GAD introduces high Side Lobe Level (SLL) with respect to SAF.

A mixed technique in between GAD and SAF has been introduced by Guo *et al.* by placing alternate elements working in TA or RA mode, as reported in Fig. 2.16c [43]. With this strategy, and by phasing the periodic elements, the authors showed the possible generation of multiple transmitted and reflected beams.

Nevertheless, as mentioned earlier, all these solutions show low aperture efficiency due to an impossible exploitation of the complete antenna effective area.

2.6.5. Energy Splitting

To have bidirectional radiation and no limits in total aperture usage, the last strategy, covered in this work, consists in designing elements that divide the incident power equally between forward and backward radiated fields, as reported in Fig. 2.17 and Fig. 2.18. Although, as consequence, a drop of −3dB is obtained for equal refracted and reflected radiation, the full array area is employed.

Yang *et al.* conceived a metal-only and single layer array with defected square ring

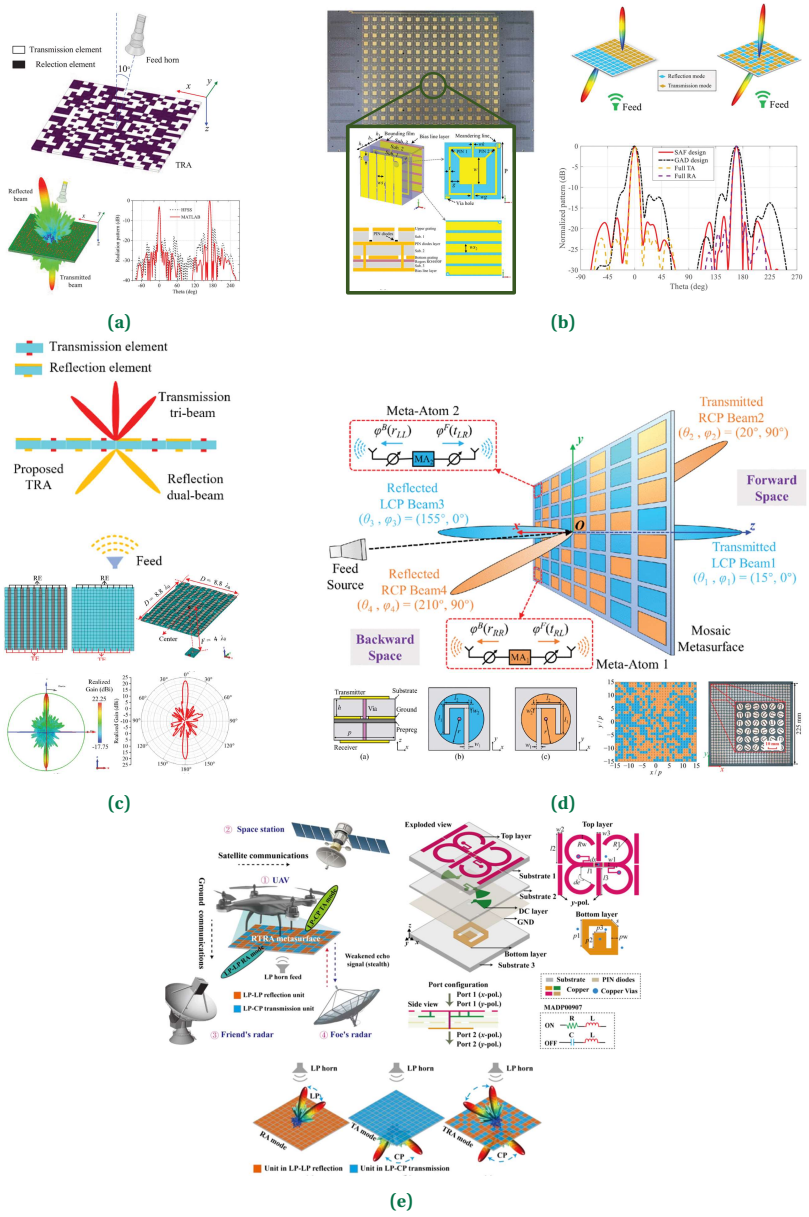

Figure 2.16: Examples of TRA based on Aperture Division Strategy. (a), (d), and (e) approaches based on SAF distribution of the array cells [41], [114], [121]. Notably, (d) employs a mosaic distribution to achieve multiple beams. (b) Comparison between GAD and SAF techniques [42]. (c) Approach based on mixing GAD and SAF: TA and RAelements are placed alternatively in the array [43].

cells [48]. The structure is fed by a y-polarized currugated horn and both transmitted and reflected beams are x-polarized due to the defected ring, as shown in Fig. 2.17a. A

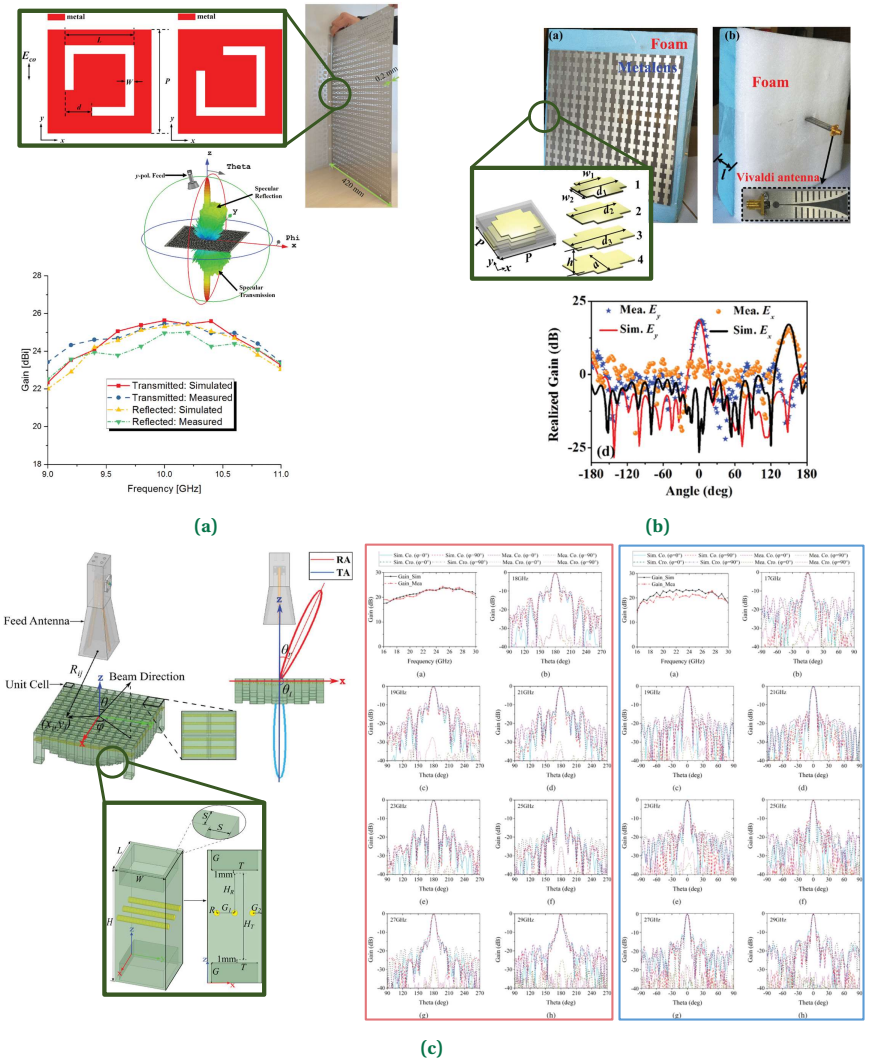

Figure 2.17: Examples of TRA based on Energy Splitting Strategy. (a) Metal-only and very thin TRA implementing polarization conversion [48]. (b) MS-based antenna achieving TA, RA and TRA operation by rotating the focal source [44]. (c) Dielectric-based TRA [111].

gain in transmission and reflection of 25.5 dBi and 25 dBi, respectively. Notably, the low aperture efficiency, 15% and 14% for TA and RA beams, is due to the power splitting of the input energy between co- and cross-polarization and the energy splitting between transmitted and reflected beams.

Other published works on TRAs considers antenna arrays that exhibits both TA and RA operation modes when the feed is aligned along the main axis [44], [49], [128], [129]. Simultaneous transmission and reflection is achieved by rotating the linear polarized

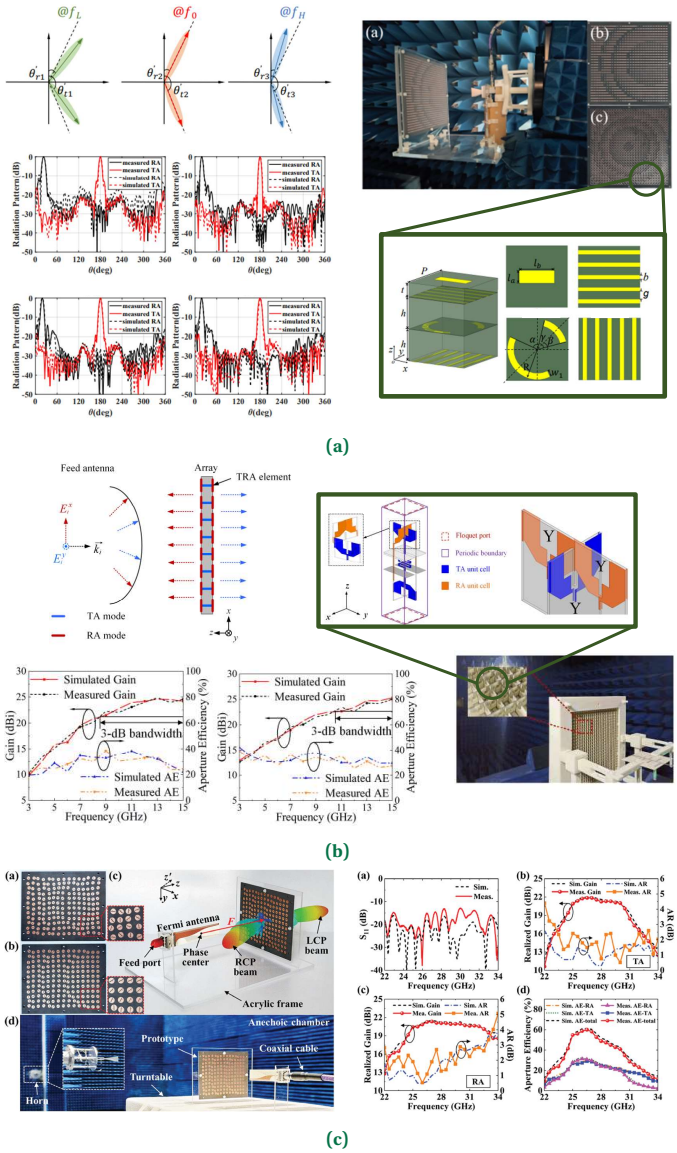

Figure 2.18: Examples of TRA based on Energy Splitting Strategy. (a) Wideband and flat gain TRA with mitigated beam squint effect [126]. (b) Ultrawideband TRA achieving with dual-polarization [112]. (c) Wideband and high-efficiency TRA with distinct circular polarizations [127]

feed of 45° on the azimuth plane. As an example, Cai *et al.* conceived a four layer array with anisotropic rotators fed by Vivaldi antenna [44]. The proposed prototype and radiation pattern is reported in Fig. 2.17b. The transmitted beam is y-polarized while the reflected is x-polarized with gain 18.6 dBi and 16.8 dBi, respectively.

Zheng *et al.* proposed an interesting work based on a 3D-Printed TRA, shown in Fig. 2.17c [111]. The antenna array is composed by 12 × 12 elements realized as a dielectric post and three copper wires. Due to an independent control of transmission and reflection phase shift of the proposed cell over a large bandwidth, a broadband behavior is obtained for transmitted and reflected beams. The fabricated prototype showed a measured peak gain of 24.4%dBi over a bandwidth of 46.8% in the 18–29 GHz band for the TA operation. In reflection, a peak gain of 22.9%dBi with a bandwidth of 52.2% in the 17–29 GHz band was obtained.

To take into account beam squint effect, Yin *et al.* developed a multi-frequency phase synthesis approach to design TRAs with tilted beams (see Fig. 2.18a) [126]. The strategy effectiveness is enhanced by introducing the pre-deviated beam direction at optimized frequency point to mitigate the beam squint, thus achieving a wide-band flat gain. A fabricated prototype has been measured achieving a 1-dB gain bandwidth of 40.2% (33.7%) and a peak aperture efficiency of 43.7% (35.3%) in transmission (reflection) mode.

Gao *et al.* presented a novel ultrawideband TRA achieving with dual-polarization [112]. In transmission the array produce a y-polarized beam while in reflection x-polarized. Moreover they can be independently controlled. The TRA comprises 24 × 24 elements designed as tightly coupled modified dipole radiators, reported in Fig. 2.18b. The fabricated prototype shows a measured peak gain of 24.9 dBi and 25 dBi and a peak aperture efficiency of 38% and 39% in transmission and reflection, respectively.

Lastly, another interested work was proposed by Yang *et al.* [127]. The authors presented a wideband high-efficiency TRA with independent manipulations of transmitted and reflected beams with distinct circular polarizations. The antenna transmit a left-handed circularly-polarized in TA operation mode, while in right-handed circularly-polarized in RA functionality. The fabricated prototype showed a measured peak gain of 22 dBi in transmission and 21.5 dBi in reflection.

A comparison between all these works and the ones that employ different strategies are reported in Table 2.2. Nevertheless, a clear analytical model for the design of TRA cells is not present. Moreover, in all these analysis, the array meta-atoms are designed through time consuming full-wave optimization.

Table 2.2: State-of-the-art: comparison of several TRAs reported in the literature.

Ref.	Array area [mm^2]	G_{FS} [dBi]	F/D	(TA/RA) FBW [GHz]	G_{max} [dBi]	η_{ap} [%]	1 dB GBW [GHz]	AR 3 dB BW [GHz]	Pol.	N. layer	Type TRA	Beam dependency	Application	Tunable device
[103]	180 × 180	17.6/14.1	1.67/0.9	5.7	12.3/10	12/7	–	–	LP-Co/LP-Co	3	MoSw	no	Reconfigurability	Varactor
[123]	108 × 108	10	0.6	10	17.3/17.2	33.2/33.7	–	–	LP/LP	5	MoSw	no	Reconfigurability	PIN
[119]	420 × 420	–	1	3.5	–	–	–	–	LP-Co/LP-Co	3	MoSw	no	Reconfigurability	PIN
[104]	135.2 × 135.2	14.47	1	19.75/19.39	17.9/19	28.2 – 32	–	–	LP-Co/LP-Co	1	FS	no	Plasmonic	–
[105]	150 × 150	–	4	8 – 9.3/ 9.3 – 10	18.5/13.1	28/7	–	–	LP-Cross/LP-Co	2	FS	no	Pol. Conversion	–
[124]	144 × 144	9	1	9 – 10.8/ 10.8 – 12.5	18.2/18.9	22/17	–	–	LP-Co/LP-Co	5	FS	no	Dual-Band	–
[125]	151.8 × 151.8	–	1.1	13.5 – 15/ (19.5 – 22, 29 – 32)	23.8/ (28, 31.5)	40/ (44, 47)	–	–	LP-Co/LP-Co	5	FS	no	Tri-Band	–
[41]	125 × 125	–	0.72	28 – 32	21.4/24.4	7/14	6.7/9.3	–	LP-Co/LP-Co	3	AD-SAF	no	Bi-HGA	–
[114]	225 × 225	–	1.25	10 – 20	19.3/19.5 19.2/19	26.5	–	30.7/47.5 33.7/50.8	LHCP/LHCP RHCP/RHCP	3	AD-SAF	no	Multi-beam	–
[121]	180 × 180	–	0.8	9.5 – 11.5	13.5/13.2	6/4.5	–	–	LP, CP	3	AD-SAF	no	RCS	PIN
[42]	240 × 240	–	–	8 – 11	17.1/16.2	7.1/5.7	–	–	LP-Co, LP-cross	4	AD-SAF	no	Multi-mode	PIN
[43]	240 × 240	7.23	2.2	30	22.25/20.32	28.23	–	–	LP-Co	1	AD-GAD	no	Multi-beam	–
[48]	420 × 420	–	–	9 – 11	25.5/25	15/14	15/14	–	LP-Co	1	ES	no	Bi-HGA	–
[44]	165 × 165	–	3.3	10	18.5/18.6	36.5	–	–	LP-Co	4	ES	yes	Multi-mode	–
[111]	145 × 145	–	0.8	10 – 30	24.4/22.9	38.5/28.1	–	–	LP-Co	1	ES	no	3D Bi-HGA	–
[126]	180 × 180	–	0.67	13 – 20	26.57/25.57	42/37	40.2/33.7	–	LP-Co	4	ES	no	Tilted Beams	–
[112]	192 × 201.6	–	1.7	2.8 – 15.2	25/24.9	38/39	–	–	LP-Co	–	ES	no	Wideband	–
[127]	79.5 × 63.6	–	1.07	22 – 34	22/21.5	–	18.2/24.6	38.5	LHCP/RHCP	3	ES	no	Pol. Conversion	–

* FBW is the frequency operation bandwidth, AR is the axial ratio and GBW is the gain bandwidth.

2.7. Chapter Landmarks

This chapter starts by tracing the births of MMs and MSs to comprehend the major differences between them and with respect to other periodic structures. Then, a MS model is proposed considering the surface as a discontinuity described by a set homogenized parameters. Based on these characteristic parameters, three classifications are proposed depending on the MS response. Moreover, isotropy, anisotropy and bi-anisotropy attributes are discussed. To complete the study, different techniques to analyze MSs are discussed and applications in which they can be employed are treated. To conclude, a review on the novel concepts of STAR-RIS and TRA are presented, emphasizing how MSs fits as perfect candidate for these usages. In this context, a classification of TRA design approaches is presented, with a focus on the energy splitting strategy that will be treated in the next chapters.

3

METASURFACES FOR SIMULTANEOUS REFRACTION AND REFLECTION

If I have seen further, it is by standing on the shoulders of Giants.

Isaac Newton

This Chapter examines reciprocal MSs with electric and magnetic response, referred as H-MS, to identify which relation between its characteristic parameters allows an arbitrary control of the transmission and reflection coefficients amplitude. Starting from this expression, the equal power division between refracted and reflected waves is explored. The minimum number of impedance sheets needed for the design of H-MS cells that acts as power dividers for the incident wave are studied. The design method and some physical implementations of these impedance sheets are reported.

Parts of this chapter have been published in [C1]–[C3] and [J1].

3.1. HUYGENS' METASURFACES

IN the last decade, Huygens' Metasurfaces (H-MS)s have been an incredible attention by the electromagnetic and optics communities, to address very diverse applications and demonstrate unprecedented field manipulations [86], [88], [99]. In particular, several studies demonstrated that, when illuminated by a space-wave, they H-MSs can accurately tailor either the reflected field or the refracted one, through a precise design of its constitutive parameters, introducing negligible losses [93], [130], [131]. The first reported designs were formed by sub-wavelength scatterers realized with co-located electric and magnetic dipoles, effectively forming Huygens' sources. Over the years, various designs and fabrication techniques have been proposed, depending on the operation frequency [86], [132]. For example, at microwave frequencies, the MS meta-atoms can be realized as a cascade of several impedance sheets [86] using planar multi-layer fabrication technologies. In this case, the metal traces support the electric currents, emulating an electric dipole, and the vertical coupling among stacked layers determines the magnetic response of the surface, emulating an orthogonal magnetic dipole.

Following the modeling approach presented in Chapter 2, the electrical and magnetic behaviors of an H-MS can be described by the constitutive parameters $\underline{\mathbf{Y}}_{\mathrm{e}}$ and $\underline{\mathbf{Z}}_{\mathrm{m}}$. Most numerical models and optimization methods in the literature focus on isotropic H-MSs, because they are completely characterized by scalar surface constitutive parameters which enable an easier mathematical treatment. [133], [134]. Nevertheless, in presence of anisotropy, $\underline{\mathbf{Y}}_{\mathrm{e}}$ and $\underline{\mathbf{Z}}_{\mathrm{m}}$ are tensors meaning they exhibit directional dependence, influencing the H-MS response. By optimizing all entries of the constitutive parameters, the polarization of the fields scattered by an H-MS can be transformed with respect to that of the incident wave [32], [135], [136].

Designs based on H-MS have been widely employed to achieve field deflection, far- and near-field beam-forming, absorption, and to realize perfect refraction or reflection. [86]–[88], [133], [136]–[139]. For instance, an H-MS at the interface between two different dielectric media can nearly perfectly refract a normally incident TE plane-wave [86], [138], [140], which would be, instead, partly reflected in absence of the surface [141]–[143]. Indeed, H-MS meta-atoms can be employed in the design of space-fed arrays, like TAs and RAs, to precisely control the phase distribution on the meta-lens and amplitude tapering of the generated radiation pattern [32], [137], [144]–[149].

Due to H-MS capability of tailoring refracting and reflected waves, the idea of performing both manipulation at the same time naturally arises. With this goal in mind, the following sections address the problem of enforcing first an arbitrary, then an equal amplitude condition on the scattering coefficients for an H-MS between different media. Then, the focus shifts to an a general power division of the incident power between transmission and reflection for an H-MS embedded in a uniform medium, followed by the specific case of equal power division. For a design perspective, H-MS cells that satisfy this condition are realized as a cascade of impedance sheets analyzing the minimum number required to cover the full phase range in both transmission and reflection. Examples of simple metal patterns that can realize these impedance sheets values are investigated.

3.2. ANALYTICAL MODEL

This analysis based on [150] discusses the scattering properties of an infinite, homogeneous, isotropic and reciprocal H-MS are analyzed. The structure lies between two semi-infinite, isotropic dielectric regions having, in general, different electric and magnetic properties and different characteristic impedances $\eta_1 = \eta_0\sqrt{\varepsilon_{r_1}/\mu_{r_1}}$ and $\eta_2 = \eta_0\sqrt{\varepsilon_{r_2}/\mu_{r_2}}$, where η_0 is the free-space characteristic impedance. The H-MS is illuminated by a normally incident plane wave, polarized along $\hat{\mathbf{y}}$ and propagating in Region 1, as showed in Fig. 3.1.

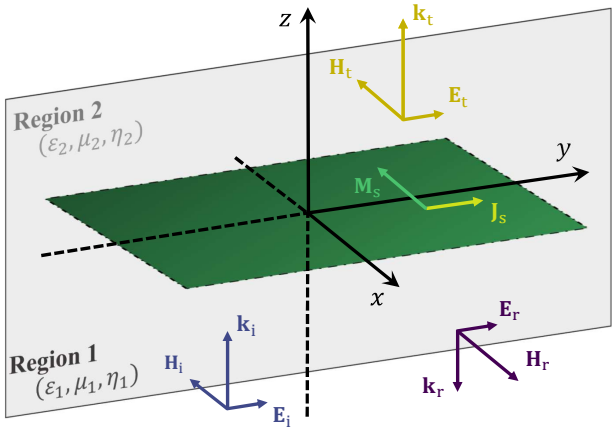

Figure 3.1: Infinite MS between two regions with the different material properties, illuminated by a normal incident field, in blue line, coming from Region 1. Reflected and transmitted fields are in purple and yellow lines, respectively.

The wavevectors of incident, $\mathbf{k}_i = k_1\hat{\mathbf{z}}$, and reflected wave, $\mathbf{k}_r$, are equal and opposite $\mathbf{k}_r = -\mathbf{k}_i$, where $k_1 = k_{op}\sqrt{\varepsilon_{r_1}}$, $k_{op} = 2\pi f_{op}/c$ is the free-space wavenumber at the operating frequency f_{op} and c is the speed of light in vacuum. The wavevector of the transmitted wave is $\mathbf{k}_t = k_2\hat{\mathbf{z}} = k_{op}\sqrt{\varepsilon_{r_2}}\hat{\mathbf{z}}$. The incident, reflected and refracted electric and magnetic fields are defined as follows:

$$\mathbf{E}_i = E_i\hat{\mathbf{y}} \qquad \mathbf{H}_i = \frac{1}{\eta_1}\mathbf{k}_i \times \mathbf{E}_i = -\frac{E_i}{\eta_1}\hat{\mathbf{x}}, \tag{3.1a}$$

$$\mathbf{E}_r = E_r\hat{\mathbf{y}} \qquad \mathbf{H}_r = \frac{1}{\eta_1}\mathbf{k}_r \times \mathbf{E}_r = \frac{E_r}{\eta_1}\hat{\mathbf{x}}, \tag{3.1b}$$

$$\mathbf{E}_t = E_t\hat{\mathbf{y}} \qquad \mathbf{H}_t = \frac{1}{\eta_2}\mathbf{k}_t \times \mathbf{E}_t = -\frac{E_t}{\eta_2}\hat{\mathbf{x}}. \tag{3.1c}$$

By applying the interface conditions at $z = 0$, as described in (2.6), the electric and magnetic currents on the surface, $\mathbf{J}_s$ and $\mathbf{M}_s$, are expressed as functions of the discontinuities of the tangential fields across the H-MS, and:

$$\hat{\mathbf{y}}\mathrm{J}_s = \hat{\mathbf{z}} \times \hat{\mathbf{x}}(\mathrm{H}_2 - \mathrm{H}_1) = \hat{\mathbf{y}}Y_e\mathrm{E}_m^{tn}, \tag{3.2a}$$

$$\hat{\mathbf{x}}\mathrm{M_s} = -\hat{\mathbf{z}} \times \hat{\mathbf{y}}\,(\mathrm{E_2} - \mathrm{E_1}) = \hat{\mathbf{x}} Z_\mathrm{m} \mathrm{H_m^{tn}}, \tag{3.2b}$$

where $\mathbf{H}_1 = (\mathrm{H_r} + \mathrm{H_i})\,\hat{\mathbf{x}}$, $\mathbf{H}_2 = \mathrm{H_t}\hat{\mathbf{x}}$, $\mathbf{E}_1 = (\mathrm{E_i} + \mathrm{E_r})\,\hat{\mathbf{y}}$ and $\mathbf{E}_2 = \mathrm{E_t}\hat{\mathbf{y}}$. The average electric and magnetic fields tangent to the surface are defined as $\mathbf{E}_\mathrm{m}^\mathrm{tn} = (\mathbf{E_i} + \mathbf{E_r} + \mathbf{E_t})/2$ and $\mathbf{H}_\mathrm{m}^\mathrm{tn} = (\mathbf{H_i} + \mathbf{H_r} + \mathbf{H_t})/2$, respectively. By replacing in (3.2a) the expressions for the average tangential electric field and for the magnetic fields as functions of incident and scattered fields, the following relation is found:

$$-\frac{E_\mathrm{t}}{\eta_2} + \frac{E_\mathrm{i}}{\eta_1} - \frac{E_\mathrm{r}}{\eta_1} = \frac{Y_\mathrm{e}}{2}\,(E_\mathrm{i} + E_\mathrm{r} + E_\mathrm{t})\,. \tag{3.3}$$

The transmission and reflection coefficients, denoted, in general, with τ and Γ, respectively are defined as:

$$\tau = \frac{E_\mathrm{t}}{E_\mathrm{i}} \qquad \Gamma = \frac{E_\mathrm{r}}{E_\mathrm{i}}\,. \tag{3.4}$$

In this Section, they will be denoted with an additional subscript indicating the half-space (Region 1 or 2) where the incident wave propagates. Therefore, in the case under analysis, τ_1 and Γ_1 are used. By multiplying each side of (3.2a) by $1/E_\mathrm{i}$, after some manipulations, the following expression for τ_1 is found:

$$\tau_1 = \Gamma_1 \frac{\eta_2}{\eta_1}\frac{-\eta_1 Y_\mathrm{e} - 2}{\eta_2 Y_\mathrm{e} + 2} + \frac{\eta_2}{\eta_1}\frac{2 - \eta_1 Y_\mathrm{e}}{\eta_2 Y_\mathrm{e} + 2}\,. \tag{3.5}$$

Starting from (3.2b) and carrying out similar steps, the following equation is obtained:

$$E_\mathrm{t} - E_\mathrm{i} - E_\mathrm{r} = \frac{Z_\mathrm{m}}{2}\left(-\frac{E_\mathrm{i}}{\eta_1} + \frac{E_\mathrm{r}}{\eta_1} - \frac{E_\mathrm{t}}{\eta_2}\right). \tag{3.6}$$

By multiplying each side of (3.6) by $1/E_\mathrm{i}$, a second expression of τ_1 as a function of Γ_1, is found:

$$\tau_1 = \Gamma_1 \frac{\eta_2}{\eta_1}\frac{2\eta_1 + Z_\mathrm{m}}{2\eta_2 + Z_\mathrm{m}} + \frac{\eta_2}{\eta_1}\frac{2\eta_1 - Z_\mathrm{m}}{2\eta_2 + Z_\mathrm{m}}\,. \tag{3.7}$$

By equating (3.5) to (3.7), the reflection coefficient is expressed as a function of the surface parameters:

$$\Gamma_1 = \frac{4Z_\mathrm{m} + \eta_2\,(4 + Z_\mathrm{m} Y_\mathrm{e}) - \eta_1\left(4 + 4\eta_2 Y_\mathrm{e} + Z_\mathrm{m} Y_\mathrm{e}\right)}{4Z_\mathrm{m} + \eta_2\,(4 + Z_\mathrm{m} Y_\mathrm{e}) + \eta_1\left(4 + 4\eta_2 Y_\mathrm{e} + Z_\mathrm{m} Y_\mathrm{e}\right)}\,. \tag{3.8}$$

Eventually, by inserting (3.8) in (3.5) or (3.7), the following expression for $\tau_1\,(Y_\mathrm{e}, Z_\mathrm{m})$ is derived:

$$\tau_1 = \frac{2\eta_2\,(4 - Z_\mathrm{m} Y_\mathrm{e})}{4Z_\mathrm{m} + \eta_2\,(4 + Z_\mathrm{m} Y_\mathrm{e}) + \eta_1\left(4 + 4\eta_2 Y_\mathrm{e} + Z_\mathrm{m} Y_\mathrm{e}\right)}\,. \tag{3.9}$$

It is straightforward to analyze the case where the incident wave arrives from the half-space above the MS ($z > 0$), as reported in Fig. 3.2.

The wavevectors of the incident, reflected and transmitted waves are $\mathbf{k_i} = -k_2\hat{\mathbf{z}}$, $\mathbf{k_r} = k_2\hat{\mathbf{z}}$ and $\mathbf{k_t} = -k_1\hat{\mathbf{z}}$, respectively. The expressions for the electric and magnetic fields are:

$$\mathbf{E_i} = E_\mathrm{i}\hat{\mathbf{y}} \qquad \mathbf{H_i} = \frac{1}{\eta_2}\mathbf{k_i} \times \mathbf{E_i} = \frac{E_\mathrm{i}}{\eta_2}\hat{\mathbf{x}}, \tag{3.10a}$$

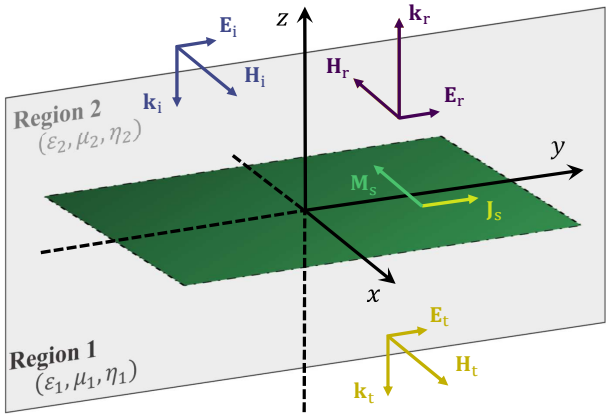

Figure 3.2: Infinite MS between two regions with the different material properties, illuminated by a normal incident field, in blue line, coming from Region 2. Reflected and transmitted fields are in purple and yellow lines, respectively.

$$\mathbf{E}_\mathrm{r} = E_\mathrm{r}\hat{\mathbf{y}} \qquad \mathbf{H}_\mathrm{r} = \frac{1}{\eta_2}\mathbf{k}_\mathrm{r} \times \mathbf{E}_\mathrm{r} = -\frac{E_\mathrm{r}}{\eta_2}\hat{\mathbf{x}}, \tag{3.10b}$$

$$\mathbf{E}_\mathrm{t} = E_\mathrm{t}\hat{\mathbf{y}} \qquad \mathbf{H}_\mathrm{t} = \frac{1}{\eta_1}\mathbf{k}_\mathrm{t} \times \mathbf{E}_\mathrm{t} = \frac{E_\mathrm{t}}{\eta_1}\hat{\mathbf{x}}. \tag{3.10c}$$

The transmission and reflection coefficients, named τ_2 and Γ_2, respectively, are derived as describe for the case of incidence from Region 1, starting from (3.2). Their expressions as functions of the surface parameters are:

$$\Gamma_2 = \frac{4Z_\mathrm{m} - \eta_2\left(4 + Z_\mathrm{m}Y_\mathrm{e}\right) + \eta_1\left(4 - 4\eta_2 Y_\mathrm{e} + Z_\mathrm{m}Y_\mathrm{e}\right)}{4Z_\mathrm{m} + \eta_2\left(4 + Z_\mathrm{m}Y_\mathrm{e}\right) + \eta_1\left(4 + 4\eta_2 Y_\mathrm{e} + Z_\mathrm{m}Y_\mathrm{e}\right)}, \tag{3.11}$$

$$\tau_2 = \frac{2\eta_1\left(4 - Z_\mathrm{m}Y_\mathrm{e}\right)}{4Z_\mathrm{m} + \eta_2\left(4 + Z_\mathrm{m}Y_\mathrm{e}\right) + \eta_1\left(4 + 4\eta_2 Y_\mathrm{e} + Z_\mathrm{m}Y_\mathrm{e}\right)}. \tag{3.12}$$

It can be noticed that $\tau_2 = \tau_1\eta_1/\eta_2$. The amplitudes and phases of the scattering coefficients of an H-MS illuminated by either the lower or the upper half-space are plotted in Fig. 3.3, as functions of the surface parameters. The relative permittivity considered for the two regions are $\varepsilon_{\mathrm{r}_1} = 10$ and $\varepsilon_{\mathrm{r}_2} = 2$. It can observed that the surface parameters can be chosen to achieve a perfect transmission or reflection of the incident wave, when it comes from the medium with higher permittivity (Region 1). On the other hand, a wave impinging from Region 2 cannot be perfectly transmitted.

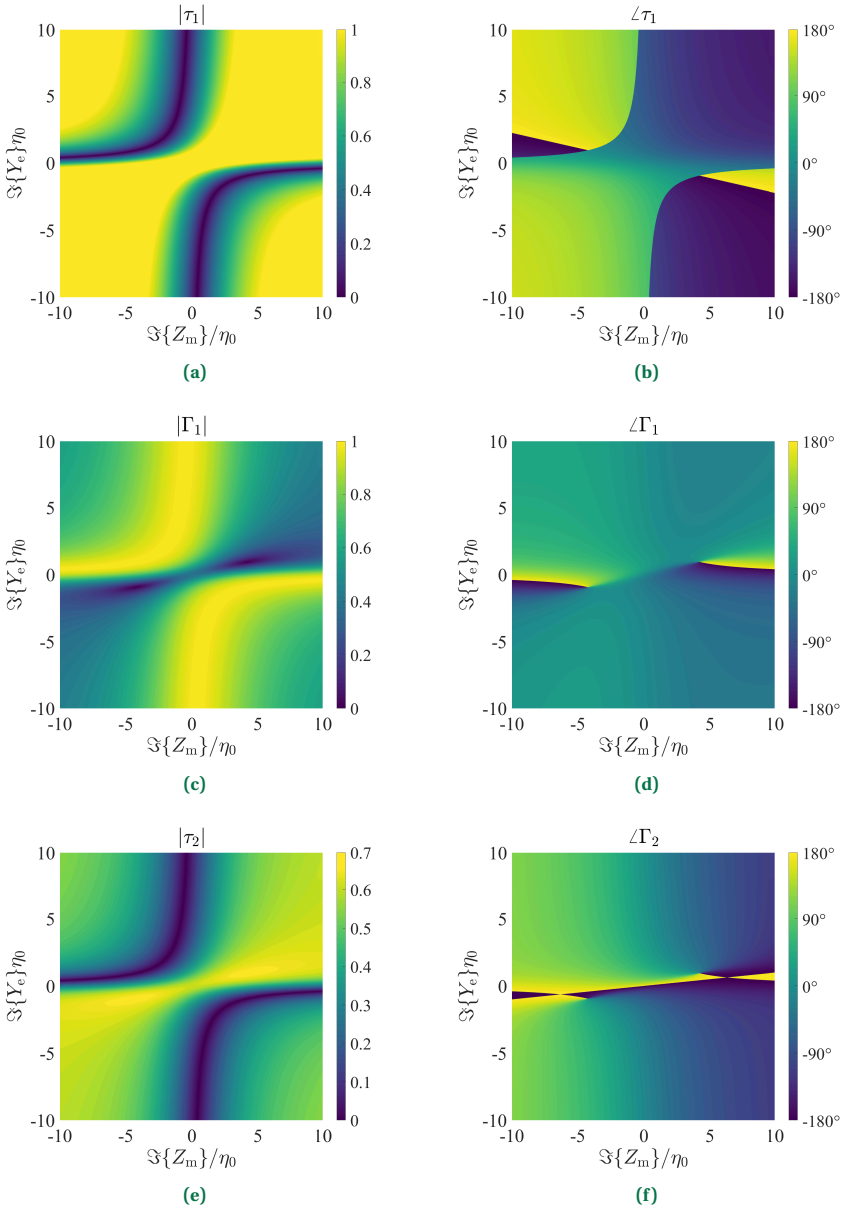

Figure 3.3: Scattering parameters of an H-MS, located between two semi-infinite dielectric media (see Fig. 3.1), having $\varepsilon_{r_1} = 10$ and $\varepsilon_{r_2} = 2$, as functions of its electrical admittance and magnetic impedance (normalized to the free-space characteristic impedance η_0). Transmission coefficient (a) magnitude and (b) phase, and reflection coefficient (c) amplitude and (d) phase for a normally incident wave coming from Region 1. (e) The magnitude of the transmission coefficient and (f) the phase of the reflection coefficient for a normally incident wave coming from Region 2. Since $\angle\tau_2 = \angle\tau_1$ and $|\Gamma_2| = |\Gamma_1|$, these functions are not reported.

3.2.1. Free space condition

If the H-MS is located in a homogeneous medium, then $\eta_1 = \eta_2$. Under this assumption, it is clear from (3.9) and (3.12) that transmission coefficients when the incident wave comes from the first or the second half-space are equal: $\tau_1 = \tau_2 = \tau$. Similarly, the reflective response at both MS side is equal, *i.e.* $\Gamma_1 = \Gamma_2 = \Gamma$. In particular, when the H-MS is in free-space ($\eta_1 = \eta_2 = \eta_0$), the scattering coefficients reduce to:

$$\tau = \frac{\eta_0 \left(4 - Y_\mathrm{e} Z_\mathrm{m}\right)}{\left(2 + \eta_0 Y_\mathrm{e}\right)\left(2\eta_0 + Z_\mathrm{m}\right)}, \tag{3.13a}$$

$$\Gamma = \frac{2\left(Z_\mathrm{m} - Y_\mathrm{e}\eta_0^2\right)}{\left(2 + \eta_0 Y_\mathrm{e}\right)\left(2\eta_0 + Z_\mathrm{m}\right)}. \tag{3.13b}$$

As explained in Chapter 2, when the system is lossless, the H-MS characteristic parameters are purely imaginary. Then, $Z_\mathrm{m} = jX_\mathrm{m}$, where X_m is the magnetic reactance, and $Y_\mathrm{e} = jB_\mathrm{e}$, where B_e is the electric susceptance. Therefore, transmission and reflection coefficients can be expressed as:

$$\tau = \frac{\eta_0 \left(4 + B_\mathrm{e} X_\mathrm{m}\right)}{\left(2 + j\eta_0 B_\mathrm{e}\right)\left(2\eta_0 + jX_\mathrm{m}\right)}, \tag{3.14a}$$

$$\Gamma = \frac{2j\left(X_\mathrm{m} - B_\mathrm{e}\eta_0^2\right)}{\left(2 + j\eta_0 B_\mathrm{e}\right)\left(2\eta_0 + jX_\mathrm{m}\right)}. \tag{3.14b}$$

Fig. 3.4 shows the amplitudes and phases of τ and Γ under these assumptions, as functions of X_m and B_e, similarly to the plots reported in Fig. 3.3 for the general case.

It is interesting to note that perfect transmission is obtained when $B_\mathrm{e} = X_\mathrm{m}$, whereas the incident wave is perfectly reflected if $B_\mathrm{e} = -4/X_\mathrm{e}$. Moreover, any value of $\angle\tau$ or $\angle\Gamma$ in a range of 360° can be achieved by properly choosing the surface parameters. On the other hand, the phases of transmission and reflection coefficients are relatively shifted by either 90° or −90°, as it can be observed from the expression of their difference:

$$\angle\tau - \angle\Gamma = \frac{\pi}{2}\left[1 - \mathrm{sgn}\left(4 + X_\mathrm{m} B_\mathrm{e}\right) - \mathrm{sgn}\left(X_\mathrm{m} - B_\mathrm{e}\right)\right] + 2l\pi, \tag{3.15}$$

where $l \in \mathbb{Z}$ and $\mathrm{sgn}(\cdot)$ denotes the signum function.

3.3. Arbitrary Amplitude Condition of Scattered Fields for a MS between Different Media

The possibility to arbitrarily stipulate the intensity of the scattered fields of an isotropic H-MS at the interface between two different media ($\eta_1 \neq \eta_1$) is analyzed. The incident wave propagates in Region 1. The energy conservation law [96], [150] stipulates the following relation between the amplitudes of reflection and transmission coefficients:

$$\left|\Gamma_1\left(X_\mathrm{m}, B_\mathrm{e}\right)\right|^2 + \frac{\eta_1}{\eta_2}\left|\tau_1\left(X_\mathrm{m}, B_\mathrm{e}\right)\right|^2 = 1. \tag{3.16}$$

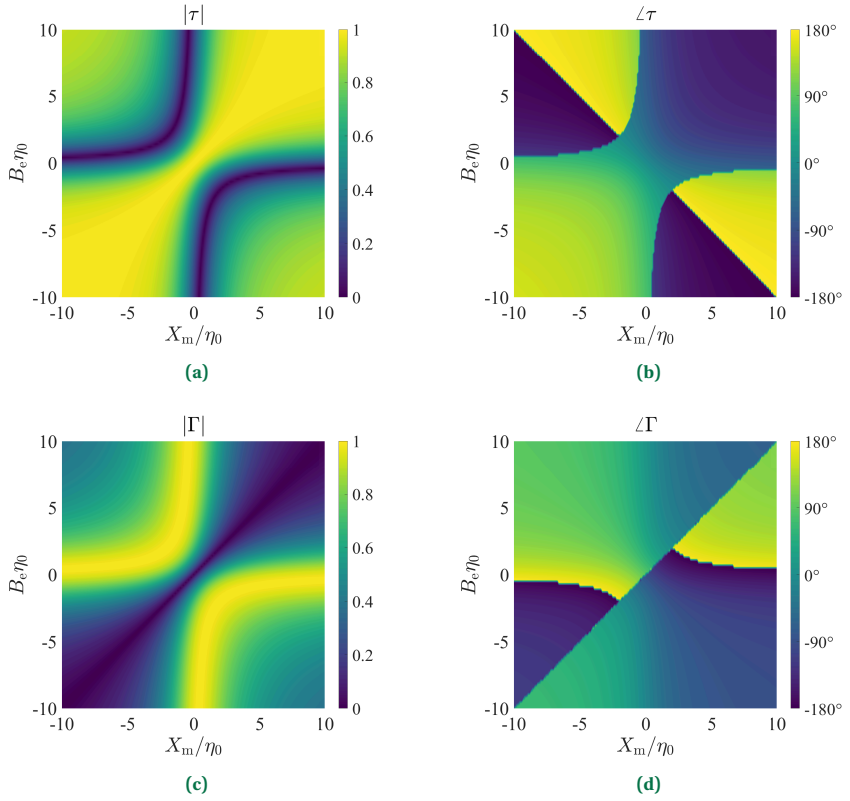

Figure 3.4: Scattering parameters of an isotropic, infinite, lossless and homogeneous H-MS located in free space as a function of its electrical susceptance and magnetic reactance. Transmission coefficient: (a) magnitude and (b) phase. Reflection coefficient: (c) amplitude and (d) phase.

The ratio between the amplitudes of reflection and transmission coefficient can be set by imposing:

$$|\Gamma_1(X_m, B_e)|^2 = \delta\,|\tau_1(X_m, B_e)|^2\,. \tag{3.17}$$

By inserting (3.17) in (3.16), the transmission coefficient amplitude squared is expressed as:

$$|\tau_1(X_m, B_e)|^2 = \frac{\eta_2}{\eta_1 + \delta\eta_2}\,. \tag{3.18}$$

The amplitude of τ_1 when the system is lossless is derived from (3.9):

$$|\tau_1| = \begin{cases} \dfrac{2\eta_2(4 + B_e X_m)}{\sqrt{16\left(X_m + \eta_1\eta_2 B_e\right)^2 + \left(\eta_1 + \eta_2\right)^2 (4 - X_m B_e)^2}} & \text{if } 4 + B_e X_m \geq 0\,, \quad (3.19a) \\ \dfrac{-2\eta_2(4 + B_e X_m)}{\sqrt{16\left(X_m + \eta_1\eta_2 B_e\right)^2 + \left(\eta_1 + \eta_2\right)^2 (4 - X_m B_e)^2}} & \text{if } 4 + B_e X_m < 0\,. \quad (3.19b) \end{cases}$$

The pairs of surface parameters $(X_\mathrm{m}, B_\mathrm{e})$ that satisfy (3.18) are found by solving the following expression, obtained by inserting (3.19) in (3.18):

$$4\eta_2\left(\eta_1+\delta\eta_2\right)\left(4+X_\mathrm{m}B_\mathrm{e}\right)^2=16\left(X_\mathrm{m}+\eta_1\eta_2B_\mathrm{e}\right)^2+\left(\eta_1+\eta_2\right)^2\left(4-X_\mathrm{m}B_\mathrm{e}\right)^2. \tag{3.20}$$

Two solutions (A and B) are found for (3.20):

$$B_{\mathrm{e}_{\mathrm{A,B}}}=\frac{-X_\mathrm{m}\left(32\delta\eta_2^2X_\mathrm{m}+8\eta_1^2+8\eta_2^2+16\eta_1\eta_2X_\mathrm{m}\right)\pm\sqrt{X_\mathrm{m}^2\left(32\delta\eta_2^2X_\mathrm{m}+8\eta_1^2+8\eta_2^2+\right.}}{2\left(2\eta_1\eta_2X_\mathrm{m}^2+4\delta\eta_2^2X_\mathrm{m}^2-16\eta_1^2\eta_2^2-\eta_1^2X_\mathrm{m}^2-\eta_2^2X_\mathrm{m}^2\right)}$$

$$\frac{\sqrt{\left.+16\eta_1\eta_2X_\mathrm{m}\right)^2-8\left(2\eta_1\eta_2X_\mathrm{m}^2+4\delta\eta_2^2X_\mathrm{m}^2-16\eta_1^2\eta_2^2-\eta_1^2X_\mathrm{m}^2-\eta_2^2X_\mathrm{m}^2\right)\left(32\eta_1\eta_2+\right.}}{}$$

$$\frac{\sqrt{\left.+64\delta\eta_2^2-16X_\mathrm{m}^2-16\eta_1^2-16\eta_2^2\right)}}{}. \tag{3.21}$$

The graph of each solution exhibits the following vertical and horizontal asymptotes:

$$X_{\mathrm{m}_{\mathrm{A,B}}}=\pm\sqrt{\frac{16\eta_1^2\eta_2^2}{2\eta_1\eta_2+4\delta\eta_2^2-\eta_1^2-\eta_2^2}}\qquad B_{\mathrm{e}_{\mathrm{A,B}}}=\pm\sqrt{\frac{16}{2\eta_1\eta_2+4\delta\eta_2^2-\eta_1^2-\eta_2^2}}. \tag{3.22}$$

Fig. 3.5 shows the two loci of $(X_\mathrm{m}, B_\mathrm{e})$ solving (3.18), when $\varepsilon_{\mathrm{r}_1}=10$ and $\varepsilon_{\mathrm{r}_2}=2$, for three different ratios δ of the reflected field intensity to the transmitted one. In the case of $\delta\to\infty$, the amplitude of τ_1 tends to 0, whereas, if $\delta=0$, perfect transmission is obtained. When $\delta=1$, the amplitudes of the two scattering parameters is equal.

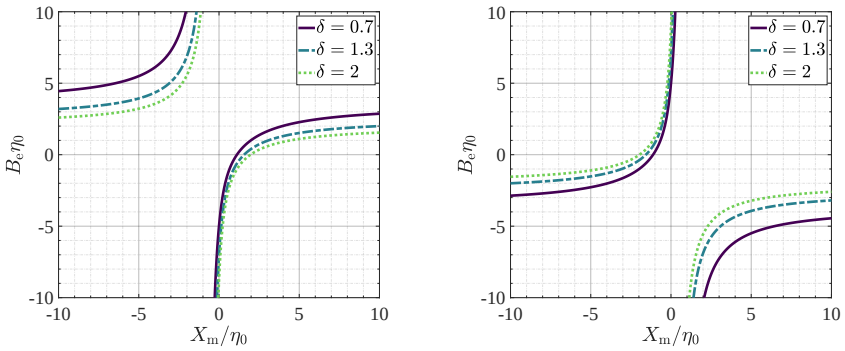

Figure 3.5: Loci of points $B_{\mathrm{e}_{\mathrm{A,B}}}(X_\mathrm{m})$ derived from (3.20) for an isotropic, lossless and reciprocal H-MS that implements an arbitrary power division for different values of δ: (a) $B_{\mathrm{e}_\mathrm{A}}$ and (b) $B_{\mathrm{e}_\mathrm{B}}$.

3.3.1. EQUAL AMPLITUDE CONDITION

By setting $\delta = 1$ in (3.18), the condition $|\Gamma_1| = |\tau_1|$ is enforced. Under this condition of equal amplitude of the scattering coefficients, (3.18) reads as:

$$|\tau(X_m, B_e)|^2 = \frac{\eta_2}{\eta_1 + \eta_2}. \tag{3.23}$$

It is clear that, only when $\eta_1 = \eta_2$, the transmission and reflection coefficient amplitudes are equal to -3 dB. When $\eta_1 \neq \eta_2$, due to the difference in the relative permittivity of both hemispaces above and below the surface, $|\Gamma_1|$ and $|\tau_1|$ are equal but different from -3 dB. Then, the second degree equation reported in (3.20) when $\delta = 1$ reduces to:

$$4\eta_2(\eta_1+\eta_2)(4+X_m B_e)^2 = 16\left(X_m + \eta_1\eta_2 B_e\right)^2 + (\eta_1+\eta_2)^2(4 - X_m B_e)^2. \tag{3.24}$$

Two solutions (A and B) are found for (3.24):

$$B_{e_{A,B}} = \frac{-X_m\left(40\eta_2^2 + 8\eta_1^2 + 16\eta_1\eta_2\right) \pm \sqrt{X_m^2\left(40\eta_2^2 + 8\eta_1^2 + 16\eta_1\eta_2\right)^2 - 4\Big(2\eta_1\eta_2 X_m^2 + \\ 2\left(2\eta_1\eta_2 X_m^2 + 3\eta_2^2 X_m^2 - 16\eta_1^2\eta_2^2 - \eta_1^2 X_m^2\right) \\ + 3\eta_2^2 X_m^2 - 16\eta_1^2\eta_2^2 - \eta_1^2 X_m^2\Big)\left(32\eta_1\eta_2 + 48\eta_2^2 - 16X_m^2 - 16\eta_1^2\right)}}{}. \tag{3.25}$$

The graph of each solution exhibits the following vertical and horizontal asymptotes:

$$X_{m_{A,B}} = \pm\sqrt{\frac{16\eta_1^2\eta_2^2}{2\eta_1\eta_2 + 3\eta_2^2 - \eta_1^2}} \qquad B_{e_{A,B}} = \pm\sqrt{\frac{16}{2\eta_1\eta_2 + 3\eta_2^2 - \eta_1^2}}. \tag{3.26}$$

The loci of points (X_m, B_e) that satisfy (3.23) and the correlated covered phase ranges in transmission and reflection are reported in Fig. 3.6. On the left column, the case with $\varepsilon_{r_1} = 10$ and $\varepsilon_{r_2} = 2$ is considered. On the right column, solutions when the incoming wave arrives from Region 2 are reported. It can be observed from Fig. 3.6 that the phases obtained for the two solutions cover the 360° range except in the asymptotic values.

3.4. ARBITRARY DIVISION OF INCIDENT POWER INTO SCATTERED FIELDS FOR A MS IN FREE SPACE

This Section analyzes isotropic, infinite and lossless H-MSs located in free space which arbitrary split the incident power into the transmitted and reflected wave. Then, the particular case of equal scattering will be studied in detail, providing a solid analytical background to the design of the TRA cells and antennas presented in the rest of this manuscript.

The optimal surface parameters to arbitrarily stipulate the intensity of the scattered fields are here presented for the relevant case of an H-MS in free-space ($\eta_1 = \eta_2 = \eta_0$). Under this assumption, (3.16) reduces to:

$$|\Gamma(X_m, B_e)|^2 + |\tau(X_m, B_e)|^2 = 1. \tag{3.27}$$

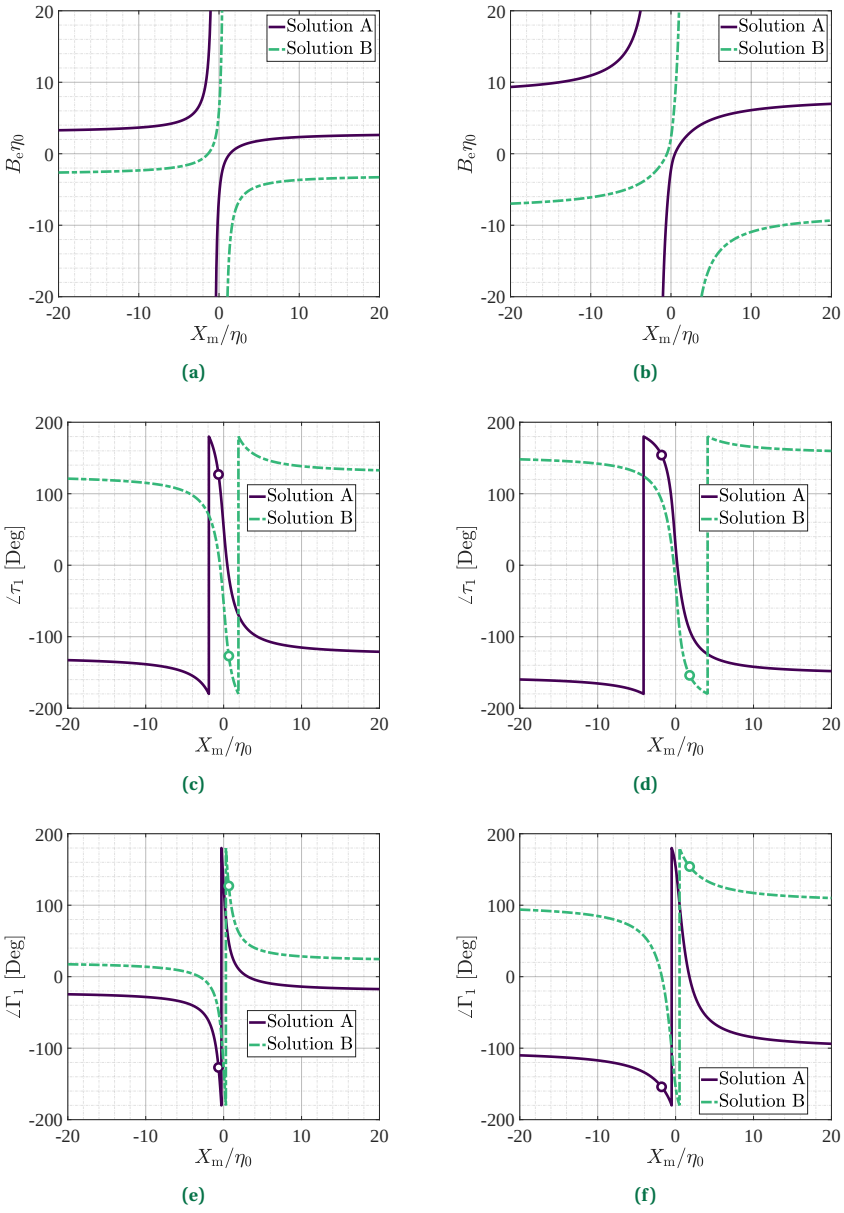

Figure 3.6: (a) Loci of (X_m, B_e) for which $|\tau_1| = |\Gamma_1|$ when $\eta_1 \neq \eta_2$. Two separate solutions are found. Phase of the (b) transmission and (c) reflection coefficients, obtained for these solutions. The left column reports the case for $\varepsilon_{r_1} = 10$ and $\varepsilon_{r_2} = 2$. On the right, $\varepsilon_{r_1} = 2$ and $\varepsilon_{r_2} = 10$.

Then, (3.18) simplifies as follows:

$$|\tau(X_m, B_e)|^2 = \frac{1}{1+\delta} = \nu\,. \tag{3.28}$$

It is straightforward to check that $\nu = 0$ when $\delta \to \infty$, $\nu = 1$ when $\delta = 0$ and $\nu = 0.5$ when $\delta = 1$. These cases correspond to perfect reflection, perfect transmission and equal power division between refracted and reflected waves. Arbitrary values of the transmitted power are fixed choosing $0 \leq \nu \leq 1$. The expression of $|\tau|$ can be derived from (3.19), using $\eta_1 = \eta_2 = \eta_0$ or from (3.14a):

$$|\tau| = \begin{cases} \dfrac{\eta_0 (4 + B_e X_m)}{\sqrt{\eta_0^2 (4 - B_e X_m)^2 + 4 \left(X_m + \eta_0^2 B_e\right)^2}} & \text{if} \quad 4 + B_e X_m \geq 0\,, \qquad (3.29a) \\ \dfrac{-\eta_0 (4 + B_e X_m)}{\sqrt{\eta_0^2 (4 - B_e X_m)^2 + 4 \left(X_m + \eta_0^2 B_e\right)^2}} & \text{if} \quad 4 + B_e X_m < 0\,. \qquad (3.29b) \end{cases}$$

Only two loci of surface parameters fulfill (3.28). They are found by substituting $\eta_1 = \eta_2 = \eta_0$ in (3.20) and solving it for B_e:

$$B_{e_{A,B}} = \frac{-4 X_m \eta \pm 2 \left(X_m^2 + 4\eta^2\right) \sqrt{\nu (1 - \nu)}}{\eta \left(X_m \sqrt{1 - \nu} - 2\eta \sqrt{\nu}\right) \left(X_m \sqrt{1 - \nu} + 2\eta \sqrt{\nu}\right)}\,. \qquad (3.30)$$

Both solutions are plotted in Fig. 3.7, when the transmitted power is 30%, 50% and 70% of the incident one.

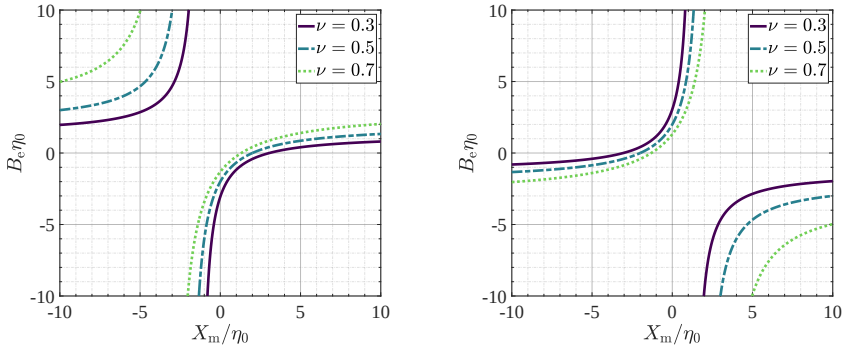

Figure 3.7: Loci of points $B_{e_{A,B}}(X_m)$ derived from (3.30) for an isotropic, lossless and reciprocal H-MS that implements an arbitrary power division for different values of ν:(a) B_{e_A} and (b) B_{e_B}.

3.4.1. EQUAL AMPLITUDE

Now, the case where $\delta = 1$ is considered. Under this specific conditions, $\nu = 0.5$ and an evenly split of the incident power in both transmission and reflection is obtained. The relation reported in (3.28) reads as:

$$|\tau(X_m, B_e)|^2 = |\Gamma(X_m, B_e)|^2 = 0.5\,. \qquad (3.31)$$

The amplitude of the reflection coefficient is found by and can be written as (3.14b):

$$|\Gamma| = \begin{cases} \dfrac{2\left(X_\mathrm{m} - B_\mathrm{e}\eta_0^2\right)}{\sqrt{\eta_0^2\left(4 - B_\mathrm{e}X_\mathrm{m}\right)^2 + 4\left(X_\mathrm{m} + \eta_0^2 B_\mathrm{e}\right)^2}} & \text{if} \quad X_\mathrm{m} - B_\mathrm{e}\eta_0^2 \geq 0\,, \qquad (3.32a) \\ \dfrac{-2\left(X_\mathrm{m} - B_\mathrm{e}\eta_0^2\right)}{\sqrt{\eta_0^2\left(4 - B_\mathrm{e}X_\mathrm{m}\right)^2 + 4\left(X_\mathrm{m} + \eta_0^2 B_\mathrm{e}\right)^2}} & \text{if} \quad X_\mathrm{m} - B_\mathrm{e}\eta_0^2 < 0\,. \qquad (3.32b) \end{cases}$$

Two solutions to (3.31) are found, which relate the electric admittance to the magnetic reactance:

$$B_{\mathrm{e}_{\mathrm{A,B}}} = \frac{2\left(X_\mathrm{m} \mp 2\eta_0\right)}{\eta_0\left(2\eta_0 \pm X_\mathrm{m}\right)}\,. \qquad (3.33)$$

They are both plotted in Fig. 3.8a. The asymptotes of first solution (A), are $B_\mathrm{e} = 2/\eta_0$ and for $X_\mathrm{m} = -2\eta_0$. On the other hand, for the second solution (B), the vertical and horizontal asymptotes are $X_\mathrm{m} = 2/\eta_0$ and $B_\mathrm{e} = -2/\eta_0$, respectively.

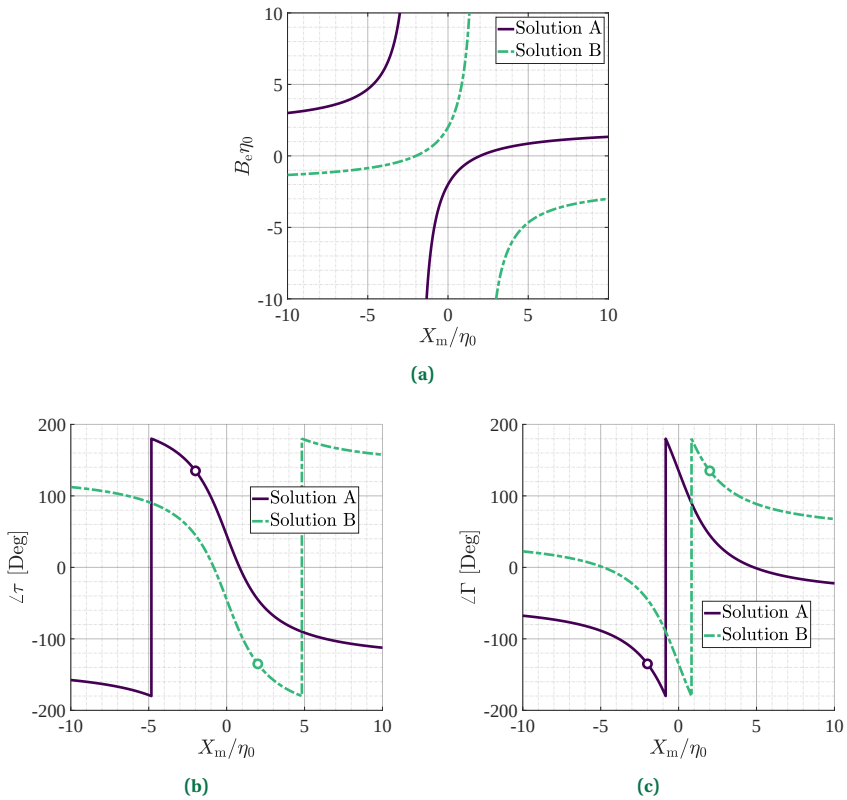

Figure 3.8: (a) Loci of $(X_\mathrm{m}, B_\mathrm{e})$ for which $|\tau| = |\Gamma|$ when $\eta_1 = \eta_2 = \eta_0$. Two separate solutions are found. Phase of the (b) transmission and (c) reflection coefficients, obtained for these solutions.

The transmission coefficient can be expressed as function of a single variable, *e.g.* the magnetic reactance, by substituting (3.33) in (3.14a):

$$\tau_{A,B} = \frac{X_m^2 + 4\eta_0^2}{4\eta_0^2 \pm 4\eta_0 X_m - X_m^2 + j\left(4\eta_0 X_m \mp 4\eta_0^2 \pm X_m^2\right)}. \tag{3.34}$$

The phases of τ_A and τ_B are shown in Fig. 3.8b. Each phase spans the entire 360° range, except for two values associated to the asymptotes of (3.33). Concerning solution *A*, $\angle\tau \to 135°$ for $X_m = -2\eta_0$ and $B_e \to \infty$, whereas $\angle\tau \to -135°$ for $X_m \to \infty$ and $B_e = 2/\eta_0$. Concerning solution *B*, the values $\angle\tau \to -135°$ and $\angle\tau \to 135°$ are obtained asymptotically, for $X_m = 2\eta_0$ and $B_e \to \infty$, and for $X_m \to \infty$ and $B_e = -2/\eta_0$, respectively.

The magnetic impedance that fulfills (3.23) and provides a given phase of the transmission coefficient can be determined using the following closed-form formula, particularly useful in the design, which is derived from (3.34):

$$X_{m_{A,B}} = \frac{2\eta_0\left[(\cos\angle\tau \pm \sin\angle\tau) - \sqrt{2}\right]}{\sin\angle\tau \mp \cos\angle\tau}. \tag{3.35}$$

Notice that $\angle\tau = 45°$ and $\angle\tau = -45°$, and values differing from them by multiples of 360°, are removable singularities of X_{m_A} and X_{m_B}, respectively. For these values, the MS has a purely electric response, $X_{m_{A,B}} = 0\,\Omega$ and $B_{e_{A,B}} = \mp 2\eta_0$. The reflection coefficient can be also written as a function of the magnetic reactance:

$$\Gamma_{A,B} = \frac{\pm j\left(X_m^2 + 8\eta_0^2\right)}{\left(2\eta_0 + jX_m\right)\left[2\eta_0 \pm X_m + j\left(X_m \mp 4\eta_0\right)\right]}. \tag{3.36}$$

The phases of Γ obtained for the two solutions are shown in Fig. 3.8c and both cover the 360° range, except for the asymptotic values. Considering solution *A*, $\angle\Gamma \to -135°$ for $X_m = -2\eta_0$ and $B_e \to \infty$, whereas $\angle\Gamma \to -45°$ for $X_m \to \infty$ and $B_e = 2/\eta_0$. When solution *B* is considered, the values 135° and 45° are obtained asymptotically, for $X_m = -2\eta_0$ and $B_e \to \infty$, and for $X_m \to \infty$, respectively. By comparing Fig. 3.8b and Fig. 3.8c, it can be observed that the difference between $\angle\tau$ and $\angle\Gamma$ is −90°, for the first (*A*) solution. This difference is, instead, 90° for the second (*B*) solution. Therefore, the phases in transmission and reflection cannot be controlled separately. Once the spatial profiles of either $\angle\tau$ or $\angle\Gamma$ is arbitrarily fixed, the other one is automatically stipulated. This fundamental property prescribes a relation between the scan angles of the beams that an H-MS-based TRA radiates in the two half-spaces.

3.5. DESIGN OF TRA H-MS CELLS AS CASCADES OF IMPEDANCE SHEETS

In this Section, the design of H-MS elements using n stacked impedance sheets interleaved by $n-1$ dielectric slabs, where $n > 1$, is discussed. In particular, an analysis on the minimum n required to freely synthesize the H-MS surface parameters is presented, with application to the design of TRA unit-cells at the interface between two half-spaces filled with vacuum. Previous studies have proved that FSSs with two identical stacked

sheets on a dielectric substrate do not enable a simultaneous control on the phase and amplitude of the transmitted field. Arbitrary phase values can only be obtained if the amplitude of the transmission coefficient is less than −3 dB. [151]. Several works reported isotropic H-MSs designed with two impedance sheets [146], [147]. In most cases, no conditions on the transmission amplitude are prescribed enabling a full phase coverage in transmission using two equal sheet impedances. [148], [149]. In these designs, the magnetic and electric polarizabilities of an H-MS are achieved through the excitation of stacked congener dipoles [152].

Isotropic H-MS meta-atoms realized with three impedance sheets (see Fig. 2.6) can achieve perfect transmission ($|\tau| = 1$) and, at the same time, any phase of the transmitted field (except for two values that are obtained asymptotically) [88], [99], [140]. However, to the best of the author's knowledge, no works in the open literature have analyzed the design of H-MSs with stacked impedance sheets and the related limitations on the achievable phase coverage when the equality of the amplitudes of transmission and reflection coefficients is stipulated.

3.5.1. DESIGN WITH TWO IMPEDANCE SHEETS

The design and performance of an H-MS comprising two impedance sheets is discussed. The structure is shown in Fig. 3.9. The substrate between the two sheets has a thickness t and a dielectric permittivity ε_{rl}. The difference of the phases of transmission and reflection coefficients is fixed by (3.15). Intuitively, two independent design parameters are necessary to stipulate both $|\tau| = |\Gamma| = 1/\sqrt{2}$ and an arbitrary value for $\angle\tau$. However, since the reciprocal H-MS under analysis lies in a homogeneous medium (free space), it is a symmetric structure, with two equal sheet impedances [150]. Therefore, for a given electrical thickness of the substrate, only a degree of freedom is available for the design, limiting the range of realizable surface parameters. This observation will be rigorously demonstrated in the following lines.

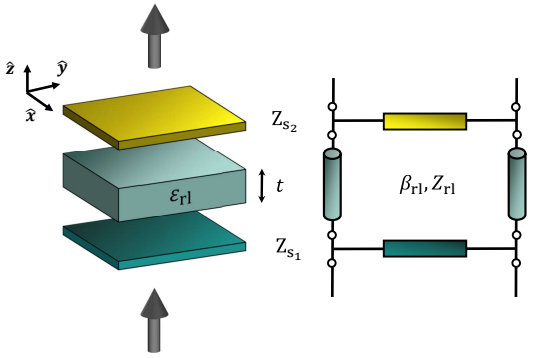

Figure 3.9: Model and equivalent circuit of a MS meta-atom comprising two sheet impedances spaced by a dielectric slab.

The transfer matrix $\mathbf{T}_{\text{TOT}}$ of the overall two-sheet isotropic unit-cell can be derived following the approach described in Chapter 2, considering two generic sheet impedances

Z_{s_1} and Z_{s_2}:

$$\underline{\mathbf{T}}_{TOT} = \begin{bmatrix} \cos(\beta_{rl} t) + j\frac{Z_{rl}}{Z_{s_2}}\sin(\beta_{rl} t) & j Z_{rl}\sin(\beta_{rl} t) \\ \frac{1}{Z_{s_1}}\cos(\beta_{rl} t) + jY_{rl}\sin(\beta_{rl} t) + & \\ + j\frac{Z_{rl}}{Z_{s_1} Z_{s_2}}\sin(\beta_{rl} t) + \frac{1}{Z_{s_2}}\cos(\beta_{rl} t) & j\frac{Z_{rl}}{Z_{s_1}}\sin(\beta_{rl} t) + \cos(\beta_{rl} t) \end{bmatrix}, \quad (3.37)$$

where $Z_{rl} = \eta_0/\sqrt{\varepsilon_{rl}}$ and β are the characteristic impedance and propagation constant in thee substrate, and $Y_{rl} = 1/Z_{rl}$. Then, by equating (3.37) to (2.23), the values of Z_{s_1} and Z_{s_2} can be computed as functions of the entries of impedance matrix of the equivalent two-port representing the H-MS cell:

$$Z_{s_1} = \frac{j Z_{21} Z_{rl}\sin(\beta_{rl} t)}{Z_{22} - Z_{21}\cos(\beta_{rl} t)}, \quad (3.38a)$$

$$Z_{s_2} = \frac{j Z_{21} Z_{rl}\sin(\beta_{rl} t)}{Z_{11} - Z_{21}\cos(\beta_{rl} t)}. \quad (3.38b)$$

Due to assumption of reciprocity, $Z_{12} = Z_{21}$. Moreover, the symmetry of the structure imposes $Z_{11} = Z_{22}$. Therefore, it is straightforward to see from (3.38) that $Z_{s_1} = Z_{s_2} = Z_s$. Moreover, as shown in [99], [153], for an isotropic and lossless H-MS, the impedance matrix reported in (2.25) reduces to:

$$\begin{pmatrix} Z_{11} & Z_{12} \\ Z_{21} & Z_{22} \end{pmatrix} = j \begin{pmatrix} -\frac{1}{B_e} + \frac{X_m}{4} & -\frac{1}{B_e} - \frac{X_m}{4} \\ -\frac{1}{B_e} - \frac{X_m}{4} & -\frac{1}{B_e} + \frac{X_m}{4} \end{pmatrix}. \quad (3.39)$$

Then, by using (3.39) and (3.38), the sheet impedance Z_s is expressed as a function of X_m and B_e:

$$Z_s = \frac{j Z_{rl}(4 + X_m B_e)\sin(\beta_{rl} t)}{4 - X_m B_e - (4 + X_m B_e)\cos(\beta_{rl} t)}. \quad (3.40)$$

The relations $B_e(X_m)$ reported in (3.33) ensure that the amplitudes of the scattering coefficients are equal. By inserting them in (3.40) the two expressions for Z_{rl} that fulfill $|\tau| = |\Gamma|$ are obtained:

$$Z_{s_{A,B}} = \frac{j Z_{rl}(X_m^2 + 4\eta_0^2)\sin(\beta_{rl} t)}{(4\eta_0^2 \pm 4X_m\eta_0 - X_m^2) - (X_m^2 + 4\eta_0^2)\cos(\beta_{rl} t)}. \quad (3.41)$$

The ranges of realizable surface parameters and achievable values of $\angle\tau$ can be determined from (3.37). The following relevant relation between the H-MS parameters and the electrical length of the slab is obtained by equating the expressions for B (or C) in (2.23) to the corresponding ones in (3.37):

$$\sin(\beta_{rl} t) = \frac{Z_{11}^2 - Z_{21}^2}{j Z_{rl} Z_{21}}. \quad (3.42)$$

After substituting (3.39) in (3.42), it is possible to express the electrical length of the slab as a function of B_e and X_m:

$$\sin\left(\beta_{rl}\, t\right) = \frac{4 X_m \sqrt{\varepsilon_{rl}}}{\eta_0 \left(4 + X_m B_e\right)}. \tag{3.43}$$

When $|\tau| = |\Gamma|$ holds, the relation in (3.43) can be reduced to the following one, using (3.33):

$$\sin\left(\beta_{rl}\, t\right) = \begin{cases} \dfrac{2 X_m \sqrt{\varepsilon_{rl}}\left(2\eta_0 + X_m\right)}{X_m^2 + 4\eta_0^2} & \text{with } B_e = B_{e_A} = \dfrac{2\left(X_m - 2\eta_0\right)}{\eta_0\left(2\eta_0 + X_m\right)}, \quad \text{(3.44a)} \\ \dfrac{2 X_m \sqrt{\varepsilon_{rl}}\left(2\eta_0 - X_m\right)}{X_m^2 + 4\eta_0^2} & \text{with } B_e = B_{e_B} = \dfrac{2\left(X_m + 2\eta_0\right)}{\eta_0\left(2\eta_0 - X_m\right)}. \quad \text{(3.44b)} \end{cases}$$

It can be easily observed that, when $|\tau| = |\Gamma|$, only H-MSs having magnetic impedances which make the right-hand side of (3.44) less or equal to 1, can be physically realized using two impedance sheets.

In Fig. 3.10 , the phase of the transmission coefficient is plotted as a function of X_m, when the first solution (3.44a) is considered. The results for $\varepsilon_{rl} = 1$ and $\varepsilon_{rl} = 10$ are reported in Fig. 3.10a and in Fig. 3.10b, respectively. The sets of realizable magnetic impedances are highlighted in green, whereas the white dots denote phase values that can be attained only asympotically. The maximum achievable phase range in transmission is 180° when $\varepsilon_{rl} = 1$. The phase coverage tends to shrink for increasing values of the substrate permittivity.

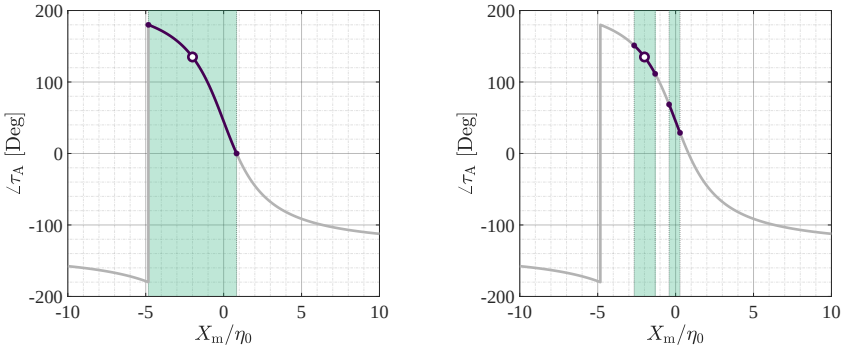

Figure 3.10: Transmission phase range coverage for the first case of (3.44). (a) $\varepsilon_{rl} = 1$ and (b) $\varepsilon_{rl} = 10$.

Fig. 3.11 shows the phase of the transmission coefficient as a function of X_m, when the solution (3.44b) is chosen to enforce $|\tau| = |\Gamma|$. The cases of substrates with $\varepsilon_{rl} = 1$ and $\varepsilon_{rl} = 10$ are analyzed, as in the previous example. Similar results are found. The maximum achievable phase range in transmission is again 180°. It is attained when $\varepsilon_{rl} = 1$.

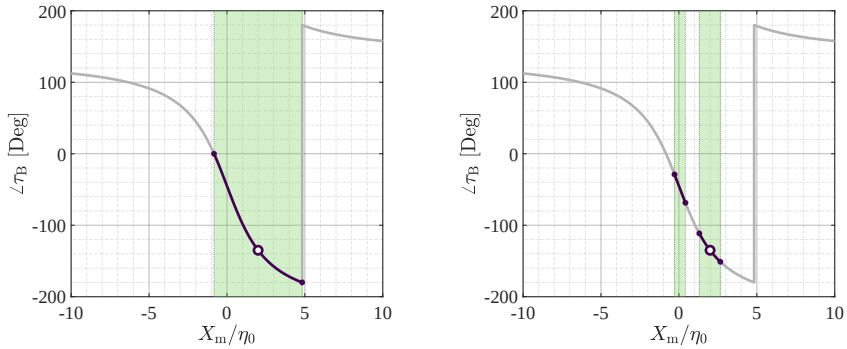

Figure 3.11: Transmission phase range coverage for the second case of (3.44). (a) $\varepsilon_{rl} = 1$ and (b) $\varepsilon_{rl} = 10$.

Therefore, it has been proved mathematically that a reciprocal, lossless and isotropic H-MS in free space, designed with two stacked impedance sheets, cannot equally split the power of a normally incident plane wave into the scattered fields, and, at the same time, cover the full phase range in transmission or reflection. Hence, three-layer H-MS designs will be considered next for the realization of TRAs.

3.5.2. DESIGN WITH THREE IMPEDANCE SHEETS

The design of a power-splitting H-MS using three stacked impedance sheets, spaced by two dielectric substrates of thickness t relative permittivity ε_{rl} (see Fig. 2.6 in Chapter 2), is discussed. As it has been demonstrated in [100], any reciprocal, lossless, omega-type bi-isotropic metasurface can be realized using this three-layer structure. It is clear that, since the H-MSs under analysis form a subset of this class of MSs, they can be also synthesized with this design. The general expressions for the three sheet impedances $(Z_{s_1}, Z_{s_2}, Z_{s_3})$ are found by substituting in (2.26) the entries of the impedance matrix reported in (3.40), yielding:

$$Z_{s_1} = Z_{s_3} = \frac{j X_m Z_{rl} \tan(\beta_{rl} t)}{-X_m + 2 Z_{rl} \tan(\beta_{rl} t)}, \tag{3.45a}$$

$$Z_{s_2} = \frac{j \left[Z_{rl} \tan(\beta_{rl} t) \right]^2 (4 + X_m B_e)}{4 X_m \sec^2(\beta_{rl} t) - 2 Z_{rl} (4 + X_m B_e) \tan(\beta_{rl} t)}. \tag{3.45b}$$

It is possible to note that external layers are equal, due to the symmetry of the H-MS, and that they depend only on the magnetic reactance. On the other hand, Z_{s_2} is determined also by the H-MS electric susceptance. The inner sheet impedance that equalizes the amplitudes of transmission and reflection coefficients is derived by inserting in (3.45b) the optimal relations (3.33) between (3.33) the surface parameters. In this way, the two following expressions for Z_{s_2} are obtained:

$$Z_{s_{2_{A,B}}} = \frac{j \left[Z_{rl} \tan(\beta_{rl} t) \right]^2 (X_m^2 + 4\eta_0^2)}{2 X_m (2\eta_0^2 \pm \eta_0 X_m) \sec^2(\beta_{rl} t) - 2 Z_{rl} (X_m^2 + 4\eta_0^2) \tan(\beta_{rl} t)}. \tag{3.46}$$

Fig. 3.12 shows how Z_{s_1} and $Z_{s_{2_{A,B}}}$ vary as functions of the H-MS magnetic reactance and normalized slab thickness when $\varepsilon_{rl} = 2.2$. Their variations are relatively smooth, except in the domain highlighted in gray.

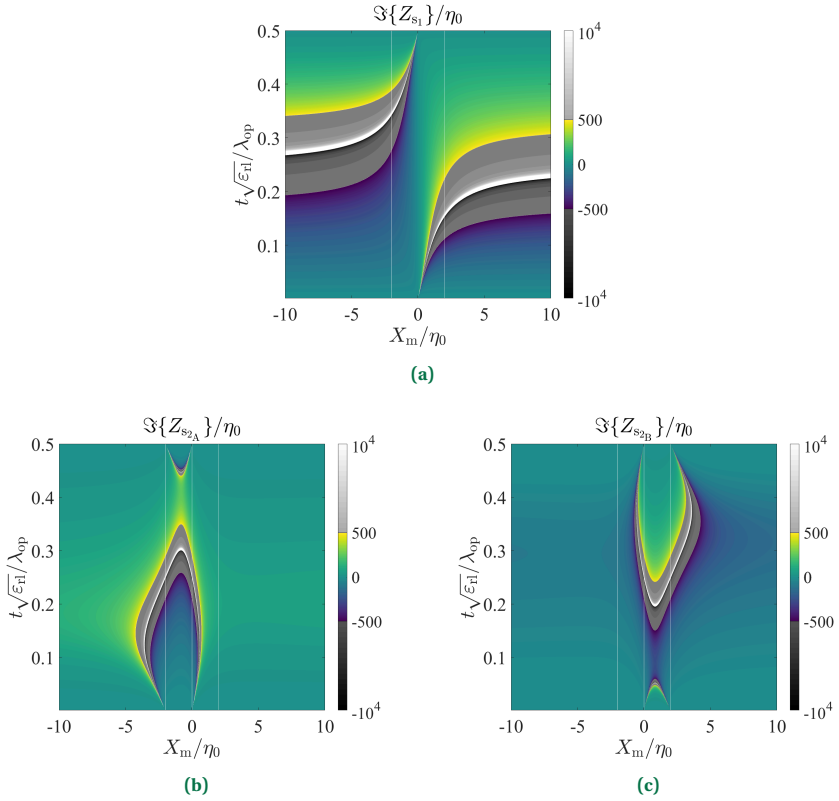

Figure 3.12: Sheet impedances of a reciprocal, isotropic and lossless three-layer H-MS cell, as functions of the magnetic reactance and the electrical thicknesses of its two substrates with $\varepsilon_{rl} = 2.2$, when (3.31) holds. (a) Impedance Z_{s_1} of the two outer sheets. The possible inner sheet impedances: (b) $Z_{s_{2_A}}$ and (c) $Z_{s_{2_B}}$.

3.6. IMPEDANCE SHEET DESIGN USING PATTERNED METAL LAYERS

Each impedance sheet of a multi-layer H-MS can be practically realized using a patterned metal layer. This Section describes a method for computing and optimizing the equivalent sheet impedance of a patterned metal layer, with the aid of a full-wave solver, and studies several basic designs exhibiting capacitive or inductive responses. The design of the TRA unit-cells presented in Chapter 4 will be based on this approach and on the preliminary guidelines here discussed. The sheet impedance is evaluated for each layer individually, using the simulation model shown in Fig. 3.13 and neglecting possible coupling with other stacked layers [95].

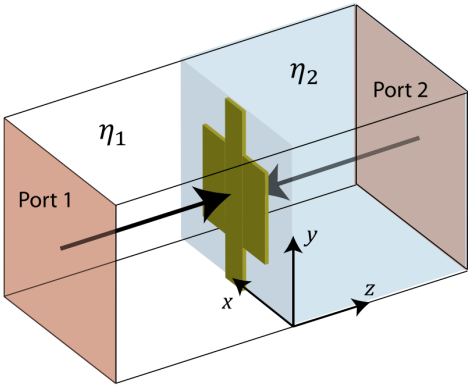

Figure 3.13: Simulation setup for the unit-cell of a general sheet impedance. The patterned layer is located at $z = 0$, between two different media with characteristic impedances η_1 and η_2. The scattering parameters are evaluated using two Floquet ports, applying a de-embedding to $z = 0$. Periodic boundaries are enforced along the other four faces of the model. Image taken from [95]

The unit-cell of the patterned layer is located, in general, between two dielectrics with characteristic impedances η_1 and η_2, which model the impact of the substrates above and below the sheet under analysis in a multi-layer metasurface. Indeed, not only the chosen geometry, but also the surrounding dielectric media affect the value Z_s of the sheet impedance. Periodic boundary conditions are enforced on the four lateral faces of the box. The incident fields are excited through two Floquet ports and the scattering matrix $\underline{\mathbf{S}}$ is evaluated after de-embedding at the plane of the patterned layer. The physical implementation is realized by using FSS theory [154], [155]. The simulated scattering coefficients are used to derive the sheet impedance, which, in the general case, is a 2×2 tensor $\underline{\mathbf{Z}}_s$. By using (2.19) and (2.21), the following expression for the sheet admittance tensor $\underline{\mathbf{Y}}_s = \underline{\mathbf{Z}}_s^{-1}$ is obtained [95]:

$$\underline{\mathbf{Y}}_s = \left(\frac{\underline{\mathbf{I}} - \underline{\mathbf{S}}_{11}}{\eta_1} - \frac{\underline{\mathbf{I}} + \underline{\mathbf{S}}_{11}}{\eta_2} \right) \left(\underline{\mathbf{I}} + \underline{\mathbf{S}}_{11} \right)^{-1} = \left(\frac{\underline{\mathbf{I}} - \underline{\mathbf{S}}_{22}}{\eta_2} - \frac{\underline{\mathbf{I}} + \underline{\mathbf{S}}_{22}}{\eta_1} \right) \left(\underline{\mathbf{I}} + \underline{\mathbf{S}}_{22} \right)^{-1} . \tag{3.47}$$

Then, the metal pattern dimensions are adjusted to maximize bandwidth and minimize loss. Under a linear y-polarized and normal incident plane wave from Region 1, the expression of Z_s can be derived from (3.47) [95]:

$$Z_s = \left[\left(\frac{1 - S_{11}}{\eta_1} - \frac{1 + S_{11}}{\eta_2} \right) (1 + S_{11})^{-1} \right]^{-1} . \tag{3.48}$$

As a proof of concept, three simple geometries widely employed to physically realize sheet impedances are presented. For each of them, a circuit model to predict the frequency behavior of Z_{sl} is proposed. Lastly, a parametric evaluation of the metallic patterns dimensions is reported.

3.6.1. PATCH

A square patch has been analyzed at the operation frequency $f_{op} = 30\,\text{GHz}$ due to its simple design and synthesis process. The metallic shape is placed in between an air filled media of thickness $\lambda_{op}/4$ and a dielectric substrate of thickness $t = 0.84\,\text{mm}$ with and $\varepsilon_{rl} = 2.2$. The simulation setup is reported in Fig. 3.14a.

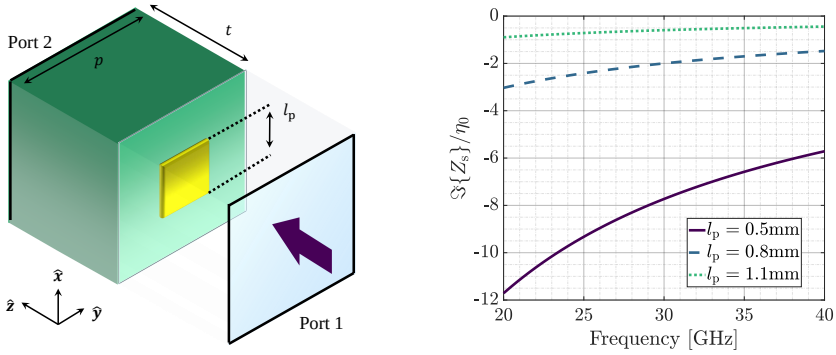

(a) (b)

Figure 3.14: (a) Squared patch simulation setup and pattern dimensions. (b) Normalized Z_s variation as function of frequency for three different patch side, l_p, values.

An element periodicity of $p = 1.2\,\text{mm}$ and patch side of $l_p = 0.8\,\text{mm}$ are considered. The performances have been evaluated enforcing periodic boundary conditions and considering a y-polarized normally incident plane wave. In Fig. 3.14b the sheet impedance variation as a function of frequency for three different values of l_p are reported. It can be noted that an increase of the patch side involves a rise of the metallic pattern capacitive response. Due to this behavior, the patch can be modeled with the equivalent circuit reported in Fig. 3.15a.

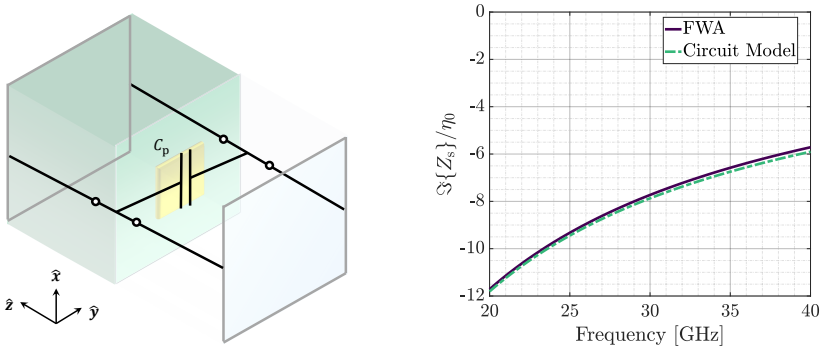

(a) (b)

Figure 3.15: (a) Patch equivalent circuit model. (b) Comparison normalized sheet impedance as a function of frequency between the model defined in (3.49) and the full wave simulation.

The sheet impedance can then be computed from the capacitance value of the patch:

$$Z_s = \frac{1}{j\omega C_p}. \tag{3.49}$$

A comparison between the equivalent circuit behavior and the full wave analysis of the patch for $l_p = 0.8\,\text{mm}$ is shown in Fig. 3.15b. The model predicts with a good agreement the simulation results of the sheet impedance variation as a function of frequency.

3

3.6.2. DOG-BONE

A dog-bone metal pattern has been studied next at the operation frequency $f_{op} = 30\,\text{GHz}$. The sheet is placed in between two dielectric substrates of thickness $t = 0.84\,\text{mm}$ and $\varepsilon_{rl} = 2.2$. The simulation setup is reported in Fig. 3.16a.

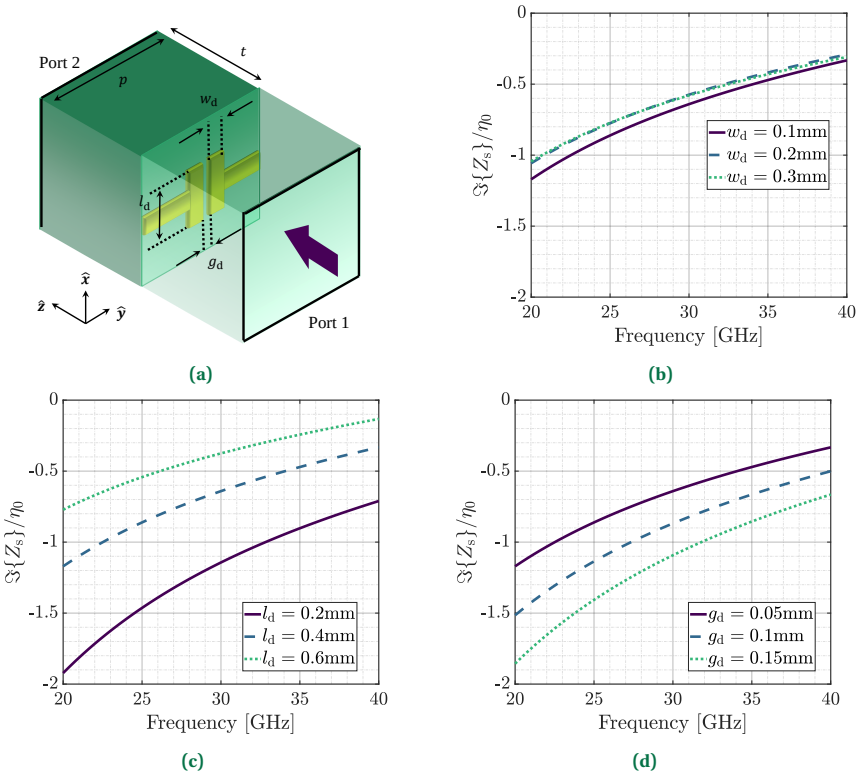

Figure 3.16: (a) Dog-bone simulation setup and pattern dimensions. Normalized Z_s variation as function of frequency for three values of: (b) w_d,(c) l_d and (d) g_d.

The dog-bone pattern is composed by two conductors having width $w_d = 0.1\,\text{mm}$ and length $l_d = 0.2\,\text{mm}$ separated by a gap of $g_d = 0.1\,\text{mm}$. The metal shape lines that connect both termination is placed along the y-axis and has a width of $w_l = 0.1\,\text{mm}$. The

geometry is symmetric with respect to the xz-plane and has periodicity $p = 1.2\,\text{mm}$. In Fig. 3.16b, the sheet impedance variation as a function of frequency for three different values of w_d is reported. It can be noted that the capacitive response of the metallic pattern rises when the dog-bone termination is increased to 0.2 mm. By rising again w_d, no appreciable increase of Z_s is obtained. Another way to achieve a noticeable high capacitive response is trough the dimension l_d. It can be noted from Fig. 3.16c that a long termination produce an high sheet impedance value. The last parameter to be considered is the gap between two consecutive dog-bone terminations. It is possible to observe from Fig. 3.15d that as for capacitors in circuit theory, an increase in the gap produce a decrease of the capacitance and then Z_sl becomes smaller.

The dog-bone pattern can then be modeled with the equivalent circuit reported in Fig. 3.17a. This model takes into account both inductive effect of the line connecting each pattern termination and the capacitive behavior due to two consecutive tails gap.

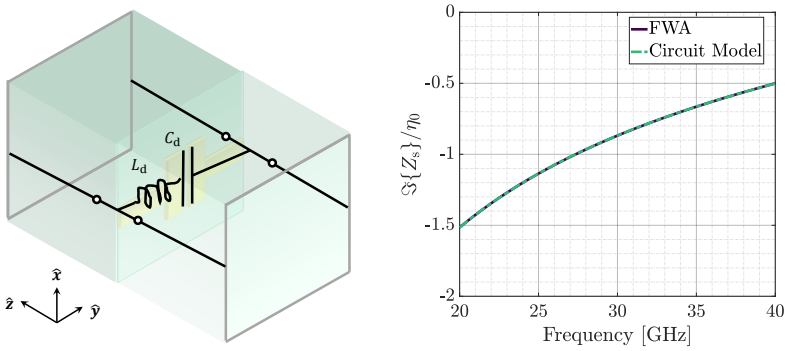

(a) (b)

Figure 3.17: (a) Dog-bone equivalent circuit. (b) Comparison normalized sheet impedance as a function of frequency between the model defined in (3.50) and the full wave simulation.

The sheet impedance can then be computed knowing the inductor and capacitor value as follows:

$$Z_\text{s} = j\omega L_\text{d} + \frac{1}{j\omega C_\text{d}}. \tag{3.50}$$

A comparison between the equivalent circuit behavior and the full wave analysis of the dog-bone for $w_\text{d} = 0.1\,\text{mm}$, $l_\text{d} = 0.4\,\text{mm}$, $g_\text{d} = 0.1\,\text{mm}$ and $w_\text{l} = 0.1\,\text{mm}$ is shown in Fig. 3.17b. The model predicts perfectly the simulation results of the sheet impedance variation as a function of frequency.

3.6.3. MEANDER

The last investigated metal pattern at the operation frequency $f_\text{op} = 30\,\text{GHz}$ is the meander line. As for the patch impedance sheet, the metallic shape is placed in between an air filled media of thickness $\lambda_\text{op}/4$ and a dielectric substrate of thickness $t = 0.84\,\text{mm}$ with and $\varepsilon_\text{rl} = 2.2$. The simulation setup is reported in Fig. 3.18a.

The meander is composed by a line placed along the y-axis of width $w_\text{l} = 0.1\,\text{mm}$ that bends and forms a shape having width $w_\text{b} = 0.5\,\text{mm}$ and length $l_\text{b} = 0.4\,\text{mm}$. The

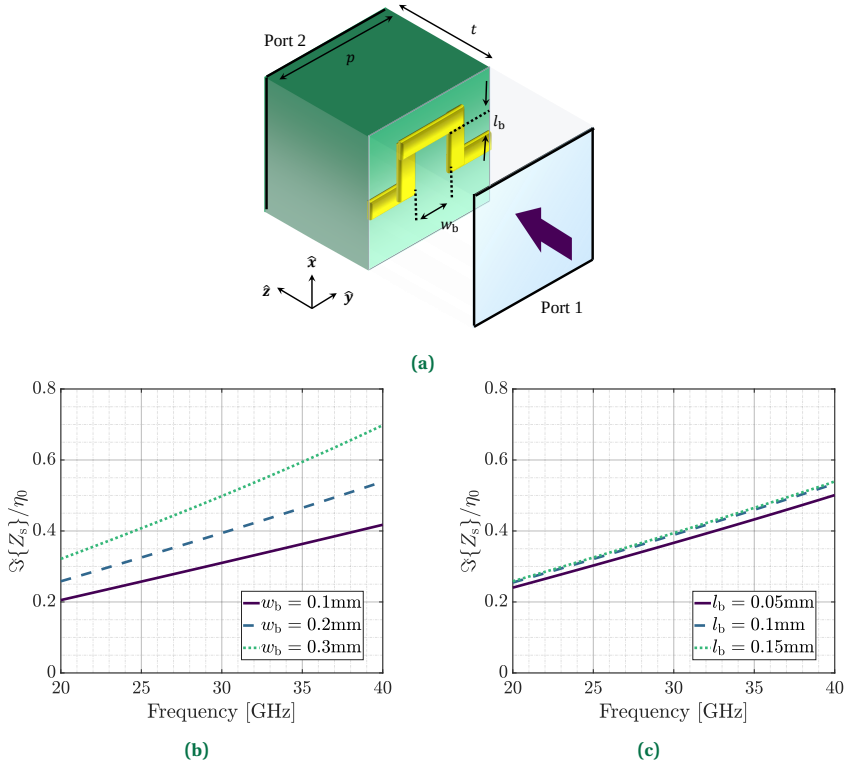

Figure 3.18: (a) Meander simulation setup and pattern dimensions. Normalized Z_s variation as function of frequency for three values of: (b) w_b and (c) l_b.

geometry is symmetric with respect to the xz-plane and has periodicity $p = 1.2$ mm. In Fig. 3.18b, the sheet impedance variation as a function of frequency for three different values of w_b is reported. It can be noted that the inductive response of the metallic pattern rises when the distance between the two bending lines along y increases. On the other hand, by varying l_b, no appreciable increase of Z_s is obtained as reported in Fig. 3.18c. From both analysis, it is possible to observe that the inductive response of the sheet impedance strengthens and Z_s becomes higher by increasing the meander line length.

The meander can then be modeled with the equivalent circuits reported in Fig. 3.19a and Fig. 3.19b. The first circuit model uses an inductance to predict the geometry behavior as a function of frequency:

$$Z_s = Z_{L_b} = j\omega L_b \,. \tag{3.51}$$

The second equivalent circuit proposed here models the distance between the two meander bends with a capacitance. Then, a shunt inductance can be used to model the transmission line:

$$Z_s = Z_{L_b} // Z_{C_b} = \frac{j\omega L_b}{1 - j\omega C_b} \,. \tag{3.52}$$

A comparison between the equivalent circuits responses and the full wave analysis of the meander for $w_b = 0.5\,\text{mm}$, $l_b = 0.3\,\text{mm}$ and $w_l = 0.1\,\text{mm}$ is shown in Fig. 3.19c. Both models match with a good agreement the simulation results of the sheet impedance variation as a function of frequency.

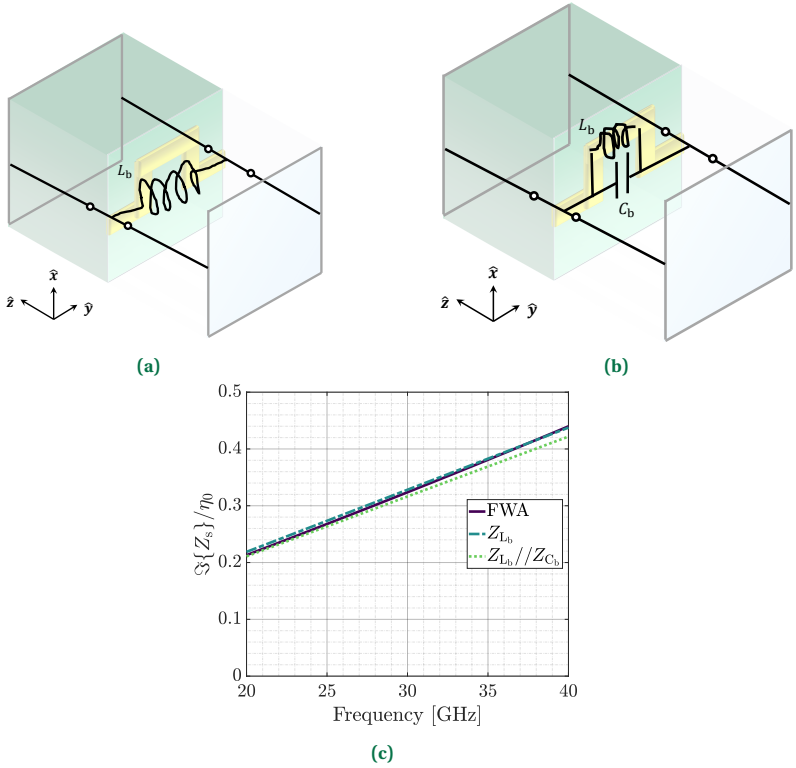

Figure 3.19: Meander equivalent circuit: (a) inductance and (b) capacitance with a shunt inductance. (c) Comparison of the normalized sheet impedance as a function of frequency between the circuit models and the full wave simulation.

3.7. CHAPTER LANDMARKS

After a general review on H-MSs, its scattering parameters under isotropy and reciprocity attributes with a normal incident illumination are derived. Starting from these expressions, relations between the H-MS constitutive parameters have been found when an arbitrary power division and an equal amplitude condition is enforced. In design perspective for TRAs, the case where the surface is located in free space has been highlighted and the direct relations between the magnetic impedance and the transmission coefficient phase have been reported. However, a constant phase difference of $\pm 90°$ between the scattering coefficients has been found. This limitation implies the realizations of TRAs with, for example, an arbitrary phase profile in transmission and a fixed one in reflection leading to the generation of dependent beams. To realize TRA cells starting

from the derived H-MS constitutive parameter relations, cascaded impedance sheets have been considered. At first, a two sheet impedance cascade has been considered. The limitation determined by the presence of equal layers does not allow to cover the full phase range in transmission and, consequently, in reflection. Then a cascade of three sheet impedance is required, confirming the choice reported in most of literature works. Finally, some examples of these sheet impedance practical implementation have been shown. Simple geometries like dipoles, patches and meanders have been considered.

4

Transmit-Reflect arrays: Design and Characterization

Experience without theory is blind,
but theory without experience is mere intellectual play.

Immanuel Kant

Following the analysis shown in Chapter 3, the design of H-MS elements for the realization of TRAs is presented here. This chapter starts with a description of TRA models suitable to develop analytical tools for the evaluation of radiation characteristics. Then, designs of uniform 2-bit TRAs are proposed. To properly realize these arrays, firstly, the H-MS optimum surface parameter are derived for four transmission coefficient phase values. Then, metal patters are designed to realize the impedance sheets yielding the constitutive parameters defined before. The cell behavior in case of normal and oblique incident field is investigated. To take into account the non-idealities due to fabrication processes and materials availability, the full-wave EM response of the elements has been verified. Lastly, several TRA designs with different aperture sizes and steering angles are presented. To validate the procedure, some prototypes have been fabricated and the measurements results are compared with the analytical simulations.

Parts of this chapter have been published in [C1]–[C3] and [J1].

4.1. Introduction

METASURFACES are effective solutions for the design of space fed array antennas, as TAs or RAs [32], [138], [144], [145], [156]. Differently from these structures, which generally adjust the wavefront phase in discrete steps through elements with half wavelength side, MSs allows a more precise control of amplitude, phase and polarization of refracted or reflected field due to theirs subwavelength meta-atoms. Already in 2007, Pozar discussed the gain bandwidth improvement of RAs employing artificial impedances spaced less then half a wavelength [157]. Later on, MSs proved their capabilities also in the design of TA, reducing unwanted reflections and SLL by achieving perfect refraction [138]. Building on this line of research, several subsequent works have emerged, further advancing the capabilities of MS array antennas, *e.g.* independent optimization of amplitude and phase distribution, synthesis of anisotropic structures for multifunctional operations [158]–[160]. Among all the possible capabilities, the latter is particularly suitable for simultaneous control of amplitude, phase and polarization of refracted and reflected field to realize TRAs [44], [50], [161].

The goal of this chapter is threefold. First, introducing a technique to compute the radiation patterns of TRAs based on physical optics and array theory capable of combining both TA and RA models. Secondly, defining a design approach to avoid brute-force optimization when realizing the metal patterns of the array elements, leveraging the theory presented in Chapter 3. Thirdly, demonstrating the accuracy of the developed tool based on the TRA model and validating the behavior of the designed MS meta-atoms through full wave simulations and measurements in anechoic chamber of several prototypes.

Based on the analysis discussed in Chapter 3, the design of four Huygens' cells of a TRA working at 30 GHz to realize a uniform 2-bit quantization of the full phase range is proposed. Four transmission coefficient phases are selected and the corresponding values of the electric admittance and impedance are computed through the relations reported in subsection 3.4.1. Then, these meta-atoms are realized as a cascade of three impedance sheets spaced by two dielectric slabs. By considering these sheets frequency independent, preliminary scattering coefficients are evaluated by mean of the optimum surface parameters previously derived. These impedance sheets are physically implemented through simple metallic patterns, *e.g.* meanders and dog-bones due to their natural inductive or capacitive behavior. Then, the complete cells are simulated in a periodic environment to verify their scattering response under normal and oblique incidence. From the perspective of manufacturing several TRA prototypes, the impact of a commercial stack-up is investigated.

Using tools based on physical optics and array theory, several TRAs having phase profile optimized to steer the forward and backward beams at different angles have been analyzed. Comparisons with full-wave simulations are presented to validate the accuracy of the developed tool. Lastly, several prototypes with different sizes have been fabricated and the measurement results are compared with simulations performed with the developed tool and full-wave software. The obtained results are further compared with existing works in the literature, highlighting improvements in the performances.

4.2. GEOMETRICAL OPTICS APPROACH

Generally, a rectangular space-fed antenna, TA , RA or TRA, comprises a planar discrete lens with $M \times N$ unit cells and a feed, aligned to its center, at a distance F, as shown in Fig. 4.1. The array sides are L_M and L_N.

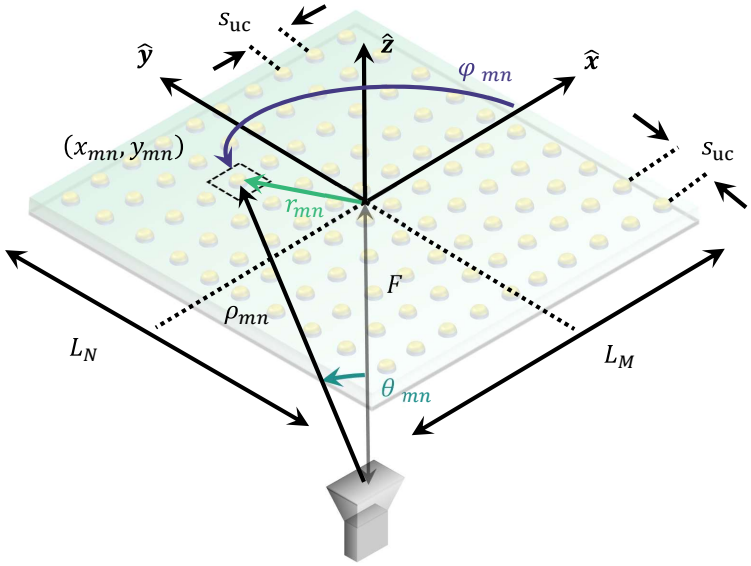

Figure 4.1: Trasmitarray with $M \times N$ squared unit cells having side s_{uc} and located at $z = 0$. The full structure has size $L_M \times L_N$ and the feed is aligned to its center, at a distance F. Each element position, with respect to the source, is determined by the angle θ_{mn}, φ_{mn} and distance ρ_{mn}.

The elements are assumed to be in the far-field region of the source and are electrically thin, with size $s_{uc} \times s_{uc}$. By assuming that the array plane is at $z = 0$ and that the origin of the reference system is at the center of the array, the position of each element on the xy-plane is determined by the simple geometrical relation $r_{mn} = \sqrt{x_{mn}^2 + y_{mn}^2}$, where x_{mn} and y_{mn} are the mn^{th} cell center value. The azimuthal angle φ_{mn} defines the mn^{th} array element angular position with respect to the origin:

$$\varphi_{mn} = \arctan 2\left(\frac{y_{mn}}{x_{mn}}\right). \tag{4.1}$$

Its location, with respect to the source, is defined by the angle θ_{mn} and distance ρ_{mn}. The latter is defined as:

$$\rho_{mn} = \sqrt{r_{mn}^2 + F^2}. \tag{4.2}$$

The angle of incidence for an incoming wave radiated by the source on each scatterer is determined by the elevation angle θ_{mn}:

$$\theta_{mn} = \arccos\left(\frac{r_{mn}}{\rho_{mn}}\right). \tag{4.3}$$

Another relevant parameter similar to the rim angle in dish reflector antennas is the angle between the primary feed and the greatest edge of the array,defined as [162]:

$$\theta_s = \arctan\left(\frac{\max\{L_M,\, L_N\}}{F}\right). \tag{4.4}$$

4.2.1. FOCAL SOURCE

Several models of the primary feed have been considered for the analysis of the array in this work. The easiest is an ideal point with a radiation pattern expressed in the following axisymmetric form [163]–[165]:

$$E_{\mathrm{FS}}(\theta) = \begin{cases} \cos^{qFS}(\theta) & \text{if } \theta \in \left[0; \frac{\pi}{2}\right] \text{ and } \varphi \in [0; 2\pi] \\ 0 & \text{elsewhere} \end{cases} \tag{4.5}$$

where qFS models the source directivity and allows a direct control of the illumination tapering on the aperture. In this way, the feed pattern is limited to the front hemisphere ($z \geq 0$) with a zero backward radiation and the antenna directivity can be directly evaluated [163]. A more realistic expression for modelling the far field radiated by a linearly polarized source, *e.g.* a horn antenna, can be obtained using the following elliptical approximation with unequal beamwidths [163], [166], [167]:

$$\mathbf{E}_{\mathrm{FS}}(\theta, \varphi) = j k_{\mathrm{op}} \frac{e^{-j k_{\mathrm{op}} r}}{2\pi r} \begin{cases} \left[C_{\mathrm{E}} \cos(\varphi)\right] \hat{\boldsymbol{\theta}} - \left[C_{\mathrm{H}} \sin(\varphi)\right] \hat{\boldsymbol{\varphi}} & \text{for } \hat{\mathbf{x}} \text{ pol.} \quad (4.6a) \\ \left[C_{\mathrm{E}} \sin(\varphi)\right] \hat{\boldsymbol{\theta}} + \left[C_{\mathrm{H}} \cos(\varphi)\right] \hat{\boldsymbol{\varphi}} & \text{for } \hat{\mathbf{y}} \text{ pol.} \quad (4.6b) \end{cases}$$

where the factors $C_{\mathrm{E}}(\theta) = [\cos(\theta)]^{qE}$ and $C_{\mathrm{H}}(\theta) = [\cos(\theta)]^{qH}$ represent the E- and H-plane patterns, respectively. The parameters qE and qH control the degree of tapering applied to the patterns in E- and H-planes, allowing for flexible adjustment of their shapes. The propagation constant k_{op} is defined as $k_{\mathrm{op}} = 2\pi/\lambda_{\mathrm{op}}$, where λ_{op} being the the free space wavelength at the operating frequency f_{op}. Since, in Chapter 3 a y-polarized incident field is considered to extract the analytical constitutive parameters of the MS, in the following of this chapter, the focal source radiated field in (4.6b) is considered.

It is important for the following description of the lens design that the field radiated by the focal source illuminates the mn^{th} unit cell of the array with an incident phase defined as [162], [168]:

$$\angle E_{\mathrm{FS}} = -k_{\mathrm{op}} \sqrt{F^2 + r_{mn}^2}\,. \tag{4.7}$$

An even better accuracy of the space-fed antenna radiation characteristics is possible by means of the extraction of fields of a real feeder obtained through full-wave analysis. In this work, the 10 dBi gain pyramidal horn antenna with aperture size $a_{\mathrm{FS}} \times b_{\mathrm{FS}}$ and manufactured by *ATM* has been employed. Its characteristics[1] are reported in Table 4.1.

[1] More information on the manufacturer site: https://www.atmmicrowave.com/waveguide/horn-antenna-standard-gain-wide-band/

Table 4.1: *ATM* 10 dBi gain pyramidal horn antenna characteristics.

				HPBW*		Aperture size [mm]	
WG size	**Frequency [GHz]**	**Model**	**Gain [dBi]**	**E-Plane**	**H-Plane**	a_{FS}	b_{FS}
WR34	22 – 33	34 – 440 – 6	10	54.2°	53.2°	13.462	9.906

* Half Power Beam-Width (HPBW)

With respect to the other available sources, the *ATM* 34 – 440 – 6 presents lower gain values between 60° and 90° and enables a good trade-off between taper and spillover efficiencies. A comparison between the full-wave simulation of this pyramidal horn performed with the commercial software Ansys HFSS and the cosine model for a y-polarized field of (4.6b) is reported in Fig. 4.2.

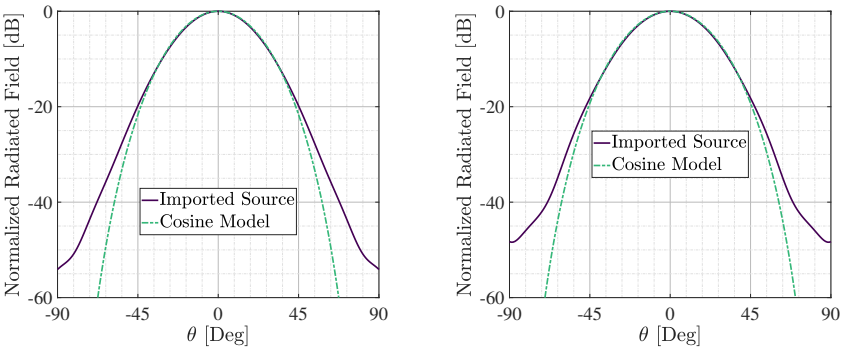

Figure 4.2: Comparison at 30 GHz between the ideal focal source pattern reported in (4.6b) and the 10 dBi gain pyramidal horn fabricated by *ATM*: (a) E-plane and (b) H-plane.

By setting $qE = 3.2$ and $qH = 3.6$, a good match between the two patterns is achieved for $-45° < \theta < 45°$. It is clear that for a lower focal distance F, the value of θ_s increases and the lens illumination includes a more significant portion of the angular region showing a discrepancy between the real horn and the cosine model.

4.2.2. UNIT CELLS

In this paragraph the computation of the radiated field of each unit cell of the lens is addressed, in order to later apply an array approach for the design of the complete structure. In order to compute the field radiated by a unit cell, the incident field on the cell due to the feed needs to be defined. Due to the small size of each cell, an approximation is done assuming a uniform illumination within each mn^{th} cell. The value of the incident field is assumed constant over the cell at $z = 0^-$ and equal to the incident field (4.6b) in the cell center. It is also assumed that the tangential electric field on the radiating side of the mn^{th} cell (at $z = 0^+$) has a single component and is uniform. As done for the feed, ideally, a first approximation of the radiation pattern of

each element can be described by a cosine function:

$$E_{\text{uc}}(\theta) = [\cos(\theta)]^{qUC}. \tag{4.8}$$

In this case, as for the general focal-source approximation with null back radiation, the pattern is axisymmetric. Differently from the feed, where high cosine exponent values are employed, here typically $0 < qUC < 1$. This choice is related to model the low directive elements present in the array.

A different "*sinc*" approximation is obtained by assuming that the far-field patterns of the unit cells are those radiated by y-polarized uniform rectangular apertures in free-space [165]:

$$E_{\text{uc}}(\theta, \varphi) = [1 + \cos(\theta)]\ \text{sinc}\left(\frac{k_x s_{\text{uc}}}{2\pi}\right) \text{sinc}\left(\frac{k_y s_{\text{uc}}}{2\pi}\right). \tag{4.9}$$

A comparison between the radiation patterns RP_{uc} normalized to their maximum values from (4.8) and (4.9) is shown in Fig. 4.3.

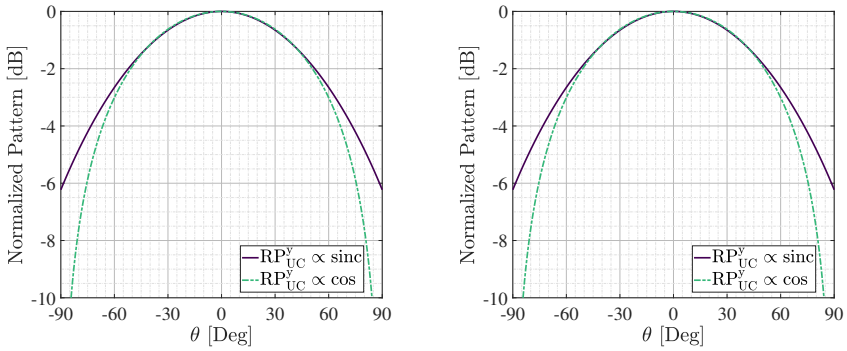

Figure 4.3: Comparison at 30 GHz between the ideal cell pattern reported in (4.8) with the one considering a uniform field distribution: (a) E-plane and (b) H-plane.

The two models start to differ from 45° to 90° where a uniform aperture model presents a higher field value. This means that for larger angle of incidence, a higher gain will be assumed in the computation of the array pattern.

4.2.3. MODEL FOR THE ANALYSIS OF THE TRANSMITTED FIELD

The field radiated in transmission ($z \geq 0$) by the array is due to the vector addition of the field contribution of each element, as for array theory [165]. The coupling between elements is neglected. The array radiation pattern is equal to the field generated by the cells plus spillover radiation. The latter is due to the power directly radiated by the feed, which does not impinge on the lens surface. The radiation due to the lens can be expressed as follows:

$$\text{AF}_{\text{TA}}(\theta, \varphi) = \sum_{n=1}^{N} \sum_{m=1}^{M} \tau(m,n)\, E_{\text{FS}}(m,n)\, e^{j(m-1)(k_x s_{\text{uc}})}\, e^{j(n-1)(k_y s_{\text{uc}})}, \tag{4.10}$$

where $k_x = k_{op}\sin(\theta)\cos(\varphi)$ and $k_y = k_{op}\sin(\theta)\sin(\varphi)$ are the propagation constants along $\hat{\mathbf{x}}$ and $\hat{\mathbf{y}}$. $E_{FS}(m,n)$ is the incident field due to the feed on the mn^{th} cell, which is assumed to be purely linearly polarized, computed as explained in the previous paragraph. The complex transmission coefficient τ is defined as:

$$\tau(m,n) = |\tau(m,n)|\, e^{j\angle\tau(m,n)}. \tag{4.11}$$

It depends on the unit-cell shape and can be obtained via full-wave periodic simulations as detailed in subsection 4.3.3. Its optimal value depends on the functionality of the MS under design. Their phase must compensate the incident feed field phase to radiate into the desired direction defined by the spherical coordinate angles $(\theta_{st}^{ta}, \varphi_{st}^{ta})$:

$$\angle\tau(m,n) = -\angle E_{FS}(m,n) - k_{op}\sin\left(\theta_{st}^{ta}\right)\left[x_{mn}\cos\left(\varphi_{st}^{ta}\right) + y_{mn}\sin\left(\varphi_{st}^{ta}\right)\right]. \tag{4.12}$$

To evaluate the pattern due to spillover, the area outside the TA is discretized with fictious cells [167] (see Fig. 4.4).

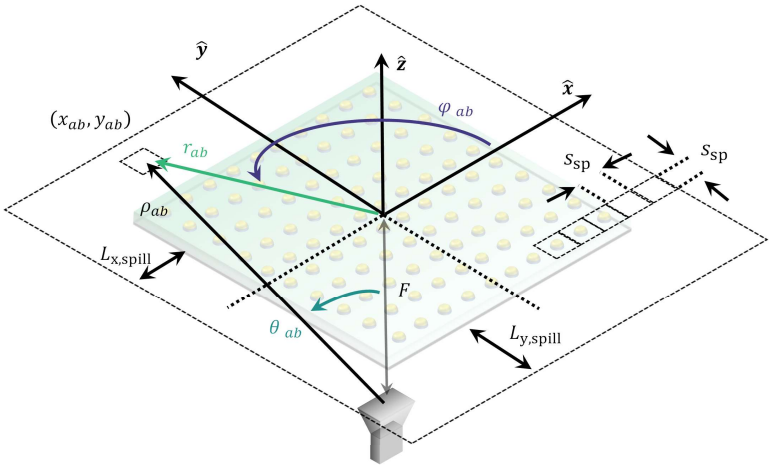

Figure 4.4: Transmitarray array with $M \times N$ squared unit cells having side s_{uc} and located at $z = 0$. The aperture is enlarged on both of its sides along $\hat{\mathbf{x}}$ by $L_{x,spill}$. The same is performed along $\hat{\mathbf{y}}$ by $L_{y,spill}$. The white space around the array delimited by dashed line is discretized by squared cells of side s_{spill} whose position, with respect to the source, is determined by the angle θ_{ab} and distance ρ_{ab}. In Cartesian coordinates, by r_{ab} and φ_{ab}.

The spillover array factor is then computed as follows:

$$AF_{sp}(\theta,\varphi) = \sum_{b=1}^{N_t}\sum_{a=1}^{M_t} u(a,b)\; E_{FS}(a,b)\, e^{j(a-1)(k_x s_{sp})}\, e^{j(b-1)(k_y s_{sp})}, \tag{4.13}$$

where $M_t = M + M_{sp}$ and $N_t = N + N_{sp}$ represent the total number of elements, with M and N being the elements of the array, and M_{sp} and N_{sp} accounting for the spillover elements of side s_{sp}. The function $u(m,n)$ is equal to 1 outside the lens and 0 inside. The total TA field is the sum of the array factor due to the TA cells radiation plus spillover degradation, all multiplied by the radiation pattern of the array element:

$$E_{tot}^{ta}(\theta,\varphi) = \left[AF_{TA}(\theta,\varphi) + AF_{sp}(\theta,\varphi)\right] E_{uc}(\theta,\varphi). \tag{4.14}$$

4.2.4. MODEL FOR THE ANALYSIS OF THE REFLECTED FIELD

The RA model is similar to the TA one with some differences (see Fig. 4.5). First of all, the coordinate system changes: the phase center of the feed lies on the positive z axis differently from Fig. 4.4.

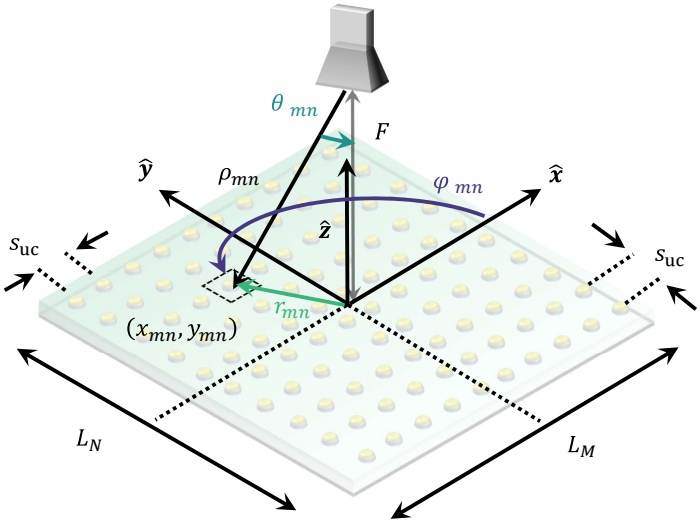

Figure 4.5: Reflectarray array with $M \times N$ squared unit cells having side s_{uc} and located at $z = 0$. The full structure has size $L_M \times L_N$ and the feed is aligned to its center, at a distance F. Each element position, with respect to the source, is determined by the angle θ_{mn} and distance ρ_{mn}. In Cartesian coordinates, by r_{mn} and φ_{mn}.

The array factor considers the complex reflection coefficient Γ of each unit cell instead of τ:

$$AF_{\text{RA}}(\theta,\varphi) = \sum_{n=1}^{N}\sum_{m=1}^{M} \Gamma(m,n)\, E_{\text{FS}}(m,n)\, e^{j(m-1)(k_{\text{x}} s_{\text{uc}})} e^{j(n-1)(k_{\text{y}} s_{\text{uc}})}. \tag{4.15}$$

Then, the complex Γ, as for τ, can be expressed as:

$$\Gamma(m,n) = |\Gamma(m,n)|\, e^{j\angle\Gamma(m,n)}. \tag{4.16}$$

Its magnitude must be equal to $|\Gamma(m,n)| = 0.5$ and its phase must compensate the impinging field phase in order to radiate into the desired direction $(\theta_{\text{st}}^{\text{ra}},\, \varphi_{\text{st}}^{\text{ra}})$:

$$\angle\Gamma(m,n) = -\angle E_{\text{FS}}\,(m,n) - k_{\text{op}} \sin\left(\theta_{\text{st}}^{\text{ra}}\right)\left[x_{\text{mn}} \cos\left(\varphi_{\text{st}}^{\text{ra}}\right) + y_{\text{mn}} \sin\left(\varphi_{\text{st}}^{\text{ra}}\right)\right]. \tag{4.17}$$

The total RA field is due to the array factor multiplied by the radiation pattern of the array element with no effect of the spillover degradation:

$$E_{\text{tot}}^{\text{ra}}(\theta,\varphi) = AF_{\text{RA}}(\theta,\varphi)\, E_{\text{uc}}(\theta,\, \varphi). \tag{4.18}$$

4.2.5. TRANSMIT-REFLECT-ARRAY MODEL

The total field of the TRA consists of contributions from both the transmitted and reflected fields, in the upper and lower hemispheres of the array, respectively.

ES-TRAs have intrinsically low aperture efficiencies η_{ap} with respect to TA or RA antennas of similar sizes, if one considers the radiation in a single half-space. In this work, an alternative definition of the maximum achievable directivity in transmission and in reflection by a TRA is defined as:

$$D = \frac{4\pi A_{ph}}{2\lambda_{op}^2}, \tag{4.19}$$

where A_{ph} is the physical area of the antenna.

Due to the −3 dB drop in the directivity introduced by the array elements to obtain equal power splitting between transmitted and reflected fields, η_{ap} is defined as:

$$\eta_{ap} = \lambda_{op}^2 \frac{2G}{4\pi A_{ph}}. \tag{4.20}$$

This efficiency factor η_{ap} includes losses due to tapering η_t, scan η_{sc}, quantization η_q, spillover η_{sp}, and element η_{uc}:

$$\eta_{ap} = \begin{cases} \eta_t \eta_{sc} \eta_q \eta_{sp} \eta_{uc}^{ta} \\ \\ \eta_t \eta_{sc} \eta_q \eta_{sp} \eta_{uc}^{ra} \end{cases} \tag{4.21}$$

While the loss due to the nonuniform amplitude distribution of the radiating aperture is captured by η_t, the power radiated by the feed that is not intercepted by the array is represented by the spillover degradation factor η_{sp}. Both losses can be directly computed for an axisymmetric feed power pattern, as given in (4.5) [168]. A non-ideal phase distribution across the array introduces quantization loss, η_q. The insertion loss, η_{uc}, of the cells is primarily caused by variations in the scattering parameters of the surface as a function of frequency. The drop in directivity due to the scan angle, η_{sc}, is given by $\eta_{sc} = 10\log_{10}[\cos(\theta_{st})]$.

4.3. UNIT CELLS DESIGN

In this section, the design of four Huygens' cells to realize a TRA with a uniform 2-bit quantization of the full phase range in both transmission and reflection is presented. With this number of bits, the quantization loss is less then 1 dB, without a significant degradation of the scanning performance [169]. First, four desired transmission coefficient phases are selected from solution A in previous chapter: $\phi_{\tau_1} = 15°$, $\phi_{\tau_2} = 105°$, $\phi_{\tau_3} = 195°$ and $\phi_{\tau_4} = 285°$.

Then, the corresponding values of magnetic reactance, X_{m_A}, and electric susceptance, B_{e_A}, are computed using (3.35) and (3.33), respectively. The MS characteristic parameters for each cell are reported in Table 4.2 and shown with markers in Fig. 4.6a. The reflection coefficient phases are shifted by 90° with respect to the transmission ones, as stated in Chapter 3. Their values are reported in Table 4.2, and shown with markers in Fig. 4.6b.

Table 4.2: Phases of the transmission and reflection coefficients, equivalent magnetic impedances and electric admittance, and sheet impedances at 30 GHz of the four H-MS-based TRA cells.

ϕ_τ [Deg]	ϕ_Γ [Deg]	X_m/η_0	$B_e\eta_0$	$\Im\mathfrak{m}\{Z_{s_1}\}$ [Ω]	$\Im\mathfrak{m}\{Z_{s_2}\}$ [Ω]
15	105	0.54	−1.16	167.52	−2128.53
105	195	−1.16	−7.46	−117.17	−82.31
195	285	−7.46	3.46	−215.13	123.76
285	15	3.46	0.54	−415.87	50.61

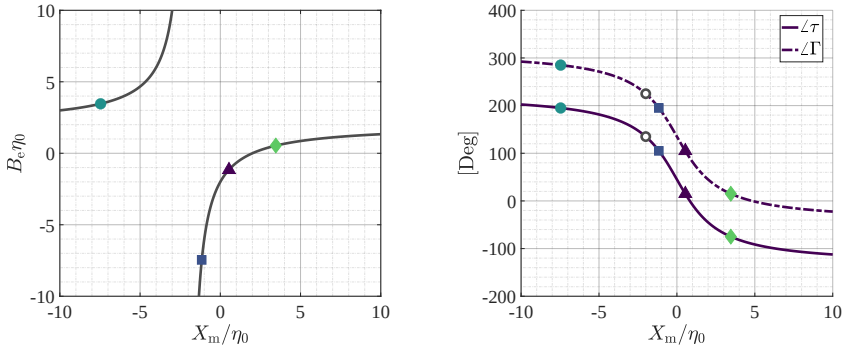

(a) (b)

Figure 4.6: (a) Locus of surface parameters described by (3.33) and (b) phases of transmission and reflection coefficients for this solution. The symbols indicate the characteristics of the four designed unit-cells.

4.3.1. DIELECTRIC SLABS: THICKNESS IMPACT

Each H-MS element is realized as stacked configuration of three impedance sheets interleaved by two dielectric slabs, as shown in Fig. 2.6. While $Z_{s_1} = Z_{s_3}$ for reciprocal and isotropic H-MSs, the presence of Z_{s_2} adds a degree of freedom that allows to independently choose $\angle\tau$ or $\angle\Gamma$ after enforcing a condition on $|\tau|$. Thus, as discussed in Chapter 3, the full phase range in transmission and reflection can be covered.

The variations of Z_{s_1} and Z_{s_2} of each cell reported in Table 4.2 as a function of the slabs thickness with $\varepsilon_{rl} = 2.2$ are shown in Fig. 4.7a and Fig. 4.7b, respectively.

Small slab thicknesses are preferable to maintain the assumption of thin MS. Moreover, for a stable behavior, a sheet impedance frequency variation far from resonances is preferable (see Fig. 4.7). Therefore, a slab permittivity thickness $t = \lambda_g/8$, where $\lambda_g = \lambda_d/\sqrt{\varepsilon_{rl}}$ and λ_d is the free-space wavelength at the design frequency $f_d = 30$ GHz, is chosen. With these parameters, using (3.45a) and (3.46), the pairs of impedance sheets Z_{s_1} and Z_{s_2} shown in Table 4.2 are found for the four TRA cells.

4.3.2. SCATTERING RESPONSE

The scattering parameters of the designed unit cells are computed as functions of frequency, using the transfer-matrix approach, [95], and the equivalent circuit of Fig. 2.6. The values of Z_{s_1} and Z_{s_2} are considered constant with respect to the frequency. The

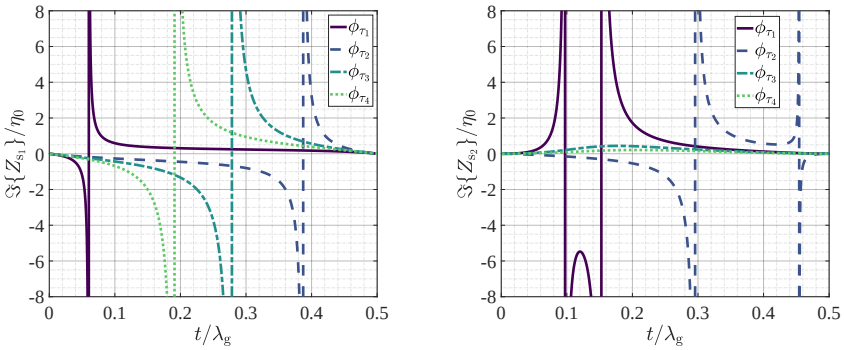

Figure 4.7: Sheet impedance variation as a function of the normalized dielectric slab thickness for each cell reported in Table 4.2: (a) the outer layers Z_{s_1} and (b) the inner layer Z_{s_2}.

4

impact of frequency dispersion introduced by the slabs in the range 28 – 32 GHz is analyzed. The frequency behavior of $|\tau|$ and $|\Gamma|$ is reported in Fig. 4.8.

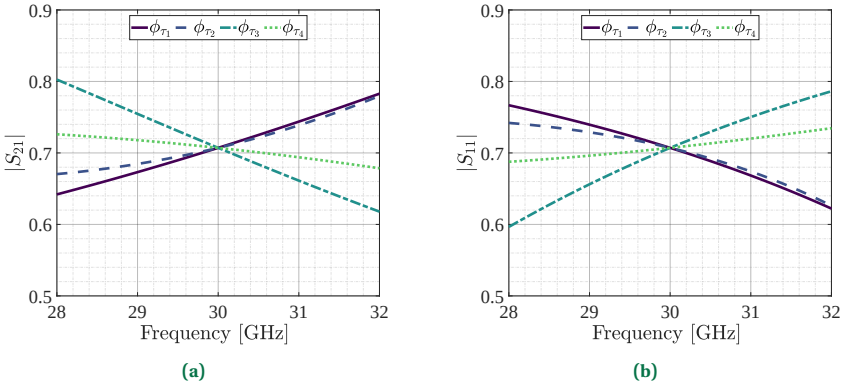

Figure 4.8: Magnitudes of the (a) transmission and (b) reflection coefficients of the TRA cells as functions of frequency.

In a 13% relative bandwidth, the variation in the amplitude of both τ and Γ is only ± 0.5 dB, with respect to their values at the central frequency of 30 GHz. The phases of reflection and transmission coefficients of the four cells are plotted versus frequency in Fig. 4.9. It can be noticed that at 30 GHz, the phases are spaced by exactly 90°. In the considered frequency range, the maximum relative phase error is 8°.

4.3.3. IMPEDANCE SHEET PHYSICAL IMPLEMENTATION

To realize the impedance sheet values reported in Table 4.2, each layer has been engineered singularly using the approach showed in section 3.6 to match with the reference sheet impedance. A periodicity $p = 0.12\lambda_d$ of the elements has been chosen to satisfy the MS condition on small scatterer with respect to the wavelength and to obtain a

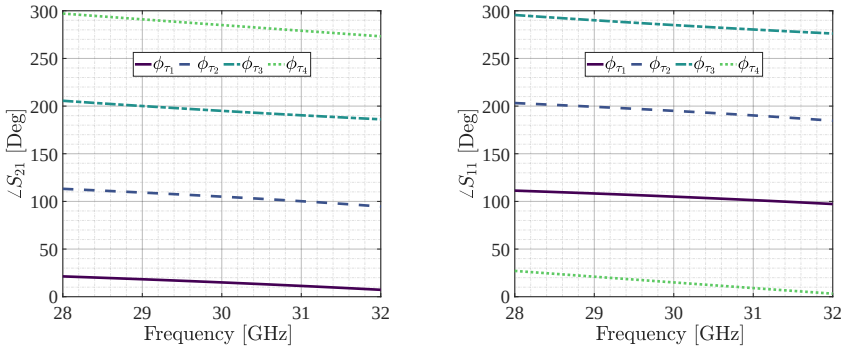

Figure 4.9: Phases of the (a) transmission and (b) reflection coefficients of the TRA cells as functions of frequency.

gradual phase variation (differently from general space fed arrays with $p = 0.5\lambda_d$). The optimized geometries are reported in Fig. 4.10 and 4.11 for the top and middle layer, respectively.

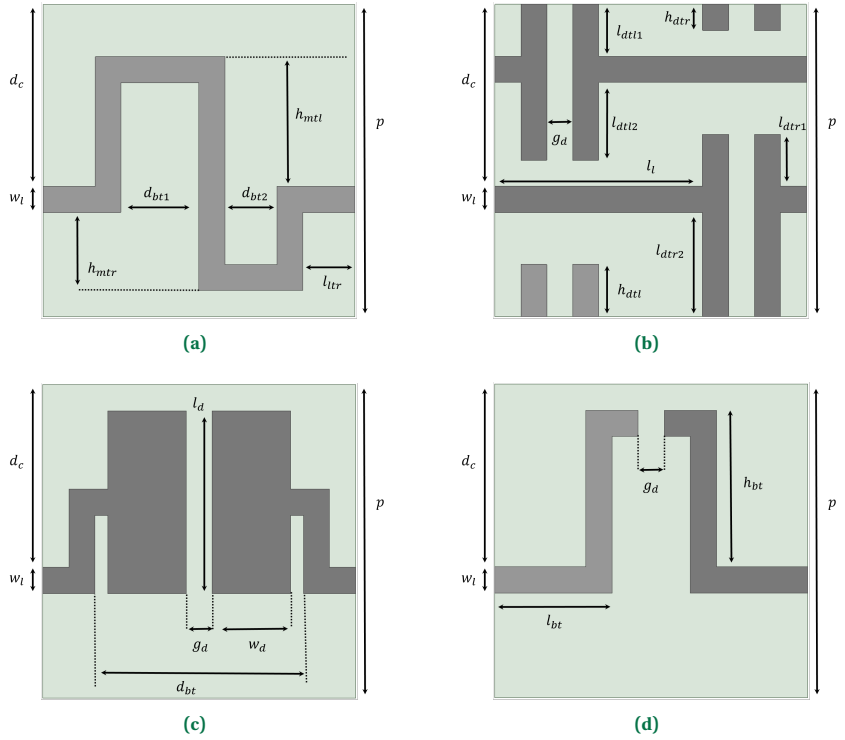

Figure 4.10: Outer layer metal pattern of each cell: (a) $\phi_\tau = 15°$, (b) $\phi_\tau = 105°$, (c) $\phi_\tau = 195°$ and (d) $\phi_\tau = 285°$.

Table 4.3: Metal patterns dimensions for $\phi_\tau = 15°$ H-MS-based TRA cell.

General [mm]		Top and Bottom Layers [mm]						Middle Layer [mm]			
w_l	d_c	d_{bt1}	d_{bt2}	h_{tmr}	h_{tml}	l_{tr}	g_{mm1}	g_{mm2}	l_{mm}	h_{bm}	l_{ml}
0.10	0.70	0.30	0.20	0.30	0.50	0.20	0.20	0.15	0.60	0.40	0.05

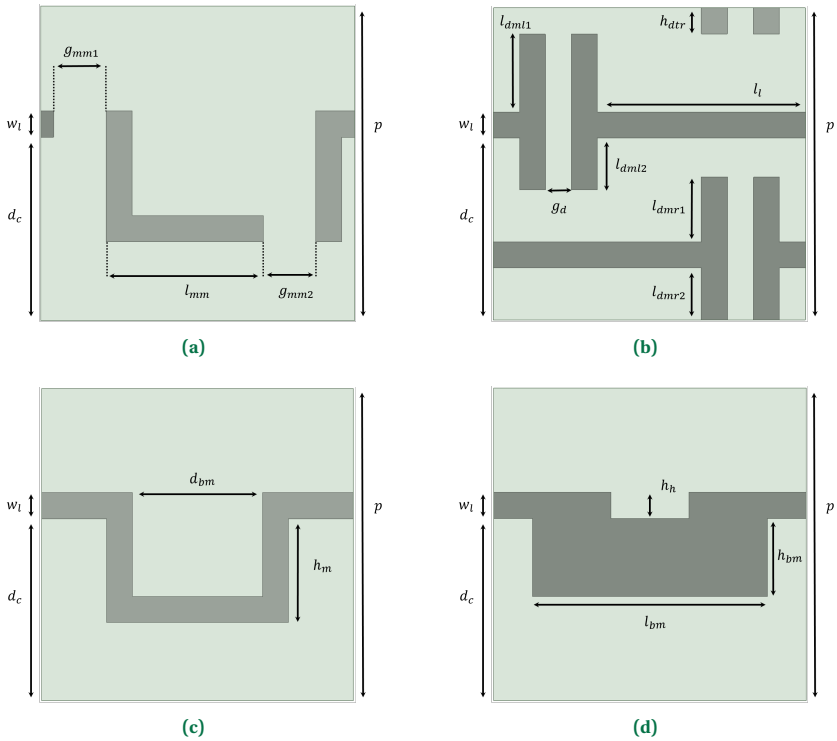

Figure 4.11: Inner layer metal pattern of each cell: (a) $\phi_\tau = 15°$, (b) $\phi_\tau = 105°$, (c) $\phi_\tau = 195°$ and (d) $\phi_\tau = 285°$.

The dimensions reported in Table 4.3, 4.4, 4.5 and 4.6 refer to the metal patterns of cell $\phi_\tau = 15°$, $\phi_\tau = 105°$, $\phi_\tau = 195°$ and $\phi_\tau = 285°$, respectively. The realized sheet impedance values at 30 GHz are reported in Table 4.7. It can be noted that the design values are very close to the reference ones.

Table 4.4: Metal patterns values for $\phi_\tau = 105°$ H-MS-based TRA cell.

General [mm]				Top and Bottom Layers [mm]						Middle Layer [mm]				
w_l	d_c	g_d	l_l	h_{dtr}	h_{dtl}	l_{dtr1}	l_{dtr2}	l_{dtl1}	l_{dtl2}	h_{dmr}	l_{dmr1}	l_{dmr2}	l_{dml1}	l_{dml2}
0.10	0.70	0.10	0.80	0.10	0.20	0.20	0.40	0.20	0.30	0.10	0.25	0.20	0.30	0.20

Table 4.5: Metal patterns values for $\phi_\tau = 195°$ H-MS-based TRA cell.

General [mm]		Top and Bottom Layers [mm]				Middle Layer [mm]	
w_l	d_c	d_{bt}	g_d	w_d	l_d	d_{bm}	h_m
0.10	0.70	0.90	0.10	0.30	0.70	0.50	0.40

Table 4.6: Metal patterns values for $\phi_\tau = 285°$ H-MS-based TRA cell.

General [mm]		Top and Bottom Layers [mm]			Middle Layer [mm]		
w_l	d_c	l_{bt}	g_d	h_{bt}	l_{bm}	h_{bm}	h_h
0.10	0.70	0.60	0.45	0.10	0.90	0.30	0.10

Table 4.7: Sheet impedances at 30 GHz of each H-MS-based TRA cells.

	$\Im\mathfrak{m}\{Z_{s_1}\}$ [Ω]		$\Im\mathfrak{m}\{Z_{s_2}\}$ [Ω]	
ϕ_τ [deg]	Theoretic	Designed	Theoretic	Designed
15	167.52	172.58	−2128.53	−2196.76
105	−117.17	−114	−82.31	−97.09
195	−215.13	−218.50	123.76	121.39
285	−415.87	−421.41	50.61	56.11

Then the complete cells have been simulated to check their scattering response. The full wave amplitudes of the reflection and transmission coefficients of the four designed cells are plotted in Fig. 4.12b and Fig. 4.12a as functions of frequency, respectively. They are all very close to −3 dB at f_d, as prescribed by the design procedure. In a 5% relative bandwidth centered at 30 GHz, they are all between −4 dB and −2 dB. The bandwidth is mainly limited by the frequency variation of the designed sheet impedances. In the same band, the relative phase shifts introduced by different cells, in transmission and reflection, are approximately multiples of 90°, as shown in Fig. 4.13b and Fig. 4.13a, respectively.

4.3.4. Oblique Incidence

Another important factor to take into account when designing space fed arrays is the oblique incidence degradation of the scattering parameter amplitude and phase. Each element supports a y-polarized field due to their geometrical design. To verify each cell robustness to oblique incidence, full wave simulations of y-polarized plane waves with incident angle θ_{ob} varying between 0° and 50° illuminating the elements have been studied. For the sake of brevity,only the amplitude degradation of the scattering coefficients for the less robust cell, $\phi_\tau = 195°$, is reported in Fig. 4.14.

The transmission coefficient amplitude shows a big variation from $\theta_{ob} = 10°$ till 30° at 30 GHz. For this angle, $|S_{21}|$ is equal to −1.3 dB. On the other hand, the $|S_{11}|$ shows a drop of more than −3 dB at 30 GHz when $\theta_{ob} = 50°$. From the viewpoint of TRA design, it

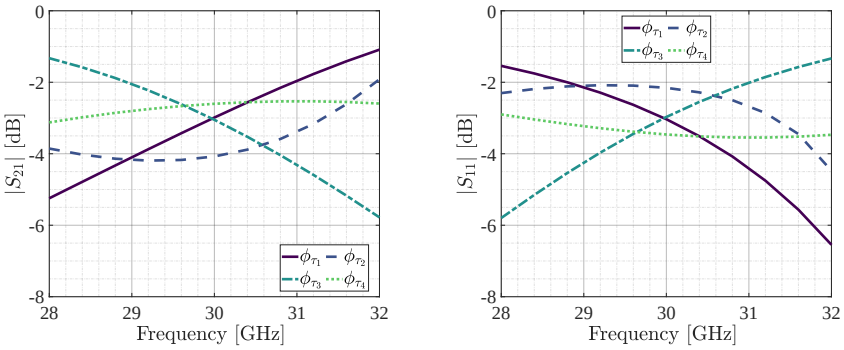

(a) (b)

Figure 4.12: Full wave simulated amplitudes of the (a) transmission and (b) reflection coefficients of the TRA cells as functions of frequency.

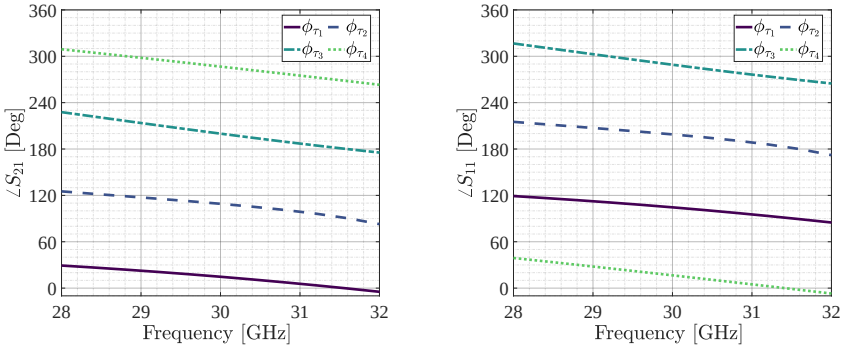

(a) (b)

Figure 4.13: Full wave simulated phases of the (a) transmission and (b) reflection coefficients of the TRA cells as functions of frequency.

would be best to place this cell in the central region of the array to avoid incidence angles greater than 20°. The scattering phases variation due to θ_{ob} are shown in Fig. 4.14. The values of $\angle S_{21}$ and $\angle S_{11}$ present a maximum variation of 40° at 30 GHz. Nevertheless, it remains within the quantization error. For completeness The scattering coefficients of the other cells are reported in Appendix A.

4.3.5. FABRICATION CONSTRAINTS

With the aim of manufacturing TRA prototypes with planar multilayer fabrication technology, e.g. PCB, it is necessary to make some considerations about the physical realization of the array elements. First of all, a pivotal issue is the dielectric availability at the manufacturer's stock. Roger RT5880 substrates having thickness $t = 0.787$ mm and $\varepsilon_{rl} = 2.2$ were available in the warehouse. They are characterized by an electrodeposited copper foils with thickness of 18 μm. In the previous elements design, spacers

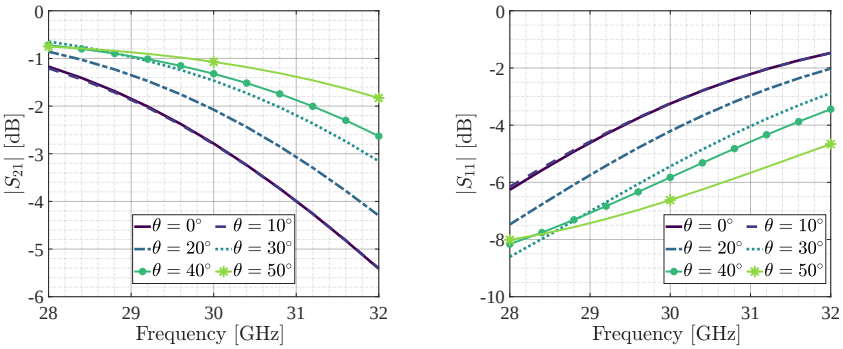

(a) (b)

Figure 4.14: Full wave simulated amplitudes of the (a) transmission and (b) reflection coefficients as functions of frequency and angle of incidence θ_{ob} of the impinging plane wave for $\phi_\tau = 195°$.

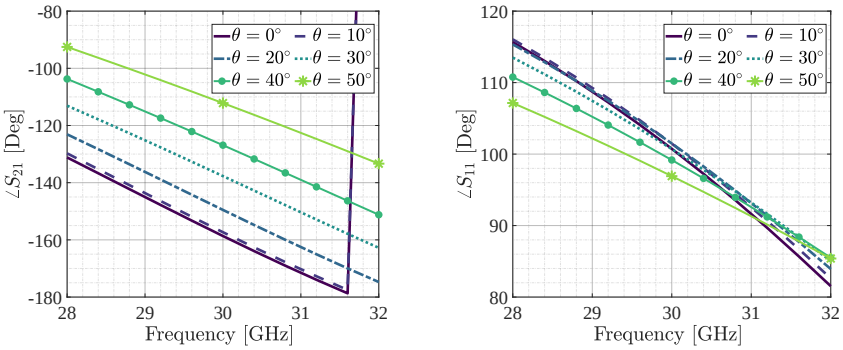

(a) (b)

Figure 4.15: Full wave simulated phases of the (a) transmission and (b) reflection coefficients as functions of frequency and angle of incidence θ_{ob} of the impinging plane wave for $\phi_\tau = 195°$.

with height of $t = 0.84$ mm have been considered. Then, by setting $t = 0.787$ mm in the evaluation of Z_{s_1}, in (3.45a), and Z_{s_2}, in (3.46), different sheet impedances values are obtained and they are reported in Table 4.8.

Table 4.8: Sheet impedances at 30 GHz of the H-MS-based TRA cells having slab thickness $t = 0.787$ mm.

	$\Im\mathrm{m}\{Z_{s_1}\}$ [Ω]		$\Im\mathrm{m}\{Z_{s_2}\}$ [Ω]	
ϕ_τ [deg]	**Theoretic**	**Designed**	**Theoretic**	**Designed**
15	180.45	178.47	−2095.68	−2890.80
105	−111.58	−104.95	−74.11	−89.06
195	−197.01	−216.31	110.48	112.73
285	−353.10	−397.48	45.32	59.45

To stick together the dielectric slabs, according to the manufacturer suggestion to achieve a better substrate alignment, Taconic FR−27 − 0040 − 43F prepreg having thickness $t' = 100\,\mu$m and $\varepsilon_{rp} = 2.77$ has been employed. Due to its small height, lower then $0.07\lambda_g$, it can be considered negligible in the sheet impedance computation with the transfer matrix approach. However, in the full wave extraction of Z_{s_2}, the prepreg presence has been considered following the simulation setup reported in Fig. 3.13.

It is clear that only the Z_s of the middle layer is affected by the prepreg presence. To match the new theoretic sheet impedances reported in Table 4.8, the metal patterns in Fig. 4.11 have been re-optimized. Whereas the cell middle layer for $\phi_\tau = 195°$ already has a good match with the reference value (see Table 4.8), the other three cases underwent minor changes. In particular, for $\phi_\tau = 105°$, the following dimensions have been changed: $l_{dml1} = l_{dml2} = 0.20\,$mm and $l_{dmr1} = 0.15\,$mm. For $\phi_\tau = 285°$, the variation affected only $h_h = 0.20\,$mm. More adjustments have been introduced in the metal pattern of the $\phi_\tau = 15°$ where the affected dimensions changed to $l_{lml} = 0.10\,$mm, $g_{mm1} = 0.15\,$mm, $l_{mm} = 0.30\,$mm and $g_{mm2} = 0.40\,$mm. The remaining space has been filled with a small bend of $l_{mm2} = 0.20\,$mm as shown in the complete cell reported in Fig. 4.17a. The designed sheet impedances at 30 GHz are reported in Table 4.8 while their variation in the 28 − 32 GHz range is shown in Fig. 4.16.

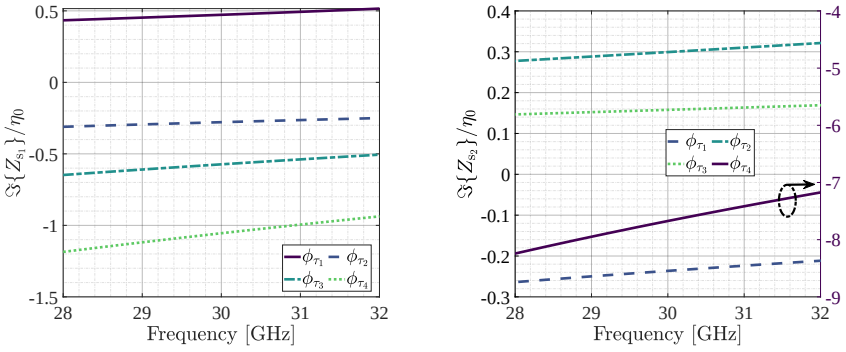

Figure 4.16: Elements sheet impedance patterns variation as a function of frequency after the re-optimization to use the commercially available substrates and prepreg: (a) external and (b) internal layers.

The final design of the four cells are shown in Fig. 4.17. The full wave amplitudes of the transmission and reflection coefficients of the four designed cells are plotted in Fig. 4.18a and Fig. 4.18b as functions of frequency, respectively.

They are all very close to −3 dB at f_d, as prescribed by the design procedure. In a 5% relative bandwidth centered at 30 GHz, they are all between −4 dB and −2 dB. The bandwidth is mainly limited by the frequency variation of the designed sheet impedances. In the same band, the relative phase shifts introduced by different cells, in transmission and reflection, are approximately multiples of 90°, as shown in Fig. 4.19a and Fig. 4.19b, respectively.

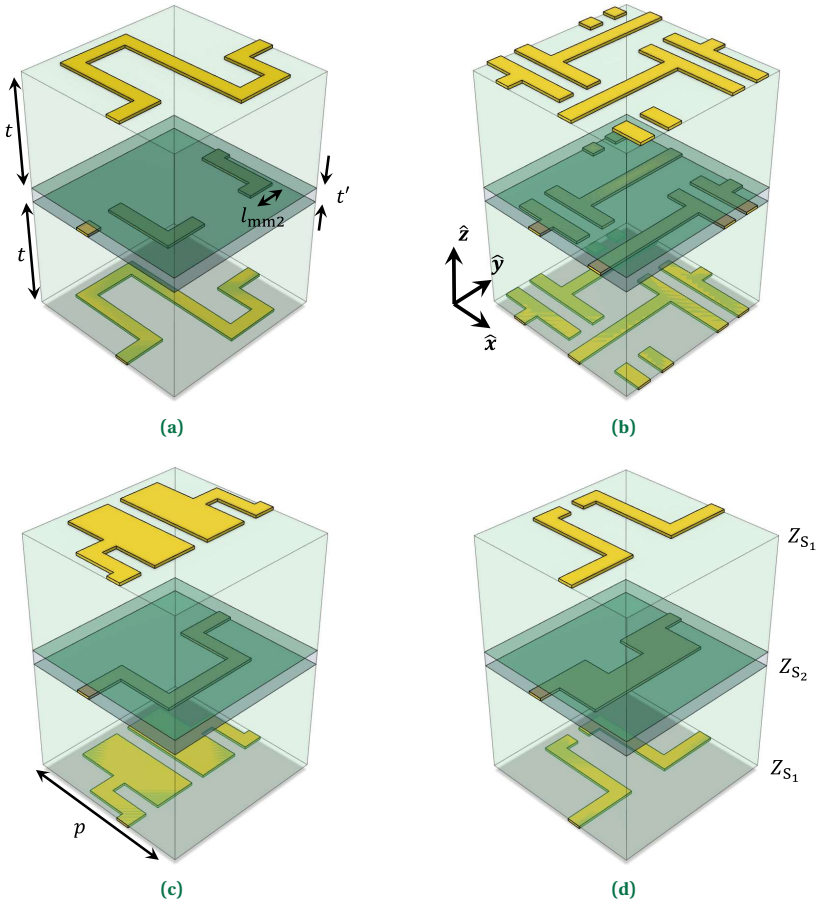

Figure 4.17: Designed TRA cells, with a period $p = 1.2$ mm, implementing at 30 GHz, in transmission, a phase shift of: (a) $\phi_{\tau_1} = 15°$, (b) $\phi_{\tau_2} = 105°$, (c) $\phi_{\tau_3} = 195°$ and (d) $\phi_{\tau_4} = 285°$. The thicknesses of substrates and bonding layers are $t = 0.787$ mm and $t' = 100\,\mu$m respectively.

4.4. Transmit-Reflect-Array Design

Based on the physical optics and array theory model presented in section 4.2, a tool to analyze the performances of several TRAs with different steering angles and aperture sizes has been developed. The radiation characteristics of the source reported in Table 4.1 have been employed in the calculations. Moreover, both transmission and reflection coefficients variations under oblique incidence, reported in subsection 4.3.4, have been considered in the far field computation. These values have been computed considering a y-polarized plane wave and several angles of incidence in the plane $\varphi = 90°$. The angular responses of all cellshave been assumed independent of the azimuthal plane.

The free space wavelength λ_d is defined at the design frequency $f_d = 30$ GHz. The tool results are compared with those obtained with a commercial full-wave solver. A preliminary parametric analysis on the focal distance has been performed. The field

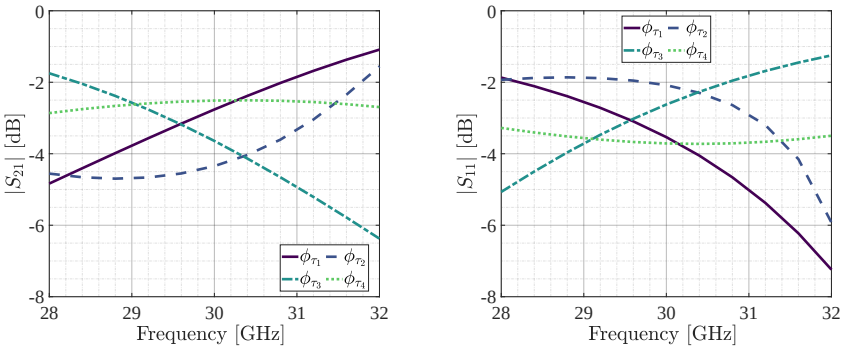

Figure 4.18: Full wave simulated magnitudes of the (a) transmission and (b) reflection coefficients of the TRA cells reported in Fig. 4.17 as functions of frequency.

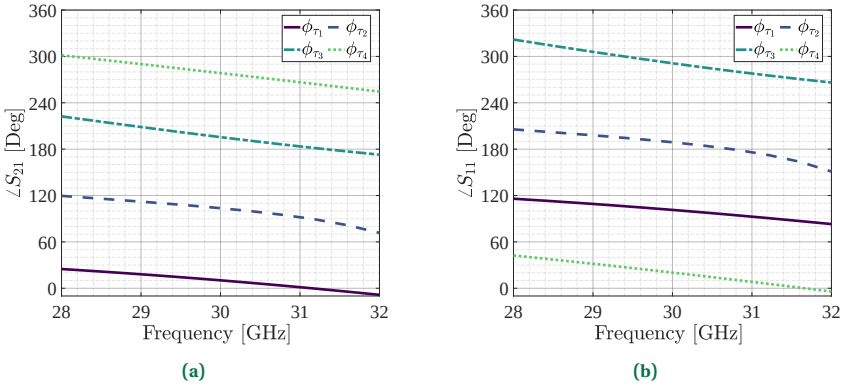

Figure 4.19: Full wave simulated phases of the (a) transmission and (b) reflection coefficients of the TRA cells reported in Fig. 4.17 as functions of frequency.

magnitude of the *ATM* 10 dBi gain horn and its incident phase on the array are reported in Fig. 4.20.

As first scenario, a broadside radiation, an ideal phase compensation on the array and $|\tau| = |\Gamma| = 1/\sqrt{2}$ for all cells have been considered. The taper and spillover losses are shown together with the aperture efficiency in Fig. 4.21a. The computed directivity and gain are reported in Fig. 4.21b.

The optimum F/D ratio to achieve the highest aperture efficiency is obtained for $F = 41.76$ mm, corresponding to $F/D = 0.58$. At this point, the gain in transmission and reflection are both $G = 23$ dBi and the aperture efficiency is $\eta_{ap} = 70\%$. However, by slightly increasing the focal distance, the gain bandwidth improves, although this introduces additional spillover losses [170]. For this reason, an $F/D = 0.67$ has been considered in the following design examples and the prototypes shown in section 4.5. Next, the scanning performance of several TRAs working at $f_d = 30$ GHz and designed with the four proposed H-MS cells are investigated. The TRAs have the same size ($D = 7.2\lambda_d$),

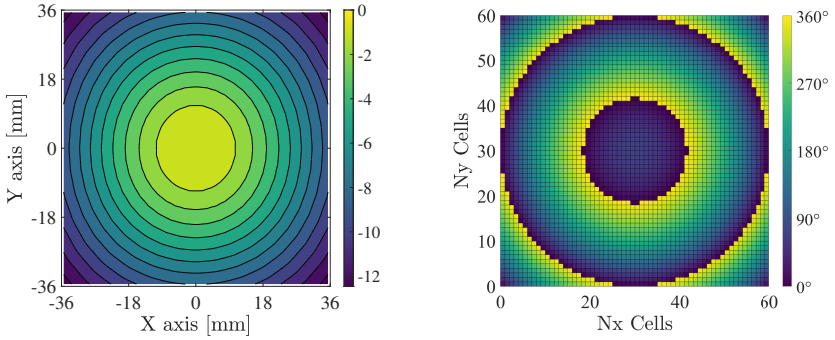

Figure 4.20: Field of the 10 dBi gain horn field intercepted by the TRA: (a) normalized magnitude on its maximum in dB and (b) incident phase.

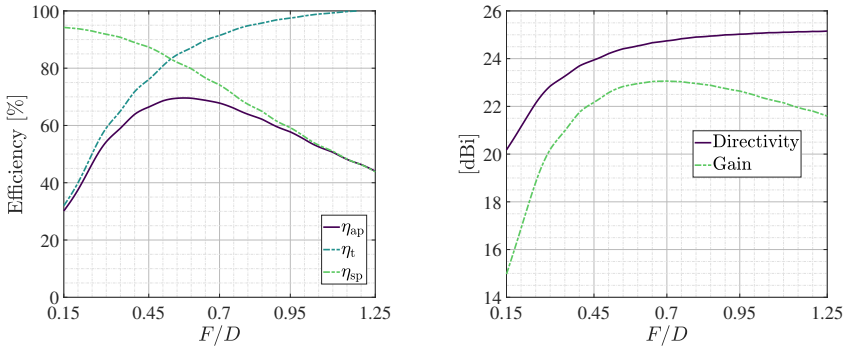

Figure 4.21: Impact of the focal-to -diameter ratio effect on a broadside TRA: (a) aperture, spillover and taper losses and (b) directivity and gain.

focal distance $F = 0.67D$ and are illuminated by the aforementioned 10 dBi horn feed. They are optimized at F/D to steer the transmitted beam at several angles, up to the horizon, in the plane $\varphi = 0°$. Results obtained with the numerical tool are presented along with full-wave simulations.

4.4.1. STEERING AT $\theta^{ta} = 15°$ AND $\varphi^{ta} = 0°$

First, a 60×60 elements TRA working at 30 GHz is considered. It steers the beam in transmission at $\theta^{ta}_{st} = 15°$ and $\varphi^{ta}_{st} = 0°$. Consequently, the reflected pattern points to $(\theta^{ra}_{st} = 165°, \varphi^{ra}_{st} = 0°)$, because of the constant 90° phase difference between $\angle\tau$ and $\angle\Gamma$ for each H-MS cell, as shown in Fig. 4.6b. The ideal and quantized phase profile in transmission are reported in Fig. 4.22.

A comparison between the total radiated field of the TRA computed analyically and simulated with the full-wave solver Ansys HFSS is reported in Fig. 4.23.

It is possible to observe that a good agreement is obtained between the analytical

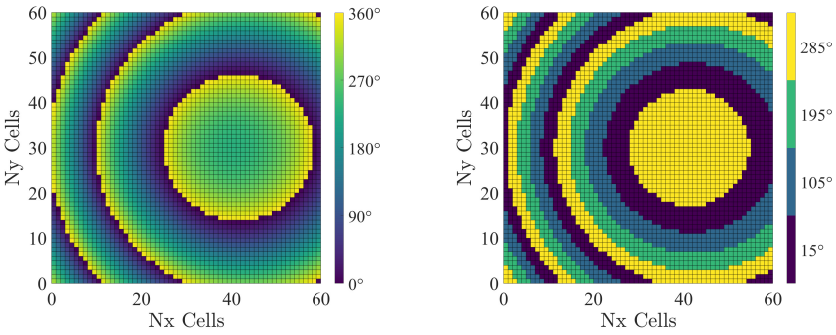

Figure 4.22: Phase distribution on a 60 × 60 elements TRA working at 30 GHz, having focal-to-diameter ratio $F/D = 0.67$ and focusing the radiated beam in transmission at $\theta_{st}^{ta} = 15°$ and $\phi_{st}^{ta} = 0°$: (a) ideal and (b) realized through a uniform 2-bit quantization.

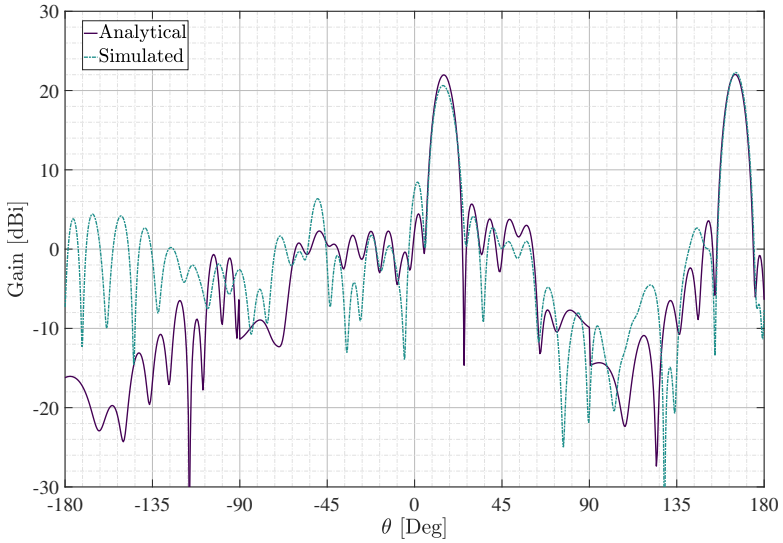

Figure 4.23: Computed and simulated TRA radiation pattern at $\varphi = 0°$ and $f_d = 30$ GHz for steering in transmission at $\theta_{st}^{ta} = 15°$ and $\varphi_{st}^{ta} = 0°$.

and simulated patterns. The maximum achievable gain in transmission derived with the analytical tool is equal to 21.97 dBi corresponding to $\eta_{ap} = 48.31\%$. On the other hand, the backward beam has $G_{max}^{ra} = 22.04$ dBi with a corresponding aperture efficiency of $\eta_{ap} = 49.01\%$. Both maximum values are reached at the nominal steering angles $(15°, 0°)$ and $(165°, 0°)$ for transmission and reflection, respectively. The maximum antenna directivity computed from (4.19) is equal to 25.13 dBi. The gain drop in transmission is due, in part, to the sum of spillover loss (1.2 dB), quantization loss (0.89 dB), amplitude taper loss (0.44 dB) and scan loss (= 0.15 dB). Another factor that impacts on the gain

is the effect of insertion loss, pattern and phase error introduced by the elements. In transmission the average unit-cell insertion loss, computed by averaging the magnitudes of the *transmission* coefficients of the four cells, is 0.48 dB. In reflection, the insertion losses of the cells computed by averaging the magnitudes of the *reflection* coefficients of the four cells, is 0.36 dB. The maximum forward simulated gain is equal to 20.63 dBi at $\theta = 14.65°$ with $\eta_{ap} = 35.48\%$. In reflection, $G^{ra}_{max} = 22.28$ dBi at $\theta = 165.38°$ with a corresponding aperture efficiency of 51.88%.

4.4.2. STEERING AT $\theta^{ta} = 30°$ AND $\varphi^{ta} = 0°$

The following 60 × 60 elements TRA working at $f_d = 30$ GHz has a phase profile to direct the transmitted beam at $\theta^{ta}_{st} = 30°$ and $\varphi^{ta}_{st} = 0°$. A comparison between the ideal and quantized phase distribution introduced by the elements to achieve this steering is reported in Fig. 4.24.

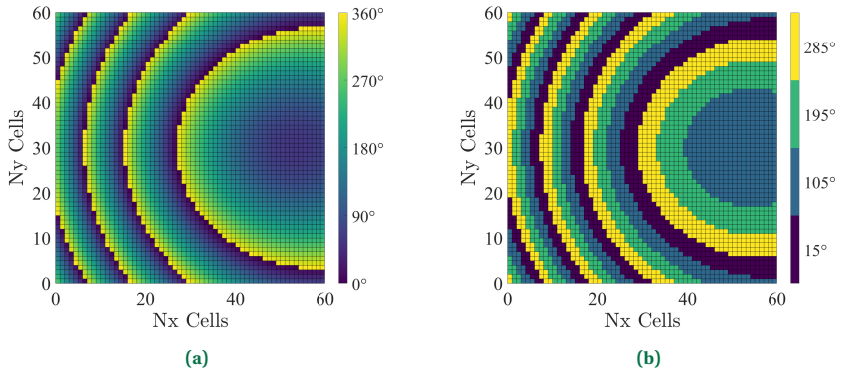

Figure 4.24: Phase distribution on a 60 × 60 elements TRA with focal to diameter ratio $F/D = 0.67$ to focus the radiated beam in transmission at $\theta^{ta}_{st} = 30°$ and $\phi^{ta}_{st} = 0°$: (a) ideal and (b) realized through a uniform 2-bit quantization.

A comparison between analytical and simulated results in the plane $\varphi = 0°$ is reported in Fig. 4.25. Once again, a good agreement between the patterns computed analytically and the simulations is obtained. The maximum gain in transmission derived with the analytical tool is equal to 21.25 dBi at $\theta = 29.5°$ corresponding to $\eta_{ap} = 40.93\%$. This time, the gain drop with respect to the maximum directivity of 25.13 dBi is determined by an additional scan loss (0.6 dB) and the loss due to the cells (average value: 0.6 dB). On the other hand, the reflected beam has $G^{ra}_{max} = 21.64$ dBi at $\theta = 150.5°$ with a corresponding aperture efficiency of $\eta_{ap} = 44.77\%$. In reflection, the average insertion losses of the cells change: 0.32 dB. The maximum simulated gain in transmission is equal to 20.16 dBi at $\theta = 29.1°$ with $\eta_{ap} = 35.89\%$. In reflection, $G^{ra}_{max} = 22.35$ dBi at $\theta = 150.1°$ with a corresponding aperture efficiency of 58.08%.

4.4.3. STEERING AT $\theta^{ta} \geq 60°$ AND $\varphi^{ta} = 0°$

The last 60 × 60 elements TRA working at $f_d = 30$ GHz studied steers the transmitted beam at $\theta^{ta}_{st} = 60°$ and $\varphi^{ta}_{st} = 0°$. The ideal and quantized phase profiles are reported in

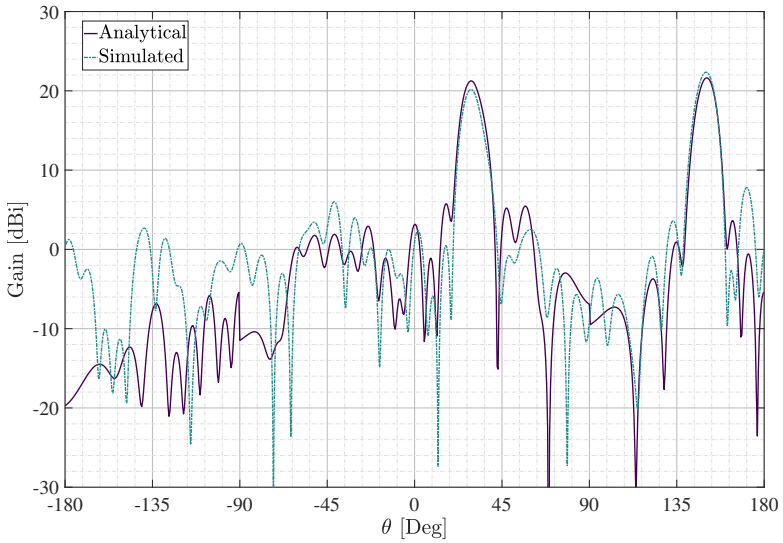

Figure 4.25: Computed and simulated TRA radiation pattern at $\varphi = 0°$ and $f_d = 30\,\text{GHz}$ for steering in transmission at $\theta_{st}^{ta} = 30°$ and $\varphi_{st}^{ta} = 0°$.

Fig. 4.26.

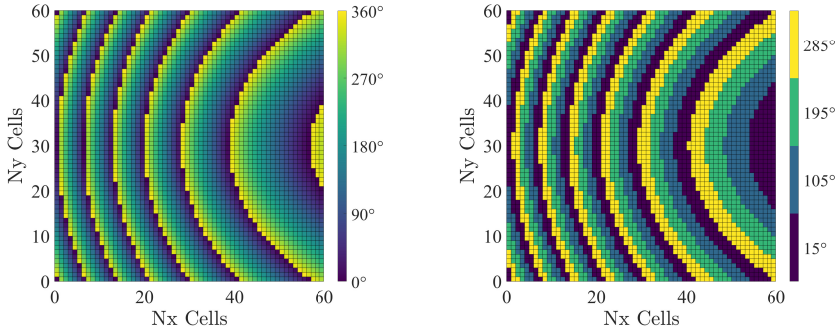

Figure 4.26: Phase distribution on a 60 × 60 elements TRA with focal to diameter ratio $F/D = 0.67$ to focus the radiated beam in transmission at $\theta_{st}^{ta} = 60°$ and $\phi_{st}^{ta} = 0°$: (a) ideal and (b) realized through a uniform 2-bit quantization.

A comparison between the computed data and the simulated results is reported in Fig. 4.27.

Also for this TRA case, a fair agreement between the patterns computed numerically and the simulations is obtained. The maximum achievable gain in transmission derived with the analytical tool is equal to 20.39 dBi at $\theta = 57°$ with $\eta_{ap} = 33.57\%$. This time, the gain drop with respect to the maximum directivity of 25.13 dBi is determined by an

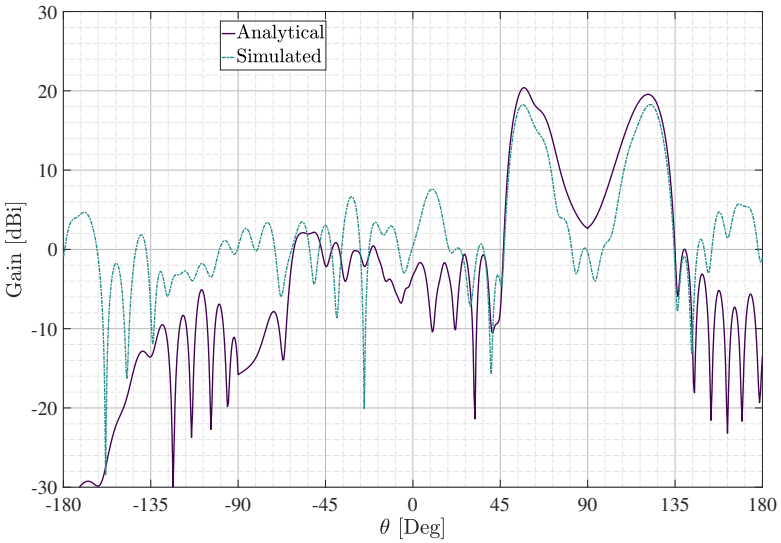

Figure 4.27: Computed and simulated TRA radiation pattern at $\varphi = 0°$ and $f_d = 30\,\text{GHz}$ for steering in transmission at $\theta_{st}^{ta} = 60°$ and $\varphi_{st}^{ta} = 0°$.

increase of the scan loss (3.01 dB) and by the elements 0.3 dB. On the other hand, the reflected beam has $G_{max}^{ra} = 19.56\,\text{dBi}$ at $\theta = 121°$ with a corresponding aperture efficiency of $\eta_{ap} = 27.73\%$. In reflection, the losses due to the cells are very small: 0.1 dB. The maximum forward simulated gain is equal to 18.25 dBi at $\theta = 56.59°$ with $\eta_{ap} = 20.51\%$. In reflection, $G_{max}^{ra} = 18.26\,\text{dBi}$ at $\theta = 122.19°$ with a corresponding aperture efficiency of 20.56%.

It is interesting to observe that, in this last TRA case, the beams are approaching to each other since they are both closer to endfire direction. The gain drop at $\theta = 90°$ is 18 dB lower than the maximum gain in transmission. Then, it is reasonable to imagine that, by increasing the steering angle, this drop can be minimized to achieve a solution where the transmitted and reflected beams merge together to obtain a single endfire beam. In order to test this hypothesis, different designs with steering beams θ_{st}^{ta} varying between 65° and 80° have being analytically computed and validated with full-wave simulations. Their gain pattern cuts at $\varphi = 0°$ are reported in Fig. 4.25.

The radiation pattern computed with the analytical tool achieves a gain drop of 1.8 dB at $\theta = 90°$ when the phase distribution on the array is designed to have $\theta_{st}^{ta} = 80°$. On the other hand, the full-wave analysis shows, for all designs, a dip between the two beams and a degraded quality of the reflected pattern and gain. These effects are probably due to the interference between transmitted and reflected fields, and to diffraction an from the TRA edges, which are not taken into account in the developed analysis tool. Moreover, the actual element patterns of the TRA cells decay more rapidly than the analytical functions used to model them, especially at grazing angles.

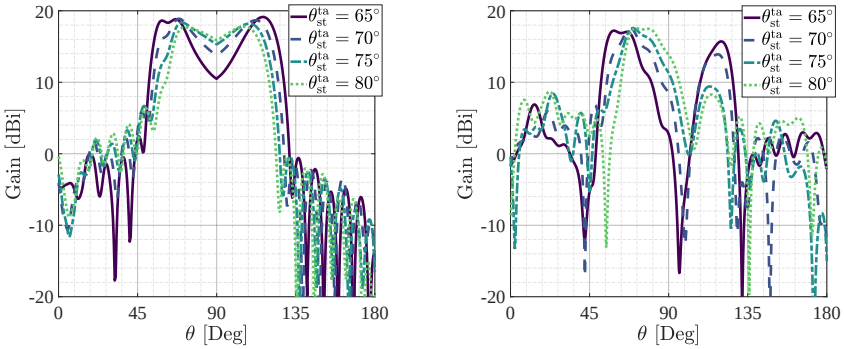

Figure 4.28: Radiation patterns (cut in the plane $\varphi = 0°$) of a 60×60 elements TRA with focal to diameter ratio $F/D = 0.67$ to focus the radiated beam in transmission at $\theta_{st}^{ta} > 60°$ and $\phi_{st}^{ta} = 0°$: (a) analytical and (b) full-wave results.

4

4.5. MEASUREMENTS

To experimentally validate the design of the H-MS unit cells presented in subsection 4.3.5, three prototypes working around 30 GHz with different aperture sizes and similar F/D have been fabricated. All the TRA prototypes are illuminated by a 10 dBi pyramidal horn by ATM (reported in Table 4.1). The sizes of the three radiating apertures are: $7.2 \times 7.2\lambda_d^2$, $9.6 \times 9.6\lambda_d^2$, $14.4 \times 14.4\lambda_d^2$. The focal-to-diameter ratio of the first two antennas is 0.67. The F/D of the third one is 0.69. The phase profiles of all prototypes have been designed to steer the transmitted field at the same scan angle $(\theta = 30°, \varphi = 0°)$, at 30 GHz. The prototypes have been characterized in the anechoic chamber of CEA-Leti (see Fig. 4.29b). A mechanical structure to hold the array feed ad the prototype has been designed and fabricated specifically for this measurement campaign, as shown in Fig. 4.29.

The measurement system comprises a receiving, R_x, and a transmitting, T_x, antenna separated by a distance $r = 3$ m. Each antenna is located in the far field region of the other one. The two antennas are connected to two ports of a vector network analyzer operating up to 70 GHz. In this link, the T_x antenna is a 20 dBi standard gain horn, whereas the Antenna Under Test (AUT) is on the receiving side.

The gain transfer method is employed to evaluate the TRA prototype gain [165]. Before characterizing the AUT, a reference measurement is performed. An antenna of known gain G_h, 20 dBi horn identical to the probe antenna on the T_x end, is used at the receiving side. The received signal level RL when the reference antenna and the T_x horn are aligned is saved as reference. Then, the TRA is placed at the R_x side and tested. A motion system is used to rotate the TRA around a single vertical axis, aligned to the its aperture, so that the radiation pattern is measured for all azimuth angles in the azimuthal plane $\varphi = 0°$. Co-polar and cross-polarization components of the gain patterns have been measured by rotating by 90° the T_x probe. The signal level SL received at R_x can be used to evaluate the prototype gain:

$$G_{dB}^{tra}(\theta,\varphi) = G_{h_{dB}} + \left(SL_{dB}(\theta,\varphi) - RL_{dB}(\theta,\varphi)\right). \tag{4.22}$$

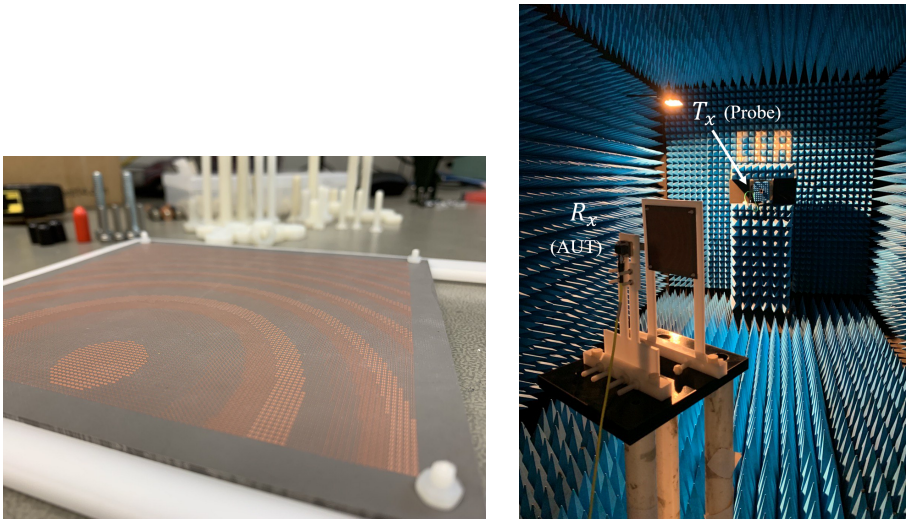

(a) (b)

Figure 4.29: (a) Prototype with $14.4 \times 14.4\lambda_d^2$. (b) Measurement setup in the anechoic chamber.

4.5.1. Transmit-Reflect-array of 60 × 60 elements

The 60 × 60 elements TRA having $F/D = 0.67$ and $\theta_{st}^{ta} = 30°$ and $\varphi_{st}^{ta} = 0°$ has been characterized first. The computed radiation characteristics obtained from the analytical tool have been previously compared with the full-wave results showing a good agreement (see Fig. 4.24). The measured gain pattern at 30 GHz for $\varphi = 0°$ and is compared, as a function of the elevation angle, with the patterns obtained using the proposed numerical tool and a commercial full-wave solver, in Fig. 4.30.

It can be noted that a very good agreement between the three curves is obtained. The measurements agree with the simulated and analytically computed HPBW in transmission of 10°. Moreover, a SLL of −16 dB is obtained. In reflection, the measured HPBW and SLL are equal to 15° and −11 dB, respectively. The differences between the characteristics of reflected and transmitted beams are probably due to the presence of the feed.

The maximum measured gain in transmission is to 22.1 dBi at $\theta = 29.5°$ corresponding to an aperture efficiency of 49.77%. Differently, in reflection, $G_{max}^{ra} = 20.1$ dBi at $\theta = 148.75°$ with $\eta_{ap} = 31.4\%$. There is a difference between the numerical and measured gains of 0.8 dB and 1.5 dB in transmission and reflection, respectively. This discrepancy, may be attributed to slight misalignments betweem the feed and the TRA, fabrication tolerances, as well as to the measurement uncertainty (in the order of ±0.5dB)

The peak gain and aperture efficiency as a function of the frequency are shown in Fig. 4.31a and Fig. 4.31b for the transmitted and reflected radiation patterns, respectively. The maximum measured gain in transmission is 22.3 dBi at 32 GHz, with an aperture efficiency of 45.4%. The 1-dB gain bandwidth covers the frequency range of 29.4 − 32 GHz that is a 8.6% around 30 GHz. The aperture efficiency is greater than 40% in the full

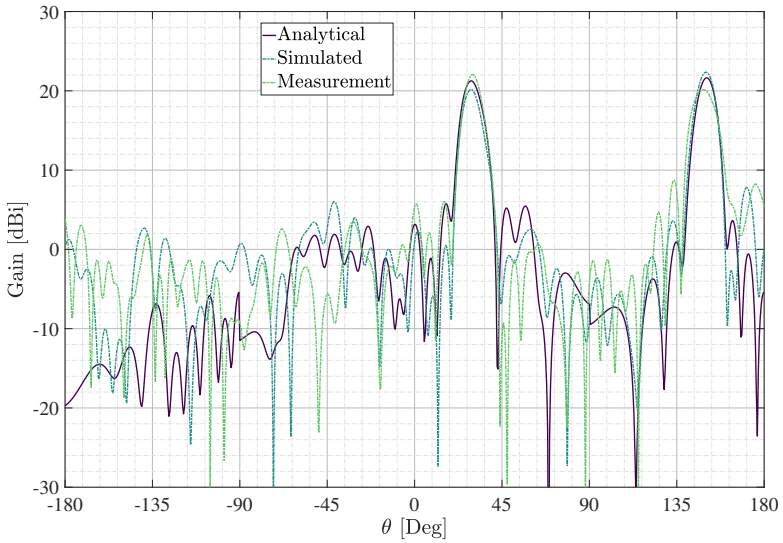

Figure 4.30: Analytically computed, full-wave simulated and measured radiation patterns at $\varphi = 0°$ and $f_d = 30\,\text{GHz}$ of the $7.2 \times 7.2\lambda_d^2$ TRA steering in transmission at $\theta_{st}^{ta} = 30°$ and $\varphi_{st}^{ta} = 0°$.

frequency range of interest (28 – 32 GHz). On the other hand, in reflection, a maximum measured gain of 20.8 dBi is observed at 32 GHz, corresponding to an aperture efficiency of 32.4%. The 1-dB bandwidth covers the frequency range of 29.8 – 32 GHz that is a 7.6% around 30 GHz. The aperture efficiency is greater than 27% between 29 and 32 GHz.

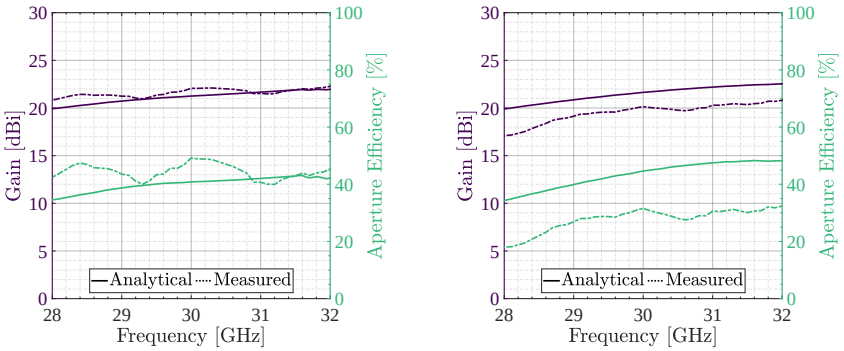

Figure 4.31: Measured and computed values of the peak gain and aperture efficiency of the 60 × 60 elements TRA pointing at $\theta_{st}^{ta} = 30°$ and $\phi_{st}^{ta} = 0°$ as a function of frequency: in (a) transmission and (b) reflection.

In Fig. 4.32, the contour plots of measured and simulated gain as functions of frequency and elevation angles are reported. It is possible to observe that, in the frequency band of interest, from 29 to 31 GHz, the beam-squint remains small and the pattern characteristics are stable.. Moreover, the cross-polarization level has a maximum of

−6 dB in the frequency band, *i.e.* 26 dB less than the co-polarized component.

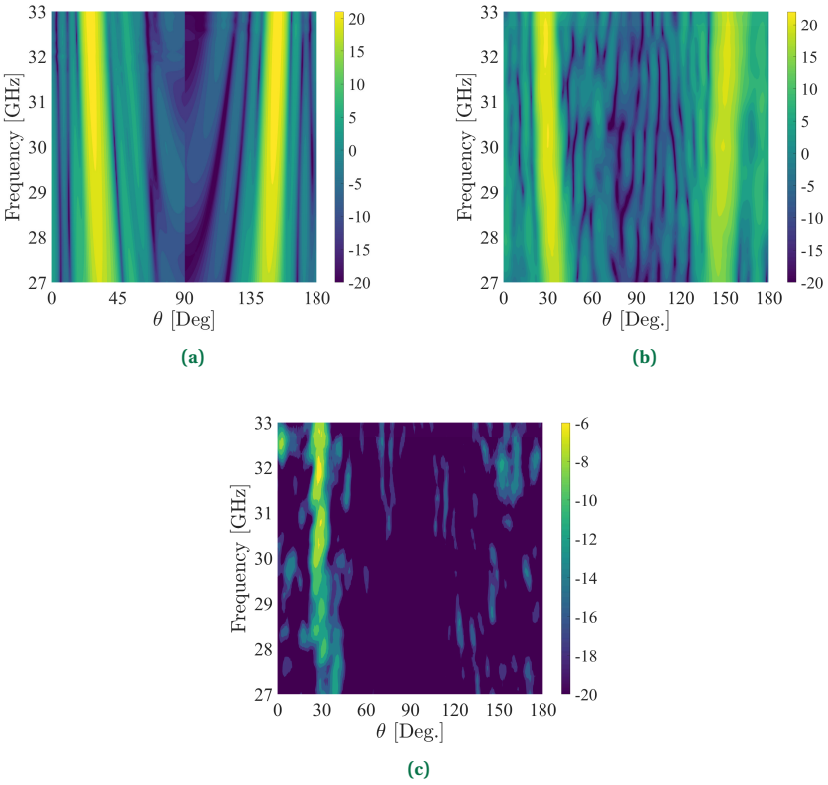

Figure 4.32: Gain patterns $(\varphi = 0°)$ as functions of frequency and elevation angle in dBi of the 60×60 elements TRA pointing at $\theta_{st}^{ta} = 30°$ and $\phi_{st}^{ta} = 0°$ as a function of frequency: (a) analytical and (b) measured. (c) Crosspolar pattern variation.

4.5.2. TRANSMIT-REFLECT-ARRAY OF 80 × 80 ELEMENTS

The second structure considered is the TRAs having aperture size $9.6 \times 9.6\lambda_d^2$. It has been designed to have a focal to diameter ratio of $F/D = 0.67$ to achieve a larger gain bandwidth, as for the TRA solutions with $7.2 \times 7.2\lambda_d^2$ physical area. The tool has been employed to compute the field radiated by the source and the total pattern of the array. The 10dBi *ATM* gain horn illuminates the array with magnitude and phase reported in Fig. 4.33.

The transmitted beam points at $\theta_{st}^{ta} = 30°$ and $\varphi_{st}^{ta} = 0°$. The ideal and quantized phase profiles are reported in Fig. 4.34.

The analytical, simulated and measured data at 30 GHz and $\varphi = 0°$ are shown in Fig. 4.35.

It can be noted that a very good agreement between the three curves is obtained. The maximum gain in transmission derived with the analytical tool is equal to 24.3 dBi

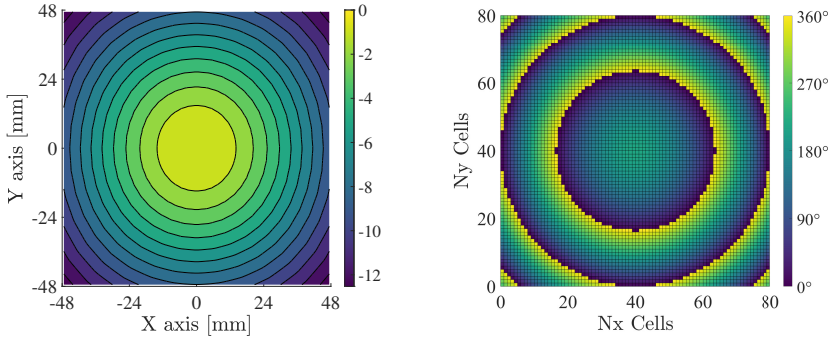

Figure 4.33: Field of the 10 dBi gain horn field intercepted by the 80 × 80 elements TRA: (a) normalized magnitude on its maximum in dB and (b) incident phase.

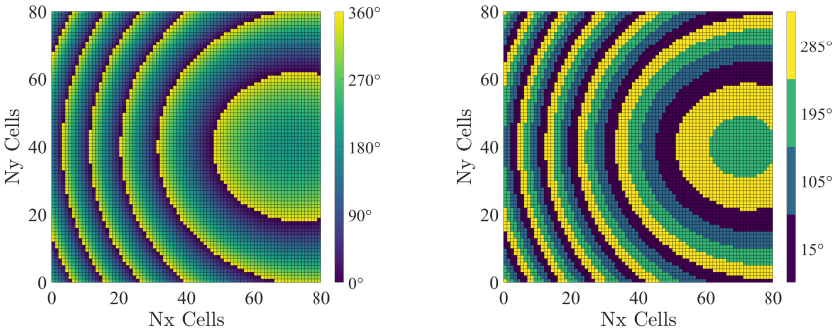

Figure 4.34: Phase distribution on a 80 × 80 elements TRA with focal to diameter ratio $F/D = 0.67$ to focus the radiated beam in transmission at $\theta_{st}^{ta} = 30°$ and $\phi_{st}^{ta} = 0°$: (a) ideal and (b) realized through a uniform 2-bit quantization.

at $\theta = 30°$ with an aperture efficiency of 46.5%, lower then the maximum directivity of 27.63 dBi computed from (4.19). The gain drop in transmission is due to the sum of spillover losses (1.2 dB), quantization losses (0.93 dB), amplitude taper losses (0.45 dB), scan losses (0.63 dB) and the losses in transmission of the unit-cell (average value: 0.1 dB). The simulated pattern shows a maximum gain in transmission equal to 23.4 dBi at $\theta = 29.7°$ with $\eta_{ap} = 37.8\%$. The measured beam shows the same maximum gain of 23.4 dBi. However, a squint in the steering direction is present making the beam to point at $\theta = 31.5°$. Both simulated and measured results agrees on a SLL of −15 dB, while the analytical tool shows a SLL equal to −18 dB. For all three refracted beams, an HPBW of 8° is achieved.

In reflection, the analytically computed beam has $G_{max}^{ra} = 24$ dBi at $\theta = 150°$ with a corresponding aperture efficiency of $\eta_{ap} = 43.4\%$. In this case, the losses of the cells are equal to 0.38 dB. The simulated pattern shows a maximum gain in reflection $G_{max}^{ra} =$

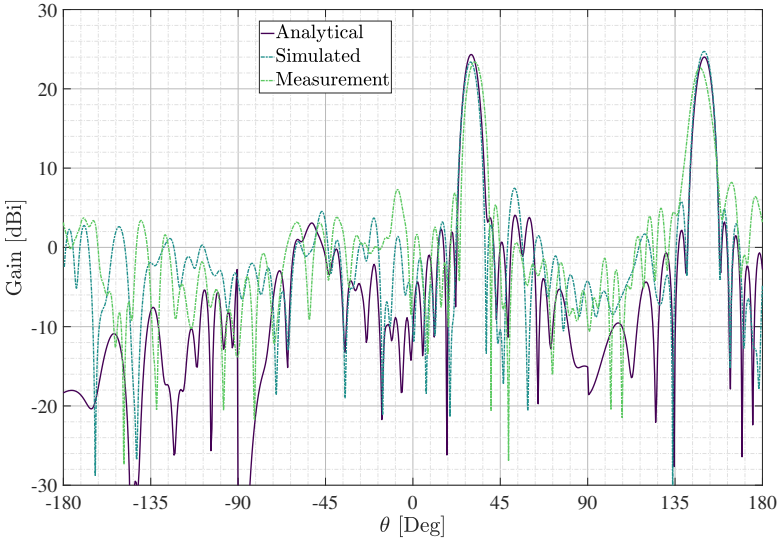

Figure 4.35: Analytically computed, full-wave simulated and measured radiation patterns at $\varphi = 0°$ and $f_d = 30\,\text{GHz}$ for a $9.6 \times 9.6\lambda_d^2$ TRA steering in transmission at $\theta_{st}^{ta} = 30°$ and $\varphi_{st}^{ta} = 0°$.

24.7 dBi at $\theta = 150°$ with a corresponding aperture efficiency of 50.9%. A smaller gain found in the measured data where $G_{max}^{ra} = 22.7\,\text{dBi}$ again with a squint at $\theta = 147.75°$. The maximum aperture efficiency of the reflected beam is 31.9%. A measured SLL of $-14.5\,\text{dB}$ is obtained. The simulation and analytical tool show lower values: $-16.5\,\text{dB}$ and $-19\,\text{dB}$, respectively. This increase is due to the feed blockage effect. For all three curves, an HPBW of 7.5° is achieved.

The peak gain and aperture efficiency as a function of the frequency are shown in Fig. 4.36a and Fig. 4.36b for the transmitted and reflected radiation patterns, respectively. A maximum measured gain in transmission of 23.8 dBi is obtained at 30.8 GHz, with an aperture efficiency of 38.7%. The 1-dB gain bandwidth covers the full frequency range of $28 - 32\,\text{GHz}$ that is a 13.3% around 30 GHz. The aperture efficiency is greater than 35% between 28 and 31 GHz. On the other hand, in reflection, a maximum measured gain of 23.1 dBi is obtained at 31 GHz, with an aperture efficiency of 33%. The 1-dB bandwidth covers the full frequency range of $29.4 - 32\,\text{GHz}$ that is a 8.7% around 30 GHz. The aperture efficiency is greater than 30% between 29.5 and 31.5 GHz.

In Fig. 4.37, the contour plots of measured and simulated gain as functions of frequency and elevation angles are reported. It is possible to observe that, in the frequency band of interest, from 29 to 31 GHz, the beam-squint remains small and the pattern characteristics are stable. Moreover, the cross-polarization level has a maximum of $-2\,\text{dB}$ in the frequency band *i.e.* 25 dB less than the co-polarized component.

4.5.3. TRANSMIT-REFLECT-ARRAY OF 120 × 120 ELEMENTS

The last design and fabricated TRA has aperture size $14.4 \times 14.4\lambda_d^2$. It has been designed to have a focal to diameter ratio of $F/D = 0.69$ to achieve a larger gain bandwidth similar

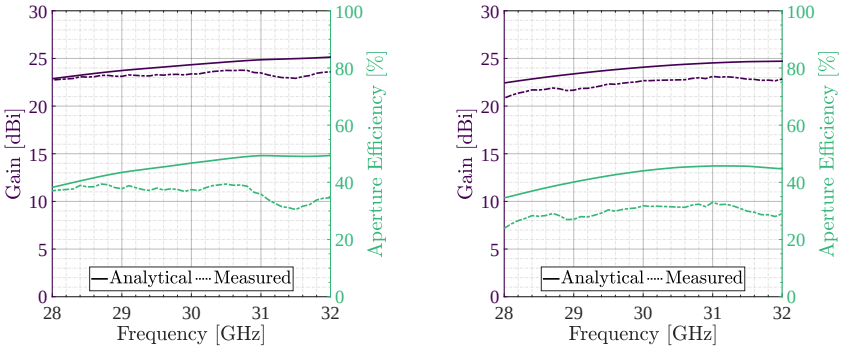

Figure 4.36: Comparison maximum gain and aperture efficiency of the 80 × 80 elements TRA pointing at $\theta_{st}^{ta} = 30°$ and $\phi_{st}^{ta} = 0°$ as a function of frequency: in (a) transmission and (b) reflection.

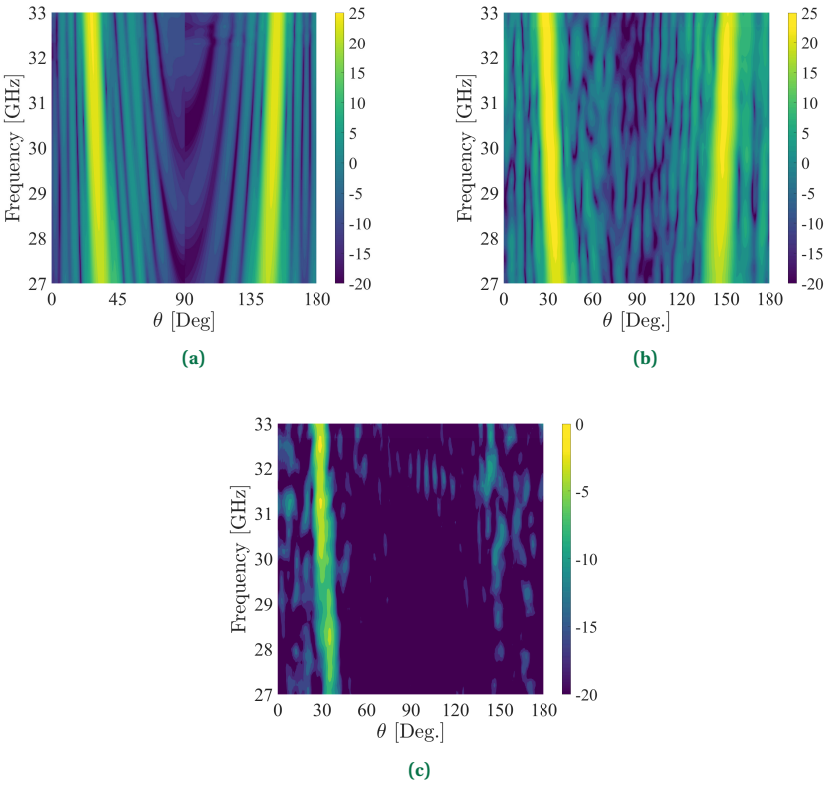

Figure 4.37: Gain patterns $(\varphi = 0°)$ as functions of frequency and elevation angle in dBi of the 80 × 80 elements TRA pointing at $\theta_{st}^{ta} = 30°$ and $\phi_{st}^{ta} = 0°$ as a function of frequency: (a) analytical and (b) measured. (c) Crosspolar pattern variation.

to the TRA solutions with physical area size. The tool has been employed to compute the field radiated by the source and the total pattern of the array. The 10 dBi *ATM* gain horn illuminates the array with magnitude and phase reported in Fig. 4.38.

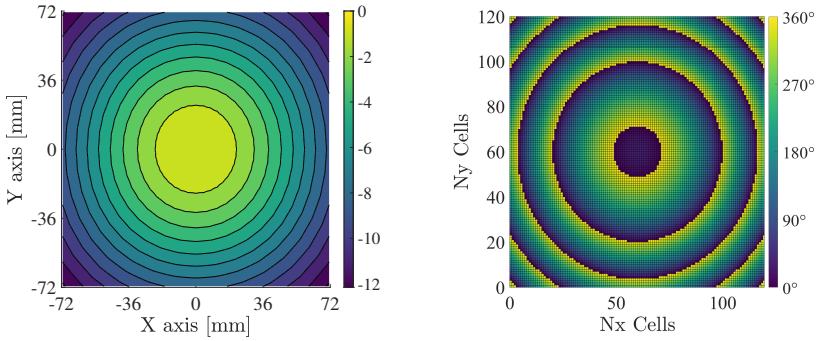

(a) (b)

Figure 4.38: Field of the 10 dBi gain horn field intercepted by the 120 × 120 elements TRA: (a) normalized magnitude on its maximum in dB and (b) incident phase..

The transmitted beam is pointed at $\theta_{st}^{ta} = 30°$ and $\varphi_{st}^{ta} = 0°$. The ideal and quantized phase profiles are reported in Fig. 4.39.

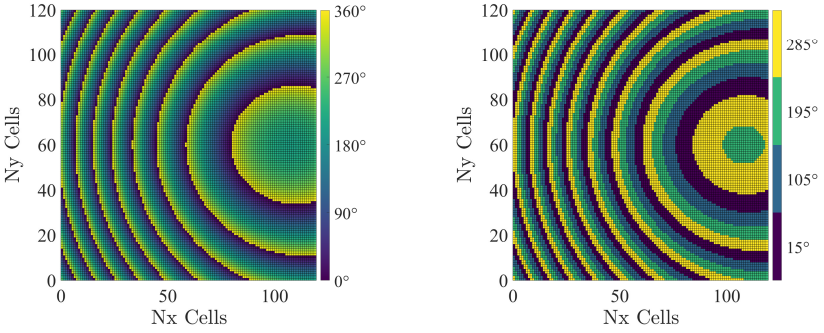

(a) (b)

Figure 4.39: Phase distribution on a 120 × 120 elements TRA with focal to diameter ratio $F/D = 0.67$ to focus the radiated beam in transmission at $\theta_{st}^{ta} = 30°$ and $\phi_{st}^{ta} = 0°$: (a) ideal and (b) realized through a uniform 2-bit quantization.

The full-wave simulation, performed using the frequency-domain solver in CST Microwave Studio Suite with open boundary conditions, required about 700 GB of RAM and several days to complete. However, an underestimation of the peak gain in transmission was obtained due to poor convergence, probably related to the large size of the surface. Then, the measured and analytically computed data at 30 GHz and $\varphi = 0°$ are shown in Fig. 4.40.

It can be noted that a very good agreement between both curves is obtained. The

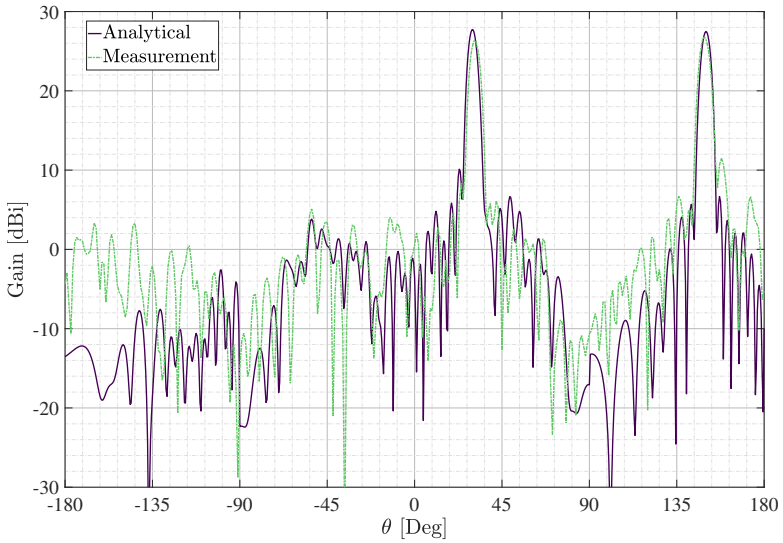

Figure 4.40: Analytically computed, full-wave simulated and measured radiation patterns at $\varphi = 0°$ and $f_d = 30$ GHz for a $14.4 \times 14.4\lambda_d^2$ TRA steering in transmission at $\theta_{st}^{ta} = 30°$ and $\varphi_{st}^{ta} = 0°$.

maximum achievable gain in transmission derived with the numerical tool is equal to 27.7 dBi at $\theta = 30°$ with an aperture efficiency of 45.7 dBi with respect to the maximum directiviy of 31.1 dBi computed from (4.19). The gain drop in transmission is due to the sum of spillover losses (1.2 dB), quantization losses (0.93 dB), amplitude taper losses (0.45 dB), the scan losses (0.63 dB) and the losses in transmission of the unit-cell (average value: 0.2 dB). The measured transmitted beam shows a maximum gain equal to 26.4 dBi with $\eta_{ap} = 36.4\%$. However, a squint in the steering direction is present making the beam to point at $\theta = 31°$. Both analytically computed and measured results agrees on a SLL of -18 dB. For both transmitted beams, an HPBW of 4° is observed.

In reflection, the analytically computed beam has $G_{max}^{ra} = 27.5$ dBi at $\theta = 150°$ with a corresponding aperture efficiency of $\eta_{ap} = 43.7\%$. In this case, the losses of the cells are equal to 0.4 dB. The measured beam presents a maximum gain of 26.7 dBi with a squint at $\theta = 149°$. The maximum aperture efficiency of the reflected beam is 36.3%. A measured SLL of -14.5 dB is obtained. The analytical tool shows a lower value: -14 dB. This increase is due to the feed blockage effect. For both curves, a HPBW of 5° is achieved.

The peak gain and aperture efficiency as a function of the frequency are shown in Fig. 4.41a and Fig. 4.41b for the transmitted and reflected radiation patterns, respectively. A maximum measured gain in transmission of 26.6 dBi is obtained at 30.8 GHz, with an aperture efficiency of 32.8%. The 1-dB gain bandwidth covers the frequency range of 29.1 – 32 GHz that is a 10% around 30 GHz. The aperture efficiency is greater than 30% between 29.1 and 31.6 GHz. In reflection, a maximum measured gain of 27.2 dBi is obtained at 30.8 GHz, with an aperture efficiency of 38%. The 1-dB bandwidth covers the frequency range of 29.5 – 32 GHz that is a 8.3% around 30 GHz. The aperture efficiency is greater than 30% between 29.2 and 32 GHz.

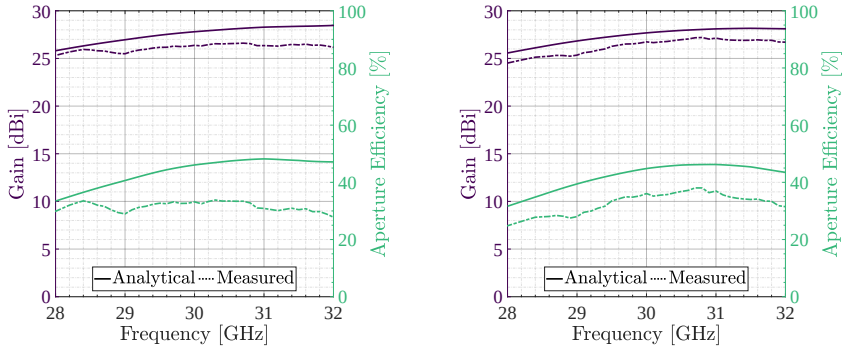

Figure 4.41: Measured and computed values of the peak gain and aperture efficiency of the 120 × 120 elements TRA pointing at $\theta_{st}^{ta} = 30°$ and $\phi_{st}^{ta} = 0°$ as a function of frequency: in (a) transmission and (b) reflection.

In Fig. 4.42, the contour plots of measured and simulated gain as functions of frequency and elevation angles are reported. It is possible to observe that, in the frequency band of interest, from 29 to 31 GHz, the beam-squint remains small and the pattern characteristics are stable. Moreover, the cross-polarization level has a maximum of −4 dB in the frequency band *i.e.* 30 dB less than the co-polarized component.

4.6. LITERATURE COMPARISON

A comparison between the performances of the measured prototypes and two state-of-the-art ES-TRAs presented in Chapter 2 is reported in Table 4.9. The prototypes shows good performances in terms of gain and aperture efficiency for the beamin transmission and reflection. Indeed better performances are obtained with respect to [48]. However, a lower aperture efficiency is obtained with respect to [127]. It's important to note that these works use elements with a bi-anisotropic response, enabling polarization conversion. Additionally, no quantization loss is considered due to the ideal phase distribution on the surface.

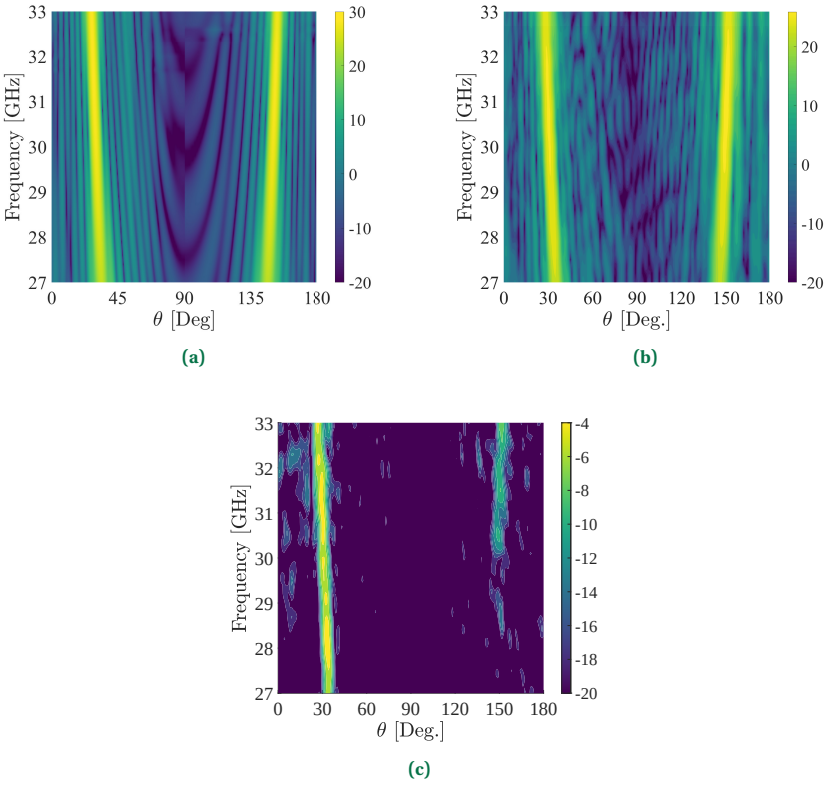

Figure 4.42: Gain patterns $(\varphi = 0°)$ as functions of frequency and elevation angle in dBi of the 120×120 elements TRA pointing at $\theta_{st}^{ta} = 30°$ and $\phi_{st}^{ta} = 0°$ as a function of frequency: (a) analytical and (b) measured. (c) Crosspolar pattern variation.

Table 4.9: Comparison between the three measured prototypes with two state-of-the-art TRAs.

Ref.	Array area $[mm^2]$	F/D	FBW [GHz]	Transmitted					Reflected				
				G_{max} [dBi]	η_{ap} [%]	1 dB GBW [%]	$(\theta_{st}, \varphi_{st})$ [Deg]	SLL [dB]	G_{max} [dBi]	η_{ap} [%]	1 dB GBW [%]	$(\theta_{st}, \varphi_{st})$ [Deg]	SLL [dB]
[48]	420 × 420	–	9 – 11	25.5	29	15	(0,0)	−19.8	25	26	14	(180,0)	−18.4
[127]	79.5 × 63.6	1.07	22 – 34	22	60	18.2	(0,0)	–	21.5	59	24.6	(180,0)	–
This work	72 × 72	0.67	28 – 32	22.3	45.4	8.6	(30,0)	−15.9	20.8	32.4	7.6	(150,0)	−11.1
This work	96 × 96	0.67	28 – 32	23.7	38.7	13.3	(30,0°)	−18.6	23.1	33	8.7	(150,0)	−15.6
This work	144 × 144	0.69	28 – 32	26.6	32.8	10	(30,0)	−20.9	27.2	38.0	8.3	(150,0)	−19.2

* FBW is the frequency operation bandwidth and GBW is the gain bandwidth.

4.7. CHAPTER LANDMARKS

In this chapter, a model for analyzing TRAs is proposed. The total field radiated by the TRA comprises two components: the refracted field, computed under the assumption that the structure behaves as a TA, and the reflected field, where the TRA functions as a RA. By leveraging physical optics and array theory, an accurate characterization of both radiated fields is achieved, taking into account the radiation patterns of a physical source and the spillover effect in the array factor evaluation.

Based on this model, a tool to design TRAs has been developed. Before showing its potential in the design of several structures, four H-MS cells having transmission phases spaced by 90° have been realized at 30 GHz. These elements comprises three metallic patterns interleaved by two dielectric slabs. Each of these metal layers have been separately designed. The behavior of each cells has been optimized for a commercial stack-up showing a phase error in transmission and reflection smaller than 8° at 30 GHz. The maximum amplitude deviation between 29 and 31 GHz is ±1.5 dB.

Several 60 × 60 elements TRAs having $F/D = 0.67$ and different steering angles have been designed and the analytical results from the developed tool have been compared with full wave simulations. It has been verified that for all angles up to $\theta_{st}^{ta} = 60°$ and $\varphi_{st}^{ta} = 0°$, the results show good agreement with the simulations. However, beyond $\theta_{st}^{ta} = 60°$, an interesting trend emerges. Specifically, as the transmission pointing direction increases, the pattern computed by the tool brings the main lobes closer together, nearly achieving endfire radiation. In contrast, full-wave simulations reveal a degradation of the reflected beam and an increase in the HPBW of the transmitted one.

Lastly, three prototypes with aperture sizes of $7.2 \times 7.2\lambda_d^2$, $9.6 \times 9.6\lambda_d^2$, and $14.4 \times 14.4\lambda_d^2$ were designed and manufactured using PCB technology. The measured patterns at $\varphi = 0°$ show good beam stability as a function of frequency and a low cross-polarization component for all structures. Moreover, a good agreement with numerical results, both analytically computed and obtained through full-wave simulations, has been observed. The differences between numerical and measured gains are within the expected measurement uncertainties (approximately ±0.5 dB), as well as misalignment inaccuracies and fabrication tolerances.

5

Towards independent beamforming

The most exciting phrase to hear in science, the one that heralds new discoveries, is not 'Eureka!' but 'That's funny...'

Isaac Asimov

This chapter takes a look to MSs that posses a bi-anisotropic response to find out whether the presence of new degrees of freedom allows a fully independent control of both transmission and reflection phases. Focusing the attention on O-BIMS illuminated by a normally incident plane wave, the scattering parameters are derived. Then, by applying the equal amplitude condition on the transmission and reflection coefficient, the optimal surface parameters are derived analytically. By varying their values, the full phase range is covered in both refraction and reflection.

Parts of this chapter have been published in [C4] and [C5].

5.1. BI-ANISOTROPIC METASURFACES

BI–ANISOTROPIC Metasurfaces represent the most broader class of surfaces. They exhibit a unique coupling of electric and magnetic responses, where each applied electric and magnetic fields induce at the same time equivalent electric and magnetic currents. As discussed in Chapter 2, these behaviors are described by the electric surface admittance $\underline{\mathbf{Y}}_{\mathrm{e}}$, the magnetic impedance $\underline{\mathbf{Z}}_{\mathrm{m}}$, the electromagnetic coupling $\underline{\boldsymbol{\chi}}$ and the magnetoelectric coefficient $\underline{\boldsymbol{\Upsilon}}$. Due to the presence of these factors, BMSs enable more exotic manipulation of EM waves with respect to H-MSs. For example, bi-anisotropic scatterers can be designed to introduce polarization transformation, be one-way fully transparent, or obtain an asymmetric response from the MS faces [95], [171]–[177]. Moreover, in wide-angle refraction applications, BMSs can match the input and output wave impedances by the presence of both magnetoelectric and electromagnetic coupling factors in the boundary condition [100]. This leads to realize a passive and lossless structure that posses a physical asymmetry [178].

In Chapter 3, an analytical procedure for designing and reciprocal H-MS capable of dividing incident power equally between transmitted and reflected waves has been presented. However, since H-MSs offer only two surface parameters for optimization, $\underline{\mathbf{Y}}_{\mathrm{e}}$ and $\underline{\mathbf{Z}}_{\mathrm{m}}$, they do not allow independent control of the phases of reflected and refracted waves. This limitation restricts the scanning capabilities of TRAs based on H-MSs, which exhibit the same phase distribution for both reflection and transmission, except for a phase offset. Consequently, when the phase profile of the TRA is designed to steer the transmitted beam at an angle of $(\theta_{\mathrm{st}}^{\mathrm{ta}}, \varphi_{\mathrm{st}}^{\mathrm{ta}})$, the reflected beam will be focused at $(\pi - \theta_{\mathrm{st}}^{\mathrm{ta}}, \varphi_{\mathrm{st}}^{\mathrm{ta}})$, as shown in Chapter 4.

To overcome this limitation, a class of MSs that provides an additional degree of freedom in design, specifically an independent surface parameter, must be considered. BMSs are ideal candidates as they exhibit non-zero electromagnetic and magnetoelectric factors, $\underline{\boldsymbol{\chi}}$ and $\underline{\boldsymbol{\Upsilon}}$, besides $\underline{\mathbf{Y}}_{\mathrm{e}}$ and $\underline{\mathbf{Z}}_{\mathrm{m}}$. Specifically, to evaluate the surface response under a normally incident y- or x-polarized wave, isotropy is imposed on the constitutive parameters of the reciprocal BMS. Then, a broken directional symmetry that maintains the polarization state is introduced. This sub-category of BMSs, defined as O-BIMS, has been extensively studied, demonstrating its capability to independently control the transmission and reflection coefficients of incident plane waves [31]. Additionally, for passive and lossless O-BIMSs, arbitrary field transformations can be achieved while locally conserving the power crossing the surface [100]. The physical realization of O-BIMS meta-atoms is based on three stacked impedance sheets, which, at microwave frequencies, are compatible with standard fabrication techniques (*e.g.* PCB) [100], [150].

In this chapter, the scattering properties of a lossless O-BIMS under a normally incident y-polarized wave are studied. Following this, a procedure is presented for designing the constitutive parameters of O-BIMS to achieve transmitted and reflected fields with equal amplitudes and an arbitrary phase shift. Based on this, a set of 16 meta-cells that provide 2-bit uniform phase quantization in both transmission and reflection is determined. These cells are preliminary designed using three stacked ideal sheet impedances, and their scattering parameters are numerically investigated.

5.2. ANALYTICAL MODEL

A planar and reciprocal O-BIMS is considered. It lies between two half-spaces filled by homogeneous, isotropic, non-dispersive materials with, in general, different electric and magnetic properties and characteristic impedances $(\eta_1 \neq \eta_2)$, as shown in Fig. 5.1.

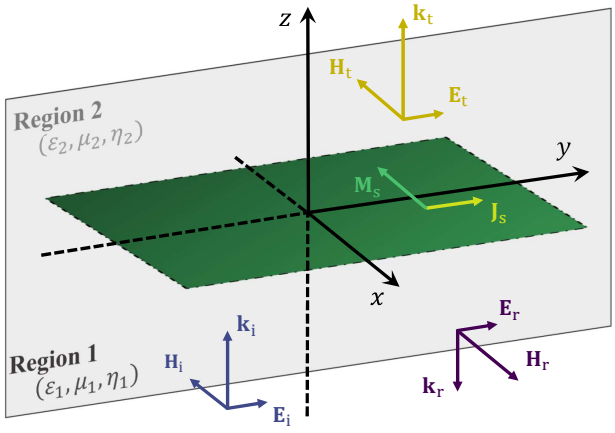

Figure 5.1: Infinite MS between two regions with the different material properties, illuminated by a normal incident field, in blue line, coming from Region 1. Reflected and transmitted fields are in purple and yellow lines, respectively.

The MS is illuminated by a normally incident plane wave with a y-polarized electric field $\mathbf{E}_\mathrm{i}$. With these assumptions, the boundary conditions reported in (2.9) reduce to the following expressions:

$$\hat{\mathbf{y}} J_\mathrm{s} = \hat{\mathbf{z}} \times \hat{\mathbf{x}} (H_2 - H_1) = \hat{\mathbf{y}} Y_\mathrm{e} E_\mathrm{m}^\mathrm{tn} - \hat{\mathbf{z}} \times \hat{\mathbf{x}} \chi H_\mathrm{m}^\mathrm{tn}, \tag{5.1a}$$

$$\hat{\mathbf{x}} M_\mathrm{s} = -\hat{\mathbf{z}} \times \hat{\mathbf{y}} (E_2 - E_1) = -\hat{\mathbf{z}} \times \hat{\mathbf{y}} \chi E_\mathrm{m}^\mathrm{tn} + \hat{\mathbf{x}} Z_\mathrm{m} H_\mathrm{m}^\mathrm{tn}, \tag{5.1b}$$

where $\mathbf{H}_1 = \hat{\mathbf{x}}(H_\mathrm{r} - H_\mathrm{i})$, $\mathbf{H}_2 = -\hat{\mathbf{x}} H_\mathrm{t}$, $\mathbf{E}_1 = \hat{\mathbf{y}}(E_\mathrm{i} + E_\mathrm{r})$ and $\mathbf{E}_2 = \hat{\mathbf{y}} E_\mathrm{t}$. The average fields tangent to the surface are defined as $\mathbf{E}_\mathrm{m}^\mathrm{tn} = (\mathbf{E}_\mathrm{i} + \mathbf{E}_\mathrm{r} + \mathbf{E}_\mathrm{t})/2$ and $\mathbf{H}_\mathrm{m}^\mathrm{tn} = (\mathbf{H}_\mathrm{i} + \mathbf{H}_\mathrm{r} + \mathbf{H}_\mathrm{t})/2$. The scattered fields and their propagation vectors are reported in (3.1). The transmission and reflection coefficients can be derived from (5.1), following the approach presented by Szymanski *et al.* [150].

By replacing in (5.1a) the expressions of the fields in both region and of the tangential fields on the surface as functions of the electric field of incident, reflected and transmitted waves, the following relation holds:

$$\left(\frac{E_\mathrm{i}}{\eta_1} - \frac{E_\mathrm{r}}{\eta_1} - \frac{E_\mathrm{t}}{\eta_2}\right) = \frac{Y_\mathrm{e}}{2}(E_\mathrm{i} + E_\mathrm{r} + E_\mathrm{t}) - \frac{\chi}{2}\left(-\frac{E_\mathrm{i}}{\eta_1} + \frac{E_\mathrm{r}}{\eta_1} - \frac{E_\mathrm{t}}{\eta_2}\right). \tag{5.2}$$

As previously mentioned in Chapter 3, the transmission and reflection coefficients are defined as the ratios of the electric fields of transmitted and reflected wave, respectively, to the incident electric field: $\tau = E_\mathrm{t}/E_\mathrm{i}$ and $\Gamma = E_\mathrm{r}/E_\mathrm{i}$. respectively. First, as in

following sections, it is assumed that the incident wavefront comes from Region 1. The two coefficients are denoted with τ_1 and Γ_1. By multiplying both sides of (5.2) by $1/E_\mathrm{i}$, after some manipulations, the following expression is found for τ_1:

$$\tau_1 = \frac{\eta_2}{\eta_1}\frac{2 - Y_\mathrm{e}\eta_1 - \chi}{2 + Y_\mathrm{e}\eta_2 + \chi} + \Gamma\frac{\eta_2}{\eta_1}\frac{-2 - Y_\mathrm{e}\eta_1 + \chi}{2 + Y_\mathrm{e}\eta_1 + \chi}. \tag{5.3}$$

After applying similar mathematical steps to (5.1b), the following equation is derived:

$$(E_\mathrm{t} - E_\mathrm{i} - E_\mathrm{r}) = \frac{\chi}{2}(E_\mathrm{i} + E_\mathrm{r} + E_\mathrm{t}) + \frac{Z_\mathrm{m}}{2}\left(-\frac{E_\mathrm{i}}{\eta_1} + \frac{E_\mathrm{r}}{\eta_1} - \frac{E_\mathrm{t}}{\eta_2}\right). \tag{5.4}$$

By multiplying both sides of (5.4) by $1/E_\mathrm{i}$, a second expression relating τ_1 and Γ_1 to the surface parameters is found:

$$\tau_1 = \frac{\eta_2}{\eta_1}\frac{2\eta_1 + \chi\eta_1 - Z_\mathrm{m}}{2\eta_2 - \chi\eta_2 + Z_\mathrm{m}} + \Gamma\frac{\eta_2}{\eta_1}\frac{2\eta_1 + \chi\eta_1 + Z_\mathrm{m}}{2\eta_2 - \chi\eta_2 + Z_\mathrm{m}}. \tag{5.5}$$

Eventually, reflection and transmission coefficients can be derived as functions of surface parameters only, by equating (5.3) to (5.5). The following expression is obtained for $\Gamma_1\left(Y_\mathrm{e}, \chi, Z_\mathrm{m}\right)$:

$$\Gamma_1 = \frac{4Z_\mathrm{m} - \eta_1\left[(\chi+2)^2 + 4\eta_2 Y_\mathrm{e} + Z_\mathrm{m}Y_\mathrm{e}\right] + \eta_2\left[Z_\mathrm{m}Y_\mathrm{e} + (\chi-2)^2\right]}{4Z_\mathrm{m} + \eta_1\left[(\chi+2)^2 + 4\eta_2 Y_\mathrm{e} + Z_\mathrm{m}Y_\mathrm{e}\right] + \eta_2\left[Z_\mathrm{m}Y_\mathrm{e} + (\chi-2)^2\right]}. \tag{5.6}$$

Then, by inserting (5.6) in either (5.3) or (5.5), $\tau_1\left(Y_\mathrm{e}, \chi, Z_\mathrm{m}\right)$ can be expressed as:

$$\tau_1 = \frac{-2\eta_2\left[Z_\mathrm{m}Y_\mathrm{e} + (\chi^2 - 4)\right]}{4Z_\mathrm{m} + \eta_1\left[(\chi+2)^2 + 4\eta_2 Y_\mathrm{e} + Z_\mathrm{m}Y_\mathrm{e}\right] + \eta_2\left[Z_\mathrm{m}Y_\mathrm{e} + (\chi-2)^2\right]}. \tag{5.7}$$

The case with a wave impinging from Region 2, i.e. the half-space above the MS in Fig. 5.1, can be analyzed in a similar manner. The transmission and reflection coefficients are named τ_2 and Γ_2, respectively. Their expressions are found starting from (5.1) and considering that the directions of the propagation vector of each scattered field is opposite with respect to that in the previous analysis, yielding:

$$\Gamma_2 = \frac{4Z_\mathrm{m} + \eta_1\left[(\chi+2)^2 - 4\eta_2 Y_\mathrm{e} + Z_\mathrm{m}Y_\mathrm{e}\right] - \eta_2\left[Z_\mathrm{m}Y_\mathrm{e} + (\chi-2)^2\right]}{4Z_\mathrm{m} + \eta_1\left[(\chi+2)^2 + 4\eta_2 Y_\mathrm{e} + Z_\mathrm{m}Y_\mathrm{e}\right] + \eta_2\left[Z_\mathrm{m}Y_\mathrm{e} + (\chi-2)^2\right]}, \tag{5.8}$$

$$\tau_2 = \frac{-2\eta_1\left[Z_\mathrm{m}Y_\mathrm{e} + (\chi^2 - 4)\right]}{4Z_\mathrm{m} + \eta_1\left[(\chi+2)^2 + 4\eta_2 Y_\mathrm{e} + Z_\mathrm{m}Y_\mathrm{e}\right] + \eta_2\left[Z_\mathrm{m}Y_\mathrm{e} + (\chi-2)^2\right]}. \tag{5.9}$$

5.2.1. ANALYSIS OF A LOSSLESS O-BIMS IN FREE SPACE

The particular case of a lossless O-BIMS located in free space, $\eta_1 = \eta_2 = \eta_0$, is now investigated. The transmission and reflection coefficients defined in the previous Section simplify as follows:

$$\tau_1 = \frac{-\eta_0 \left[Z_\mathrm{m} Y_\mathrm{e} + \left(\chi^2 - 4 \right) \right]}{2 Z_\mathrm{m} + \eta_0 \left(4 + \chi^2 + 2 \eta_0 Y_\mathrm{e} + Z_\mathrm{m} Y_\mathrm{e} \right)}, \tag{5.10a}$$

$$\Gamma_1 = \frac{2 \left[Z_\mathrm{m} - \eta_0 \left(2\chi + \eta_0 Y_\mathrm{e} \right) \right]}{2 Z_\mathrm{m} + \eta_0 \left(4 + \chi^2 + 2 \eta_0 Y_\mathrm{e} + Z_\mathrm{m} Y_\mathrm{e} \right)}, \tag{5.10b}$$

$$\tau_2 = \frac{-\eta_0 \left[Z_\mathrm{m} Y_\mathrm{e} + \left(\chi^2 - 4 \right) \right]}{2 Z_\mathrm{m} + \eta_0 \left(4 + \chi^2 + 2 \eta_0 Y_\mathrm{e} + Z_\mathrm{m} Y_\mathrm{e} \right)}, \tag{5.11a}$$

$$\Gamma_2 = \frac{2 \left[Z_\mathrm{m} + \eta_0 \left(2\chi - \eta_0 Y_\mathrm{e} \right) \right]}{2 Z_\mathrm{m} + \eta_0 \left(4 + \chi^2 + 2 \eta_0 Y_\mathrm{e} + Z_\mathrm{m} Y_\mathrm{e} \right)}. \tag{5.11b}$$

Hence, it is clear from (5.10a) and (5.11a) that $\tau_1 = \tau_2$ for reciprocal O-BIMS. On the other hand, $\Gamma_1 = \Gamma_2$ only when $\chi = 0$, *i.e.* when the O-BIMS degenerate in an isotropic H-MS. As discussed in Chapter 2, the electric admittance and magnetic impedance of a lossless MS are purely imaginary, *i.e.* $Y_\mathrm{e} = jB_\mathrm{e}$ and $Z_\mathrm{m} = jX_\mathrm{m}$. Moreover, the magneto-electric and electromagnetic factors of a lossless O-BIMS are pure real: $\chi = R$.

With these assumptions, the scattering coefficients reported in (5.10) and (5.11) can be rewritten as:

$$\tau_1 = \tau_2 = \frac{\eta_0 \left(4 + B_\mathrm{e} X_\mathrm{m} - R^2 \right)}{\eta_0 \left(R^2 - B_\mathrm{e} X_\mathrm{m} + 4 \right) + 2j \left(\eta_0^2 B_\mathrm{e} + X_\mathrm{m} \right)}, \tag{5.12a}$$

$$\Gamma_1 = \frac{2j \left(X_\mathrm{m} - \eta_0^2 B_\mathrm{e} \right) - 4R\eta_0}{\eta_0 \left(R^2 - B_\mathrm{e} X_\mathrm{m} + 4 \right) + 2j \left(\eta_0^2 B_\mathrm{e} + X_\mathrm{m} \right)}, \tag{5.12b}$$

$$\Gamma_2 = \frac{2j \left(X_\mathrm{m} - \eta_0^2 B_\mathrm{e} \right) + 4R\eta_0}{\eta_0 \left(R^2 - B_\mathrm{e} X_\mathrm{m} + 4 \right) + 2j \left(\eta_0^2 B_\mathrm{e} + X_\mathrm{m} \right)}. \tag{5.12c}$$

5.3. CONDITIONS FOR AN ARBITRARY DIVISION OF THE SCATTERED POWER

The analyses presented in the rest of this Chapter will consider, without loss of generality, that the O-BIMS lies in free space and is illuminated from Region 1. For simplicity of notation, the transmission and reflection coefficient in this case will be denoted with τ and Γ, instead of τ_1 and Γ_1, respectively. Their expressions are given in (5.12a) and (5.12b).

Next, as done for H-MSs in Chapter 3, a relation among the constitutive surface parameters is sought to transmit in Region 2 an arbitrary fraction of the incident power.

The amount of power to be transmitted can be set enforcing the following relation:

$$|\tau|^2 = \nu\,, \tag{5.13}$$

where $\nu \in [0,1]$ is a real number. Since the MS is passive, the amplitude of the reflection coefficient is easily found by applying the energy conservation law:

$$|\Gamma|^2 = 1-\nu\,. \tag{5.14}$$

The square of the amplitude of $\tau\,(B_\mathrm{e}, X_\mathrm{m}, R)$ can be written as:

$$|\tau|^2 = \frac{\eta_0^2\left(4+B_\mathrm{e}X_\mathrm{m}-R^2\right)^2}{\eta_0^2\left(R^2-B_\mathrm{e}X_\mathrm{m}+4\right)^2+\left(2\eta_0^2B_\mathrm{e}+2X_\mathrm{m}\right)^2}\,. \tag{5.15}$$

Then, by inserting (5.15) in (5.13) and solving for B_e, two possible optimal values for the susceptance are found as a function of X_m, R and ν, *i.e.*:

$$B_{e_{A,B}} = \frac{X_\mathrm{m}\left[R^2(1-\nu)-4\right]}{X_\mathrm{m}^2(1-\nu)-4\eta_0^2\nu}\left\{1\pm\sqrt{1-\frac{\left[X_\mathrm{m}^2(1-\nu)-4\nu\eta_0^2\right]\left[R^4(1-\nu)+16(1-\nu)-8R^2(1+\nu)-4\nu\dfrac{X_\mathrm{m}^2}{\eta_0^2}\right]}{X_\mathrm{m}^2\left[R^2(1-\nu)-4\right]^2}}\right\}. \tag{5.16}$$

5.4. CONDITIONS FOR EQUALIZING TRANSMITTED AND REFLECTED POWER

The design of an infinite and uniform O-BIMS to equally splits the power of a normally incident wave into the transmitted and reflected fields is thoroughly analyzed. This case is relevant to the optimal design of the unit-cells of TRAs forming transmitted and reflected beams with similar gain values. Under this condition, the variable ν reported in (5.13) is set to 0.5. Closed-form expressions relating each of the three surface parameters to the remaining two can be derived. Two solutions, i.e. $B_\mathrm{e}\,(X_\mathrm{m}, R)$ and $R\,(B_\mathrm{e}, X_\mathrm{m})$, will be presented in this Section to highlight fundamental properties of O-BIMS and guidelines for the design of TRAs. To ease calculations, it is convenient to solve, for either B_e or R, the following equation, rather than (5.13) and (5.14):

$$|\tau\,(X_\mathrm{m}, B_\mathrm{e}, R)\,| = |\Gamma\,(X_\mathrm{m}, B_\mathrm{e}, R)\,|\,. \tag{5.17}$$

Using (5.12b) and (5.15), (5.17) can be recast as:

$$\left[\eta_0\left(4+B_\mathrm{e}X_\mathrm{m}-R^2\right)\right]^2 = \left(2\eta_0^2B_\mathrm{e}+2X_\mathrm{m}\right)^2+16\eta_0^2R^2\,. \tag{5.18}$$

5.4.1. SOLUTION FOR THE ELECTRICAL SUSCEPTANCE

First, the optimal electrical susceptance of the O-BIMS is derived and analyzed. To this end, (5.18) is recast as a second-order equation:

$$B_e^2\left(\eta_0^2 X_m^2 - 4\eta_0^4\right) + B_e\left(16\eta_0^2 X_m - 2\eta_0^2 R^2 X_m\right) + \eta_0^2 R^4 + 16\eta_0^2 - 24\eta_0^2 R^2 - 4X_m^2 = 0\,. \quad (5.19)$$

The two mathematical solutions of (5.18) are:

$$B_{e_{A,B}} = \frac{X_m\left(R^2-8\right) \pm \sqrt{X_m^2\left(8-R^2\right)^2 - \left(X_m^2 - 4\eta_0^2\right)\left[R^4 + 16 - 24R^2 - 4\frac{X_m^2}{\eta_0^2}\right]}}{X_m^2 - 4\eta_0^2}\,. \quad (5.20)$$

It can be observed that the optimal susceptance obtained for achieving an arbitrary ratio of transmitted to reflected power, reported in (5.16), reduces to (5.20) for $\nu = 0.5$.

The optimal susceptance normalized to the free-space impedance ($B_e\eta_0$) is plotted as a function of the other two parameters in Fig. 5.2, for both solutions. The white areas in these graphs represent domains where the expressions (5.18) provide non-physical susceptances, *i.e.* values with a non-null imaginary part. It worth noting the physical values obtained from both solutions can be considered for realizing the unit-cells of a single TRA, thus enhancing the degrees of freedom in the design.

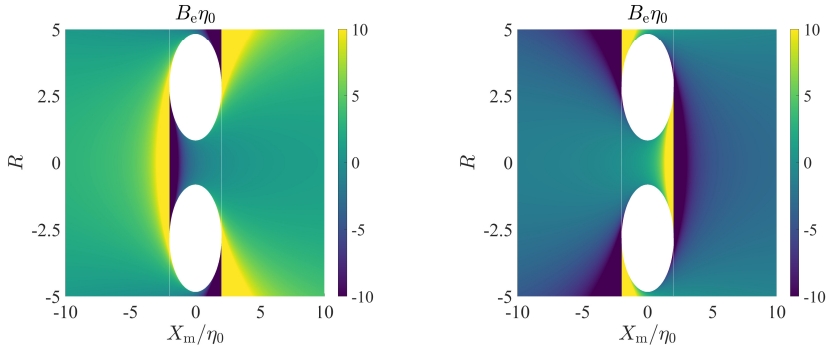

Figure 5.2: Normalized electric susceptance fulfilling (5.17), as a function of X_m/η_0 and R: solutions (a) B_{e_A} and (b) B_{e_B} obtained from (5.20) are shown.

The phases of the reflection and transmission coefficients obtained considering each of the two solutions are reported in Fig. 5.3 and Fig. 5.4, respectively. It is found out that both phases cover with continuity the 360° range, even considering a single susceptance solution (B_{e_A} or B_{e_B}).

Next, the difference between the phases of transmission and reflection coefficient is analyzed. Its general expression as a function of the three surface parameters is obtained starting from (5.12a) and (5.12b):

$$\angle\tau - \angle\Gamma = \begin{cases} -\angle g(B_e, X_m, R) & \text{if } 4 + B_e X_m \geq R^2\,, \quad (5.21a) \\ \pi - \angle g(B_e, X_m, R) & \text{if } 4 + B_e X_m < R^2\,. \quad (5.21b) \end{cases}$$

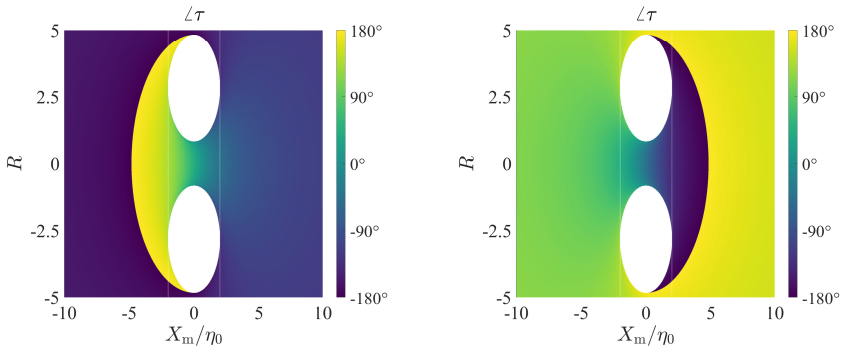

Figure 5.3: Phase of the transmission coefficient, as a function of X_m/η_0 and R, computed for the optimal susceptances (a) B_{e_A} and (b) B_{e_B}, reported in (5.20).

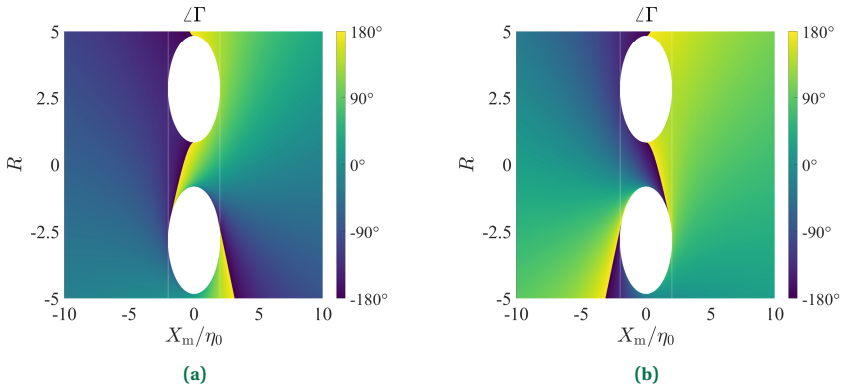

Figure 5.4: Phase of the reflection coefficient, as a function of X_m and R, computed for the optimal susceptances (a) B_{e_A} and (b) B_{e_B}, reported in (5.20).

It is clear from (5.21) that if $R = 0$, *i.e.* in the particular case of H-MSs, the phases of τ and Γ are shifted by either $-\pi/2$ or $\pi/2$, for all values of B_e, X_m, as observed in Chapter 3. The phase difference obtained considering the susceptance values that equalize transmitted and reflected power is found by inserting (5.20) in (5.21). It is plotted, for both B_{e_A} and B_{e_B}), in Fig. 5.5. It emerges that the two independent surface parameters can be selected to shift the phases of transmission and reflection coefficients by an arbitrary value in a 360° range. It will be demonstrated in Section 5.6 that this fundamental property allows one, in practical designs, to independently tailor the transmissive and reflective aperture phase profiles of a TRA.

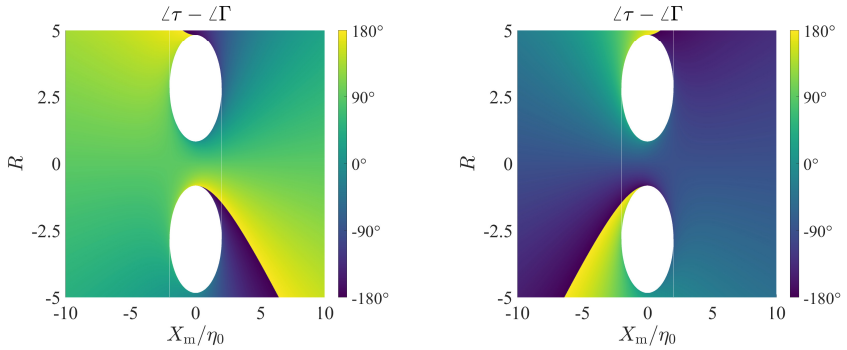

Figure 5.5: Difference of the phases the transmission and reflection coefficients, as a function of X_m/η_0 and R, computed for the optimal susceptances (a) B_{e_A} and (b) B_{e_B},reported in (5.20).

5.4.2. SOLUTION FOR THE MAGNETO-ELECTRIC COUPLING FACTOR

Equation (5.17) can be alternatively solved for the magneto-electric coupling factor R. To this end, the following bi-quadratic equation is derived from (5.18):

$$\eta_0^2 R^4 - 2R^2\eta_0^2(12 + B_e X_m) + 16\eta_0^2 + \eta_0^2 B_e^2 X_m^2 - 4X_m^2 - 4\eta_0^4 B_e^2 = 0\,. \tag{5.22}$$

The four solutions of (5.22) can be expressed in compact form as:

$$R_{A,B} = \pm\sqrt{12 + B_e X_m + \sqrt{(12 + B_e X_m)^2 - 16 + B_e^2 X_m^2 + 4\eta_0^2 B_e^2 + \frac{4X_m^2}{\eta_0^2} - 16 B_e X_m}}\,, \tag{5.23a}$$

$$R_{C,D} = \pm\sqrt{12 + B_e X_m - \sqrt{(12 + B_e X_m)^2 - 16 + B_e^2 X_m^2 + 4\eta_0^2 B_e^2 + \frac{4X_m^2}{\eta_0^2} - 16 B_e X_m}}\,. \tag{5.23b}$$

The solutions R_A and R_C, given by (5.23a) and (5.23b), respectively, are plotted in Fig. 5.6. The white regions represent domains where the solutions are complex and thus non-physical. Indeed, the hypothesis of absence of loss prescribes that R is purely real. It is interesting to observe in Fig. 5.6 that the regions of admissible values for the magnetoelectric coupling factor are bounded by the curves representing the optimal surface parameters derived in (3.33) for an H-MS ($R = 0$) achieving $|\tau| = |\Gamma|$, which are shown in the plot with solid black lines.

Similarly to the case examined in Section 5.4.1, by sweeping the two independent parameters X_m and B_e in the domain where physical solutions for R exist, the phases of both τ and Γ, as well as their difference, cover the entire 360° range.

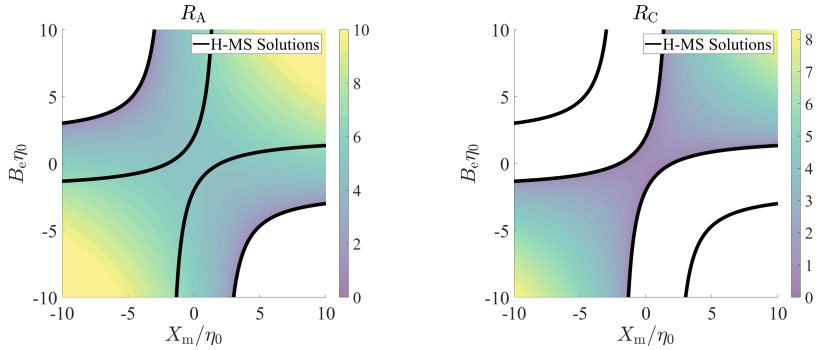

(a) (b)

Figure 5.6: Magnetoelectric and electromagnetic factors of the MS for (a) R_A and (b) R_C. The relations of B_e (X_m) for a H-MS to achieve equal amplitude for both scattering coefficients are superimposed.

5

5.5. DESIGN OF A POWER-SPLITTING O-BIMS AS A CASCADE OF SHEET IMPEDANCES

This Section investigates the possibility of designing an O-BIMS with stacked impedance sheets so that, in free space, it equally splits the power of a normally incident wave into the reflect the transmitted power. Similarly to the study presented in Chapter 3 for H-MS, structures comprising either two or three impedance sheets, interleaved by lossless, isotropic and homogeneous dielectric substrates, are considered. Each substrate section has a thickness t, a relative permittivity ε_{rl}, a characteristic impedance $Z_{rl} = \eta_0/\sqrt{\varepsilon_{rl}}$. The propagation constant of the wave in the dielectric is denoted with $\beta_{rl} = 2\pi f_{op}\sqrt{\varepsilon_{rl}}/c$, where f_{op} is the frequency and c the speed of light in vacuum. For both configurations, the optimal sheet impedances are determined in closed form. Properties and limitations of the two designs are discussed.

5.5.1. TWO-SHEET DESIGN

It has been demonstrated in Chapter 3 that H-MSs realized with two impedance sheets on a single substrate do not enable a full phase range coverage in transmission and reflection when, at the same time, the powers of transmitted and reflected waves are equal. Indeed, as shown in Fig. 3.10a and Fig. 3.11a, a phase range of maximum 180° is covered in transmission, when $|\tau| = |\Gamma|$ and the slab has $\varepsilon_{rl} = 1$.

The enhancement of the achievable phase range that a two-layer O-BIMS can enable, thanks to its additional degree of freedom (R), while ensuring that the amplitudes of the scattered waves are equal, is analyzed next. Most planar multi-layer O-BIMSs reported in the literature comprise three impedance sheets and two dielectric spacers. Indeed, this configuration allows one to design an arbitrary O-BIMS, *i.e.* to synthesize any combination of its three surface parameters [100], [140], [150], [179]. Nevertheless, some works proposed two-layer O-BIMSs to perform specific functions, *e.g.* absorption [177], [180]. These designs rely on the joint optimization of the two sheet impedances and of the electrical thickness of the substrate.

The possibility of realizing O-BIMS unit-cells for TRAs using only two optimized impedance sheets, for arbitrary values of t and $\varepsilon_{\mathrm{rl}}$, is studied here for the first time. The schematic representation of this two-sheet structure and its transmission-line model are equal to those examined in Chapter 3 for an H-MS and shown in Fig. 3.9. The sheet impedances Z_{s_1} and Z_{s_2} of the O-BIMS are derived as functions of surface parameters using the approach described in Chapter 3 The general expression for the transfer matrix of an O-BIMS is equated to that obtained using the transmission-line model of a two-sheet design. In particular, after inserting (2.25) in (3.38), the sheet impedances can be written as:

$$Z_{\mathrm{s}_1} = \frac{j Z_{\mathrm{rl}} \sin\left(\beta_{\mathrm{rl}} t\right)\left(4 - R^2 + B_{\mathrm{e}} X_{\mathrm{m}}\right)}{(R+2)^2 - B_{\mathrm{e}} X_{\mathrm{m}} - \cos\left(\beta_{\mathrm{rl}} t\right)\left(4 - R^2 + B_{\mathrm{e}} X_{\mathrm{m}}\right)}, \tag{5.24a}$$

$$Z_{\mathrm{s}_2} = \frac{j Z_{\mathrm{rl}} \sin\left(\beta_{\mathrm{rl}} t\right)\left(4 - R^2 + B_{\mathrm{e}} X_{\mathrm{m}}\right)}{(R-2)^2 - B_{\mathrm{e}} X_{\mathrm{m}} - \cos\left(\beta_{\mathrm{rl}} t\right)\left(4 - R^2 + B_{\mathrm{e}} X_{\mathrm{m}}\right)}. \tag{5.24b}$$

Differently from an H-MS, which is inherently symmetric, a two-layer O-BIMS is characterized, in general by $Z_{\mathrm{s}_1} \neq Z_{\mathrm{s}_2}$. As in Chapter 3, an additional equation relating the thickness and permittivity of the substrate to the surface parameter is found with this analysis method, for instance by inserting (2.25) in (3.42):

$$\sin(\beta_{\mathrm{rl}} t) = \frac{\sqrt{\varepsilon_{\mathrm{rl}}}\left\{\left[(R-2)^2 - B_{\mathrm{e}} X_{\mathrm{m}}\right]\left[(R+2)^2 - B_{\mathrm{e}} X_{\mathrm{m}}\right] - \left(B_{\mathrm{e}} X_{\mathrm{m}} - R^2 + 4\right)^2\right\}}{-4\eta_0 B_{\mathrm{e}}\left(4 - R^2 + B_{\mathrm{e}} X_{\mathrm{m}}\right)}. \tag{5.25}$$

This equation limits the range of surface parameters that can be realized using the two-layer O-BIMS under analysis, since it admits physical solutions only if the absolute value of its right-hand side is less or equal to 1. Next, the realizable surface parameters and the phase coverage that they enable are evaluated in the case of interest of O-BIMS achieving an even division the incident power into the transmitted and reflected fields. To this end, B_{e} is replaced in (5.25) with the optimal susceptances $B_{\mathrm{e_A}}$ and $B_{\mathrm{e_B}}$, reported in (5.20). Fig. 5.7 shows, for $\varepsilon_{\mathrm{rl}} = 2.2$, the value of the right-hand side of (5.25) as a function of X_{m} and R, when the solution $B_{\mathrm{e_A}}$ is chosen. The white elliptical areas, already observed in Fig. 5.2a, denote sets where $B_{\mathrm{e_A}}$ is non-physical. The additional domains shown in white represent surface parameters that cannot be synthesized using a two-sheet design. In these points, the right-hand side of (5.25) is greater than 1. The difference between the phases of transmission and reflection coefficients for the realizable surface parameters is plotted in Fig. 5.7b. It spans the entire 360° range, proving that a two-layer O-BIMS can equalize the amplitudes of transmitted and reflected fields, and, the same time, enforce an arbitrary phase shift between them.

The results obtained for the solution $B_{\mathrm{e_B}}$ are reported in Fig. 5.8. The surface parameters that cannot be obtained with a two-sheet design, while ensuring $|\tau| = |\Gamma|$ make the right-hand side of (5.25) less than -1. They are represented by the lateral white areas in the plots. Even for this second solution, any value of $\angle\tau - \angle\Gamma$ in a range of 360° can be attained by properly choosing the surface parameters.

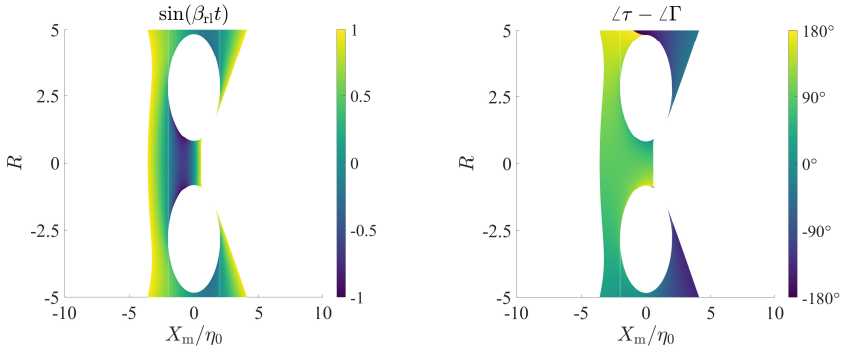

Figure 5.7: (a) Realizable magneto-electric factors and magnetic impedance of a two-layer O-BIMS when the optimal susceptance B_{e_A} is used to achieve $|\tau| = |\Gamma|$. The value of one of the sides of (5.25) is plot to define the validity range ($|\sin(\beta_{rl} t)| \leq 1$), considering a substrate permittivity $\varepsilon_{rl} = 2.2$. (b) Difference of the phases of transmission and reflection coefficient, in the same case.

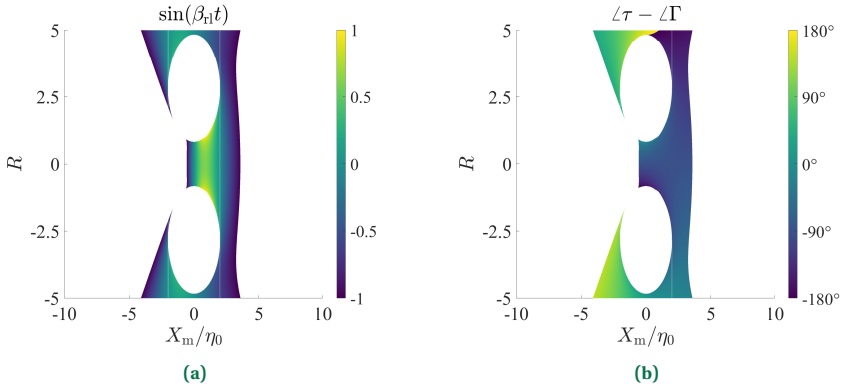

Figure 5.8: (a) Realizable magneto-electric factors and magnetic impedance of a two-layer O-BIMS when the optimal susceptance B_{e_B} is used to achieve $|\tau| = |\Gamma|$. The value of one of the sides of (5.25) is plot to define the validity range ($|\sin(\beta_{rl} t)| \leq 1$), considering a substrate permittivity $\varepsilon_{rl} = 2.2$. (b) Difference of the phases of transmission and reflection coefficient, in the same case.

5.5.2. THREE-SHEET DESIGN

A cascade of three impedance sheets spaced by two identical dielectric substrates can be employed to realize an arbitrary O-BIMS [100], [150]. Therefore, a three-layer design can achieve all the transmissive and reflective properties relevant to TRA cells that have been discussed in this Chapter. The three sheet impedances ($Z_{s_1}, Z_{s_2}, Z_{s_3}$) are found by substituting in (2.26) the expressions for the impedance matrix elements as functions of surface parameters:

$$Z_{s_1} = \frac{j X_m Z_{rl} \tan(\beta_{rl} t)}{-X_m + Z_{rl} \tan(\beta_{rl} t)(2 + R)}, \tag{5.26a}$$

$$Z_{s_2} = -\frac{-\left[Z_{rl}\tan\left(\beta_{rl}t\right)\right]^2\left(4-R^2+B_eX_m\right)}{4jX_m\sec\left(\beta_{rl}t\right)^2-2jZ_{rl}\tan\left(\beta_{rl}t\right)\left(4-R^2+B_eX_m\right)}, \tag{5.26b}$$

$$Z_{s_3} = \frac{jX_mZ_{rl}\tan\left(\beta_{rl}t\right)}{-X_m+Z_{rl}\tan\left(\beta_{rl}t\right)(2-R)}. \tag{5.26c}$$

It is possible to see that as for H-MS, the impedance middle layer is the only one depending on B_e. The impedance sheet of the outer layers can be tuned by choosing the values of R and X_m. The sheet impedances ensuring $|\tau| = |\Gamma|$ are obtained, for instance, by replacing B_e in (5.26b) with the physical values of the electrical susceptance given in (5.20). In this case, they depend only on R and X_m. More details on the design of three-layer O-BIMS for TRA cells are presented in Section 5.6.

5.6. PRELIMINARY DESIGN OF TRA UNIT-CELLS USING O-BIMSS

The independent control of the phases of the fields scattered by a power-splitting O-BIMS is demonstrated through the preliminary design of sixteen TRA unit-cells enabling a 2-bit uniform quantization of the full phase range in both reflection and transmission. For each transmission (reflection) state, four cells are designed to achieve the same value of $\angle\tau$ ($\angle\Gamma$) and four values of $\angle\Gamma$ ($\angle\tau$) spaced by 90°.

Direct relations among the surface parameters can be easily found by stipulating the desired value of either transmission or reflection coefficient. For instance, by imposing $\Im\{\tau\} = 0$ to set $\angle\tau = 0°$ in (5.12a), the following relation between B_e and X_m is obtained:

$$B_e = -\frac{X_m}{\eta_0^2}. \tag{5.27}$$

When (5.27) holds, the transmission coefficient in (5.12a) will reduce to:

$$\tau = -\frac{4\eta_0^2 - X_m^2 - \eta_0^2R^2}{4\eta_0^2 + X_m^2 + \eta_0^2R^2}. \tag{5.28}$$

The optimal magneto-electric coupling factor to equalize the amplitudes of transmitted and reflected fields can be found choosing the proper expression among those given in (5.22). As an alternative, $\tau = 1/\sqrt{2}$ is imposed in (5.28). In this way, two expressions for R are derived:

$$R = \pm\sqrt{\frac{4\eta_0^2\left(\sqrt{2}-1\right) - X_m^2\left(1+\sqrt{2}\right)}{\eta_0^2\left(1+\sqrt{2}\right)}}. \tag{5.29}$$

that provide physical values only when the argument of the square root is positive or equal to zero, *i.e.* when:

$$-2\eta_0\sqrt{\frac{\sqrt{2}-1}{\sqrt{2}+1}} \le X_m \le 2\eta_0\sqrt{\frac{\sqrt{2}-1}{\sqrt{2}+1}}. \tag{5.30}$$

The reflection coefficient of an O-BIMS fulfilling (5.27) and (5.29) is plotted in Fig. 5.9 as a function of X_m, in its range of validity. It is possible to see that any phase of the reflection coefficient can be achieved between 0° and 360° by varying the magnetic impedance, ensuring at the same time $\tau = 1/\sqrt{2}$.

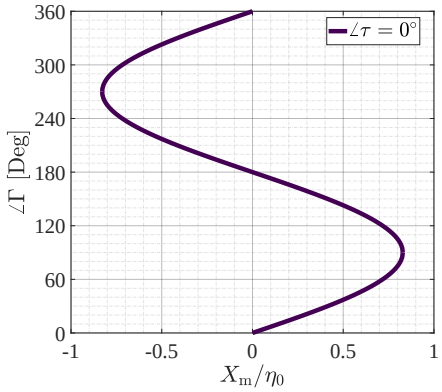

Figure 5.9: Phase of the reflection coefficient of the O-BIMS under analysis, as a function of the normalized magnetic impedance, when B_e and R are set to ensure that $\tau = 1/\sqrt{2}$.

Conditions on the surface parameters similar to (5.27) and (5.29) are obtained when $\angle\tau$ is fixed to 90°, 180° and 270°, to realize a 2-bit quantization of the transmitted phase. The phases of the reflection coefficients obtained for the four examined values of $\angle\tau$ are plotted as functions of X_m/η_0 in Fig. 5.10, considering the respective ranges of realizable surface parameters.

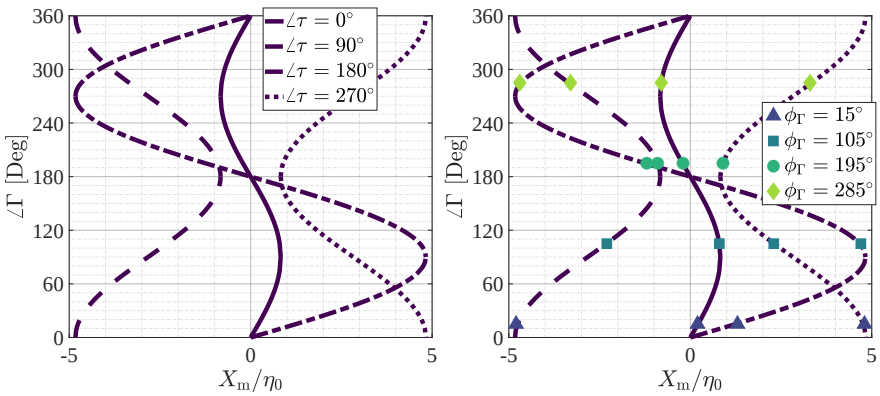

Figure 5.10: (a) Phase of the reflection coefficient of the O-BIMS under analysis, as a function of the normalized magnetic impedance, when B_e and R are set to achieve $|\tau| = |\Gamma|$ and the following phases of the transmission coefficient: $\angle\tau = 0°$, 90°, 180° and 270°. (b) Values of the normalized magnetic impedance and of the phase of reflection coefficient, chosen along with the aforementioned values of $\angle\tau$ for the sixteen TRA cells.

For each value of the phase of the transmission coefficient, the phase of the reflec-

tion coefficient spans over the entire 360° range by properly choosing the magnetic impedance.

Then, four values of $\angle\Gamma$ at the design frequency (15°, 105°, 195° and 285°) were selected to attain a 2-bit quantization of the reflected phase. The magnetic impedances corresponding to the sixteen chosen pairs of $\angle\Gamma$ and $\angle\tau$ are shown with symbols in Fig. 5.10. The constitutive parameters of each TRA cell were determined, with the aid of Fig. 5.9 and Fig. 5.10, to obtain the desired phase states, referred to as ϕ_τ and ϕ_Γ in transmission and in reflection, respectively. They are reported in Table 5.1.

Table 5.1: Designed values of $(B_e\eta_0, X_m/\eta_0, R)$ of sxteen O-BIMS-based TRA cells.

ϕ_τ	0°				90°				180°				270∘			
ϕ_Γ	15°	105°	195°	285°	15°	105°	195°	285°	15°	105°	195°	285°	15°	105°	195°	285°
$B_e\eta_0$	−0.2	−0.8	0.2	0.8	−0.9	−3.4	−4.8	−2.3	−1.3	−4.7	1.3	4.7	0.9	3.4	4.8	2.4
X_m/η_0	0.2	0.8	−0.2	−0.8	−4.8	−2.3	−0.9	−3.3	1.3	4.7	−1.2	−4.7	4.8	2.3	0.9	3.3
R	−0.8	0.2	0.8	−0.2	−0.5	−1.9	0.5	1.9	−4.7	1.1	4.7	−1.1	0.6	1.9	−0.5	−1.9

Table 5.2: Normalized sheet impedances $(Z_{s_1}/\eta_0, Z_{s_2}/\eta_0, Z_{s_3}/\eta_0)$ of each O-BIMS-based TRA cell.

ϕ_τ	0°				90°				180°				270∘			
ϕ_Γ	15°	105°	195°	285°	15°	105°	195°	285°	15°	105°	195°	285°	15°	105°	195°	285°
$\Im\{Z_{s_1}\}/\eta_0$	0.22	0.78	−0.07	−0.27	−0.56	−0.66	−0.23	−0.37	−0.28	−1.23	−0.14	−0.60	−1.05	4.42	6.58	−0.68
$\Im\{Z_{s_2}\}/\eta_0$	−0.53	0.78	−0.25	−0.14	−0.07	−0.13	−0.20	−0.10	−0.24	−0.14	−0.53	0.86	0.14	0.48	−1.01	0.23
$\Im\{Z_{s_3}\}/\eta_0$	0.08	1.34	−0.13	−0.24	−0.50	−0.31	−0.32	−0.66	0.28	−0.77	1.35	−0.47	−0.85	−0.69	0.75	−3.47

A realization of the designed O-BIMS cells is presented. It uses the three-sheet structure described in Section 5.5.2 and shown in Fig. 2.6. The three sheet impedances are spaced by two substrates of relative permittivity $\varepsilon_{rl} = 2.2$ and thickness $t = \lambda_g/8$, where $\lambda_g = \lambda_d/\sqrt{\varepsilon_{rl}}$ and λ_d is the free-space wavelength at the design frequency $f_d = 30\,\text{GHz}$. The impedances Z_{s_1}, Z_{s_2} and Z_{s_3} are computed from (5.26) by using the optimized surface parameters of Table 5.1. They are reported in Table 5.2.

The scattering parameters of the designed cells are computed using the transfer-matrix approach reported in Chapter 2 and considering that the sheet impedances are frequency-independent. The numerical results have been also validated by full-wave simulations. The targeted phase states are achieved. Fig. 5.12 shows the phase and amplitude responses of the four cells with transmission phase state $\phi_\tau = 90°$. In the 28-32 GHz band, the phases $\angle\Gamma$ of these cells are subsequently spaced by $90° \pm 10°$. The phases $\angle\tau$ are 90° at f_d and almost equal in the entire band.

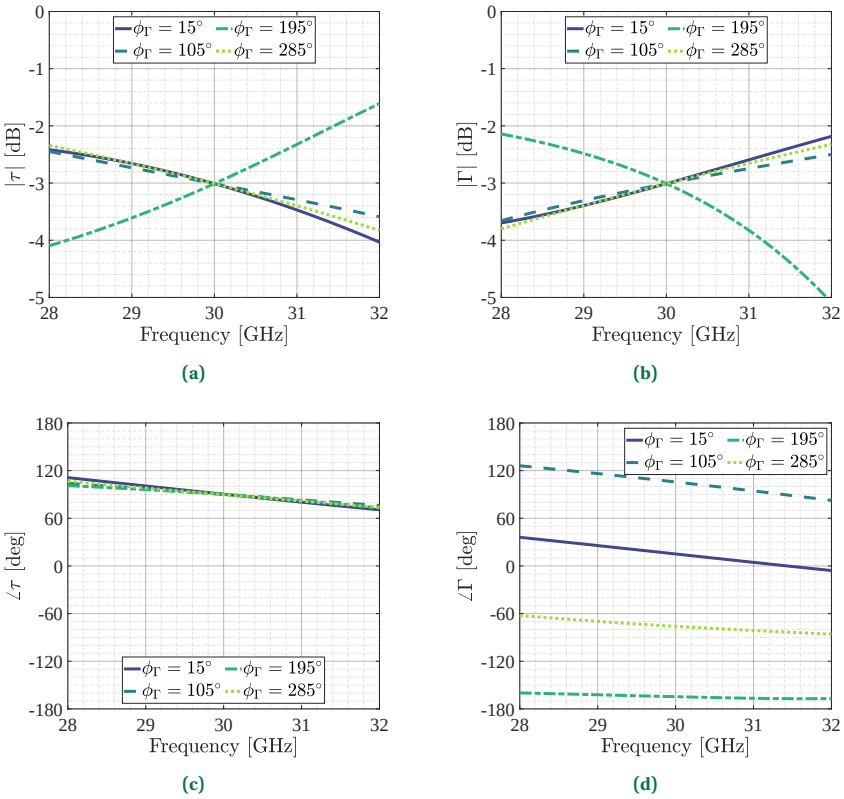

Figure 5.11: Computed scattering parameters of the four designed TRA cells with $\angle\tau = 90°$ at 30 GHz. Amplitudes of (a) transmission and (b) reflection coefficients. Phases of (c) transmission and d) reflection coefficients.

A 10% relative bandwidth is achieved from 28 to 31 GHz with the amplitudes of both τ and Γ between −4 dB and −2 dB. Fig. 5.11 shows that a similar wideband behavior is

observed for the four cells characterized by the reflection phase state $\phi_\Gamma = 105°$. The values of $|\tau|$ and $|\Gamma|$ are very close to -3 dB at f_d, as prescribed by the design procedure. A 13% relative bandwidth centered at 30 GHz is obtained, with the scattering coefficients between -4 dB and -2 dB. Similar amplitude and phase responses, not reported for brevity, were found for the other unit-cells.

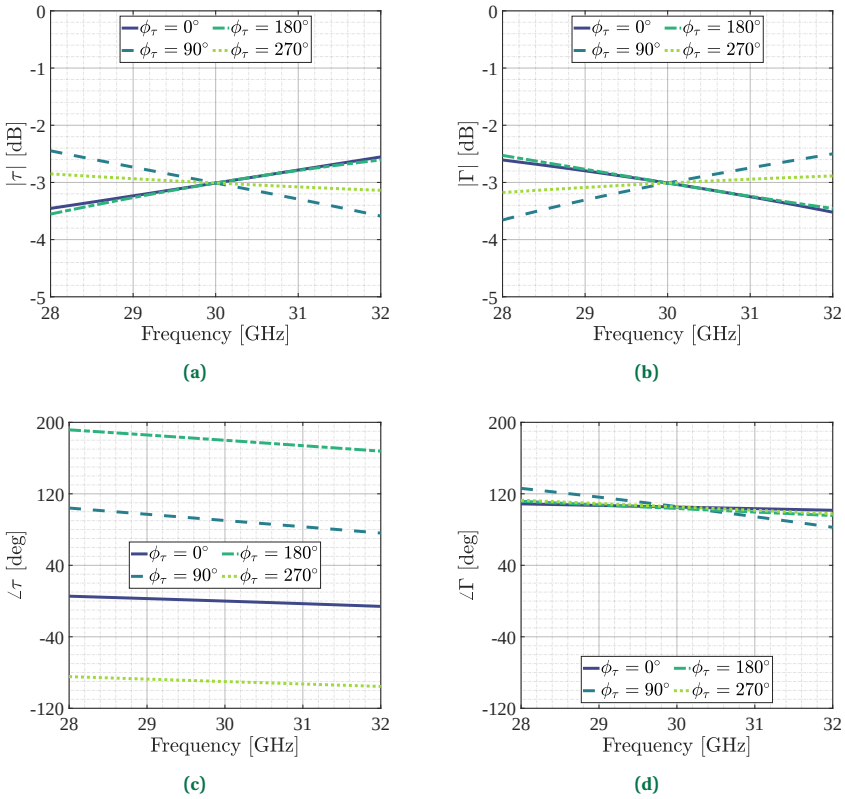

Figure 5.12: Computed scattering parameters of the four designed TRA cells with $\angle\Gamma = 105°$ at 30 GHz. Amplitudes of (a) transmission and (b) reflection coefficients. Phases of (c) transmission and d) reflection coefficients.

5.7. CHAPTER LANDMARKS

In this Chapter, a review on the extraction of the scattering parameters of O-BIMSs has been presented. Their inherent properties relevant to the realize TRAs achieving independent beamforming in both transmission and reflection have been discussed and guidelines for their design have been proposed. Optimal relations between the surface parameters have been derived enable an arbitrary and, in particular, an even division of the incident power into the scattered fields, as well as a simultaneous manipulation of their phases. It has been proved that, with the proposed design, the phases of transmission and reflection coefficients cover the full 360° range. Arbitrary values of their difference can also been attained. These properties allow one to optimize individually the aperture phase distributions in transmission and reflection of a spatially modulate O-BIMS. The possibility to design a power splitting O-BIMS with independent transmitted and reflected phases using only two metal layers and a dielectric substrate has been demonstrated for the first time, enabling reduced costs of fabrication. As a proof of concept, a set of 16 O-BIMS-based TRA unit-cells has been designed, following the presented procedure. It enables a 2-bit uniform quantization of two arbitrary phase profiles in transmission and reflection. A preliminary design of these cells using three impedance sheets and two substrates has been presented and analyzed using a transmission-line model in a 13% relative bandwidth. The computed scattering parameters validate the expected behavior of the O-BIMS cells and the proposed design approach, paving the way for the realization of TRAs which manipulate independently transmitted and reflected fields.

6

Conclusion

The scientific man does not aim at an immediate result. He does not expect that his advanced ideas will be readily taken up... His duty is to lay the foundation for those who are to come, and point the way.

Nikola Tesla

This last chapter serves as a concise summation of all the contributions and achievements presented throughout the thesis. A closing consideration is provided through an outlook on future analysis and research directions.

6.1. RESEARCH SUMMARY

In the last decade, the concept of STAR-RIS arose to enhance indoor and outdoor signal coverage, improve wireless networks quality and use efficently the EM spectrum. Due to a combination of transmission and reflection functionalities in a single device, STAR-RISs represents a cutting-edge development of RISs. The work presented in this manuscript lays the theoretical foundations of MSs employed as devices capable of splitting incident electromagnetic waves into transmitted and reflected beams for the design of TRAs, usable in STAR-RIS scenarios. Along all chapters, the following approach is employed: first, assumption and rigorous analyses are stated; then, analytical and simulation results demonstrating the proposed models are presented.

In Chapter 3, a rigorous derivation of the optimal H-MS parameters for an arbitrary power division between transmission and reflection is reported. Based on the analysis of Szymanski *et al.* [150], the scattering coefficients are derived from the boundary conditions when a normal incident plane wave illuminates a reciprocal H-MS. An amplitude condition on transmission and reflection coefficients can be enforced to extract the relations between the H-MS electric admittance and magnetic impedance. The cases of an H-MS in half-spaces with different dielectrics and in free space have been analyzed and the optimum H-MS parameters have been derived. From the perspective of STAR-RIS networks, the second scenario is the one that seems more promising as it is compatible with the application. Then, a direct relation between the magnetic impedance and the transmission coefficient phase have been reported. In view of TRA cells design, these expressions allow a fast extractions of the MS characteristics parameters. However, a constant phase difference of $\pm 90°$ between the scattering coefficients has been found, determining dependent beam generation in a TRA design.

To realize TRA cells starting from the derived H-MS constitutive parameter relations, cascaded impedance sheets interleaved by dielectric slabs have been considered. In literature, most of the works employ three layered meta-atoms [88], [99], [140]. Nevertheless, there are works on H-MS using just two sheet impedances [146]–[149]. However, in these cases, relaxed conditions on the scattering coefficients amplitude were imposed. The analysis of Abdelrahman *et al.* showed limitations in the transmission phase range for a two layer FSS depending on the slab thickness and its relative permittivity [151]. In Chapter 3, the sheet impedance expressions for a two layer structure are presented as a function of the surface parameters. Due to reciprocity, both layers of a H-MS are equal. This limitation prevents from covering the full phase range in transmission and, consequently, in reflection. Then, at least a cascade of three sheet impedances is required. In Chapter 4, four H-MS cells comprising three sheet impedances and having transmission phases spaced by $90°$ have been realized at 30 GHz. Based on the preliminary analysis of Chapter 3 on the physical implementation of these layers, meanders and dog-bones like patterns have been considered in the cell design. Each element behavior has been optimized for a commercial stack-up showing an error of the phase range in transmission and reflection smaller than $8°$ at 30 GHz and a maximum amplitude imbalance of ± 1.5 dB between 29 and 31 GHz.

To properly design TRAs based on these elements, a model has been proposed in Chapter 4. Based on physical optics and array theory [162], [163], [165], a very accurate description of the radiated field in both transmission and reflection is obtained taking

into account the patterns of a physical source and the spillover effect in the array factor evaluation. Several 60×60 elements TRAs having $F/D = 0.67$ and different steering angles have been designed, and the analytical results from the developed tool have been compared with full-wave simulations. It has been verified that in all cases a good agreement with the simulation results is obtained. Lastly, three prototypes, having aperture size $7.2 \times 7.2\lambda_d^2$, $9.6 \times 9.6\lambda_d^2$ and $14.4 \times 14.4\lambda_d^2$, have been manufactured in PCB technology. The measured patters at $\varphi = 0°$ shows a good beam stability as a function of frequency and low cross-polarization component for all the structures. Moreover, a good agreement with the numerical results, simulated and computed with the developed tool, have been showed. The observable differences between numerical and measured gains are due to measurement uncertainties, around ± 0.5 dB, misalignment inaccuracies and fabrication tolerances.

Nevertheless, as showed in Chapter 3 and Chapter 4, once the direction of the transmitted beam is chosen, the reflected beam is fixed. To overcome this limitation, in Chapter 5, a third degree of freedom has been introduced in the expressions of the scattering coefficients in the form of an additional surface parameter. By extending the analysis to O-BIMS, other than the electric admittance and magnetic impedance, the magnetoelectric coupling factor is present too. Indeed, starting from derivations of transmission and reflection coefficients by Szymanski *et al.* [150], optimal relations between the surface parameters have been derived to enable an arbitrary and, in particular, an even division of the incident power into the scattered fields, as well as a simultaneous manipulation of their phases. It has been proved that, with the proposed design, the phases of transmission and reflection coefficients cover the full 360° range. Arbitrary values of their difference can also been attained. These properties allow one to optimize individually the aperture phase distributions in transmission and reflection of a spatially modulated O-BIMS. The possibility to design an O-BIMS power splitting with independent transmitted and reflected phases using only two metal layers and a dielectric substrate has been demonstrated for the first time, enabling reduced costs of fabrication. As a proof of concept, a set of 16 O-BIMS-based TRA unit-cells has been designed, following the presented procedure. It enables a 2-bit uniform quantization of two arbitrary phase profiles in transmission and reflection. A preliminary design of these cells using three impedance sheets and two substrates has been presented and analyzed using a transmission-line model in a 13% relative bandwidth.

6.2. PERSPECTIVE

In this section, several aspects of the analysis presented along the manuscript, not dealt in the research frame, will be discussed. They forms good opening points to future works, allowing to approach possible issues and enhance functionalities.

6.2.1. TRA DESIGN WITH INDEPENDENT BEAMS

In Chapter 5, a preliminary design of 16 O-BIMS-based TRA unit cells enabling a 2-bit uniform quantization of two arbitrary phase profiles in transmission and reflection was presented. Based on this, the next steps involve the physical realization of each cell's sheet impedance, as discussed in Chapter 4 for H-MS, along with the design

of several TRAs. To validate the proposed approach, multiple prototypes could be fabricated and measured. Furthermore, their performance could be compared with that of O-BIMS-based TRAs using unit cells with only two stacked metal layers separated by a dielectric substrate. In this context, further studies on two-layer O-BIMSs could be conducted to assess their potential advantages and limitations compared to multi-layer designs, particularly in terms of fabrication complexity, performance, and practical implementation.

6.2.2. CIRCULAR POLARIZATION

Circularly polarized waves are often employed for their robustness in multipath environments, leading to improved coverage. It is well established that H-MSs can achieve polarization conversion by using two cascaded surfaces spaced a distance on the order of the lattice periodicity [136]. A similar approach can be used to design H-MS-based TRAs capable of generating circularly polarized waves. Alternatively, chiral bi-isotropic metasurfaces provide a potential solution. However, by imposing polarization conversion and ensuring equal amplitude of the scattering coefficients, a degree of freedom necessary to independently control transmission and reflection phases might be lost in the boundary conditions. In this regard, chiral bi-isotropic metasurfaces offer a more compact and cost-effective solution compared to cascaded H-MSs. Achieving both polarization conversion and independent scattering phases would require the introduction of generic bi-anisotropy. Extending the analysis from Chapter 5 to BMS could provide further insights for the design of TRA cells.

6.2.3. RECONFIGURABILITY

The final aspect to consider for future work is reconfigurability. Kim *et al.* presented a tunable H-MS capable of dynamically controlling both the amplitude and direction of the radiated field [52]. This concept can be applied to TRA design as well. By determining the optimal surface parameters to achieve the desired phase in both transmission and reflection, active devices could be integrated into the cell design. These active elements would allow for the dynamic adjustment of the sheet impedances, enabling real-time control over the radiated field. Such reconfigurability could open up new possibilities for adaptive beamforming and on-demand reorientation of the radiated energy, providing significant flexibility in applications where beam steering or energy shaping is required. Furthermore, combining these active elements with the proposed TRA structures could enable more efficient, versatile, and adaptive systems for a wide range of communication and sensing technologies.

A

Cells robustness under oblique incidence

A

In subsection 4.3.4 of Chapter 4, the robustness of the cell having $\phi_\tau = 195°$ under an incident angle θ_{ob} of a y-polarized wave varying between between 0° and 50° has been presented. In this appendix, the scattering coefficients variation for each other cell are discussed.

A.1. OBLIQUE INCIDENCE: $\phi_\tau = 15°$

The amplitude of the scattering coefficients for the cell with $\phi_\tau = 15°$ is reported in Fig. A.1. The transmission coefficient amplitude shows a small variation of a maximum of −0.5 dB from $\theta_{ob} = 10°$ to 50° at 30 GHz. On the other hand, the reflection coefficient magnitude increases by 0.4 dB at $\theta_{ob} = 50°$. In the frequency range of interest, from 29 to 31 GHz, a stronger variation of $|S_{21}|$ and $|S_{11}|$ is observed at 31 GHz, though it remains within acceptable limits. The variation of the scattering phases due to θ_{ob} is shown in Fig. A.4. The values of $\angle S_{21}$ and $\angle S_{11}$ present a maximum variation of 20° at 30 GHz, introducing a small error compared to the shift of 90° caused by the quantization.

A.2. OBLIQUE INCIDENCE: $\phi_\tau = 105°$

Since three capacitive metal layers are stacked, it is expected that this cell will be less robust compared to the one with $\phi_\tau = 15°$. Indeed, the amplitude of the scattering coefficients for the cell with $\phi_\tau = 105°$ is reported in Fig. A.2. The transmission coefficient amplitude shows a variation of 2.9 dB from $\theta_{ob} = 0°$ to 50° at 30 GHz, while $|S_{11}|$ varies by 1.3 dB. It can be observed that up to $\theta_{ob} = 30°$, both scattering coefficient amplitudes show only a small variation. For this cell, the TA functionality may impact the insertion losses due to the elements affecting antenna radiation characteristics (similar to the case for $\phi_\tau = 195°$). However, $\angle S_{21}$ and $\angle S_{11}$ present a maximum variation of 30° at 30 GHz, indicating good stability (see Fig. A.4). The variation of the scattering phases due to θ_{ob} is shown in Fig. A.5. The values of $\angle S_{21}$ and $\angle S_{11}$ present a maximum variation of 20° at 30 GHz.

A.3. OBLIQUE INCIDENCE: $\phi_\tau = 285°$

The last cell, in contrast to $\phi_\tau = 105°$, shows stable behavior from 29 to 31 GHz. The amplitude of the scattering coefficients for the cell with $\phi_\tau = 285°$ is reported in Fig. A.3. As for $\phi_\tau = 105°$, the transmission coefficient amplitude shows a variation of 1.5 dB from $\theta_{ob} = 10°$ to 50° at 30 GHz. On the other hand, the reflection coefficient magnitude increases by 1.2 dB at $\theta_{ob} = 50°$. However, it remains within the range of 2 dB to 4dB in the frequency band. The variation of the scattering phases due to θ_{ob} is shown in Fig. A.6. The values of $\angle S_{21}$ and $\angle S_{11}$ present a maximum variation of 20° at 30 GHz.

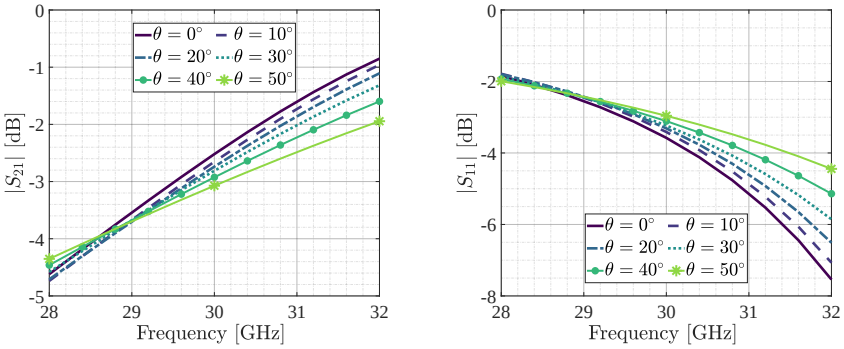

Figure A.1: Full wave simulated amplitudes of the (a) transmission and (b) reflection coefficients as functions of frequency and angle of incidence θ_{ob} of the impinging plane wave for $\phi_\tau = 15°$.

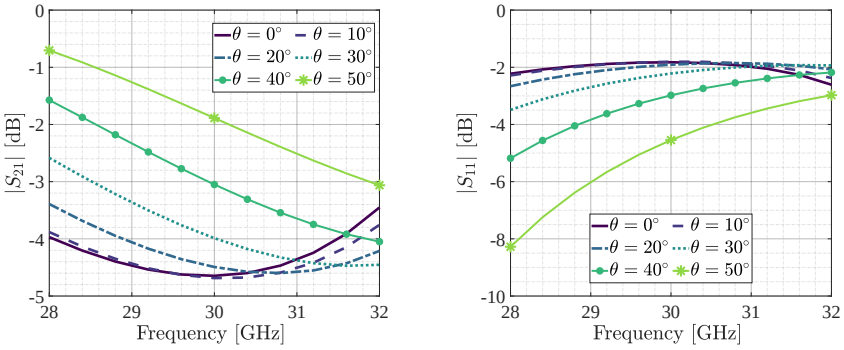

Figure A.2: Full wave simulated amplitudes of the (a) transmission and (b) reflection coefficients as functions of frequency and angle of incidence θ_{ob} of the impinging plane wave for $\phi_\tau = 105°$.

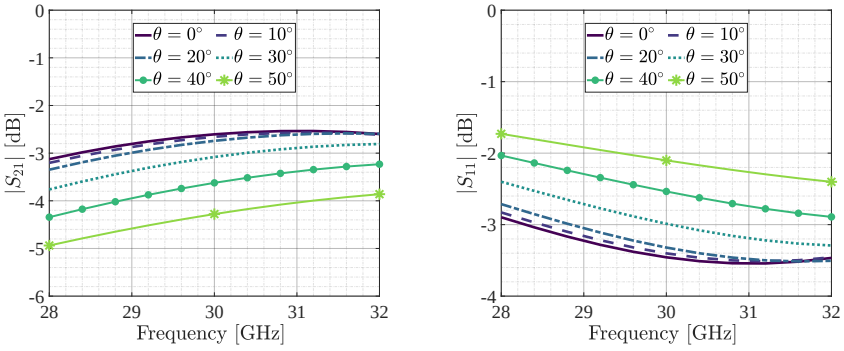

Figure A.3: Full wave simulated amplitudes of the (a) transmission and (b) reflection coefficients as functions of frequency and angle of incidence θ_{ob} of the impinging plane wave for $\phi_\tau = 285°$.

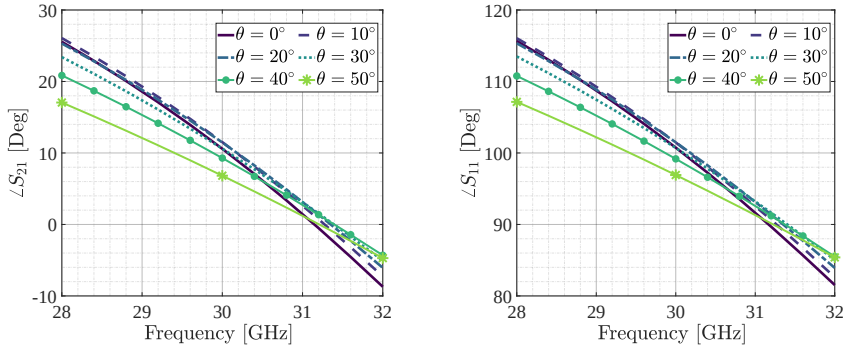

Figure A.4: Full wave simulated phase of the (a) transmission and (b) reflection coefficients as functions of frequency and angle of incidence θ_{ob} of the impinging plane wave for $\phi_\tau = 15°$.

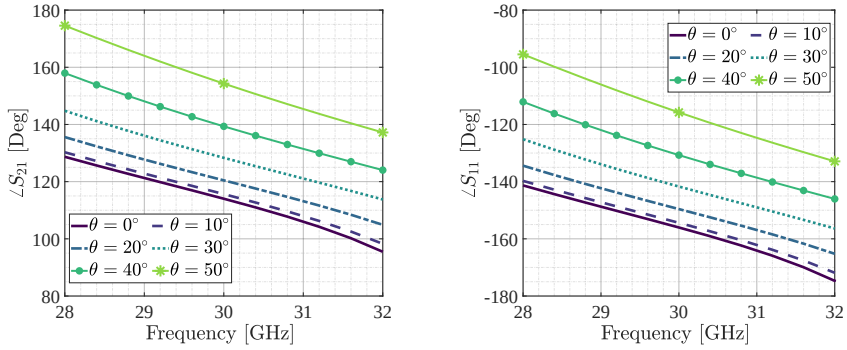

Figure A.5: Full wave simulated phases of the (a) transmission and (b) reflection coefficients as functions of frequency and angle of incidence θ_{ob} of the impinging plane wave for $\phi_\tau = 105°$.

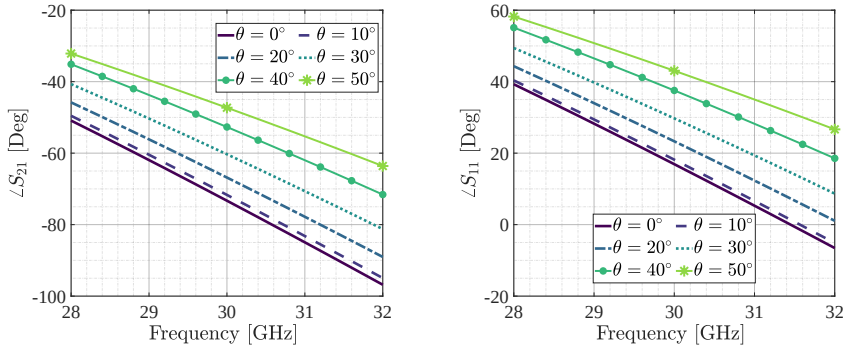

Figure A.6: Full wave simulated phases of the (a) transmission and (b) reflection coefficients as functions of frequency and angle of incidence θ_{ob} of the impinging plane wave for $\phi_\tau = 285°$.

List of Publications

Journal Papers

[J1] A. Berto, F. Foglia Manzillo, and G. Valerio, "Huygens' metasurfaces for simultaneous transmission and reflection: analysis and experiments", *IEEE Trans. Antennas Propag.*, submitted.

Conference Papers

[C1] A. Berto, F. Foglia Manzillo, and G. Valerio, "Analysis of Huygens' metasurfaces for the design of transmit-reflect arrays", in *17th Eur. Conf. Antennas Propag. (EuCAP) 2023*, Florence, Italy, Mar. 2023, pp. 1–4.

[C2] A. Berto, F. Foglia Manzillo, and G. Valerio, "Design of Huygens' cells for transmit-reflect-arrays at 30 GHz", in *2023 IEEE Int. Symp. Antennas Propag. USNC-URSI Radio Sci. Meet.*, Portland, OR, USA, Jul. 2023, pp. 1591–1592.

[C3] A. Berto, F. Foglia Manzillo, and G. Valerio, "Design and characterization of a transmitting and reflecting metasurface at 30 GHz", in *27th Eur. Microw. Week 2024*, Paris, France, Sep. 2024.

[C4] A. Berto, F. Foglia Manzillo, and G. Valerio, "Bianisotropic metasurfaces for bidirectional arrays with independent reflected and transmitted beams", in *2024 IEEE Int. Symp. Antennas Propag. INC/USNC-URSI Radio Sci. Meet.*, Florence, Italy, Jul. 2024.

[C5] A. Berto, F. Foglia Manzillo, and G. Valerio, "Design of simultaneously transmitting and reflecting bianisotropic metasurfaces", in *19th Eur. Conf. Antennas Propag. (EuCAP) 2025*, Stockholm, Sweden, Mar. 2025, accepted.

References

[1] H. Q. Flacco, *Epistulae*, Liber I, Epistle II.

[2] I. Kant, "Beantwortung der frage: was is aufklaerung?", *Berlinische Monatsschrift*, vol. I-V, pp. 481–494, Dec. 1784.

[3] A. Tobler, *Li Proverbe au vilain, Die Sprichwörter des gemeinen Mannes*. LEIPZIG, 1895.

[4] C. J. Maxwell, "A dynamical theory of the electromagnetic field", *Philos. Trans. R. Soc.*, vol. VIII, no. 155, pp. 459–512, Jan. 1865.

[5] B. J. Hunt, "Oliver Heaviside: a first-rate oddity", *Physics Today*, vol. 65, no. 11, pp. 48–54, Nov. 1, 2012.

[6] I. Yavetz, *From Obscurity to Enigma: The Work of Oliver Heaviside, 1872-1889*. Basel: Springer Basel, 1995.

[7] C. Donaghy-Spargo and A. Yakovlev, "Oliver Heaviside's electromagnetic theory", *Phil. Trans. R. Soc. A.*, vol. 376, no. 2134, p. 20 180 229, Dec. 13, 2018.

[8] D. P. Hampshire, "A derivation of Maxwell's equations using the Heaviside notation", *Phil. Trans. R. Soc. A.*, vol. 376, no. 2134, p. 20 170 447, Dec. 13, 2018.

[9] O. Heaviside, "Electromagnetic induction and its propagation", *The Electrician*, Jan. 1885-1887.

[10] O. Heaviside, *Electrical papers*. Macmillan and Co., 1892-1894, vol. I-II.

[11] N. Tesla, "Apparatus for the utilization of radiant energy.", US685957A, 1901.

[12] G. Marconi, "Improvements in apparatus employed in wireless telegraphy.", GB190007777A, 1900.

[13] S. Cherry, "Edholm's law of bandwidth", *IEEE Spectr.*, vol. 41, no. 7, pp. 58–60, Jul. 2004.

[14] W. D. Williams, M. Collins, D. M. Boroson, *et al.*, "RF and optical communications: a comparison of high data rate returns from deep space in the 2020 timeframe", in *12th Ka Broadband Commun. Conf.*, 2007.

[15] A. D. Panagopoulos, P.-D. M. Arapoglou, and P. G. Cottis, "Satellite communications at Ku, Ka, and V bands: propagation impairments and mitigation techniques", *IEEE Commun. Surv. Tutorials*, vol. 6, no. 3, pp. 2–14, 2004.

[16] H. Kaushal and G. Kaddoum, "Optical communication in space: challenges and mitigation techniques", *IEEE Commun. Surv. Tutorials*, vol. 19, no. 1, pp. 57–96, 2017.

[17] R. E. Hall, B. Bowerman, J. Braverman, J. Taylor, H. Todosow, and U. Von Wimmersperg, "The vision of a smart city", *2nd Int. Life Extens. Technol. Workshop*, Oct. 30, 2000.

[18] Q. C. Li, H. Niu, A. T. Papathanassiou, and G. Wu, "5G network capacity: key elements and technologies", *IEEE Veh. Technol. Mag.*, vol. 9, no. 1, pp. 71–78, Mar. 2014.

[19] M. Giordani, M. Polese, M. Mezzavilla, S. Rangan, and M. Zorzi, "Toward 6G networks: use cases and technologies", *IEEE Commun. Mag.*, vol. 58, no. 3, pp. 55–61, Mar. 2020.

[20] P. Hu, P. Zhang, M. Rostami, and D. Ganesan, "Braidio: an integrated active-passive radio for mobile devices with asymmetric energy budgets", in *Proc. 2016 ACM SIGCOMM Conf.*, Florianopolis Brazil, Aug. 22, 2016, pp. 384–397.

[21] A. Welkie, L. Shangguan, J. Gummeson, W. Hu, and K. Jamieson, "Programmable radio environments for smart spaces", in *Proc. 16th ACM Workshop Hot Topics Netw.*, Nov. 2017, pp. 36–42.

[22] C. Liaskos, S. Nie, A. Tsioliaridou, A. Pitsillides, S. Ioannidis, and I. Akyildiz, "Realizing wireless communication through software-defined hypersurface environments", in *19th IEEE Int. Symp. World Wirel. Mob. Multimed. Netw. WoWMoM 2018*, Chania, Greece, Jun. 2018, pp. 14–15.

[23] E. Basar, M. Di Renzo, J. De Rosny, M. Debbah, M.-S. Alouini, and R. Zhang, "Wireless communications through reconfigurable intelligent surfaces", *IEEE Access*, vol. 7, pp. 116 753–116 773, Aug. 2019.

[24] M. D. Renzo, M. Debbah, D.-T. Phan-Huy, *et al.*, "Smart radio environments empowered by reconfigurable AI meta-surfaces: an idea whose time has come", *Eurasip J. Wirel. Commun. Netw.*, vol. 2019, no. 1, p. 129, Dec. 2019.

[25] R. Alaee, M. Albooyeh, and C. Rockstuhl, "Theory of metasurface based perfect absorbers", *J. Phys. D: Appl. Phys.*, vol. 50, no. 50, p. 503 002, Dec. 20, 2017.

[26] G. Labate, A. Alù, and L. Matekovits, "Surface-admittance equivalence principle for nonradiating and cloaking problems", *Phys. Rev. A*, vol. 95, no. 6, p. 063 841, Jun. 26, 2017.

[27] Y. Chen, J. Gao, and X. Yang, "Direction-controlled bifunctional metasurface polarizers", *Laser Photonics Rev.*, vol. 12, no. 12, p. 1 800 198, Dec. 2018.

[28] E. Abdo-Sanchez, M. Chen, A. Epstein, and G. V. Eleftheriades, "A leaky-wave antenna with controlled radiation using a bianisotropic Huygens' metasurface", *IEEE Trans. Antennas Propagat.*, vol. 67, no. 1, pp. 108–120, Jan. 2019.

[29] M. Khorasaninejad, F. Aieta, P. Kanhaiya, *et al.*, "Achromatic metasurface lens at telecommunication wavelengths", *Nano Lett.*, vol. 15, no. 8, pp. 5358–5362, Aug. 12, 2015.

[30] Q. Yang, J. Gu, D. Wang, *et al.*, "Efficient flat metasurface lens for terahertz imaging", *Opt. Express*, vol. 22, no. 21, p. 25 931, Oct. 20, 2014.

[31] Y. Ra'di, V. S. Asadchy, and S. A. Tretyakov, "Tailoring reflections from thin composite metamirrors", *IEEE Trans. Antennas Propagat.*, vol. 62, no. 7, pp. 3749–3760, Jul. 2014.

[32] C. Pfeiffer and A. Grbic, "Millimeter-wave transmitarrays for wavefront and polarization control", *IEEE Trans. Microw. Theory Tech.*, vol. 61, no. 12, pp. 4407–4417, Dec. 2013.

[33] S. R. Biswas, C. E. Gutiérrez, A. Nemilentsau, *et al.*, "Tunable graphene metasurface reflectarray for cloaking, illusion, and focusing", *Phys. Rev. Appl.*, vol. 9, no. 3, p. 034 021, Mar. 23, 2018.

[34] Q. Wu and R. Zhang, "Towards smart and reconfigurable environment: intelligent reflecting surface aided wireless network", *IEEE Commun. Mag.*, vol. 58, no. 1, pp. 106–112, Jan. 2020.

[35] H. Zhang, S. Zeng, B. Di, *et al.*, "Intelligent omni-surfaces for full-dimensional wireless communications: principles, technology, and implementation", *IEEE Commun. Mag.*, vol. 60, no. 2, pp. 39–45, Feb. 2022.

[36] J. Xu, Y. Liu, X. Mu, and O. A. Dobre, "STAR-RISs: simultaneous transmitting and reflecting reconfigurable intelligent surfaces", *IEEE Commun. Lett.*, vol. 25, no. 9, pp. 3134–3138, Sep. 2021.

[37] Y. Liu, X. Mu, J. Xu, *et al.*, "STAR: simultaneous transmission and reflection for 360° coverage by intelligent surfaces", *IEEE Wirel. Commun.*, vol. 28, no. 6, pp. 102–109, Dec. 2021.

[38] M. Ahmed, A. Wahid, S. S. Laique, *et al.*, "A survey on STAR-RIS: use cases, recent advances, and future research challenges", *IEEE Internet Things J.*, vol. 10, no. 16, pp. 14 689–14 711, Aug. 15, 2023.

[39] J. Xu, J. Zuo, J. T. Zhou, and Y. Liu, "Active simultaneously transmitting and reflecting (STAR)-RISs: modeling and analysis", *IEEE Commun. Lett.*, vol. 27, no. 9, pp. 2466–2470, Sep. 2023.

[40] Y. Liu, J. Xu, Z. Wang, X. Mu, J. Zhang, and P. Zhang, "Simultaneously transmitting and reflecting (STAR) RISs for 6G: fundamentals, recent advances, and future directions", *Front. Inf. Technol. Electron. Eng.*, vol. 24, no. 12, pp. 1689–1707, Dec. 2023.

[41] S. L. Liu, X. Q. Lin, Y. H. Yan, and Y. L. Fan, "Generation of a high-gain bidirectional transmit–reflect-array antenna with asymmetric beams using sparse-array method", *IEEE Trans. Antennas Propag.*, vol. 69, no. 9, pp. 6087–6092, Sep. 2021.

[42] H. Yu, P. Li, J. Su, Z. Li, S. Xu, and F. Yang, "Reconfigurable bidirectional beam-steering aperture with transmitarray, reflectarray, and transmit-reflect-array modes switching", *IEEE Trans. Antennas Propag.*, vol. 71, no. 1, pp. 581–595, Jan. 2023.

[43] X. Guo, Y. Luo, N. Yan, W. An, and K. Ma, "Multibeam transmit-reflect-array antenna using alternating transmission and reflection elements for space–air–ground–sea integrated network", *IEEE Trans. Antennas Propag.*, vol. 71, no. 11, pp. 8668–8676, Nov. 2023.

[44] T. Cai, G.-M. Wang, X.-L. Fu, J.-G. Liang, and Y.-Q. Zhuang, "High-efficiency metasurface with polarization-dependent transmission and reflection properties for both reflectarray and transmitarray", *IEEE Trans. Antennas Propag.*, vol. 66, no. 6, pp. 3219–3224, Jun. 2018.

[45] W. Song, Q. Xue, Y. Cai, *et al.*, "A single-layer reflect-transmit-array antenna with polarization-dependent operation", *IEEE Access*, vol. 9, pp. 167 928–167 935, Dec. 2021.

[46] M. Wang, S. Xu, F. Yang, and M. Li, "A 1-bit bidirectional reconfigurable transmit-reflect-array using a single-layer slot element with PIN diodes", *IEEE Trans. Antennas Propag.*, vol. 67, no. 9, pp. 6205–6210, Sep. 2019.

[47] P. Jiang, W. Jiang, W. Hu, and S. Gong, "A mesh-type shared-aperture dual-band circularly polarized transmit- reflect-array antenna", *IEEE Trans. Antennas Propagat.*, vol. 71, no. 2, pp. 1590–1601, Feb. 2023.

[48] F. Yang, R. Deng, S. Xu, and M. Li, "Design and experiment of a near-zero-thickness high-gain transmit-reflect-array antenna using anisotropic metasurface", *IEEE Trans. Antennas Propag.*, vol. 66, no. 6, pp. 2853–2861, Jun. 2018.

[49] S. Liu and Q. Chen, "A wideband, multifunctional reflect-transmit-array antenna with polarization-dependent operation", *IEEE Trans. Antennas Propag.*, vol. 69, no. 3, pp. 1383–1392, Mar. 2021.

[50] L.-X. Wu, K. Chen, T. Jiang, J. Zhao, and Y. Feng, "Circular-polarization-selective metasurface and its applications to transmit-reflect-array antenna and bidirectional antenna", *IEEE Trans. Antennas Propag.*, vol. 70, no. 11, pp. 10 207–10 217, Nov. 2022.

[51] X. Liu, Z. Yan, E. Wang, X. Zhao, T. Zhang, and F. Fan, "Bifunctional full-space metasurface combining pancharatnam–berry and propagation phases", *IEEE Antennas Wirel. Propag. Lett.*, vol. 21, no. 10, pp. 2110–2114, Oct. 2022.

[52] M. Kim and G. V. Eleftheriades, "Guided-wave-excited binary Huygens' metasurfaces for dynamic radiated-beam shaping with independent gain and scan-angle control", *Phys. Rev. Appl.*, vol. 15, no. 5, p. 054 037, May 17, 2021.

[53] D. Sivukhin, "The energy of electromagnetic waves in dispersive media", *Opt. Spektrosk*, vol. 3, no. 4, pp. 308–312, 1957.

[54] V. G. Veselago, "The electrodynamics of substances with simultaneously negative values of ϵ and μ", *Sov. Phys. Usp.*, vol. 10, no. 4, pp. 509–514, Apr. 30, 1968.

[55] H. Lamb, "On group - velocity", *Proc. Lond. Math. Soc.*, vol. s2-1, no. 1, pp. 473–479, 1904.

[56] A. Schuster, *An introduction to the theory of optics*. E. Arnold, 1904.

[57] D. R. Smith, W. J. Padilla, D. C. Vier, S. C. Nemat-Nasser, and S. Schultz, "Composite medium with simultaneously negative permeability and permittivity", *Phys. Rev. Lett.*, vol. 84, no. 18, pp. 4184–4187, May 1, 2000.

[58] J. B. Pendry, "Negative refraction makes a perfect lens", *Phys. Rev. Lett.*, vol. 85, no. 18, pp. 3966–3969, Oct. 30, 2000.

[59] R. A. Shelby, D. R. Smith, and S. Schultz, "Experimental verification of a negative index of refraction", *Science*, vol. 292, no. 5514, pp. 77–79, Apr. 6, 2001.

[60] W. J. Padilla, D. N. Basov, and D. R. Smith, "Negative refractive index metamaterials", *Materials Today*, vol. 9, no. 7, pp. 28–35, Jul. 2006.

[61] R. M. Walser, "Metamaterials: What are they? What are they good for?", in *APS March Meet. Abstr.*, Mar. 2000, Z5.001.

[62] R. M. Walser, "Electromagnetic metamaterials", in *Int. Symp. Opt. Sci. Technol.*, A. Lakhtakia, W. S. Weiglhofer, and I. J. Hodgkinson, Eds., San Diego, CA, USA, Jul. 9, 2001, p. 1.

[63] R. W. Ziolkowski, "Metamaterials: the early years in the USA", *EPJ Appl. Metamat.*, vol. 1, p. 5, 2014.

[64] S. Maci, "Electromagnetic metamaterials and metasurfaces: a historical journey", *IEEE Antennas Propag. Mag.*, vol. 66, no. 3, pp. 84–101, Jun. 2024.

[65] E. Shamonina and L. Solymar, "Metamaterials: how the subject started", *Metamaterials*, vol. 1, no. 1, pp. 12–18, Mar. 2007.

[66] A. Sihvola, I. Semchenko, and S. Khakhomov, "View on the history of electromagnetics of metamaterials: evolution of the congress series of complex media", *Photonics Nanostruct. Fundam. Appl.*, vol. 12, no. 4, pp. 279–283, Aug. 2014.

[67] A. Sihvola, "Electromagnetic emergence in metamaterials", in *Adv. Electromagn. Complex Media Metamaterials*, S. Zouhdi, A. Sihvola, and M. Arsalane, Eds., Dordrecht: Springer Netherlands, 2002, pp. 3–17.

[68] A. Sihvola, "Metamaterials in electromagnetics", *Metamaterials*, vol. 1, no. 1, pp. 2–11, Mar. 2007.

[69] A. Sihvola, "Metamaterials: a personal view", *Radioengineering*, vol. 18, no. 2, pp. 90–94, Jun. 2009.

[70] W. Cai, U. K. Chettiar, A. V. Kildishev, and V. M. Shalaev, "Optical cloaking with metamaterials", *Nat. Photon.*, vol. 1, no. 4, pp. 224–227, Apr. 2007.

[71] J. Hunt, T. Driscoll, A. Mrozack, *et al.*, "Metamaterial apertures for computational imaging", *Science*, vol. 339, no. 6117, pp. 310–313, Jan. 18, 2013.

[72] T. Chen, S. Li, and H. Sun, "Metamaterials application in sensing", *Sensors*, vol. 12, no. 3, pp. 2742–2765, Feb. 29, 2012.

[73] M. T. Islam, M. Samsuzzaman, M. T. Islam, and S. Kibria, "Experimental breast phantom imaging with metamaterial-inspired nine-antenna sensor array", *Sensors*, vol. 18, no. 12, p. 4427, Dec. 14, 2018.

[74] Yuandan Dong and T. Itoh, "Metamaterial-based antennas", *Proc. IEEE*, vol. 100, no. 7, pp. 2271–2285, Jul. 2012.

[75] F. Ding, Y. Cui, X. Ge, Y. Jin, and S. He, "Ultra-broadband microwave metamaterial absorber", *Appl. Phys. Lett.*, vol. 100, no. 10, p. 103 506, Mar. 5, 2012.

[76] N. I. Landy, S. Sajuyigbe, J. J. Mock, D. R. Smith, and W. J. Padilla, "Perfect metamaterial absorber", *Phys. Rev. Lett.*, vol. 100, no. 20, p. 207 402, May 21, 2008.

[77] A. N. Lagarkov, V. N. Kisel, and A. K. Sarychev, "Loss and gain in metamaterials", *J. Opt. Soc. Am. B*, vol. 27, no. 4, pp. 648–659, Apr. 1, 2010.

[78] Z. Liang, T. Feng, S. Lok, *et al.*, "Space-coiling metamaterials with double negativity and conical dispersion", *Sci. Rep.*, vol. 3, no. 1, p. 1614, Apr. 8, 2013.

[79] G. Yoon, I. Kim, and J. Rho, "Challenges in fabrication towards realization of practical metamaterials", *Microelectronic Engineering*, vol. 163, pp. 7–20, Sep. 2016.

[80] P. Cheben, J. H. Schmid, R. Halir, *et al.*, "Recent advances in metamaterial integrated photonics", *Adv. Opt. Photon.*, vol. 15, no. 4, p. 1033, Dec. 31, 2023.

[81] I. Radko, V. Volkov, J. Beermann, *et al.*, "Plasmonic metasurfaces for waveguiding and field enhancement", *Laser Photonics Rev.*, vol. 3, no. 6, pp. 575–590, Nov. 2, 2009.

[82] C. L. Holloway, E. F. Kuester, J. A. Gordon, J. O'Hara, J. Booth, and D. R. Smith, "An overview of the theory and applications of metasurfaces: the two-dimensional equivalents of metamaterials", *IEEE Antennas Propag. Mag.*, vol. 54, no. 2, pp. 10–35, Feb. 2012.

[83] N. Yu, P. Genevet, M. A. Kats, *et al.*, "Light propagation with phase discontinuities: generalized laws of reflection and refraction", *Science*, vol. 334, no. 6054, pp. 333–337, Oct. 21, 2011.

[84] X. Ni, N. K. Emani, A. V. Kildishev, A. Boltasseva, and V. M. Shalaev, "Broadband light bending with plasmonic nanoantennas", *Science*, vol. 335, no. 6067, pp. 427–427, Jan. 27, 2012.

[85] X. Ni, S. Ishii, A. V. Kildishev, and V. M. Shalaev, "Ultra-thin, planar, Babinet-inverted plasmonic metalenses", *Light Sci. Appl.*, vol. 2, no. 4, e72–e72, Apr. 26, 2013.

[86] C. Pfeiffer and A. Grbic, "Metamaterial Huygens' surfaces: tailoring wave fronts with reflectionless sheets", *Phys. Rev. Lett.*, vol. 110, pp. 1–5, 19 May 2013.

[87] M. Selvanayagam and G. V. Eleftheriades, "Discontinuous electromagnetic fields using orthogonal electric and magnetic currents for wavefront manipulation", *Opt. Express*, vol. 21, no. 12, p. 14 409, Jun. 17, 2013.

[88] F. Monticone, N. M. Estakhri, and A. Alù, "Full control of nanoscale optical transmission with a composite metascreen", *Phys. Rev. Lett.*, vol. 110, no. 20, p. 203 903, May 14, 2013.

[89] C. Huygens, *Traité de la lumière : Où sont expliquées les causes de ce qui lui arrive dans la reflexion, & dans la refraction et particulièrement dans l'étrange réfraction du cristal d'Islande*. Leiden: Chez Pieter van der Aa, marchand libraire, 1690.

[90] A. E. H. Love, "The integration of the equations of propagation of electric waves", *Philos. Trans. R. Soc. Lond. A*, vol. 197, pp. 1–45, 1901.

[91] S. A. Schelkunoff, "Some equivalence theorems of electromagnetics and their application to radiation problems", *Bell Syst. Tech. J.*, vol. 15, no. 1, pp. 92–112, Jan. 1936.

[92] R. F. Harrington, *Time-harmonic electromagnetic fields*. New York: IEEE Press: Wiley-Interscience, 2001, 480 pp.

[93] V. G. Ataloglou, M. Chen, M. Kim, and G. V. Eleftheriades, "Microwave Huygens' metasurfaces: fundamentals and applications", *IEEE J. Microw.*, vol. 1, no. 1, pp. 374–388, Jan. 2021.

[94] M. Albooyeh, V. Asadchy, J. Zeng, *et al.*, "Classification of bianisotropic metasurfaces from reflectance and transmittance measurements", *ACS Photonics*, vol. 10, no. 1, pp. 71–83, Feb. 2023.

[95] C. Pfeiffer and A. Grbic, "Bianisotropic metasurfaces for optimal polarization control: analysis and synthesis", *Phys. Rev. Appl.*, vol. 2, no. 4, pp. 1–11, Oct. 2014.

[96] D. M. Pozar, *Microwave Engineering, 4th Edition*. USA: John Wiley & Sons, 2011.

[97] F. Mesa, G. Valerio, R. Rodriguez-Berral, and O. Quevedo-Teruel, "Simulation-assisted efficient computation of the dispersion diagram of periodic structures: a comprehensive overview with applications to filters, leaky-wave antennas and metasurfaces", *IEEE Antennas Propag. Mag.*, vol. 63, no. 5, pp. 33–45, Oct. 2021.

[98] T. Reveyrand, "Multiport conversions between S, Z, Y, h, ABCD, and T parameters", in *2018 Int. Workshop Integr. Nonlinear Microw. Millimetre-wave Circuits (INMMIC)*, Brive La Gaillarde, France, Jul. 2018, pp. 1–3.

[99] A. Epstein and G. V. Eleftheriades, "Huygens' metasurfaces via the equivalence principle: design and applications", *J. Opt. Soc. Am. B*, vol. 33, no. 2, A31–A50, Feb. 2016.

[100] A. Epstein and G. V. Eleftheriades, "Arbitrary power-conserving field transformations with passive lossless omega-type bianisotropic metasurfaces", *IEEE Trans. Antennas Propag.*, vol. 64, no. 9, pp. 3880–3895, Sep. 2016.

[101] L. B. Felsen and N. Marcuvitz, *Radiation and scattering of waves* (IEEE Press series on electromagnetic waves). New York: Inst. of Electrical and Electronics Engineers, 2003, 888 pp.

[102] F. F. Manzillo, M. Ettorre, R. Sauleau, and A. Grbic, "Systematic design of a class of wideband circular polarizers using dispersion engineering", in *11th Eur. Conf. Antennas Propag. (EuCAP) 2017*, Paris, France, Mar. 2017, pp. 1279–1281.

[103] J. Y. Lau and S. V. Hum, "A planar reconfigurable aperture with lens and reflectarray modes of operation", *IEEE Trans. Microw. Theory Tech.*, pp. 3547–3555, Dec. 2010.

[104] H. A. E.-A. Malhat, M. M. Badawy, S. H. Zainud-Deen, and K. H. Awadalla, "Dual-mode plasma reflectarray/ transmitarray antennas", *IEEE Trans. Plasma Sci.*, vol. 43, no. 10, pp. 3582–3589, Oct. 2015.

[105] H.-X. Xu, S. Tang, G.-M. Wang, *et al.*, "Multifunctional microstrip array combining a linear polarizer and focusing metasurface", *IEEE Trans. Antennas Propagat.*, vol. 64, no. 8, pp. 3676–3682, Aug. 2016.

[106] T. Cai, G. Wang, S. Tang, *et al.*, "High-efficiency and full-space manipulation of electromagnetic wave fronts with metasurfaces", *Phys. Rev. Applied*, vol. 8, no. 3, p. 034 033, Sep. 28, 2017.

[107] H. Yi, S.-W. Qu, K.-B. Ng, C. K. Wong, and C. H. Chan, "Terahertz wavefront control on both sides of the cascaded metasurfaces", *IEEE Trans. Antennas Propagat.*, vol. 66, no. 1, pp. 209–216, Jan. 2018.

[108] Á. Palomares-Caballero, C. Molero, J. F. Valenzuela-Valdés, P. Padilla, M. García-Vigueras, and R. Gillard, "Metal-only reflect-transmit-array unit cell with polarization-dependent performance", in *17th Eur. Conf. Antennas Propag. (EuCAP) 2023*, Florence, Italy, Mar. 2023, pp. 1–5.

[109] Z. An, T. Makdissy, M. García-Vigueras, S. Vaudreuil, and R. Gillard, "3d metal-only phoenix cell and its application for transmit-reflect-array", *IEEE Access*, vol. 11, pp. 137 343–137 351, 2023.

[110] Q. Zhou, L. Gao, and L. Guo, "A metal-only reflect-transmit-array antenna with polarization-dependent operations", *IEEE Antennas Wirel. Propag. Lett.*, pp. 1–5, 2024.

[111] Z. Zheng, L. Zhang, Q. Luo, C. Mao, Y. He, and S. Gao, "Wideband 3D-printed transmit-reflect-array antenna with independent beam control", *IEEE Trans. Antennas Propag.*, vol. 71, no. 7, pp. 6196–6201, Jul. 2023.

[112] Y. Gao, Z. Wang, H. Tang, Q. Luo, and W. Hu, "Ultrawideband transmit-reflect-array antenna for 6G communication", *IEEE Antennas Wirel. Propag. Lett.*, pp. 1–5, 2024.

[113] G. Shang, H. Li, Z. Wang, *et al.*, "Transmission–reflection-integrated multiplexed janus metasurface", *ACS Appl. Electron. Mater.*, vol. 3, no. 6, pp. 2638–2645, Jun. 22, 2021.

[114] W. Yang, K. Tang, Y. Zhu, K. Chen, and Y. Feng, "Wideband transmit-reflect-array using optimized mosaic metasurface: toward dual-circularly polarized beam coverage in full space", in *2023 IEEE 11th Asia-Pac. Conf. Antennas Propag. (APCAP)*, Guangzhou, China, Nov. 22, 2023, pp. 1–2.

[115] H. L. Wang, H. F. Ma, M. Chen, S. Sun, and T. J. Cui, "A reconfigurable multifunctional metasurface for full-space control of electromagnetic waves", *Adv. Funct. Mater.*, vol. 31, no. 25, p. 2 100 275, Jun. 2021.

[116] L. Bao, Q. Ma, R. Y. Wu, X. Fu, J. Wu, and T. J. Cui, "Programmable reflection–transmission shared-aperture metasurface for real-time control of electromagnetic waves in full space", *Adv. Sci.*, vol. 8, no. 15, p. 2 100 149, Aug. 2021.

[117] S. A. Qureshi, M. R. Kamarudin, M. I. Abbasi, *et al.*, "VO_2-based switchable transmit-reflect-array for THz applications", in *2023 IEEE Int. Symp. Antennas Propag. USNC-URSI Radio Sci. Meet.*, Portland, OR, USA, Jul. 23, 2023, pp. 1507–1508.

[118] H. Li, K. Xin, H. Ding, T. Li, G. Hu, and H.-X. Xu, "Programmable metasurface for front-back scattering communication", *Nanophotonics*, vol. 12, no. 18, pp. 3653–3661, Sep. 12, 2023.

[119] T. Yin, J. Ren, B. Zhang, P. Li, Y. Luan, and Y. Yin, "Reconfigurable transmission-reflection-integrated coding metasurface for full-space electromagnetic wavefront manipulation", *Adv. Opt. Mater.*, vol. 12, no. 2, p. 2 301 326, Jan. 2024.

[120] Y. Liu, J. Kelly, M. Holm, S. Gopal, S. R. Aghdam, and Y. Liu, "Unit cell design for intelligent reflecting and refracting surface (IRS) with independent electronic control capability", *IEEE Antennas Wirel. Propag. Lett.*, vol. 23, no. 1, pp. 414–418, Jan. 2024.

[121] Y. Mu, D. Xia, J. Han, H. Liu, and L. Li, "Low in-band RCS reconfigurable metasurface with LP feed for CP transmission, LP reflection and simultaneous transmission-reflection modes switching", *IEEE Trans. Antennas Propagat.*, pp. 1–1, 2024.

[122] Y. Zhao, D. Wang, H. Gu, *et al.*, "Design of a novel wideband reconfigurable transmit-reflect-array antenna utilizing twin lines", *IEEE Trans. Antennas Propagat.*, vol. 72, no. 3, pp. 2897–2902, Mar. 2024.

[123] C. Zhang, Y. Luo, N. Yan, X. Guo, Y. Guo, and K. Ma, "A reconfigurable metasurface with precise phase distribution for both transmission and reflection functions", *IEEE Trans. Antennas Propagat.*, vol. 72, no. 9, pp. 7154–7163, Sep. 2024.

[124] X. Zhong, H.-X. Xu, L. Chen, W. Li, H. Wang, and X. Shi, "An FSS-backed broadband phase-shifting surface array with multimode operation", *IEEE Trans. Antennas Propag.*, vol. 67, no. 9, pp. 5974–5981, Sep. 2019.

[125] S. Yang, Z. Yan, T. Zhang, M. Cai, F. Fan, and X. Li, "Multifunctional tri-band dual-polarized antenna combining transmitarray and reflectarray", *IEEE Trans. Antennas Propag.*, vol. 69, no. 9, pp. 6016–6021, Sep. 2021.

[126] J. Yin, Y. Zhang, and S. He, "Wideband transmit-reflect-array with tilted beams considering beam squint effect", *IEEE Antennas Wirel. Propag. Lett.*, pp. 1–5, 2024.

[127] W. Yang, K. Chen, J. Zhao, T. Jiang, and Y. Feng, "A wideband high-efficiency transmit-reflect-array antenna for bidirectional radiations with distinct circular polarizations based on a metasurface", *IEEE Trans. Antennas Propagat.*, vol. 71, no. 4, pp. 3695–3700, Apr. 2023.

[128] B. Xi, Q. Xue, Y. Cai, *et al.*, "Design of a dual-polarized reflect-transmit-array", *Microw. Opt. Technol. Lett.*, vol. 62, no. 2, pp. 949–955, Feb. 2020.

[129] X. Liu, Z. Yan, E. Wang, X. Zhao, T. Zhang, and F. Fan, "Dual-band orthogonally-polarized dual-beam reflect-transmit-array with a linearly polarized feeder", *IEEE Trans. Antennas Propag.*, vol. 70, no. 9, pp. 8596–8601, Sep. 2022.

[130] M. Chen, M. Kim, A. M. Wong, and G. V. Eleftheriades, "Huygens' metasurfaces from microwaves to optics: a review", *Nanophotonics*, vol. 7, no. 6, pp. 1207–1231, Jun. 27, 2018.

[131] G. V. Eleftheriades, M. Kim, V. G. Ataloglou, and A. H. Dorrah, "Prospects of Huygens' metasurfaces for antenna applications", *Engineering*, vol. 11, pp. 21–26, Apr. 2022.

[132] P. Jin and R. W. Ziolkowski, "Metamaterial-inspired, electrically small Huygens sources", *IEEE Antennas Wirel. Propag. Lett.*, vol. 9, pp. 501–505, 2010.

[133] C. Pfeiffer, N. K. Emani, A. M. Shaltout, A. Boltasseva, V. M. Shalaev, and A. Grbic, "Efficient light bending with isotropic metamaterial huygens' surfaces", *Nano Lett.*, vol. 14, no. 5, pp. 2491–2497, May 14, 2014.

[134] M. Decker, I. Staude, M. Falkner, *et al.*, "High-efficiency dielectric Huygens' surfaces", *Adv. Opt. Mater.*, vol. 3, no. 6, pp. 813–820, Jun. 2015.

[135] C. Pfeiffer and A. Grbic, "Controlling vector bessel beams with metasurfaces", *Phys. Rev. Applied*, vol. 2, no. 4, p. 044 012, Oct. 23, 2014.

[136] M. Selvanayagam and G. V. Eleftheriades, "Polarization control using tensor Huygens surfaces", *IEEE Trans. Antennas Propag.*, vol. 62, no. 12, pp. 6155–6168, Sep. 2014.

[137] M. Kim, A. M. H. Wong, and G. V. Eleftheriades, "Optical Huygens' metasurfaces with independent control of the magnitude and phase of the local reflection coefficients", *Phys. Rev. X*, vol. 4, no. 4, p. 041 042, Dec. 9, 2014.

[138] J. P. S. Wong, M. Selvanayagam, and G. V. Eleftheriades, "Polarization considerations for scalar Huygens metasurfaces and characterization for 2-d refraction", *IEEE Trans. Microw. Theory Tech.*, vol. 63, no. 3, pp. 913–924, Mar. 2015.

[139] A. Epstein, J. P. S. Wong, and G. V. Eleftheriades, "Cavity-excited Huygens' metasurface antennas for near-unity aperture illumination efficiency from arbitrarily large apertures", *Nat. Commun.*, vol. 7, no. 1, p. 10 360, Jan. 21, 2016.

[140] J. P. S. Wong, A. Epstein, and G. V. Eleftheriades, "Reflectionless wide-angle refracting metasurfaces", *IEEE Antennas Wireless Propag. Lett.*, vol. 15, pp. 1293–1296, Dec. 2015.

[141] D. Brewster, "IX. on the laws which regulate the polarisation of light by reflexion from transparent bodies.", *Phil. Trans. R. Soc.*, vol. 105, pp. 125–159, Dec. 31, 1815, LL. D. F. R. S. Edin. and F. S. A. Edin. In a letter addressed to Right Hon. Sir Joseph Banks, Bart. K. B. P. R. S.

[142] E. Hecht, *Optics, 5th Edition*. Boston: Pearson Education, Inc, 2017, 714 pp.

[143] Y. Tamayama, T. Nakanishi, K. Sugiyama, and M. Kitano, "Observation of Brewster's effect for transverse-electric electromagnetic waves in metamaterials: experiment and theory", *Phys. Rev. B*, vol. 73, no. 19, p. 193 104, May 17, 2006.

[144] M. Selvanayagam and G. V. Eleftheriades, "Design and measurement of tensor impedance transmitarrays for chiral polarization control", *IEEE Trans. Microw. Theory Tech.*, vol. 64, no. 2, pp. 414–428, Feb. 2016.

[145] A. M. H. Wong, P. Christian, and G. V. Eleftheriades, "Binary Huygens' metasurfaces: experimental demonstration of simple and efficient near-grazing retroreflectors for TE and TM polarizations", *IEEE Trans. Antennas Propagat.*, vol. 66, no. 6, pp. 2892–2903, Jun. 2018.

[146] L. W. Wu, H. F. Ma, Y. Gou, *et al.*, "High-transmission ultrathin Huygens' metasurface with 360° phase control by using double-layer transmitarray elements", *Phys. Rev. Appl.*, vol. 12, no. 2, p. 024 012, Aug. 7, 2019.

[147] L.-Z. Song, P.-Y. Qin, and Y. J. Guo, "A high-efficiency conformal transmitarray antenna employing dual-layer ultrathin Huygens element", *IEEE Trans. Antennas Propagat.*, vol. 69, no. 2, pp. 848–858, Feb. 2021.

[148] J.-W. Lian, Y.-L. Ban, and Y. J. Guo, "Wideband dual-layer Huygens' metasurface for high-gain multibeam array antennas", *IEEE Trans. Antennas Propagat.*, vol. 69, no. 11, pp. 7521–7531, Nov. 2021.

[149] C. Xue, J. Sun, X. Gao, *et al.*, "An ultrathin, low-profile and high-efficiency metalens antenna based on chain Huygens' metasurface", *IEEE Trans. Antennas Propagat.*, vol. 70, no. 12, pp. 11 442–11 453, Dec. 2022.

[150] L. Szymanski, B. O. Raeker, C.-W. Lin, and A. Grbic, "Fundamentals of lossless, reciprocal bianisotropic metasurface design", *Photonics*, vol. 8, no. 6, p. 197, Jul. 2021.

[151] A. H. Abdelrahman, A. Z. Elsherbeni, and F. Yang, "Transmission phase limit of multilayer frequency-selective surfaces for transmitarray designs", *IEEE Trans. Antennas Propagat.*, vol. 62, no. 2, pp. 690–697, Feb. 2014.

[152] T. Feng, A. A. Potapov, Z. Liang, and Y. Xu, "Huygens' metasurfaces based on congener dipole excitations", *Phys. Rev. Appl.*, vol. 13, p. 021 002, 2 Feb. 2020.

[153] M. Selvanayagam and G. V. Eleftheriades, "Circuit modeling of Huygens surfaces", *IEEE Antennas Wireless Propag. Lett.*, vol. 12, pp. 1642–1645, Mar. 2013.

[154] J.-F. Ma, R. Mittra, and N. Huang, "Analysis of multiple FSS screens of unequal periodicity using an efficient cascading technique", *IEEE Trans. Antennas Propagat.*, vol. 53, no. 4, pp. 1401–1414, Apr. 2005.

[155] B. Munk, *Frequency selective surfaces: theory and design*. New York: John Wiley, 2000.

[156] J. Budhu and A. Grbic, "Perfectly reflecting metasurface reflectarrays: mutual coupling modeling between unique elements through homogenization", *IEEE Trans. Antennas Propag.*, vol. 69, no. 1, pp. 122–134, Jan. 2021.

[157] D. Pozar, "Wideband reflectarrays using artificial impedance surfaces", *IEEE Electron. Lett.*, vol. 43, no. 3, p. 148, 2007.

[158] L. Yin, C. Jin, Q. Lv, *et al.*, "Amplitude and phase independently adjustable transmitarray aperture and its applications to high gain and low sidelobe antenna", *IEEE Trans. Antennas Propagat.*, vol. 70, no. 6, pp. 4498–4506, Jun. 2022.

[159] O. Koutsos, F. F. Manzillo, A. Clemente, and R. Sauleau, "Analysis, rigorous design, and characterization of a three-layer anisotropic transmitarray at 300 GHz", *IEEE Trans. Antennas Propagat.*, vol. 70, no. 7, pp. 5437–5446, Jul. 2022.

[160] A. A. Elsakka, V. S. Asadchy, I. A. Faniayeu, S. N. Tcvetkova, and S. A. Tretyakov, "Multifunctional cascaded metamaterials: integrated transmitarrays", *IEEE Trans. Antennas Propagat.*, vol. 64, no. 10, pp. 4266–4276, Oct. 2016.

[161] W. Yang, K. Chen, and Y. Feng, "Multifunctional metasurface for broadband reflect-transmit-array antenna at 5G millimeter-wave band", in *16th Eur. Conf. Antennas Propag. (EuCAP) 2022*, Madrid, Spain, Mar. 2022, pp. 1–5.

[162] D. Pozar, S. Targonski, and H. Syrigos, "Design of millimeter wave microstrip reflectarrays", *IEEE Trans. Antennas Propagat.*, vol. 45, no. 2, pp. 287–296, Feb. 1997.

[163] T. A. Milligan, *Modern antenna design*, 2nd ed. Hoboken, N. J: John Wiley & sons, 2005.

[164] A. Yu, F. Yang, A. Z. Elsherbeni, J. Huang, and Y. Rahmat-Samii, "Aperture efficiency analysis of reflectarray antennas", *Micro Opt. Tech. Lett.*, vol. 52, no. 2, pp. 364–372, Feb. 2010.

[165] C. A. Balanis, *Antenna Theory: Analysis and Design, 4th Edition*. New Jersey, USA: John Wiley & Sons, 2015.

[166] Y. T. Lo and S. W. Lee, Eds., *Antenna handbook: theory, applications, and design*, Softcover reprint of the hardcover 1st edition 1988, New York: Springer Science + Business Media, 1988, 3 pp.

[167] E. Plaza, G. Leon, S. Loredo, and F. Las-Heras, "A simple model for analyzing transmitarray lenses", *IEEE Antennas and Propagation Magazine*, vol. 57, no. 2, pp. 131–144, Apr. 2015.

[168] A. H. Abdelrahman, F. Yang, A. Z. Elsherbeni, and P. Nayeri, *Analysis and design of transmitarray antennas*. Cham, Switzerland: Springer, 2017.

[169] H. Yang, F. Yang, S. Xu, *et al.*, "A study of phase quantization effects for reconfigurable reflectarray antennas", *IEEE Antennas Wireless Propag. Lett.*, vol. 16, pp. 302–305, Feb. 2017.

[170] A. H. Abdelrahman, P. Nayeri, A. Z. Elsherbeni, and F. Yang, "Bandwidth improvement methods of transmitarray antennas", *IEEE Trans. Antennas Propagat.*, vol. 63, no. 7, pp. 2946–2954, Jul. 2015.

[171] Y. Zhao, M. Belkin, and A. Alù, "Twisted optical metamaterials for planarized ultrathin broadband circular polarizers", *Nat Commun*, vol. 3, no. 1, p. 870, May 29, 2012.

[172] T. Niemi, A. O. Karilainen, and S. A. Tretyakov, "Synthesis of polarization transformers", *IEEE Trans. Antennas Propagat.*, vol. 61, no. 6, pp. 3102–3111, Jun. 2013.

[173] V. S. Asadchy, Y. Ra'di, J. Vehmas, and S. A. Tretyakov, "Functional metamirrors using bianisotropic elements", *Phys. Rev. Lett.*, vol. 114, no. 9, p. 095 503, Mar. 6, 2015.

[174] Y. Ra'di, V. S. Asadchy, and S. A. Tretyakov, "One-way transparent sheets", *Phys. Rev. B*, vol. 89, no. 7, p. 075 109, Feb. 11, 2014.

[175] V. S. Asadchy, I. A. Faniayeu, Y. Ra'di, S. A. Khakhomov, I. V. Semchenko, and S. A. Tretyakov, "Broadband reflectionless metasheets: frequency-selective transmission and perfect absorption", *Phys. Rev. X*, vol. 5, no. 3, p. 031 005, Jul. 14, 2015.

[176] C. Pfeiffer, C. Zhang, V. Ray, L. J. Guo, and A. Grbic, "High performance bianisotropic metasurfaces: asymmetric transmission of light", *Phys. Rev. Lett.*, vol. 113, no. 2, p. 023 902, Jul. 10, 2014.

[177] M. Yazdi, M. Albooyeh, R. Alaee, *et al.*, "A bianisotropic metasurface with resonant asymmetric absorption", *IEEE Trans. Antennas Propag.*, vol. 63, no. 7, pp. 3004–3015, Apr. 2015.

[178] M. Chen, E. Abdo-Sánchez, A. Epstein, and G. V. Eleftheriades, "Theory, design, and experimental verification of a reflectionless bianisotropic Huygens' metasurface for wide-angle refraction", *Phys. Rev. B*, vol. 97, no. 12, p. 125 433, Mar. 29, 2018.

[179] B. O. Raeker and A. Grbic, "Compound metaoptics for amplitude and phase control of wave fronts", *Phys. Rev. Lett.*, vol. 122, p. 113 901, 11 Mar. 2019.

[180] R. Alaee, M. Albooyeh, M. Yazdi, *et al.*, "Magnetoelectric coupling in nonidentical plasmonic nanoparticles: theory and applications", *Phys. Rev. B*, vol. 91, p. 115 119, 11 Mar. 2015.

Curriculum Vitæ

Alessio Berto

Antenna & RF Engineer

Antenna and RF engineer with a deep interest in electromagnetic fields, radiofrequency circuits and telecommunication. My research interests are millimiter-wave antennas, periodic structures, leaky-wave antennas, metasurfaces, transmit-array, reflect-array and transmit-reflect-array.

Contact

Phone
+39 3391102214

Email
alessioberto@yahoo.com

Address
6 Rue Marcel Porte, 38100
Grenoble, France

Linkedin
www.linkedin.com/in/alessio-berto-8518b4149

Expertise

- Antenna, RF, electromagnetics
- HFSS, CST, AWR Microwave office, ADSimRF
- PSpice, Altium
- Matlab, Simulink
- Altera Quartus II, ModelSim
- VHDL, C, C++
- Autocad Fusion 360

Language

Italian C2
Mother tongue

English C1

Spanish B1

French B1

Experience

11/2021 - 11/2024 | PhD Candidate – Antenna Research Scientist
CEA - Leti | Grenoble, FRANCE

French public government-funded research organisation where I pursued my PhD in collaboration with Sorbonne University. In these years I have:

- defined the mathemathical framework to design metasurfaces for arbitrary and equal power splitting in both transmission and reflection
- developed a tool, on MATLAB, for the analysis of Transmit-Reflect-Arrays based on array theory and physical optics
- designed the unit cells on commercial software (CST, Ansys HFSS)
- designed and simulated multiple Transmit-Reflect-Arrays with different sizes and steering angles by mean of commercial software (CST, Ansys HFSS)
- realized several prototypes to verify the mathematical approach and the final performances
- designed and fabricated supports for the measurement setup by mean of mechanical software (Autocad Fusion 360)
- performed several measurement campaigns in the CEA-Leti anechoic chamber to extract the radiated patterns of the measured structures
- partecipated at several conferences

04/2020 - 10/2021 | Antenna & RF Engineer
PICOSATS SRL | Trieste, ITALY

Company committed to the research, development and commercialisation of cutting-edge telecommunications systems for the small satellite market and beyond. During my stay at the company I have worked on:

- design of a V-band antenna for ESA (project: *ARTES AT 5B.165)* in collaboration with ESTECO S.p.A. and University of Trieste;
- design and specification definition of a Ku-band Transponder;
- fabrication and testing campaign of the Ka-band horn antenna company product;
- design finalization and testing campaign project manager for the Ka-band Transponder for small satellites for ESA (project: *ARTES ITT AO/1-8465/15/UK/AD*).

Education

11/2021 - 11/2024 | Sorbonne University | Paris, FRANCE
Doctor of Philosophy - Ph.D. in Electrical Engineering

03/2017 - 12/2019 | Politecnico di Torino | Torino, ITALY
Master's Degree in Electrical Engineering - Wireless System Design
Thesis conducted in collaboration with the University of California Irvine (UCI) under the supervision of Prof. Ladislau Matekovits and Prof. Filippo Capolino on Fabry-Perot Cavity Antennas capable of generating overlapping apertures.

09/2013 - 03/2017 | Politecnico di Torino | Torino, ITALY
Bachelor's Degree in Electrical Engineering